City Research Online

City, University of London Institutional Repository

School of Engineering & Mathematical Sciences

OPTICAL CHARACTERISATION AND MODELLING OF RETURN VALVE FLOW IN DIESEL

FUEL INJECTION EQUIPMENT

Alberto Bonifacio

A thesis submitted for the fulfilment of the requirements of City, University of London for the degree

of Doctor of Philosophy

September 2018

Contents

List of Tables

List of Figures

Abstract

Extensive research has been carried out to understand the effects of cavitation in modern diesel injectors. In particular, the deposit formation causing damage to the injection system and injector itself, was linked to the pyrolytic reactions occurring during cavitating bubble collapse of the recirculating diesel fuel in the common rail. While the focus has mainly been on injector nozzles, where the soot was found, little research has been done on the return valve system, which presents a geometry susceptible to hydrodynamic cavitation.

This project consisted of creating optical accessible models of return valve systems in modern diesel injectors in order to carry out different experimental work on cavitation. Two acrylic models were designed with varying the outlet throttle diameter, $\emptyset225\mu m$ and $\emptyset245\mu m$, and one fused silica model with modified geometry due to manufacturing limitations. The solenoid mechanism responsible for sealing the return valve was also modelled using a needle regulated manually.

First of all, a characterisation of different fuel mixtures – a paraffinic model diesel fuel and n-hexadecane and n-octane mixtures in 80:20 v/v and 95:5 v/v proportions – was attained utilising a customised low pressure mechanical flow rig and high speed camera. Onset of cavitation was found to occur uniquely at the entrance of the outlet throttle, without affecting the high pressure fuel in the valve control chamber that regulates injection. Low needle lift, large outlet throttle diameter and small saturation vapour pressure of the fuel were all responsible of generating a pressure gradient that would therefore increase the upstream-to-downstream pressure ratios for incipient cavitation.

Moreover a high pressure recirculation rig was setup along an in-situ extinction measurement equipment in order to study the chemical variations of new conventional diesel fuel in the fused silica return model due to hydrodynamic cavitation. Following a spectral attenuation and UV-Vis spectrum analyses, changes were found for a 62:38 v/v proportion of respectively new conventional diesel and previously cavitated at high pressures diesel fuel. In particular, an increase of polycyclic aromatic hydrocarbons (PAH) as a consequence of the presence of particulates from the mixture. Conversely, whilst the UV-Vis measurements for the fresh batch of diesel fuel were inconclusive due to dilution complications, no variations were observed in spectral attenuation and the colouring of the fuel with time. Therefore, the upstream pressures were too low to initiate pyrolytic reaction forming soot formation.

Observations were made of a fluorescent phenomenon resembling a flame occurring in the high pressure recirculation rig, which after a spectral analysis, showed the presence of CH and H_2 molecules. It was thought to be an electroluminescence occurrence due to glowing of ionised particles in a fluid turned into plasma.

Finally a new comprehensive soot formation chemical model including paraffins mechanisms of PAH formation was developed and validated against previous experimental and computational data, allowing to study PAHs and aggregates formation in a surrogate diesel fuel cavitating bubble collapse. Simulations were carried out in an isotropic and polytropic temperature and pressure profiles, showing from the reaction pathways the importance of n-paraffins and naphthenes in the formation of mono-aromatics leading to soot formation.

Nomenclature

a: .... Polynomial coefficient.

Å: .... Angstrom.

Abs: ....Absorbance.

AC: .... Alternating current.

A_i: .... Pre-exponential factor.

amu: ....Atomic massu unit.

ASTM: American Society for Testing and Materials.

b: ....Length of light path through a sample.

BDC: ....Bottom dead centre.

BDN: .... Base diesel new.

BIN: ....Class of lumped pseudo-species.

BSS: .... Burner stabilised stagnation.

c: ....Concentration of chromophores.

C: ....Carbon.

C°_p: Standard state specific heat at constant pressure.

CFD: ....Computational Fluid Dynamics.

CGS: .... Centimeter-gram-second.

CR: .... Common Rail.

CW: ....Continuous wave.

DC: ....Direct current.

DI: ....Direct injection.

DOC: ....Diesel oxydation catalysts.

DPF: .... Diesel particulate filters.

ECU: ....Electronic control unit.

EDC: ....Electronic Diesel Control.

EFP: .... Electric fuel pump.

EGR: ....Exhaust gas recirculation.

E_i: .... Activation energy.

EUI: ....Electronic unit injector.

FAEE: .... Fatty acid ethyl ester.

FAME: .... Fatty acid methyl ester.

FBP: ....Final boiling point.

FCC: .... Fluid Catalytic Cracking.

FEM: ....Finite Element Method.

fps: ....frames per second.

f_x: .... Mole fraction of a species.

GC: ....Gas chromatography.

H: ....Hydrogen.

H°: ....Standard state enthalpy.

HACA: Hydrogen-abstraction-carbon-addition.

HMN: .... 2,2,4,4,6,7,7-heptamethylnonane.

i: ....Condition at specific time.

IBP: ....Initial boiling point.

I_o: Initial laser power incident to the absorptive sample.

I_P: ....Laser power measured by the detector.

I_{ref}: .... Reference detector laser power.

I_t: ....Transmitted laser power.

J: ....Joules.

k_B: .... Boltzmann Constant.

LNT: ....Lean NO_x traps.

MBSL: ....Multi-bubble sonoluminescence.

MUI: ....Mechanical unit injector.

n: .... Polytropic coefficient.

N: ....Nitrogen.

NIR: .... Near Infrared.

NOx: .... Oxides of Nitrogen.

N_P: ....Number of primary particles.

o: .... Initial condition.

O: .... Oxygen.

p: ....Pressure (bar).

PAH: ....Polycyclic aromatic hydrocarbons.

PDPA: .... Phase Doppler Particle Analyser.

PEMS: Portable emission measurement systems.

PIV: ....Particle Imaging Velocimetry.

PM: ....Particulate matter.

PN: ....Particulate number.

PZT: ....Lead zirconate titanate.

R: ....Universal gas constant.

r_f: Reflectivity of the ND0.03 neutral density beam filter.

S°: .... Standard state entropy.

SBSL: .... Single-bubble sonoluminescence.

SCR: ....Selective catalytic reduction.

SLE: .... Selective laser etching.

t: ....Time.

T: ....Absolute temperature.

TDC: .... Top dead centre.

t_f: Transmission coefficient through the neutral density filter.

t_{fs}: Transmission coefficient through the fused silica cell window.

Tr: .... Transmittance.

ULSD: .... Ultra-low sulphur diesel.

V: .... Volume.

VCO: ....Valve covered orifice.

W: .... Watt.

Z_{rot}: .....Rotational relaxation collision number.

Greek Letters

α: .... Spectral attenuation coefficient.

$α_{abs}$: .... Absorption coefficient.

$α_p$: ....Polarizability.

$α_{sc}$: ....Scattering coefficient.

$β_i$: Temperature exponent in the Arrhenius rate form.

γ: ....Polytropic ratio.

ε: ....Lennard-Jones potential well depth.

$μ_d$: .... Dipole moment.

σ: .... Standard deviation.

$σ_{col}$: ....Lennard-Jones collision diameter.

Acknowledgement

I would like to thank first of all my supervisor Dr. R. Lockett for choosing me to undertake this research project and trusting my abilities and determination to fulfil my objective of completing a PhD. His support, extensive knowledge, commitment to work and strive to perfection have taught me a lot throughout my research, and I will be forever grateful for this unique opportunity he has given me. His support, along with the financial support of Shell Global Solution, has allowed me to develop as an engineer. The small PhD team under his supervision at City, University of London, have been of enormous support to me and have always been ready to give me advice. In particular, Kassandra and Zeeshan who I would like to thank them not only for being my work colleagues and for sharing one of the most exiting chapters of my life, but also for becoming my closest friends and for supporting me in every circumstance.

Also City, University of London has been my second home for the past 8 years of my undergraduate and postgraduate studies. During this time, I have met many inspiring people, but I would like to mention Judit in particular, who I studied with during my undergraduate degree and gave me precious advice when starting my PhD research, and Israt, who inspires me every day to be happy and positive. I would like to thank other members of City staff, my second supervisor Pr. J. Nouri, and the technicians J. Ford and R. Cherry. In particular I am deeply grateful to the latter, for his professional expertise in providing me with the acrylic blocks and all his advice in assuring my experiments would not fail.

Other important people in my life who I owe my deepest gratitude are my closest friends Antonio and Federica, who despite the distance in miles, continue to bring joy to my life and I appreciate our friendship with all my heart.

Finally, I could have not made it without the relentless support of my family, who brought me up to believe in myself and to always aim high: to my younger brother Alessandro, who has followed my research progress with interest and is fascinated by anything related to engineering; to my older sister Guendalina, who is my role model in her way of living and loving; to my father Piero, who made sure I had the best education possible and gave me all the resources necessary to reach this point; and to my

mother Lesley, who I would like to dedicate this PhD thesis as a sign of gratitude for all she has given me and for allowing me to be the person I am today. Thank you.

Last but not least I would like to thank two other special people. To Toby, words are not enough to explain how grateful I am to have you in my life; you are a new chapter that I am looking forward to living. And to my grandmother Luisa, you represent all my grandparents who are not with us anymore; I am the proudest grandson having had you by my side. As you once mentioned to me, "*Sii buono ma non fesso*"… this is a quote I kept in mind throughout my studies and I will keep forever.

To my mother,

my source of inspiration

Chapter 1 Introduction

In recent years, common rail injection systems have taken over the traditional fuel injection systems for diesel engines, with the aim to improve the combustion process affecting the power cycle. In particular, a common rail system has the advantage of a better control, where injection rate shaping, duration, and variable timing and pressure are some of the feature that characterise this assembly. While in the past all these elements were controlled altogether at the same time during the engine camshaft rotation, instead the common rail is able to decouple pressure generation and injection. In particular the presence of the rail in the system acts as an accumulator of high pressure fuel which then is directed to different injectors through different fuel lines [1].

There have been many experimental and computational studies with the aim to analyse the diesel flow in a common rail system and to detect where changes are necessary.[2][3] A critical part of diesel injectors (DI) is the fuel injection system, i.e. when the high pressure fuel moves from an injector and gets sprayed in the combustion engine. Research has mostly focused on the atomisation of a fuel spray, which depends on factors such as upstream and downstream pressures, chemical and physical properties of fuels and the geometry of the nozzle holes in the injector.[4] Computational studies have aided the experimental work, especially when having to work with pressures as high as 3000bar upstream.[5] However, there are limitations when using computational simulations, especially in the modelling of cavitating diesel fuel, which is a predominant feature in common rail diesel engines.

Apart from the advantages reported earlier, issues have been uncovered in common rail diesel engines, in particular with deposit formation in the injectors. Despite improvements in the chemical properties of diesel fuel, such as ultra-low sulphur diesel and bio blends to remain in conformity with pollution regulations, deposits cause serious damage in the injector itself, such as blocking passages. Previous studies have led to the conclusion that variation in the chemical properties of diesel, i.e. adding lubricant oils and other additives, might have had an impact to this issue.[6] Nevertheless, by shifting the attention to the behaviour of the fuel in the injector has provided new results.

For instance, the high pressure accumulated in the common rail and directed onto the injectors in order to improve atomisation and fuel spray properties, has found to affect deposit formation. In particular, it

was found that in the parts of the system where high pressure fuel is released on to a low pressure region, a release of high temperatures and heat accompanied aging of the fuel and formation of soot traces. [6] For example, such areas correspond in the return system of a common rail, where an amount of the pressurised fuel does not get used for injection in the combustion chamber, but it returns back to the fuel tank for re-use through fuel lines. Returning the fuel to the tank allows keeping the system running with no hazards, such as over-pressurising the system. For the high pressure fuel to return back to the tank, it has to drop back to ambient pressure without affecting the rest of the injection process. Modern designs consist in utilising valves to regulate fuel through small orifices in order to keep the pressure in the injection line high and the pressure in the return line low.[7] However, these result in the fuel experiencing cavitation when flowing at high pressures through micro-passages.

Since the fuel that returns back to the fuel tank is the same fuel that will be re-utilised in the following injection cycle, it will have experienced cavitation already as it went through the high pressure pump, the common rail and the injector. Therefore a substantial amount of the fuel that eventually gets injected to the engine for combustion is the fuel that previously underwent cavitation when returning to the fuel tank in previous cycles. Hints of deposit formation have in fact been found in nozzle holes, and in other parts of the high pressure line in modern diesel injectors.[8] This impacts not only the internal flow in the common rail, but also the atomisation which occurs through the nozzle holes. As a consequence, the overall engine performance is reduced and chain reactions of issues are generated from there. The fouling presents itself carbonaceous in structure, and has a mixed amorphous and graphitic-like carbon composition.[9] Regardless of the type of diesel blend utilised, the properties of the deposits remain the same.

The cavitation phenomenon was found to occur in many parts of an injector, thus affecting the engine performance. In general, in order for creating the right environment for cavitation to occur, a fluid needs to flow through a narrow passage generating a high pressure difference. Locally, the static pressure may fall below the saturated vapour pressure, resulting in local boiling (hydrodynamic cavitation). As the pressure recovers, the previously generated vapour pockets collapse due to the work done by the surrounding liquid, thereby generating large vapour pressures and temperatures during collapse. The collapse of the bubbles, cloud or sheet generates a series of reactions that reflect pyrolytic degradation

and dehydrogenation.[9] In diesel engines, when cavitation becomes aggressive, it may present itself in forms of hydro-erosion and hydro-erosive grinding that can eventually destroy the engine.[10] Even though fuel injector industries are pushing to raise the common rail pressure as mentioned before to achieve better spray atomisation, it will not resolve the issue of deposit formation which could instead worsen due to greater occurrence of cavitation and pyrolytic reactions.

Ultrasonic cavitation has proved to be resourceful in understanding the correlation between cavitation and soot formation. Suslick et al.[11] demonstrated that n-alkanes can be broken down to lower alkanes and alkenes by sonication with similar characteristics to high-temperature pyrolysis. Price and McCollom[12] followed this with an assessment of testing diesel fuel stability using ultrasonic excitation.[13] It has been reported from ultrasonic cavitation that bubble temperature would reach 5000K when collapsing.[14]

From the observation found with the acoustic cavitation, attempts have been made to find the same correlations between hydrodynamic cavitation on diesel fuel and soot formation. Lockett and Jeshani[15] followed by Lockett et al.[16], found by recirculating diesel fuel in a high pressure cavitation test rig that mono-aromatics concentrations were decaying while the population of poly-aromatic hydrocarbons (PAH) and soot particles were increasing.

The objective of this project was to continue the research of hydrodynamic cavitation on diesel fuel shifting the attention to the return system in modern diesel injector systems. Little research has in fact been carried out on the hydrodynamic cavitation occurring when the high pressure fuel returns back to the fuel tank in an injector. Payri et al.[17]–[19] used silicone moulds in order to gain access to the internal geometry dimensions of the spill mechanism for computational purposes, while Aleiferis et al.[20] utilised 20x super scale transparent acrylic models of the spill mechanism to validate CFD cavitation models.

The project aimed first of all to characterise the flow arising when the solenoid armature lifts the return valve allowing fuel to flow back to the fuel tank. Acrylic models were designed to replicate the geometry of the two-stage pressure mechanism allowing the fuel spill. The material was chosen in order to allow optical access to the internal flow. The flow circulation was obtained using a customised

mechanical flow low-pressure test rig, designed to pressurise the upstream fuel before entering the inlet port of the model and to return it to fuel tanks from the outlet port. The solenoid mechanism responsible in injectors to open the return valve was modelled using a manually controlled needle. The characterisation of the flow involved taking images at different pressure, different fuels and needle lift conditions.

Secondly, the project target was to further investigate the effects of hydrodynamic cavitation on diesel fuel by utilising a high-pressure cavitation recirculation rig. A fused silica model, being a stronger material able to sustain higher pressures, was manufactured again to replicate the geometry of the two-stage pressure mechanism allowing the fuel spill. The flow recirculation rig allowed high upstream pressures to continuously flow through the model and produce hydrodynamic cavitation for a prolonged duration of time.

To track the variation in chemical properties of the diesel fuel, an in-situ laser extinction equipment was installed along with the high pressure recirculation rig. This enabled to evaluate the optical attenuation change while the fuel would run in the rig due to the cavitation phenomenon through the model. Samples of the same fuel were also taken at different intervals during the recirculation and analysed using a spectrophotometer, allowing to track the variation of particles concentration in the fuel through a larger bandwidth.

Finally, the project involved creating a new comprehensive soot-model mechanism to allow bubble collapse simulation due to cavitation in a surrogate diesel fuel. The purpose of this part of the project was to track down pathways leading to soot formation in surrogate diesel fuel under cavitating conditions.

The work presented in this thesis was distributed in ten different chapters. The content of each chapter is summarised as follows:

Chapter 1 introduces the topic of discussion in the thesis. A brief background of correlations between cavitation and soot formation in diesel fuel is presented, which then links to the purpose and objective of this project.

The introduction is followed straight away by Chapter 2, which consists of the literature review necessary to understand in more detail the topic of discussion in the thesis. The literature review spans over diesel fuel background, modern diesel engines and the topic of cavitation. In order to introduce the rest of the work involved in the project, this chapter reviews technical information published on diesel fuels and modern diesel engines, with particular attention to spill valves and the mechanism in which they work, along with reviews of previous work on cavitation and its correlation with diesel fuels, such as deposit formation.

The work carried out in the project is introduced in Chapter 3 and Chapter 4, on the characterisation of fuel mixtures arising when flowing in the two-pressure step mechanism involving the return of the fuel in the tanks. Chapter 3 explains the stages followed to the design of the acrylic models and fused silica model replicating the return valve, followed by a carful description of the setup of the customised mechanical flow low-pressure test rig and the methodology of the experiment. While Chapter 4 presents the results obtained from the experiments of all the models, focusing on comparison and implication to modern diesel injectors.

The second part of the project is described in Chapter 5 and in Chapter 6, where the effects of hydrodynamic cavitation are studied for diesel fuel recirculating at higher pressures through the fused silica model. Chapter 5 describes the experimental setup, in particular of the recirculating test rig, of the extinction measurement equipment and the UV-Vis absorption spectrophotometer. Due to the complexity of the experiment, the methods will also be included along with design modifications of the fused silica model to comply with the setup. Chapter 6 on the other hand will focus on analysing the results, in particular evaluating the spectral attenuation and the discrete sample spectral analysis to investigate the change in diesel fuel properties, and comparison between different experimental conditions. This chapter will also provide a repeatability statistical analysis effectuated for dilution in UV-Vis experiment.

Chapter 7 consists of a description of a new investigation on a fluorescence phenomenon detected while running the high pressure recirculation experiment. This chapter will firstly describe the equipment utilised, followed by the presentation of results and comments on the unexpected finding.

The final part of the project is presented in Chapter 8 and in Chapter 9, in regards of the kinetic mechanism modelling. The development of the new comprehensive soot mechanism is described in Chapter 8, along with a review of previous work carried out on computational chemical modelling and validation procedures carried out. Chapter 9 is focused entirely on examples of the application of the new mechanism. The examples provided are setup with the purpose to track the reaction pathways to deposit formation of a surrogate diesel fuel under temperature/pressure profiles encountered during a cavitating bubble collapse.

Finally, Chapter 10 is the conclusion of the thesis, summarising the major results of the different experiments and analyses carried out, along with recommendations for future work in this project field.

Chapter 2 Literature Review

2.1 Diesel Fuel Background

2.1.1 Refinement Process

Crude oil taken from the ground contains paraffin, naphthalene and aromatic hydrocarbon compounds, and can come either as 'light crude' or 'heavy crude', according whether the density is respectively low or high. The crude oil then needs to go through a refining process, in order to take out the high value products needed, from transportation fuels – i.e. gasoline, jet fuel and diesel fuel - to products such as wax or asphalt. The light crudes will contain more lighter products and less sulphur and nitrogen, and thus is easier to refine, while high crudes will need more processing in order to get the end product.[21]

The refinement process consists in three major steps:

1. *Separation process*: where components are separated according to their physical properties, such as boiling, without changing the feedstock

2. *Upgrading process*: where the quality of the material is improved by eliminating unwanted compounds through chemical processes, without changing the bulk properties of the feedstock

3. *Conversion process*: where the molecular structure of the feedstock is modified – 'cracking' of large molecules.

The most common type of separation process is distillation where different products are obtained from the crude oil according to the different boiling range. The oil, after being heated to remove vapour in a preheated train, is pumped into a distillation column where fractionation occurs: lighter elements rise in the column, while the heavier ones are collected at the bottom of the atmospheric column. [22] The products are drawn off on the side from the column at different heights, for instance light hydrocarbons such as propane and butane rise to the top, gasoline below it, followed by kerosene and diesel which are heavier. All that remains, the heavier products also called atmospheric bottoms, undergo a further distillation process at a reduced pressure, allowing a further separation which was not possible in the previous boiling conditions.

The products escaping the column need to be refined before being sold to a client, which is why hydro-processing is needed. It consists of a hydrogen addition option where hydrogen together with an active catalyst react together to give a more flexible and higher yields of liquid fraction in the products. The process will vary according to the type of feed, where catalysts are chosen well in size and shape in order to match the organometallic compounds found in the straight-run products. [23]

A more drastic change is when using thermal processes, also known as carbon rejected processes, to breakdown heavy hydrocarbons into lighter ones in a method called *cracking*, occurring in a network of one or more reactors along with furnaces, heat exchangers and other vessels. The main types of cracking are *fluid catalytic cracking* (FCC), also known as *cat cracking*, where the conversion occurs utilizing high heat, low pressure and powdered catalyst, and *hydrocracking*, where the conversion occurs utilizing slightly lower heat but greater pressure and hydrogen with different catalysts. Some of the other forms of conversions other than cracking are *coking*, where heat and moderate pressure turn residuum into lighter and hard coal-like products, *alkylation* where products of cracking are combined together in horizontal vessels, and *reforming* where heat, moderate pressure and catalysts turn naphtha into high-octane. [24]

The final diesel fuel product will depend on the blending of the different products stages during crude oil refinery, from straight-run products to hydrocracked gas oil, as shown in the schematic diagram in Figure 2.1.1. The blue path describes in particular the process to obtain diesel fuel, as explained above. It is difficult to control thoroughly the final composition of the fuel, since the blending is overruled by the initial composition of the crude oil, hence availability and cost play a major role when it comes to refinery.

A distillation profile curve can be generated, taking into account the initial boiling point (IBP), i.e. the minimum temperature at which the first drop of condensate starts evaporating, the final boiling point (FBP), i.e. the maximum temperature at which all the liquid has evaporated leaving just the final product, and the percent evaporated, i.e. the sum of the percentage recovered and the percentage loss. The curve is obtained plotting the percentage recovered against the boiling temperature.[25]

Figure 2.1.1   Crude oil modern refinery schematic diagram process[21]

2.1.2   Diesel Fuel Composition

Diesel fuel has a complex mixture belonging mainly to the hydrocarbon family, with carbon numbers between 10 and 22. As the word itself suggests, a hydrocarbon is a compound of carbon and hydrogen atoms, which can be divided again into 4 subclasses i.e. paraffins, naphthenes, olefins and aromatics. Each of these are different in size or geometry, in the ratio of hydrogen to carbon atoms and in the way the atoms are bonded together.

Paraffins follow the general formula of C_nH_{2n+2}, hence methane CH_4, ethane C_2H_6 and so on as the number of carbon atoms n increases. If the carbon skeleton follows a chain structure then the compound is called a *n-paraffin* (or *normal paraffin*), while if some carbon atoms branch of from the main backbone then is called a *isoparaffin*. One or more isoparaffins may have the same chemical formula, but will vary only structurally.

Figure 2.1.2   N-paraffin (above) and isoparaffin (below) structure examples[21]

$$CH_3\text{-}CH_2\text{-}CH_2\text{-}CH_2\text{-}CH_2\text{-}CH_2\text{-}CH_2\text{-}CH_2\text{-}CH_2\text{-}CH_3$$

$$CH_3\text{-}CH\text{-}CH_2\text{-}CH\text{-}CH_2\text{-}CH_2\text{-}CH_2\text{-}CH_3$$
$$\quad\quad CH_3 \quad\quad CH_3$$
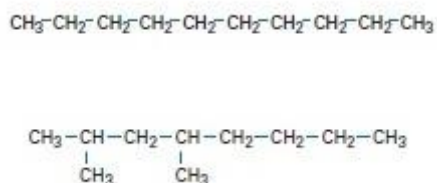
Olefins are regarded to be similar to paraffins for having the same linear structure, only that one or more double bonds between carbon atoms are present. The general formula for olefins with a double bond is C_nH_{2n}, thus less hydrogen. Even though they are less present in nature, they can be obtained through the refinery process. The double bond is shown in the example below.

Figure 2.1.3   Olefin structure example[21]

$$CH_2=CH\text{-}CH_2\text{-}CH_2\text{-}CH_2\text{-}CH_2\text{-}CH_2\text{-}CH_2\text{-}CH_2\text{-}CH_3$$
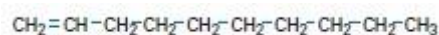
Naphthenes, similarly known as *cycloalkanes* and *cycloparaffins*, differ from the paraffins in their ring carbon structure, where five or six carbon atoms are bonded together to form a ring. These rings can then bond with each other to form even more complex structures. It is possible to observe the differences between Figure 2.1.2 above and Figure 2.1.4 below.

Figure 2.1.4   Naphthens structure examples[21]
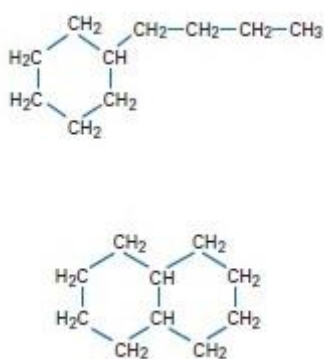
Aromatics are regarded to be similar to naphthenes from the ring structural point of view, only that the carbon atom bonds alternate between single and double bonds. The simplest aromatic is benzene C_6H_6 shown in Figure 2.1.5, thus with the general one ring formula is C_nH_{2n-6}, but more aromatic rings can bond together to form polycyclic aromatics.

Figure 2.1.5   Aromatic structure example [21]
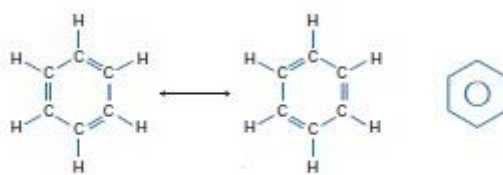
The single bonded compounds, i.e. paraffins and naphthenes, are saturated hydrocarbons, since no more hydrogen can be added without breaking the bonds; while on the other hand, olefins and aromatics are unsaturated since hydrogen can be added by simply breaking the double bonds, converting respectively into paraffins and naphthenes when all the bonds are single once again.

Other compounds present in diesel fuels are the *heteroatoms* such as sulphur, nitrogen and oxygen. Examples of this category are dibenzothiphene and carbazole, containing respectively an atom of sulphur, and both atoms of nitrogen and hydrogen.[21]

2.1.3   Diesel Fuel Specification

Following the refining process, the diesel fuel needs to comply with certain specifications related to ignition quality, self-ignition temperature, calorific value, flashpoint, cloud point, viscosity, sulphur content and surface tension.

The *ignition quality* or *readiness to burn* is measured using *cetane number*, an arbitrary scale measured from 1 to 100 using high and low ignition quality standards, i.e. 100 for hexadecane (also called cetane) for the high-quality and 15 for 2,2,4,4,6,7,7-heptamethylnonane (HMN) for the low-quality.[26] The quality of the fuel will determine; the diesel knock, i.e. rough running of the diesel through the engine and potentially damaging the apparatus; the anti-foaming, i.e. avoiding the foaming and odour originating as it re-fuels; starting of the engine, which will be faster and at lower efficient temperature as the quality increases.[7]

The *self-ignition temperature* is the temperature at which the diesel fuel is able to auto-ignite without means of a spark. For this reason, the lower this temperature is, the higher the fuel quality will be.

The *calorific value* is the amount of heat released by any fuel when burnt (J/kg) and is around 44 MJ/kg for diesel or slightly higher for low grade fuels. The more heat gets released during combustion, the more effect it will have on the power output.

The *flashpoint* of a fuel is the temperature at which vapour produced during combustion of the fuel burns momentarily and then goes out. Flashpoint of a fuel is a very important parameter in regards of safety precautions while storing or handling the fuel.

The *cloud point* is the temperature at which the wax present in diesel fuel starts to crystalize and to form solid particles. The fuel, in doing so, will have a cloudy appearance. It is possible to differentiate grades of diesel according to the season, where the winter diesel will have a lower cloud point than summer diesel due to weather conditions.

The *viscosity* in general is defined as the reluctance of a fluid to flow, hence the higher the viscosity is, the harder it will be for the fluid to flow smoothly. For instance, if a fuel is not viscous enough, then the interaction between moving parts in the injector may eventually fail due to the lack of lubrication. It is for this reason that it is important to use the right type of fuel in an engine, since each fuel has the right amount of lubrication for the operating engine.

The *sulphur content* has a profound effect on the fuel emission to the environment. Sulphur is actually an undesirable element in any fuel, since it can form sulphur trioxide when burnt, which combined with water produces sulphuric acid, responsible for erosion and harmful emissions. Nowadays ultra-low sulphur diesel (ULSD) fuels exist, and together with advanced oxidation catalyst the exhaust emissions due to sulphur are reduced even more.[7]

The *surface tension* is the tension force exerting at the boundary surface between two immiscible liquids – i.e. that do not mix – due to the out-of-balance attraction force between molecules.[27] This property is particularly important for atomization in fuel sprays, since it represents the force that resists the formation of new surface area. The minimum amount of energy required to achieve atomization is equal to the surface tension multiplied by the amount of surface area increase. This property decreases with increase in temperature and increases with increase in density.[28]

2.1.4 Emission standards

Diesel exhaust gases have been found to be carcinogenic, and their effect can vary according to size distribution, surface area, chemical composition and agglomerate state. It was found for instance that smaller particles can reach the bloodstream and then spread throughout the human body, leading to premature death.[29] A lot of research has gone into studying the environmental life cycle of diesel vehicles, and emission standards have been established in order to improve air quality.

Most countries in the world follow the European emission regulations, that go back 20 years ago to Euro 1/I in 1992 all the way to the most updated one Euro 6/VI in 2015, and apply for both light-duty (Arabic numerals) and heavy-duty (Roman numerals) vehicles. Considering that out of the 20 countries forming the G-20 international group, 17 are following the European emissions, that makes almost 90% of the global vehicle sales.

The aim of these standards is to reduce transportation emissions, in particular NO_x and sulphur content, for both light and heavy-duty vehicles. Euro 6 has decreased the NO_x limit from 0.18 g/km to 0.08g/km, i.e. a 56% reduction, which can be achieved by improvements in the after treatment technologies such as lean NO_x traps (LNT) or selective catalytic reduction (SCR) such as diesel oxidation catalysts (DOC) and diesel particulate filters (DPF).

EURO 5	EURO 6
Combustion improvements over EURO 4	Increased fuel injection pressure
Variable fuel injection timing for DPF regeneration	Smaller and medium-size engines (<2l) tend to use DOC + DPF and primarily LNT for NO_x control
DOC + DPF	Larger cars (>2l) use DOC + DPF +SCR
Some engines use lean NO_x	Some manufacturers offer EGR-only NO_x control (with no after treatment control) and DOC + DPF on medium and larger cars
EURO V	EURO VI
High fuel injection pressure	DPFs required for EURO VI compliance with PM and PN standards
Variable fuel injection timing and quantity	
Redesigns to combustion chamber	SCR catalyst changes from Vanadium to Zeolite
NO_x controlled mainly by SCR-Vanadium based systems	EGR no longer offered
EGR offered by few manufacturers and mainly for small trucks	

Table 2.1.1   European emission compliances for light and heavy-duty vehicles[30]

above in Table 2.1.1 is a summary of the EURO 5/V and EURO 6/VI compliances for both light and heavy-duty vehicles.

When applying these conformities to real-world driving conditions, light-duty cars have shown deficiencies in reaching the targets. Portable emission measurement systems (PEMS) as well as remote instrumentations have shown a higher emissions by a factor of 2-4 for NO_x over entire test routes (in rural, urban, uphill/downhill and motorway routes) and 14 for individual averaging windows. [31] On the other hand, heavy-duty cars have met expectations compared to previous EURO IV/V, by ensuring proper operation of the NO_x at low exhaust temperatures with stricter certification test protocols.[32]

2.1.5   Alternative diesel fuels

Apart from diesel fuel obtained through the refinement process explained in section 2.1.1, new research is finding ways to obtain economical replacements that meet the emission standards and have similar properties to the refined crude oil. These fuels are known as the alternative fuels, and can be used on their own or blended with the conventional fossil fuel.[33]

Biodiesel for instance is defined in the ASTM as the "fuel comprised of mono-alkyl esters of long chain fatty acids derived from vegetable oils or animal fats"[34], and thus is a form of renewable energy. The vegetable oils and animal fats are comprised of three fatty acids, i.e. hydrocarbon chains of varying lengths, bonded to a glycerol molecule in what is known as a "triglyceride". These undergo a transesterification process where the triglyceride reacts with an alcohol group forming three fatty acids bonded to the methyl group. The most common alcohol form is methanol to produce methyl esters, commonly referred as Fatty Acid Methyl Ester (FAME) and the cheapest one available. Or if ethanol is used instead to produce ethyl esters, it will be referred as Fatty Acid Ethyl Ester (FAEE). The final product has similar characteristics to conventional diesel fuel, with better lubricating properties, more complete combustion and no sulphur content but there is still research being done on the emissions from biodiesel fuel combustion.[35]

GTL represents the gas-to-liquid diesel produced from natural gas using the Fischer-Tropsch® refining process, where synthetic crude oil (also called syncrude) is produced by converting natural gas through a carbon monoxide-hydrogen intermediate using the Fischer-Tropsch catalyst. Further steps are then necessary to refine the fuel including isomerisation, hydrocracking/hydrotreating and fractionation process (See Section 2.1.1). It is mainly comprised of paraffins, nearly free of aromatics, olefins, sulphur

and nitrogen, with a cetane number in the range of 70 to 75, along with poor lubricity and poor cold flow properties. On the other hand, it is compatible with diesel fuel, so they can be mixed together in an engine. Improvements to production technology of GTL diesel are showing positive signs to this fuel in the marketplace.[21]

2.1.6   Fuel additives

The purpose of fuel additives in general is to improve or overcome operational issues when utilizing hydrocarbon fuels in any type of situation. These can be applied from the refinery process all the way to the storage tank and during use of the fuel, and can be used as a one-off to solve a specific problem or multiple times as part of a fuel. Generally, the amount of these additives is much lower than when blending fuels, typically 0.035 to 0.35% of the fuel volume compared to 3 to 20% in fuel blends. According to their use, they can be divided for refinery products, distribution system products and automotive performance enhancement products.[36]

A list of fuel additives for diesel fuels can be found in Ref. [37], two of which are explained in more detail in the following paragraphs.

The *cetane improver additives* include a series of compounds such as peroxides, nitrites, nitrates, nitroso-carbomates, tetra-azoles and thioaldehydes, which are able to decompose to form free radicals. These eventually accelerate the rate of chain initiation and ignition of diesel fuel. Since diesel fuel is made up of different components as shown in Sec. 2.1.2, it is important to carefully handle these products to avoid potential explosions. Cetane numbers can be increased normally to a maximum of 8 or 10 numbers. In general they improve fuel economy, the engine durability and emissions in heavy-duty diesel engines.

The *lubricity improver additives* are utilized to protect the fuel conducts from wear by forming an extremely thin adsorption layer in between two surfaces, which eventually squeeze out as the loads increase. The additives are generally fats, fatty esters, amides, fatty oils and esters that get adsorbed to the metal surface of the fuel pump by physical forces resulting in the formation of layers. These will have a strong effect from a molecular point of view, since they will change the kinetics and molecular interaction between the surfaces. Sometimes fuels have already enough lubricity properties due to the

heavier hydrocarbons present, such as sulphur. Due to the removal of sulphur in the new diesel fuels as explained in Section 2.1.3, the lubricants become a useful tool.

2.2 Modern Diesel Engines

2.2.1 Overview

Modern diesel engines operate in general in a cycle with a low pressure fuel supply system to link the fuel from the fuel tank to the fuel injection pump where it will reach the injection pressure. Along the route, there are fuel filters to clean as much as possible before starting the combustion process, and fuel return lines to allow the excess fuel to reach back the fuel tank. The three major components that control the running of a diesel engine are: the camshaft, which provides the timing of injection; the fuel injector, which actuated by the camshaft can meter and inject fuel to the cylinder for combustion at the desired pressure; the governor, which regulates the amount of fuel to be injected at the right speed.[38]

The main types of modern diesel fuel supply system are listed below:

- The *in-line injection pump* is characterised by the presence of a plunger fuel supply pump, which takes the fuel from the tank and pumps it to the secondary fuel filters to then reach the injection pump. Here the fuel has two options: the required portion is transported to the injector at the specified pressure, while the remaining excess portion goes through an overflow valve. An overflow restriction is also positioned at the fuel filters, to allow some fuel to always return back to the tank while in operation and to bleed off trapped air in the fuel.

- The *rotary fuel injection pump* has a vane type fuel supply pump mounted inside the injection pump, which takes the fuel from the tank through a single filter and pumps it directly to the injection pump housing. An overflow restricting orifice is located in this system to allow excess fuel to always flow back to the tank self-bleeding and cooling itself. In contrast to the in-line injection pump, where there are different high pressure lines for the different outlets, the rotary injection pump has a single high pressure system that delivers fuel through a distributor groove to multiple outlets corresponding to the number of engines.

- The *common rail fuel system* utilizes either an electric or gear pump as a fuel supply, which takes the fuel from the tank through a pre-filter and delivers it to the high pressure pump, where it undergoes a further cleansing through another fuel filter. Fuel is then collected in a common rail, and pumped to the different injectors and thus different engines. Return lines are located from the high pressure pump, common rail and injector.

- The *unit injection fuel system*, often referred as *tank-to-tank system* since almost all the fuel returns back to the tank, has a fuel supply pump which takes the fuel from the tank through a primary fuel filter and a heat exchanger electronically controlled and delivers it to a fuel gallery, where the pressure increases due to a fuel pressure regulator orifice. The majority of this fuel flows back to the tank, the rest is injected through the individual unit injectors. A check valve is also located before reaching the tank, to avoid fuel leaking while not in operation.[7]

2.2.2   Common Rail Fuel System

The most established definition of a "common rail" (CR) consists of the system described in Sec. 2.2.1 where a single stage high pressure pump increases the fuel pressure to the required injection pressure for combustion, and then distributed to the various injectors by means of a distribution gallery or know as rail. It can be found in passenger' cars, light and heavy-duty trucks, railway locomotives and ships up to 200kW/cylinder. One main feature of this system is its flexibility, in particular the ability to decouple pressure generation and injection cycle by means of the rail that acts as an accumulator. High injection pressure a decade ago would reach up to 1,800 bar, while more recent developments have allowed to reach pressures as high as 3000bar.[39] This can be achieved even at low engine speed and load. The different parts comprising the common rail are the low-pressure system, high-pressure pump, the rail, high pressure pipes, common rail injector, control valves and the electronic control unit (ECU).[40], [41] below is the general cycle of a common rail system:

Figure 2.2.1   Common rail system[42]

1. Fuel tank
2. Pre-supply pump
3. Fuel filter
4. High pressure pump
5. Rail
6. Pressure control valve
7. Rail pressure sensor
8. Injector
9. ECU
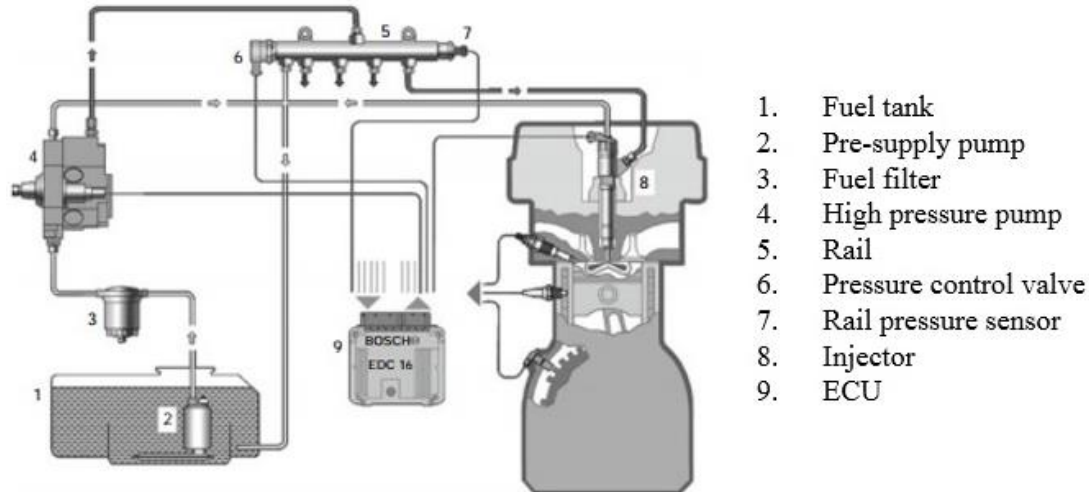
The *low-pressure system* is made up of elements 1 to 3 in Figure 2.2.1, and links the fuel tank with the high pressure pump. The fuel is drawn continuously from the fuel tank by means of an electric fuel pump (EFP) located either inside the tank or in the feed line, and any excess is returned back to the tank by means of an overflow valve. Before reaching the high pressure pump, the fuel is cleaned from impurities passing through a fuel filter. Finally a metering unit adjusts the quantity reaching the high pressure pump, returning the excess back to the tank.

The *high-pressure system* is made up of the pressure generation region, i.e. high pressure pump, the pressure accumulator region, i.e. the rail with pressure sensor and pressure control valve/pressure limiting valve, and the fuel metering, i.e. high pressure pipe lines and common rail injector. In this system, the fuel is transferred from the high pressure pump, driven by the engine to synchronize injection timing and pressures, to the injectors passing through the rail. The rail acts as an accumulator and as a pressure oscillation damper, which is why its design has to be optimized in order not to be either too big – as it would slow down pressure generation – or too small – as it would not be capable to eliminate pressure oscillations. Pressures in the system are controlled in three different ways:

*   High pressure side control, where the pressure control valve is positioned on the high pressure side so that excess fuel will go straight back to the tank in the low pressure region. In this way, pressure is maintained almost always constant in the rail, but there will be energy loss due to the direct channelling from high to low pressure systems. This control system can therefore be applied only to lower pressure injections, maximum 1400bar;

- Suction side control, where the metering of fuel is applied on the low pressure side on the high pressure pump. In this way, only the required amount of fuel is pressurized and transferred to the rail, thus better control of energy loss and lower temperature of the fuel returning to the tank. Furthermore a pressure limiting valve is mounted on the rail as a safety precaution in case of a fault while fuel is highly pressurized in the rail;

- Suction and high pressure side control, where the advantages of the two previously mentioned pressure control systems are united, with a metering unit mounted on the high pressure pump on the low pressure side and a pressure control valve mounted on the rail. The pressure is therefore controlled initially by the metering unit, and then further controlled in the rail in order to adjust to changes in the loading cycles. Another advantage of this combination is that more fuel can be drawn from the high pressure pump because of the additional pressure control on the high pressure side.

The high pressure lines connect the different elements of the high pressure system, and are made of seamless precision steel tube of equal cross-sectional area and short length to allow no alteration in pressure. From the rail, the fuel is directed in different injectors mounted and sealed on the cylinder head of the engine.

The *Electronic Diesel Control (EDC)*, finally, is responsible in coordinating the injection timing and injection fuel quantity throughout the system. The extreme precision of the duration of control by the actuators mounted in the injectors will determine the efficiency of the common rail. The most used types of actuators in diesel common rail are electromagnetic and piezo-electric.[42]

2.2.3 Pumps

The fuel injection pumps fundamental roles are: to raise the pressure of the fuel ready for injection; to accurately meter the amount of fuel that is necessary throughout the injection process; to accurately time the injection for each engine cylinder. Since there are different diesel engine systems as described in Sec. 2.2.1, there are also different high pressure pumps that can fulfil these requirements. Some of them are described below.

A *flange mounted pump* is a single constant stroke plunger type of pump, which is then mounted to the engine system by means of a flange mounting plate operated by a camshaft running in the engine block. The pumping elements are made up of a high quality alloy steel barrel and a plunger. The former is firmly positioned inside the pump house and has two diametrically opposed holes that correspond to the inlet and outlet (or spill) ports; the latter reciprocates inside the barrel and its main objective is to pressurise and meter the fuel by means of the helix or control edge, i.e. a vertical channel from which an annular groove is developed. The angular movement of the camshaft is converted into a linear movement of the plunger, facilitated also by a roller cam follower and a plunger return spring that allow the plunger also to rotate and to return to its initial position.

Figure 2.2.2 below shows the different steps that make the pumping mechanism. Initially the fuel enters through the inlet port filling up the volume above the plunger, which is at BDC, and the vertical channel and the annular groove volume – i.e. the helix. As the plunger moves upwards cam driven, it also rotates, closing the inlet port. The fuel is trapped and pressurised in the volume mentioned above until the delivery valve opens above allowing the fuel to reach all the way to the injector. Delivery will terminate once the plunger has moved far enough to open the spill port, where fuel is instead returned back to the tank, dropping the fuel pressure that was keeping the delivery valve open. By means of the plunger return spring positioned in the above area where the delivery valve is located, the plunger will return to its initial state ready for another cycle. [7], [43]

Figure 2.2.2   Flange mounted pump mechanism[44]

a) Bottom dead centre
b) Port closing (start of delivery) Maximum delivery
c) Port opening (end of delivery)
d) Port closing (start of delivery)
e) Port opening (end of delivery) Partial delivery
f) No delivery
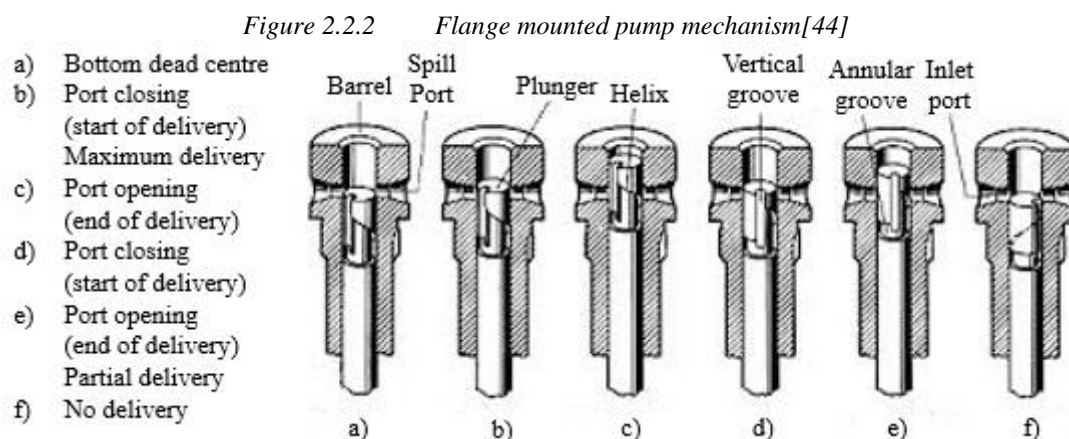
In an *in-line injection pump* there is the same single constant stroke plunger type of pump as in the previously explained flange mounted case, only that it is operated by a camshaft running in a separate fuel pump housing. Each pumping element linked to the camshaft have a plunger return spring, an upper

spring plate and a lower spring plate. While the plunger stroke is always constant, the fuel delivered is variable, and it depends a lot on the plunger design and precision. The alignment of the helix with the spill port can be anticipated or postponed according to whether more or less fuel needs to be delivered. Or other modifications such as machining retard grooves and upper helix are useful to control the start of injection.

Another kind of pump is the *distributor injection pump*, which has a single high pressure pumping chamber and plunger, serving multiple engine cylinders, allowing less weight and a more compact structure. There are different modifications to the distributor pumps depending on the method of fuel-quantity control, on the method of high-pressure generation and on the type of control system. This is summarised in Table 2.2.1 below.

Distributor injection pumps				
Volume control	Port-controlled		Solenoid-valve controlled	
Control method	Mechanical	Electronic (EDC)	Electronic (EDC)	
Generation of high pressure	Axial-piston pump		Axial-piston pump	Radial-piston pump
	VE..F	VE..EDC	VE..MV	VR

Table 2.2.1   Types of distributor injection pumps [45]

The first distinction is in the fuel-quantity control, which can be either port controlled – i.e. using ports, valves and channels to control injection duration and timing – or solenoid-valve controlled – i.e. using solenoids as an actuator. The former can be either mechanically driven, using governors, or electronically driven, using sensors, while the latter can only be electronically driven. A further distinction is in the high-pressure generation, which can be either using an axial-piston if the piston moves in an axial direction to the pump drive shaft, or using a radial-piston if there are different pistons located radially to the pump drive shaft. The four final distributor pumps distinction in Table 2.2.1 are a combination of all these qualities. As specified in the Bosch type code of Ref. [[45]], V stands for distributor type pump, E/R stand for axial/radial piston, F stands for mechanical governor, E stands for electric actuator and M stands for high-pressure solenoid valve.

The different parts of an axial-piston distributor pump are put together in Figure 2.2.3. The fuel from the tank enters the distributor pump through the vane-type supply pump (section 1), where a first

separation occurs for fuel going to the pump housing and fuel returning back to the inlet side. To insure self-bleeding and cooling of the equipment, an overflow restricting orifice allows fuel to return back to the tank (section 3). Fuel gets pressurised in the high-pressure stage (section 2) using a rotating plunger, with same characteristics as in the previously mentioned injector pumps, which moves horizontally from BDC to TDC. Each plunger stroke is called delivery phase and is divided in four stages:

Figure 2.2.3   Distributor axial-piston pump [7], [46]

1. Fuel supply pump
2. Pumping and distribution section
3. Mechanical governor
4. Solenoid shut off valve
5. Automatic advance unit
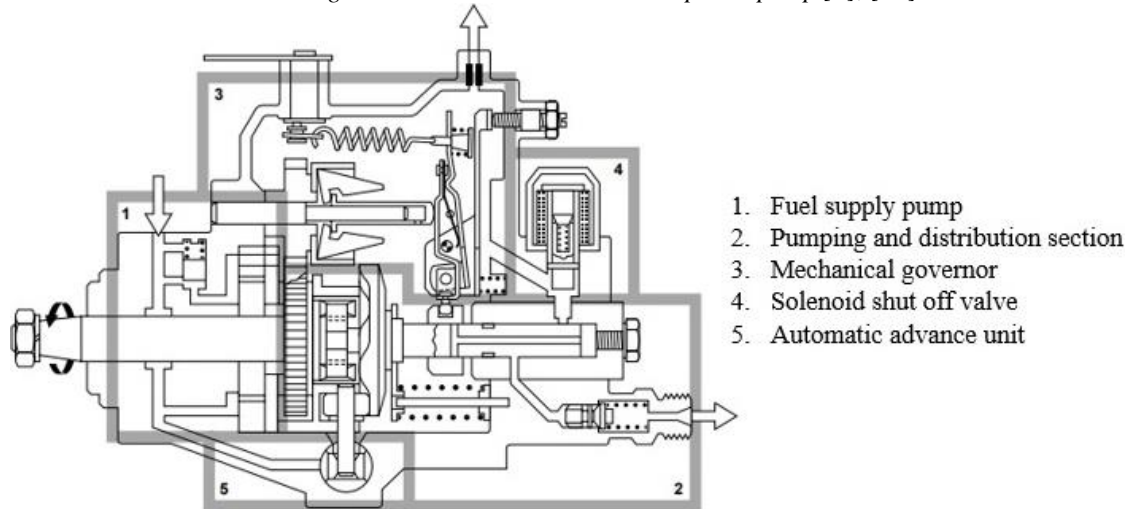
- Pre-stroke: once reached BDC, the plunger moves back towards TDC, closing the inlet passage. Fuel is gathered in the metering slot.

- Fuel delivery: Fuel gets pressurised as the plunger compresses the trapped fuel in the high-pressure chamber until the rotation of the plunger reaches the point where the annular groove coincides with the opening of the outlet port

- Residual stroke: delivery of the high pressurised fuel terminates once the control collar has moved the plunger far enough to open the cut-off port where the fuel is discharged in the pump housing. The decrease in the fuel pressure allows the plunger the move back to BDC. In a four-cylinder engine, the delivery phase coincides with one fourth of a plunger turn; while in a six-cylinder engine, the delivery phase coincides with one sixth of a plunger turn.

- Suction: the plunger moves from TDC to BDC, allowing fuel to enter from the supply pump occupying the volume above the plunger, also known as element chamber. The visual description of the cycle is shown in Figure 2.2.4.[7], [45], [46]

The delivery valve opens up once the pressurised fuel is strong enough to lift the piston flowing all the way to the common rail and diesel injectors (section 2). The whole engine is activated by means of a solenoid shut off valve, which gets energised and lifts the valve open when a key starts the engine, allowing the fuel to start flowing inside the plunger pumping mechanism (section 4), and vice versa. The injection timing is finally controlled in the pump in the automatic advance unit (section 5).

Figure 2.2.4   Pumping cycle in a distributor type fuel injection pump [46]

1. Metering slot
2. Distributor slot
3. High-pressure chamber
4. Outlet port passage
5. Control collar
6. Cut-off bore
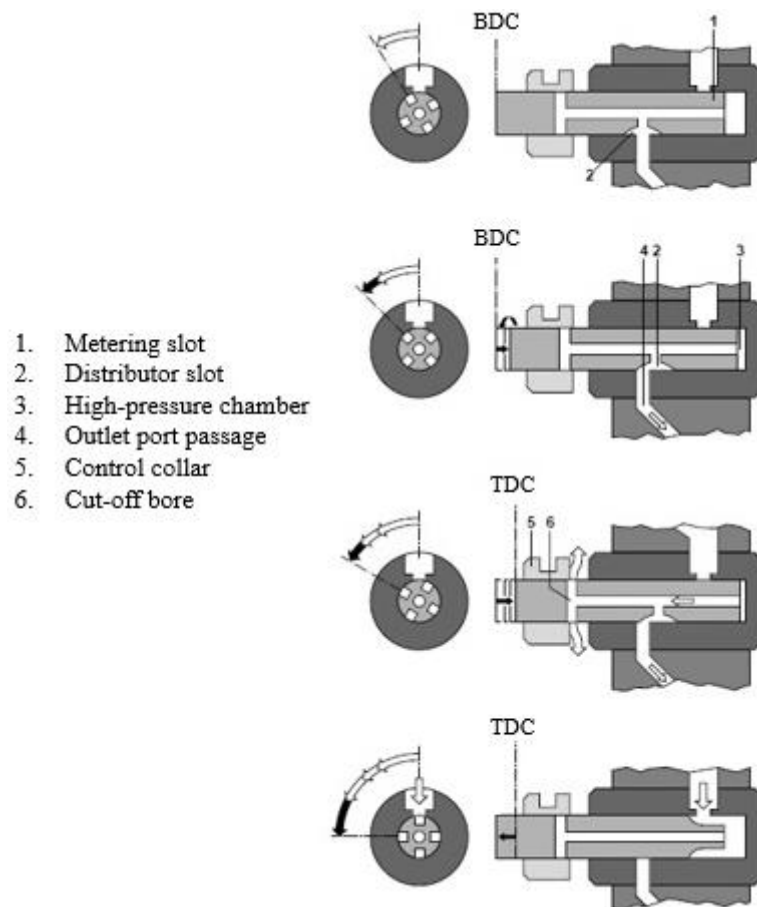
A radial-piston pump differs from an axial-piston pump mainly in the intake chamber, which is made up of a diaphragm chamber enclosed by an accumulator diaphragm, i.e. higher pressures can be reached compared to an axial design since there are multiple plungers sharing the delivery work – two plungers for either four or six cylinders, three plungers for six cylinders or four plungers for four cylinders. The delivery stroke consists of an induction phase and an effective stroke. In the former, the plungers move outwards allowing fuel to flow in the diaphragm chamber, past a solenoid needle all the way to the plunger chamber, while the excess fuel flows back to the

diaphragm chamber through the return valve. In the latter, the solenoid valve shuts and the fuel is trapped in the plunger chamber and increases its pressure due to the inward movement of the plunger, causing fuel delivery as soon as the cam shaft moves from BDC. When the solenoid valve opens again, the pressure drops bringing the injection stage to an end.[45] Figure 2.2.5 below shows a schematic of the two phases in the radial-piston pump.

Figure 2.2.5   Cross section view of distributor radial-piston pump [45]

a) Induction phase
b) Effective stroke

1. Delivery plunger
2. Distributor shaft
3. Control sleeve
4. Valve needle
5. Fuel return
6. Distributor body
7. Solenoid coil
8. Plunger chamber
9. High-pressure fuel
10. Annular groove
11. Accumulator diaphragm
12. Diaphragm chamber
13. Low-pressure inlet
14. Distributor slot
15. High-pressure outlet
16. Orifice check valve
17. Delivery-valve body

2.2.4   Injectors

Fuel injectors are mounted inside the cylinder, where the atomised fuel passing through microscopic holes at high pressures in the injector gets in contact with the hot compressed air from the cylinder causing combustion. This kind of injection is referred to also as direct injection (DI). Controlling the timing and amount of high pressure fuel to be injected are the injector needle and injector nozzle, the former responsible in opening and sealing the nozzle holes, the latter responsible in delivering the fuel in the combustion chamber at the optimal atomization and efficiency.

Fuel pumps and injectors work together in maintaining the fuel at high pressure. The most common types of fuel pumps/diesel injectors systems can be classified as follows:

The conventional *fuel pump and injector system*, where pump and injector are separated from one another, connected via fuel lines;

The *unit injection system* where the fuel pump and injector are assembled in the same housing. The camshaft, which operates the pump plunger (as explained in Sec. 2.2.3), will therefore operate the injector' needle valve at the same time. Operation can be mechanical or electronic. In the mechanical case (MUI), when the fuel is flowing through the delivery port (see Figure 2.2.2, Figure 2.2.4 or Figure 2.2.5), the high pressure of the fuel causes the spring that controls the needle to compress and thus open the valve for injection until the delivery port is shut again. In the electronic case (EUI), a solenoid valve controls the operation of the injection by energising and lifting the solenoid valve;

The *common rail injection system* where the fuel from the pump to the injector go through a common rail that stores the high pressure fuel and meters it to the different injectors. These injectors are controlled using both an electric actuator and hydraulic valves. A fundamental difference with the other systems is that high pressure generation and injection are decoupled[7]

Injector nozzles are the linkage between the high pressure pump system and the combustion cylinder. Here pressure energy previously accumulated is converted into kinetic energy. The whole nozzle assembly consists of a nozzle body with a high pressure inlet, a needle guide and seat, a spray-hole zone and an inward opening needle.

Nozzle bodies consist of three main designs: a pintle nozzle, with a single pin, not used anymore in DI engine designs; hole-type nozzle and nozzle modules, further divided in valve covered orifice (VCO) and conical or cylindrical sac-hole design (the difference stands in the volume under the seat edge, where in VCO the hole is covered by the needle in sealed positon, while in sac-hole the hole is not covered – shown in Figure 2.2.6). The needle guide centres the needle on the body seat in order to divide the high pressure region inside the injector and the low pressure externally. It allows a clearance of 1 to 5μm clearance maximum, since the higher the pressure is the more likely leakages can occur. The nozzle seat needs to be well sealed while no injection is taking place, and the diameter needs to be right for the pressure and amount of fuel being sprayed in the combustion chamber.

Needles are either lift-controlled or pressure-controlled. The former are especially used in common rail systems, where the pressure is constant from the injector inlet all the way to the nozzle tip, whereas the latter is used in cam-driven injection systems, where a metering valve prior entrance to the injector increases the pressure in the nozzle chamber until the needle is lifted.[42]

Figure 2.2.6   Nozzle bodies [42]

VCO   Conical sac hole   Cylindrical sac hole

2.2.5   Common Rail Injectors and Spill Valve Mechanism

There are two parts in a common rail diesel injector, a control and an injector section. The former is in the upper part of the injector, and it is responsible for setting the start and end of injection by using either a solenoid or a piezo actuator and a spill valve return system; while the latter is in the lower part of the injector, and it is responsible to deliver the high pressure fuel coming from the pump through the needle valve and nozzle body assembly into multi spray holes and eventually atomise into the engine cylinder. The combination of the two parts allow the whole injection mechanism to work in a cyclic and accurate manner. A description of the coordination of the different parts of the injection is explained below.[7], [47]

In a solenoid common rail injector, when the fuel reaches the injector from the high pressure pump it separates, flowing either through an inlet passage to the injection nozzle, or through an inlet throttle to the valve control chamber which is connected to the control section of the injector and regulated by the opening and sealing actions of the solenoid armature and ball valve on the outlet throttle (See Figure 2.2.7). The whole process can be summarised in four steps:

Figure 2.2.7   Solenoid injector [42]

a)   Injector closed
b)   Start of injection
c)   End of injection

1.   Fuel return
2.   Solenoid coil
3.   Overlift spring
4.   Solenoid armature
5.   Ball valve
6.   Valve control chamber
7.   Nozzle spring
8.   Nozzle needle pressure shoulder
9.   Chamber volume
10. Spray hole
11. Solenoid valve spring
12. Outlet throttle
13. High pressure port
14. Inlet throttle
15. Valve piston
16. Nozzle needle

- Injector closed: or resting state, is when the solenoid coil is not energised. Thus the solenoid spring keeps the ball valve sealing the outlet throttle, trapping the high pressure fuel in the injector section, i.e. in the valve control chamber and in the nozzle chamber volume (See Figure 2.2.7). The needle also is sealing the nozzle holes due to the pressure exerted by the fuel in the valve control chamber above the valve piston, connected to the nozzle needle;

- Start of injection: when the solenoid coil is energised by the ECU, an actuated electromagnetic force is generated that overcomes the solenoid spring force, allowing the ball valve to open the outlet throttle. The previously trapped fuel is now allowed to spill in the control section and return to the tank through the fuel return lines. At the same time the fuel pressure in the valve control chamber drops as the fuel flows from a high pressure region (injector section) to a low pressure region (control section). Meanwhile the inlet throttle to the valve control chamber keeps the pressure in the nozzle chamber volume at the rail pressure, creating therefore a pressure differential on the valve piston. This will cause the needle to lift and inject the fuel to the engine cylinder;

- Injector opened: when the needle reaches the top position, the injector is fully opened. The amount of fuel injected is proportional to the amount of time to the solenoid valve being opened (determined by the ECU), but it is independent from the engine and pump speed;

- <u>End of injection</u>: when the solenoid coil is de-energised, the ball valve returns to sealing the outlet throttle. The fuel therefore halts spilling back to the control section, and consequently the pressure in the valve control chamber starts increasing again all the way to the rail pressure. The pressure exerted on the valve piston matches the one in the chamber volume pushing the needle nozzle back to its sealing position, ending the injection. The injector is once again in a resting state, ready for another cycle. [42]

A piezo common rail injector differs with the previously explained solenoid injector mainly in the use of a piezo actuator. A piezo stack consists of a series of thin layer piezo crystals enclosed in a ceramic core that have the ability to expand when energised. The actuator stroke pressurises the hydraulic coupler which in turn exerts a force onto the servo valve. This will open once the pressure exceeds the one keeping the valve closed. The injection and fuel return stages are then the same as the ones shown in Figure 2.2.7. The advantages of this injector over the solenoid one are: reduction of moving parts in the injector; shorter interval between injections due to the direct link of the servo valve with the needle (in the solenoid valve, the control and injector section were linked via the valve control chamber); there are no spillages from high to low pressure region; lighter and smaller in size. [42] The piezo injector parts are shown in Figure 2.2.8.

Figure 2.2.8   Piezo injector [42]

1. Fuel return
2. High pressure port
3. Piezo actuator module
4. Hydraulic coupler (amplifier)
5. Servo valve (control valve)
6. Nozzle module with nozzle needle
7. Spray hole
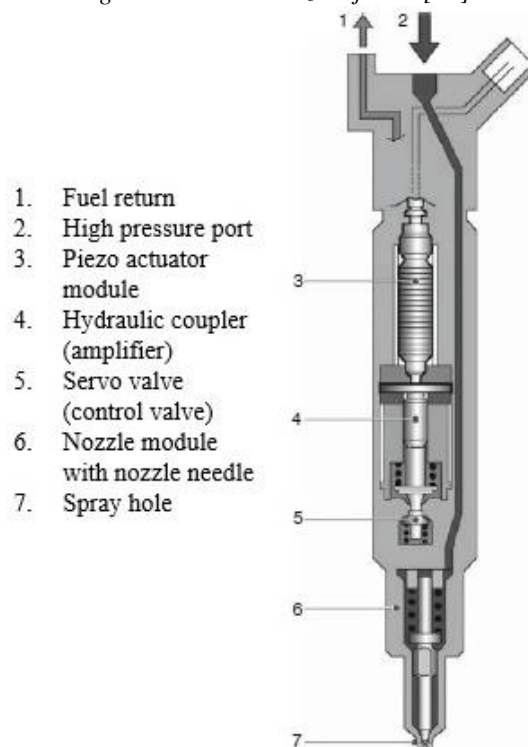
2.3 Cavitation

2.3.1 Overview

A general definition of cavitation is that of a drop of local pressure in a liquid below the vapour pressure of the liquid, causing the nuclei present locally to form vapour cavities which eventually collapse. The local pressure is defined as the sum of the mean pressure, which is the same throughout the area of the flow, and the dynamic pressure, which depends on the fluid motion. In a boiling process, for instance, the vapour cavities formed from nuclei when increasing the temperature start rising to the surface and enlarging due to decrease in pressure. At the surface they then explode, releasing the vapour to the surrounding environment. Therefore cavitation differs from boiling in the way vapour cavities are formed and destroyed. In a cavitation scenario, the vapour cavities will continue to grow as long as the local pressure is higher or equal to the vapour pressure. Once the critical diameter is reached, the bubble becomes unstable and ready to collapse if the surrounding vapour pressure is above the vapour pressure. [48]

Bubble formation in liquids can occur through four types of mechanisms: by homogenous nucleation, when within the liquid small gaps are formed between molecules due to thermal motions of the molecules; by heterogeneous nucleation, occurring at the interface between a liquid and a solid surface; by presence of microbubbles, which are stable under surface tension but grow into macroscopic bubble as tension increases; by external radiation, due to the energy released as the high cosmic particle hits a molecule in the liquid, causing nucleation. The mechanism that prevails in a liquid is the one that occurs at the lowest tension, and this can differ between liquids according to the thermodynamic state and the characteristic of the sites where nucleation would occur. In the cavitation context, the focus of nucleation site is within the body of the liquid, while for boiling this is at the liquid surface boundary. For this reason cavitation prediction and control of nucleation sites is more challenging. [49]

There are various definitions of cavitation number, i.e. a non-dimensional quantity defining how close the liquid pressure is to its vapour pressure, according to the situation to analyse. In Ref. [48], [50] for instance a definition of cavitation number is given for valves or any other device that create a head loss:

$$\sigma = \frac{p_d + p_b - p_{va}}{\Delta p} = \frac{p_d - p_{vg}}{\Delta p}$$

<div align="right">2.3.1</div>

$$\sigma = \frac{\Delta p}{p_u - p_{vg}}$$

<div align="right">2.3.2</div>

where σ is the cavitation number, p_d is the downstream pressure (unit Pa), p_b is the barometric pressure, p_{va} is the absolute vapour pressure, Δp is the net pressure drop $(p_u - p_d)$, p_{vg} is the saturated gauge vapour pressure $(p_{vg} = p_{va} - p_b)$ and p_u is the upstream pressure. The choice of using either Eq.2.3.1 or Eq.2.3.2 is subjective and depends on whether p_d or p_u is known or constant.

Another definition where Δp is not easily determined experimentally is given by the following equation:

$$\sigma = \frac{p_u - p_{vg}}{\frac{1}{2}\rho_L v^2}$$

<div align="right">2.3.3</div>

where ρ_L is the fluid density (unit $\frac{kg}{m^3}$) and v is the mean velocity (unit m^2) – the term $\frac{1}{2}\rho v^2$ represents the dynamic pressure. [48], [49]

Cavitation inception will depend however not only on the cavitation number, but also on other factors such as the Reynolds number Re, the liquid temperature, the liquid quality (i.e. nuclei and amount of gas present within the fluid) and the quality of the bounding surfaces. For this reason it is not possible to assume cavitation inception to occur at the minimum pressure coefficient C_{pmin} of the fluid, since viscous and turbulent effects add ulterior aspects to take into consideration. In an experimental environment the calculation of cavitation inception becomes problematic as well due to cavitation hysteresis, where the measured pressure at which cavitation disappears when raised may be different to the one at which cavitation occurs when decreased.[51]

2.3.2 Bubble dynamics

The three main requirements for cavitation to develop are therefore the presence of nuclei in the system, the local pressure to drop below of vapour pressure and the ambient pressure surrounding the vapour cavity to be greater than the vapour pressure to allow collapsing. The bubble dynamics is

best described using the non-linear Rayleigh-Plesset equation or variations of it, which relates the bubble spherical radius with the upstream far pressure:

$$\frac{p_B(t) - p_u(t)}{\rho_L} = R\frac{d^2R}{dt^2} + \frac{3}{2}\left(\frac{dR}{dt}\right)^2 + \frac{4v_L}{R}\frac{dR}{dt} + \frac{2S}{\rho_L R}$$

<div align="right">2.3.4</div>

where p_B is the pressure within the bubble, R is the radius of the bubble (units in m), v_L is the liquid kinematic viscosity (units in $\frac{m^2}{s}$) and S is the surface tension (units in $\frac{N}{m}$). Equation 2.3.4 can only be applied if the bubble is far from a solid surface to avoid disturbances during collapse, and it assumes a spherical shape of the bubble with constant liquid density and kinematic viscosity, along with uniform temperature and pressure inside the bubble. Rayleigh was the first to analyse the problem of cavitation and bubble dynamics, disregarding however the viscous and surface tension terms, while Plesset later on extended it to travelling cavitating bubbles. [51], [52]

Bubble growth once the cavitation nuclei are formed will depend on other factors as well apart from the compressibility of the fluid, such as mass diffusion and thermal effects (also excluded in Eq. 2.3.4). For the mass diffusion, Henry's law applies as follows:

$$p_{GE} = Hc_\infty$$

<div align="right">2.3.5</div>

where p_{GE} is the partial pressure of the equilibrium gas, H is Henry's law constant for the gas and liquid combination and c_∞ is the saturated concentration. This law correlates the concentration of a gas in a liquid with the partial pressure of that gas in equilibrium with the liquid, stating that they are proportional by a given constant H, which is also temperature dependent. In the case of a cavitation nucleus filled with a particular gas, when there is a pressure drop inside, it follows that also the concentration will reduce due to Eq. 2.3.5, forcing the gas to diffuse in the surrounding liquid. If then the surrounding pressure of the liquid is much greater than the partial pressure of the gas filling the microbubble, then this will eventually dissolve completely. The indefinite presence of these nuclei in the liquid despite this law can be explained either by the bubble interface which is immobilised by the effects of surface contamination, or by the bubble imbedded in a solid particle in the liquid known as the Harvey nucleus. Moreover, the bubble growth by mass diffusion is encouraged by the external

pressure oscillations occurring also in an under-saturated liquid, known as 'rectified mass diffusion'. In fact, with the assumption of the spherical shape of a bubble, the average surface area during mass inflow is greater than the surface during mass outflow, hence causing an increase of mass inside the bubble.[51]–[53]

The thermal effect plays a role on the bubble growth on a later stage, after what is known as the 'first critical time' given by:

$$t_{cr} = \frac{p_v - p_\infty}{\rho_L} \frac{1}{\Sigma^2}$$

2.3.6

where p_∞ is the ambient pressure and $\sum$ is the thermodynamic parameter dependent only on the liquid temperature (unit $m/s^{3/2}$). After this time, the inertial, viscous, gaseous and surface tension terms in the Rayleigh-Plesset equation become less significant. A temperature difference develops between the bubble interface and the rest of the liquid, becoming a thermodynamic benefit since it slows down the cavitation while initiating a thermally controlled growth of the bubble. The higher temperature inside the bubble increases the vapour density and therefore the size of the bubble. Other factors may compromise the thermal effect, such as non-equilibrium effects at the interface, surface roughness, heat convection between the bubble and the liquid. [48], [52]

The bubble collapse begins when the bubble reaches a maximum radius generally 100 times greater than the original size, and a very small partial pressure of the gas. Rayleigh-Plesset equation can be integrated from the bubble surface interface and a position in the liquid far away from the bubble, giving a solution for time of collapse in terms of maximum bubble radius:

$$t_{collapse} = 0.915 R_{max} \sqrt{\frac{\rho_L}{\Delta p}}$$

2.3.7

where Δp is the pressure difference at the bubble interface. As a consequence high pressures and temperatures are generated, and potentially shock waves and noise can develop. In general, the energy released by the bubble collapse dissipates in creating: a new bubble due to a partially elastic rebound; shockwaves; electromagnetic radiation (when visible, this is known as *sonoluminescence*); liquid jets; thermal motion; cold nuclear fusion. [49], [54]

Not all bubbles follow the sphericity assumed with Rayleigh-Plesset equation, and the energy released during collapse will depend on its geometry. A bubble becomes most unstable when under the influence of non-spherical perturbations. For instance, when a bubble is close to a solid wall or a free surface, it will develop a re-entrant jet as the result of the surface of the bubble further from the wall accelerating faster inward compared to the rest of the bubble. Researchers such as Lauterborn and Bolle, and Plesset and Chapman have theoretically and computationally analysed the asymmetrical bubble collapse when close to a solid boundary. [55], [56]

When more than one bubble in a fluid experience the same level of unsteadiness, they create a cloud of cavitating bubbles which form and collapse periodically causing what is known as *cloud cavitation*. These may originate naturally due to vortices in a flow filled with bubbles, typically turbulent flows, or due to external disturbances. Once the cavitation has spread throughout the flow due to pressures being very low to the extent that the cavity length is greater than the body dimension, the cavitation cloud will turn into *super-cavitation* ($\sigma << \sigma_{inception}$). In turbulent flows for instance, eddies play an important role in contributing to cavitation as their pressure is lower than the surrounding mean pressure. If the cavitation nucleus gets trapped in the turbulent eddy when the pressure drops to vapour pressure, then it will start to grow until reaching the critical diameter. As it continues to grow however the eddy loses eventually its rotational speed, allowing the pressure to no longer be vapour pressure and hence the surrounding mean pressure is able to collapse the now unstable bubble. If however at the moment of collapse the bubble had not reached the critical diameter yet, then it would not be considered as a cavitation. [48], [49], [57]

There are different shapes and forms for cavitation to occur.

Gogate et al. [58] have differentiated the different types of cavitation in four categories:

- Hydrodynamic cavitation: the pressure varies due to the geometry that affects the velocity change;

- Acoustic cavitation: the pressure varies due to sound waves, usually ultrasound waves in the range of 16kHz to 100MHz;

- Optic cavitation: the pressure varies due to photons of high intensity, such as laser, that cross the liquid continuum;

- Particle cavitation: the pressure varies due to a beam of elementary particles, such as a neutron beam, that cross the liquid continuum.

This chapter will focus on analysing hydrodynamic and acoustic cavitation, which are more related to diesel fuel.

2.3.3   Hydrodynamic cavitation

Reynolds was the first to notice the formation of bubbles in glass Venturi tubes in the area where the tube is constricted. In particular, he noticed how these bubbles would explode as the tube cross-sectional area increased when close to the saturated vapour pressure. The explanation lies behind the fact that as the tube narrows down to the orifice, the velocity of the fluid increases while the pressure head reduces. At the exit of the orifice, the opposite occurs but at the same time the liquid separates and becomes turbulent along with the formation of eddies: in this region the pressure loss is inevitable. If at a specific velocity the pressure becomes below the vapour pressure in the Venturi, this will cause the formation of bubble cavities that eventually collapse once the pressure recovers downstream, releasing gases in the cavitating liquid.[59], [60]

Hydrodynamic cavitation is therefore obtained any time a fluid goes through a geometry similar to a venture or orifice plates, where the change in geometry allows the pressure change and the generation of cavities. Many studies of this type of cavitation have been carried out on different types of fluids, such as Gogate et al. [61], where they have analysed the dependence of the cavitation bubble dynamics while varying different parameters such as upstream pressure, initial cavity size and orifice geometry. It was found that: an increase in inlet pressure would increase the throat pressure and cavitation number while decreasing the cavity generation; smaller initial radius of cavity would lead to a higher pressure at which collapse would occur; a greater orifice radius would mean a higher cavitation inception number and thus a higher pressure needed for collapse.

This form of cavitation therefore develops in a liquid in motion. Impurities or any other gas bubbles present will cause the fluid streamlines to curve around them and form a stagnation point where the

flow is split into outer flow – that carries on downstream – and re-entrant jet – that moves upstream around the cavity. As the re-entrant jet loses momentum upstream, it splits the cavity forming a cavitation cloud – shedding. Eventually, as the cloud moves downstream with the fluid it will collapse and the same process will repeat itself as show in Figure 2.3.1. [62]

Figure 2.3.1   Developed hydrodynamic cavitation [62]
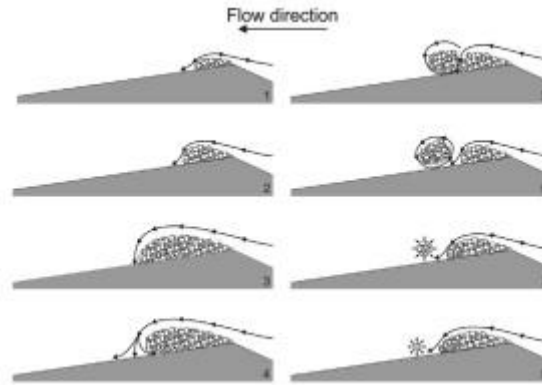
There are different factors that affect the intensity of hydrodynamic cavitation. First of all the difference in upstream and downstream pressure to where the cavitation occurs plays an important role. In general, by increasing the upstream pressure, which energises the flow, the cavitation will become more aggressive. This intensity will reach a maximum threshold when the pressure ratio between downstream and upstream pressure is 0.01. It is possible therefore to vary the intensity of the bubble collapse by simply varying either the upstream or downstream pressure, until the optimum pressure for the cavitating region is obtained. [63]

Figure 2.3.2 below shows how Soyama and Hoshino [63] investigated in a Venturi tube the hydrodynamic cavitation developing at the throttle, where the cross sectional area is at its minimum. By keeping a constant downstream pressure of 0.12 MPa and varying the upstream pressure from 0.4 to 0.6 MPa, it was noticed that the intensity of the cavitation – shown by the white bubble cloud – would increase as the cavitation number σ (calculated using Eq. 2.3.1) decreases. While on the other hand, constant upstream pressure of 0.6 MPa, and small increase in downstream pressure from 0.12 MPa to 0.2 MPa, showed that the length of the cavitation region would decrease as a consequence of the increase in σ.

Figure 2.3.2   Cavitation in a Venturi tube with constant downstream (left) or upstream (right) pressure [63]
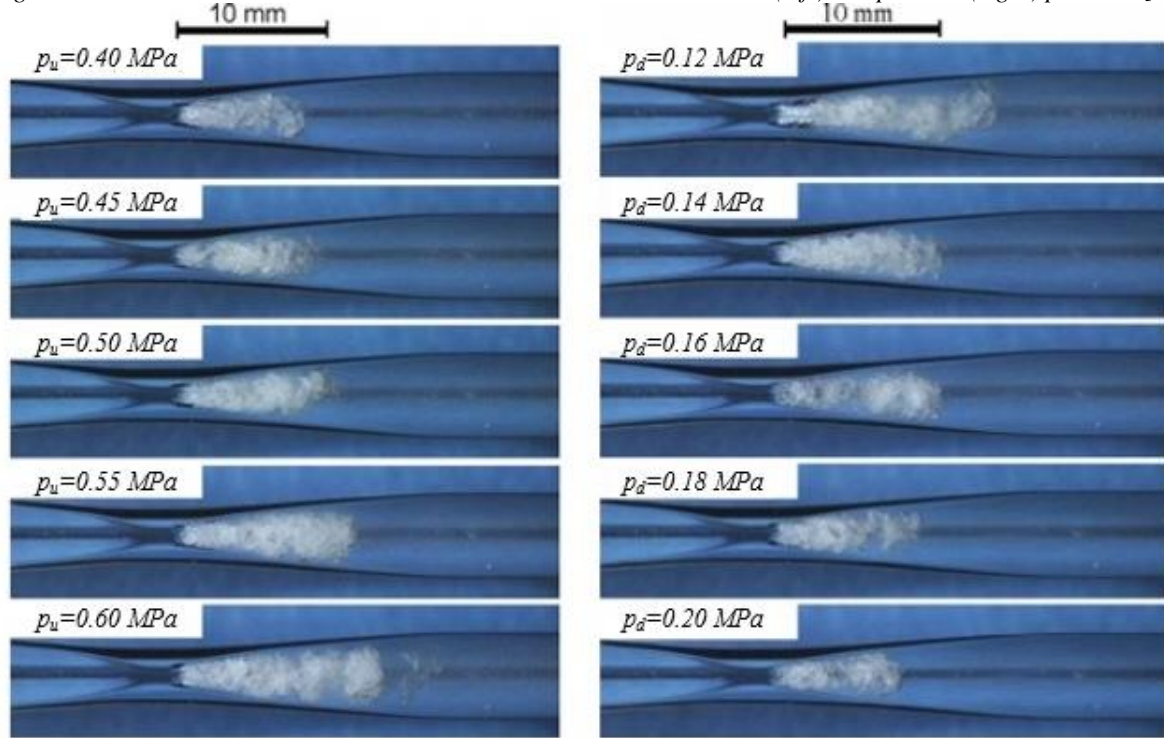
Another important parameter that affects the efficiency of the hydrodynamic cavitation is the geometry of the cavitating device. There have been studies on degradation of different pollutants when going through a single or multi-hole orifice, where it was concluded that changing the flow geometry – the perimeter of cavitating hole, divergence angle, etc. – improves the hydrodynamic cavitational yield. In particular, for the same flow area, the frequency of turbulence is more likely in the case of a multiple smaller hole rather than less greater holes, which will eventually lead to cavitation. [64], [65] Other studies have focused on the actual design and optimisation of cavitating devices, such as Saharan et al. [66] who have taken a Venturi tube and tested the degradation of orange-G dye through different geometries, a circular Venturi, a slit Venturi and orifice plate. While the intensity and number of cavitational events could be controlled by the geometry of the cavitating device – for same inlet pressure a lower σ was recorded for both Venturi designs compared to the orifice plate – the maximum cavitational yield for a specific geometry could only be determined when considering different parameters at the same time, such as inlet pressure, cavitation number and flow properties.

2.3.4 Acoustic cavitation

The general definition of acoustic cavitation is that of the growth and collapse of pre-existing microbubbles present in a fluid due to the influence of ultrasonic waves. The presence of dissolves gas nuclei in a liquid, which is the case under a general circumstance, has a strong impact on this form of cavitation, since an ultrasound passing through a liquid medium will progressively grow and collapse the microbubbles. [67]

Back in the 1930s ultrasound was utilised already for degradation of chemical chains, as it was observed that the viscosity of the solutions of starch and agar would then decrease. As years went by, high-intensity ultrasound was utilised to allow breakage near the middle of the chain. Ultrasound nowadays is used from medical imaging to industrial applications. The focus of ultrasound is to initiate chemical reaction to create, enlarge and then implode gaseous cavities in a liquid in the form of cavitation, known as *sonochemistry*. [68] The acoustic pressure from the sound wave in the liquid can be described by:

$$p_A = p_M \sin(2\pi \nu t) \qquad\qquad 2.3.8$$

where p_A is the acoustic pressure (Pa), p_M is the wave amplitude (Pa) and ν is the sound frequency (Hz).[69]

Sound waves in general always consist of a compression cycle and an expansion cycle, where the former exerts a positive pressure on the fluid, keeping molecules together, while the latter exerts a negative pressure on the fluid, keeping the molecules away from one another. Every liquid has a tensile strength, and if during the expansion process of the ultrasound the negative pressure that pulls the molecules away is greater than the tensile strength, then the cavities are formed. Tensile strength in a liquid is reduced as gases are trapped in small solid particles.

Bubbles are generally unstable, and if large they will float and burst at the liquid surface, while if small they will dissolve in the liquid. Under the effect of ultrasonic waves, these bubbles will continue to absorb energy from the waves, and can either oscillate in size or the size can continue to grow. The intensity of the wave has therefore a great impact: if the intensity is high, during the expansion cycle the bubble will grow so much that it will not have time to shrink during the compression cycle; if the intensity is low, the bubble will oscillate in size during the compression and expansion waves. Low

intensity waves will cause the bubble to grow progressively since the diffusion of the particles in and out of the bubble varies according to the surface area; as the outer surface is always greater than the inner one, there will be more diffusion in the bubble during the expansion process compared to the diffusion out during the compression process.

The critical size of the bubble is reached once the optimal amount of energy is absorbed from the ultrasound in the bubble. Once the amount of energy is not absorbed as efficiently anymore from the sound waves, then the bubble has no more energy to sustain itself causing the surrounding liquid to collapse the bubble and the cavity therefore implodes. The image below shows the bubble journey from formation all the way to implosion, as it goes through oscillation in size due to positive pressure, represented by the dark colour blue, and negative pressure, represented by the light colour white.[14]

Figure 2.3.3   Bubble growth and implosion in acoustic cavitation [14]
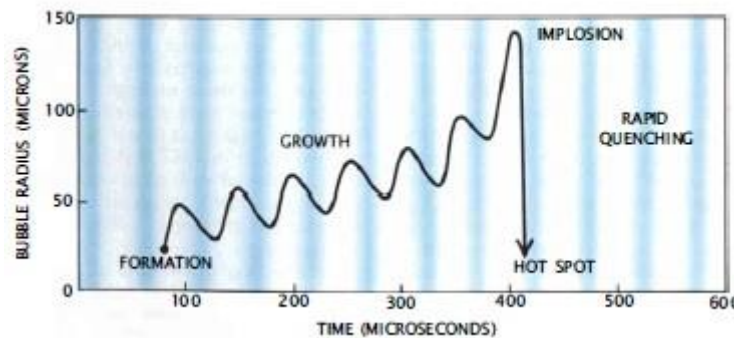
The hot spot in Figure 2.3.3 represents the moment after the implosion of the bubble, where the content inside the bubble is compressed to the point that very high temperatures and pressures are generated in a form of hot spot. The intensity of the implosion will vary according to the acoustic frequency, the acoustic intensity, the ambient temperature, the static pressure, the type of liquid and the type of ambient gas.

Due to the nature of this type of cavitation and the possibility to recreate ultrasonic waves, many studies have been performed by researchers to understand the parameters affecting the formation and implosion of bubbles under these circumstances.

The effect of the acoustic frequency and intensity was studied by Moholkar et al. [59] for example, using numerical methods and simulations on the Rayleigh-Plesset equation. In particular, they found

that high frequency and high intensity play an important role in longer bubble life. The higher the frequency is, the longer time is required to collapse a bubble or to create a bubble during compression cycle. Hence, a high intensity is necessary in order to form the bubble in the short period of the compression cycle. Also they found that according to the initial size of the cavity produced during the compression cycle there would be different consequences: a smaller cavity will grow more than larger bubbles but will have a shorter lifespan, and it will produce a higher pressure pulse upon collapse (since the pressure pulse is directly proportional to the ratio of the initial to final bubble radius).

Ambient pressure and ambient temperature surrounding the bubble are also crucial in the development of the acoustic cavitation. In particular Nagalingam et al. [70] investigated material removal mechanism in vibratory ultrasonic machining by varying pressure and temperature of the fluid, respectively from 100kPa to 400kPa and 10˚C to 90˚C. From results of the material removal, they concluded: that an increase in pressure forces vapour pressure bubbles to implode inside the liquid medium far from the solid surfaces, creating shock waves that will eventually corrode the material; and that an increase in temperature will also intensify the bubble implosion up to the boiling point, at which point bubbles are unable to trap vapour gases inside them and just grow in size until they explode. An increase in ambient temperature will follow an increase in vapour pressure which will result in a less intense cavitational effect, since it will reduce the maximum pressure and temperature reached during collapse. [71]

The types of liquid and gas considered during an acoustic cavitation were also found to be of interest in research. In particular, a liquid surface tension was found to be inversely proportional to cavitational threshold, as demonstrated by Crum [72]; or a liquid viscosity was found to increase the cohesive forces within the liquid, requiring higher pressures to produce the same cavitational effect as in less viscous fluids. Similarly, increasing the gas content of a liquid will lower both: the cavitational threshold since there are more gas nuclei in the liquid; and the intensity of the shock wave released as the bubble collapses since the gas nuclei act as a 'cushion'. [71]

The generation of high temperatures and pressures due to acoustic waves can be expressed in the adiabatic equations:

$$T_{max} = \frac{Tp_M(\gamma - 1)}{p} \qquad\qquad \textit{2.3.9}$$

$$p_{max} = p\left[\frac{p_M(\gamma - 1)}{p}\right]^{\frac{\gamma}{\gamma - 1}}$$

where T is the ambient temperature (K), p is the pressure inside the bubble before collapsing (Pa) and γ is the polytropic ratio of specific heat capacities at constant pressure and constant volume. [13]

An interesting phenomenon obtained as a consequence of acoustic cavitation is that of *sonoluminescence*. This is light emission of a cavitating bubble in a liquid under high-temperature and high-pressure conditions in an ultrasonic field. In the hot spots created due to cavitation the excited molecules emit visible light (similar in colour to a flame from a gas stove).[14] The unusual phenomenon can be explained as the molecules in the hot spot created during the acoustic cavitation go from being initially excited to return back in their ground state, emitting as a consequence visible light. The figure below in particular shows the resemblance of spectra between the sonoluminescence of dodecane $C_{12}H_{24}$ and the combustion of methane CH_4, due to the formation and emissions of diatomic carbon in both cases.

Figure 2.3.4   Comparison of spectra produced by sonoluminescence of dodecane (top) and the combustion of methane (bottom) [14]
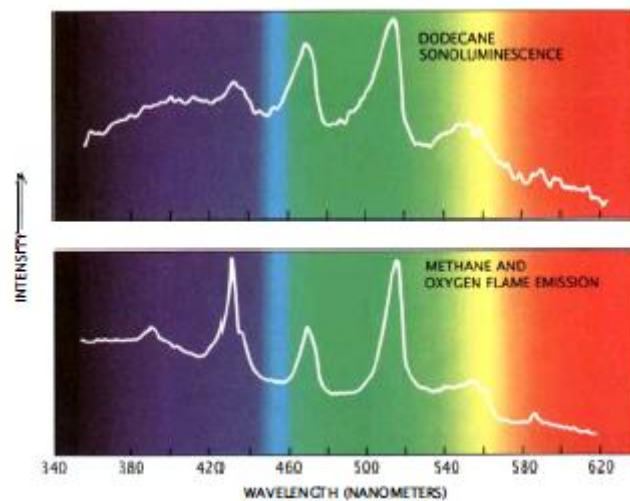
There are two types of sonoluminescence: multi-bubble sonoluminescence (MBSL), highlighted by Frenzel and Schulter [73]; and single-bubble sonoluminescence (SBSL), highlighted by Gaitan et al. [74]. When Frenzel and Schulter discovered the phenomenon in 1934 while exposing acoustic waves to photographic plates, they did not understand what were the necessary conditions for producing

sonoluminescence until in 1988 when Crum and Gaitan set up an experiment to generate sonoluminescence in a laboratory and find its association with the sound field.

The experiment set up by Crum and Gaitan consisted in levitating a gas bubble in an acoustic field, by using the acoustical pressure force to balance out the buoyancy force until the pressure was increased enough to allow the bubble to undergo non-spherical pulsations. The moment the bubble motion would then stabilise, a faint glow would appear from the bubble. The light therefore represents the collapse of bubbles in the sound field and the existence of high local temperatures enough to incandesce gas and cause a series of chemical reactions. It was found moreover by further research that SBSL is dependent on the gas concentration of the bubble, the ambient temperature of the fluid and the makeup of the surrounding fluid.[75]

Multi-bubble sonoluminescence is the emission of light from cavitating bubbles in a cloud with an applied ultrasound. The emission of light in a MBSL case was found to be synchronous with the applied ultrasound. A lot of research was done to investigate features of this kind of sonoluminescence and the difference with the SBSL. [76]

For instance, research by Didenko et al. [77] in the spectra of water showed a peak at 310nm, due to the excited state of OH radicals, and a broad continuum throughout the visible region. Flint and Suslick [78] extended later on the research on non-aqueous fluids, using various hydrocarbons. They observed that for some hydrocarbons the emission of light comes from excited states of C_2, the same as in flames. While for other hydrocarbons with presence of N_2, the emission of light comes from excited states of CN. When there is presence of O_2, the emission of light comes from excited states of CO_2, CH radicals and OH radicals, similar to flames. The same Flint and Suslick [79] used the MBSL spectra from silicone oil under argon to determine the temperature of cavitation. In particular they observed that the emission of light comes from excited C_2, and by comparing the measured spectra with the synthetic spectra of the Swan band transition of C_2, they found that the effective rotational and vibrational emission temperature to be in the region of $5075\pm156K$. The great match between the two spectra shows that the MBSL effect is strongly related to thermal and chemical effects.[80]

There are various differences between the two types of sonoluminescence mentioned above, as for example while SBSL has a high light intensity and only one bubble is oscillating without dissolving or changing its average size, MBSL has spectral bands that are comparable to a synthetic spectra. Another difference is in the sphericity of collapse, as in SBSL the bubble collapse is more spherical than in MBSL since the acoustic wave affects a single bubble compared to the multitude of the bubble cloud.[80]

2.3.5 Cavitation Induced Pyrolysis

Pyrolysis is defined as the thermochemical decomposition of organic material at high temperature without the presence of oxygen or inert gases [81]. Since both hydrodynamic and acoustic cavitation impact the chemical properties of a fluid, there have been studies to investigate the relation between these forms of cavitation with pyrolysis, and what advantages would result in this connection.

One of the first researchers to study this relation in non-aqueous solutions were Suslick et al.[11], who analysed the chemical effects of ultrasound on alkane solutions. By using a titanium amplifying horn that produced ultrasonic irradiations with a 20kHz beam and using a glass sonication cell under Ar atmosphere for reactions, they found strong similarities to high temperature (>1200˚C) alkane pyrolysis products as shown by Rice radical chain mechanism. Comparing to low temperature pyrolysis (approx. 500˚C), there was a larger yield of principal products from sonolysis of H_2, CH_4, C_2H_2 and smaller 1-alkanes, which are instead produced at higher temperature pyrolysis. This is justifiable in terms of the cavitation "hot-spot" explanation of sonochemistry.

Fuel stability tests have been carried out along with the study of cavitation. It was noticed in fact that over time insoluble sediments were formed in injectors and filters which would eventually clog filters and fuel lines and in the long term reduce the efficiency of the engine. High presence of oxygen, nitrogen, and/or sulphur compounds were found for instance to all increase the fuel instability, along with the high degree of unsaturated fuel (aromatics, alkenes and dienes), due to autoxidation of radical intermediates with atmospheric oxygen and oxygenated fuel components leading to the formation of hydroperoxides and polymeric hydrocarbon components. High intensity ultrasound was found useful in

this instance since it accelerated the cracking process through cavitation or rapid growth followed by explosive collapse of microscopic bubbles as sound waves passes through the liquid. [12]

Price and McCollom [82] used for example ultrasound in order to evaluate whether it can determine diesel fuel instability. The experiment was made up of a sonic horn at 23 kHz propagating the ultrasound in a liquid through a titanium alloy horn, a large-walled tube that contains the diesel fuel sample immersed in the thermostat bath, and g.c.-mass spectrometry. It was discovered that the reactions occurring by sonication of alkanes can be also induced in diesel fuels along with the formation of nitrogen and other aromatic components similar to the gums formed in the fuel left in storage or in high temperature accelerated test. These results were obtained by firstly testing a $100cm^3$ sample stored in a sealed bottle at $70°C$ without ultrasound, which showed no variation of soot formation over a period of 6 months, and secondly by testing a $150cm^3$ sample irradiated with ultrasound, which instead showed the presence of sediments after only a few hours.

Price et al. [13] observed how the degradation of molecular weight during sonication time was faster for greater molecules when irradiating different polystyrenes in toluene, reaching a plateau in the long-term (where polymers are not affected any longer by ultrasound). Moreover, it was observed how the degradation would vary in terms of: the intensities of the wave, being faster and shifted to higher intensities; and of the lower limiting molecular weight due to the formation of larger bubbles and greater shear forces upon collapse (up to a point, since large bubbles will obstruct acoustic waves). However when changing temperature, important variations were noticed. Higher temperatures were found to slow the degradation process, since higher solvent vapour pressures would allow more vapour to enter the cavitation bubble, thus slower movement of solvent molecules and weaker shock waves.

The properties of the dissolved gas in the solution play an important role in sonochemistry, in particular the diffusion of the gas (the more soluble the solution is, the slower the degradation) and the polytropic ratio of the gas in the bubble. Greater shear forces in fact will lead to greater collapse, and hence higher γ will cause faster degradation. However the degradation will also depend on how reactive the molecule is, in the same way that oxygen reacts very easily with radicals and degrades faster despite having a lower γ than for example argon. [13]

2.3.6 Cavitation in Modern Return Valve

Studies on cavitation in diesel injectors have been broad, such as Arcoumanis et al.[50] for instance investigated the effect of needle injector lift on cavitation and correlated it with turbulence. It was found that high needle lift would cause cavitation generating on the top part of the injector, while low needle lift would generate bubbles around the nozzle at higher turbulence levels. Arcoumanis et al. [50] also showed that string cavitation occurs in diesel injectors and the structure can be replicated from the real size to a scaled size injector. Other flow information of diesel in injectors were found by Know-Kelecy and Farrel [83], who measured velocities in fifty-times scaled up injector models using PDPA (Phase Doppler Particle Analyzer) to conclude that sharp-edged nozzles have lower velocities close to the wall while rounded-edged nozzles have a flat velocity profile.

There have been few investigations however of cavitation in modern return valve systems of DI, most of which are computational analyses. For example, Aleiferis et al. [20] study was concentrated on comparing both experimental and CFD results of different parts of a DI to see if a close agreement is achievable. This was obtained using laser sheet of PIV (particle imaging velocimetry) on a super scaled transparent acrylic models of three different parts of a diesel injector, one of which corresponded to the ball valve acting as a seal in the return system using a mixture of turpentine oil and tetraline (1,2,3,4-tetrahydronapthalene) with a matching Reynolds number. For the CFD calculations, STAR-CD code was utilised with the barotropic cavitation model (isothermal flow) and High Reynolds k-ε model/ k-ε RNG model.

The ball valve section showed a good agreement in results. Differences were only noticed in the magnitude of velocity and separation zones, which the authors suggest could have been improved with a better grid resolution along the two-phase calculations. The following images compare the results obtained by Aleiferis et al. [20] between CFD, PIV and shadowgraph:

Figure 2.3.5   Outlet throttle in modern return valve analyses using CFD (top) and shadowgraph (bottom)[20]
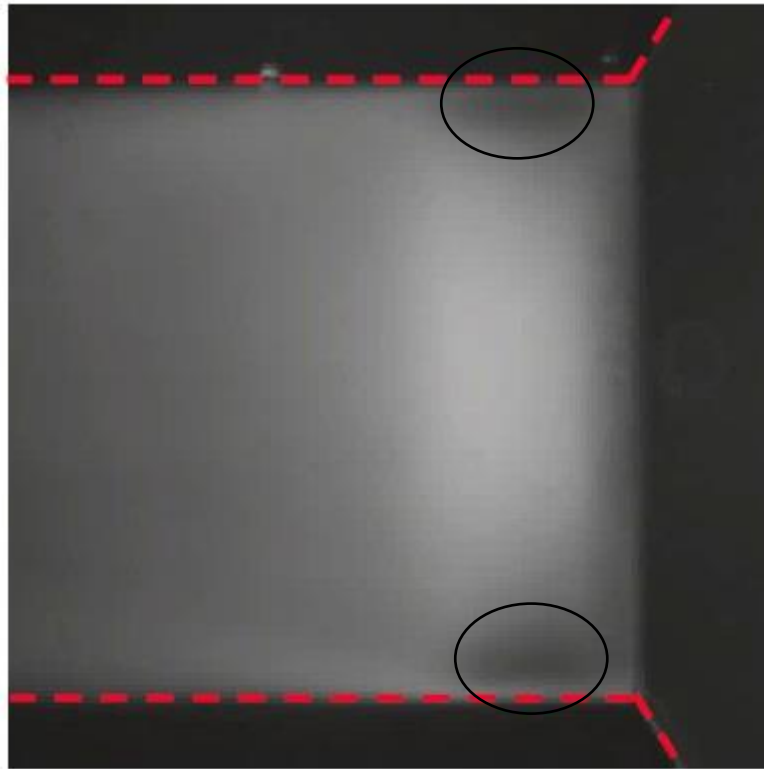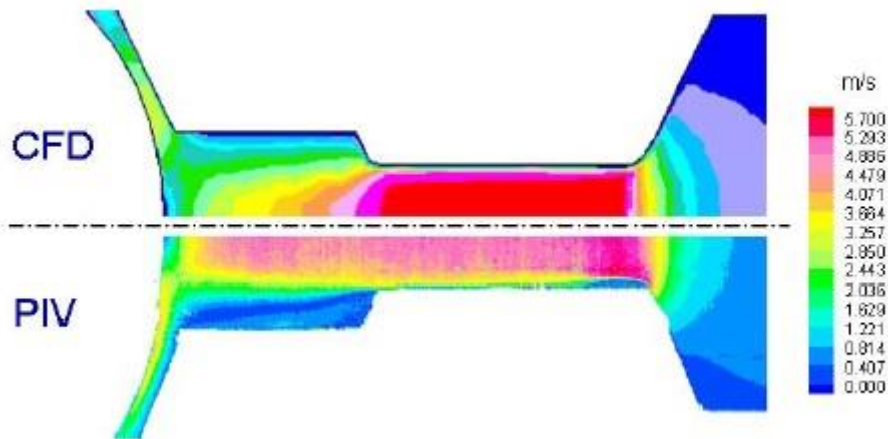
The presence of a boundary region at the entrance of the outlet throttle shown in both velocity profile in the CFD image and the obscure area in the shadowgraph suggested already the presence of cavitated flow.

Chapter 3 Flow characterisation of optical accessible model of modern return valve at low pressure

3.1   Reverse Engineering

Previous works where the spill valve of a diesel injector was taken into consideration can be found with Payri et al. [17]–[19],where experimental fuel injection rate and dynamics through the critical parts of the injector were compared with computational analysis such as AMESim and Flowmaster. The internal geometry of the diesel injector was accurately determined using silicone moulds. These were then analysed with digital cameras on an electronic microscope. This process was found to be problematic as sometimes extracting the mould can cause complications.

A different approach was taken for this project. It consisted in disassembling modern diesel injectors from a number of various manufacturing companies to observe how the spill valve mechanism changes and what would the best suitable design be.

Three injectors were cut apart: in particular a Nissan, a Vauxhall and a Toyota injector, which had slightly different configurations, as shown in the following images:

Figure 3.1.1   NISSAN injector solenoid spill valve

Figure 3.1.2   VAUXHALL injector solenoid spill valve

Figure 3.1.3   TOYOTA injector piezo spill valve

Figure 3.1.1 and Figure 3.1.2 show the conventional solenoid spill valve system, which follows the configuration explained in detail in the literature review (circled in red are the solenoid actuators, circled in yellow are the spill valve sections), while Figure 3.1.3 shows the conventional piezo spill valve system (circled in red is the piezo stack). Due to its practicality, the solenoid design was chosen as the prototype model to be used as the basis of the model to be tested in the new test rig.

Using a microscope it was possible to zoom into the narrow holes of both inlet and outlet throttle and measure the diameters:

Figure 3.1.4 VAUXHALL inlet and outlet spill ports

Figure 3.1.5 NISSAN inlet and outlet spill ports
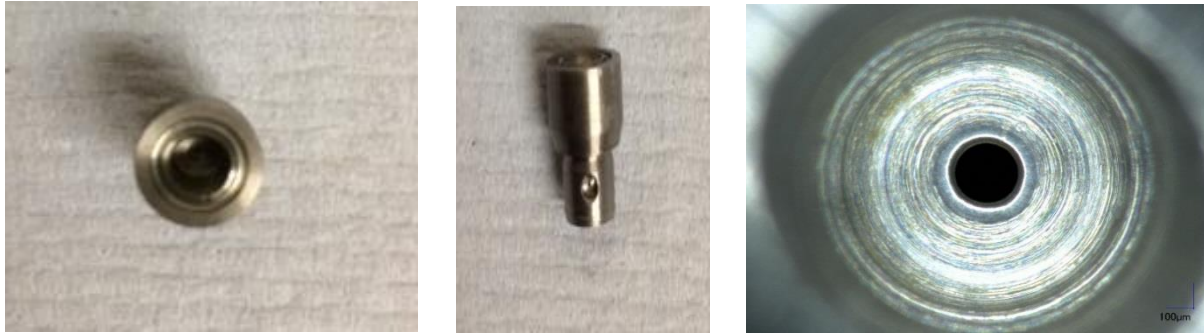
In both Figure 3.1.4 and Figure 3.1.5, the three pictures counting from left to right represent the outlet, the inlet, and the zoomed-in inlet spill port respectively. By means of the microscope equipment, it was possible to take measurements of the diameter of each hole and take it as a reference for the design of the model.

3.2 Model Assembly Design

3.2.1 Acrylic Assembly

Having the main dimensions and shape of the internal passages of the spill valve from Sec. 3.1, by means of Solidworks, it was possible to sketch a 3D drawing taking into account the limitations of manufacturing and material properties. In order to gain optical access to the internal passages of the spill valve model and to analyse the flow at high pressure such as those experienced in real vehicles, a transparent and strong material is necessary. For this reason, a clear cast acrylic material was selected, having the following properties specifications:

Properties	
Density [gcm⁻³]	1.19
Modulus of elasticity [Nmm⁻²]	3200
Tensile strength [Nmm⁻²]	74
Flexural strength [Nmm⁻²]	120

Table 3.2.1   Clear Cast Acrylic properties specifications [84]

From these considerations, the following 3D sketches in Solidworks show the spill valve geometric model using dimensions taken from the samples described in Sec.3.1:

Figure 3.2.1   3D and cross-sectional view of spill valve model

Encircled in Figure 3.2.1 are the inlet and outlet ports to the valve control chamber, using diameters and lengths previously measured. For internal pressures up to 100bar, the material selected was chosen to be acrylic, since it is transparent and will allow optical access to the internal flow. At the same time it is strong enough to withstand these pressures. The remaining passages with greater diameter were constructed uniquely to allow the fuel to flow from/to the test rig and therefore were shaped purely to ease the manufacturing process. In particular, the upper passage was chosen to have a greater diameter and a conical shape to allow a better sealing for the ball valve when simulating the needle lifting movement.

A finite element analysis (FEM) stress analysis was performed in Solidworks on the model block, for 70bar and 100bar upstream pressure from the inlet port to the needle sealing point and 1bar downstream pressure for the outlet port, to find the weakest points at operating pressures:

Figure 3.2.2   FEM analysis on acrylic model block at 70bar
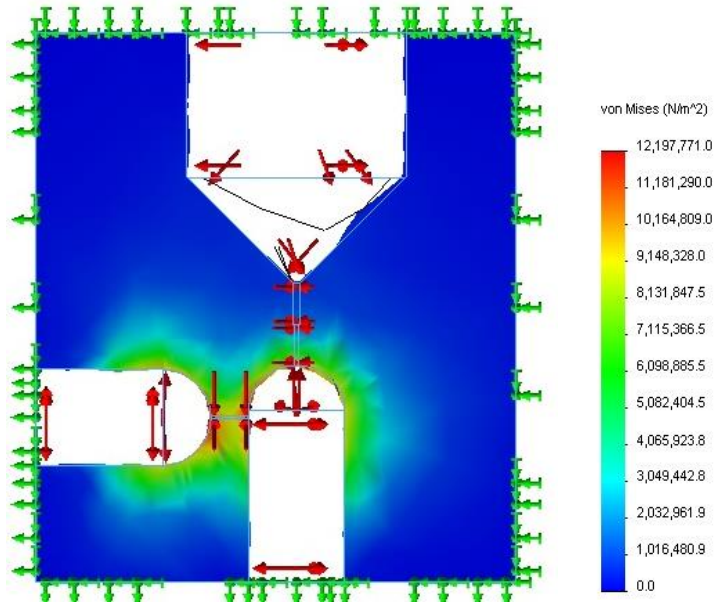
Figure 3.2.3   FEM analysis on acrylic model block at 70bar
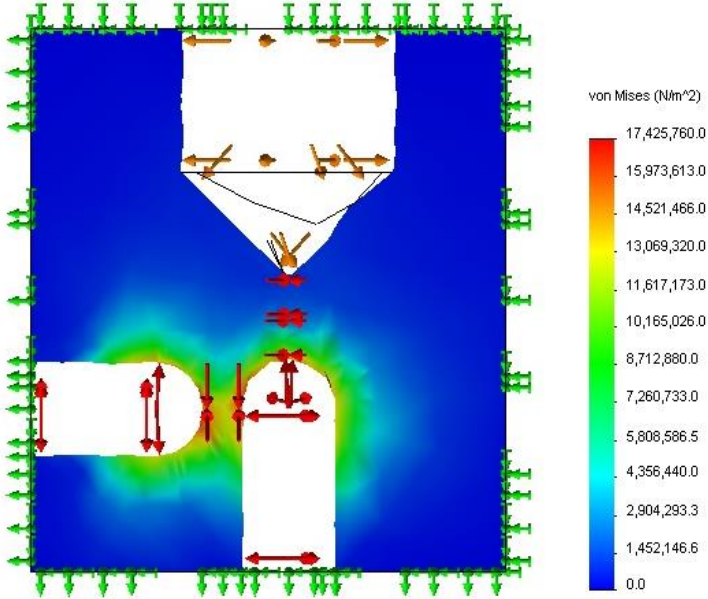
Von Mises stresses shown in Figure 3.2.2 and Figure 3.2.3 present intensified areas along the inlet throttle, the valve control chamber and the inlet of the outlet throttle.

Along with the lower pressure model design is another assembly design constructed in order to seal the ports during experimental work. For this reason, an external structure was designed to enclose the model geometry in Figure 3.2.1 and the seal in an appropriate way:

Figure 3.2.4   3D and cross-sectional view of spill valve along with cage assembly
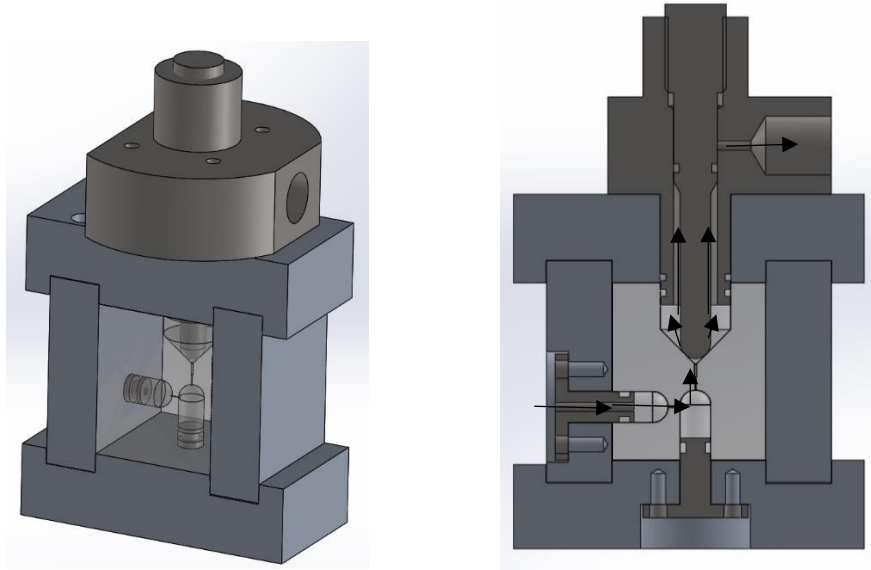
The cage structure as depicted in Figure 3.2.4 shows four metal plates that surround four faces of the fused silica cube giving optical access to the front view and the whole fuel flow across the model. The three passages adjacent to the metal plates have stainless steel metal fittings with radial O-ring seals in order to prevent high pressure fuel to hazardously escape and damage the equipment. Following the black arrows in Figure 3.2.4 it is possible to track the fuel flow across the model. From the side port, the high pressure fuel enters, crossing the inlet valve and once filled the valve control chamber, it enters the outlet valve until it reaches the plunger. The plunger system, as shown in Figure 3.2.4, is designed with a needle screwing mechanism, so it initially seals the outlet valve passage and it lifts by rotating manually the top in order to create a gap and allowing the fuel to spill in the return valve, and simulate the spilling procedure envisaged in a real fuel injector as explained in Sec. 2.2.5. The final manufactured product of the acrylic spill valve model assembly is shown in Figure 3.2.5 below.

Figure 3.2.5   *Acrylic model assembly*
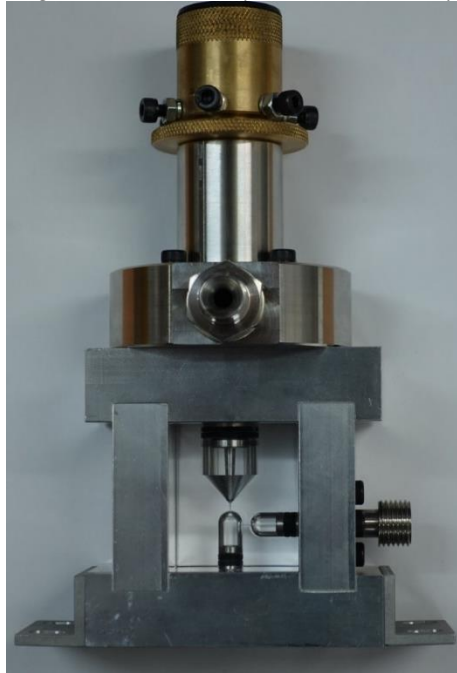
Two different versions of the acrylic block were designed, where the outlet throttle presented different diameters, as shown in Figure 3.2.6.

Figure 3.2.6   *Acrylic model version 1 (above) and version 2 (below) drawings*
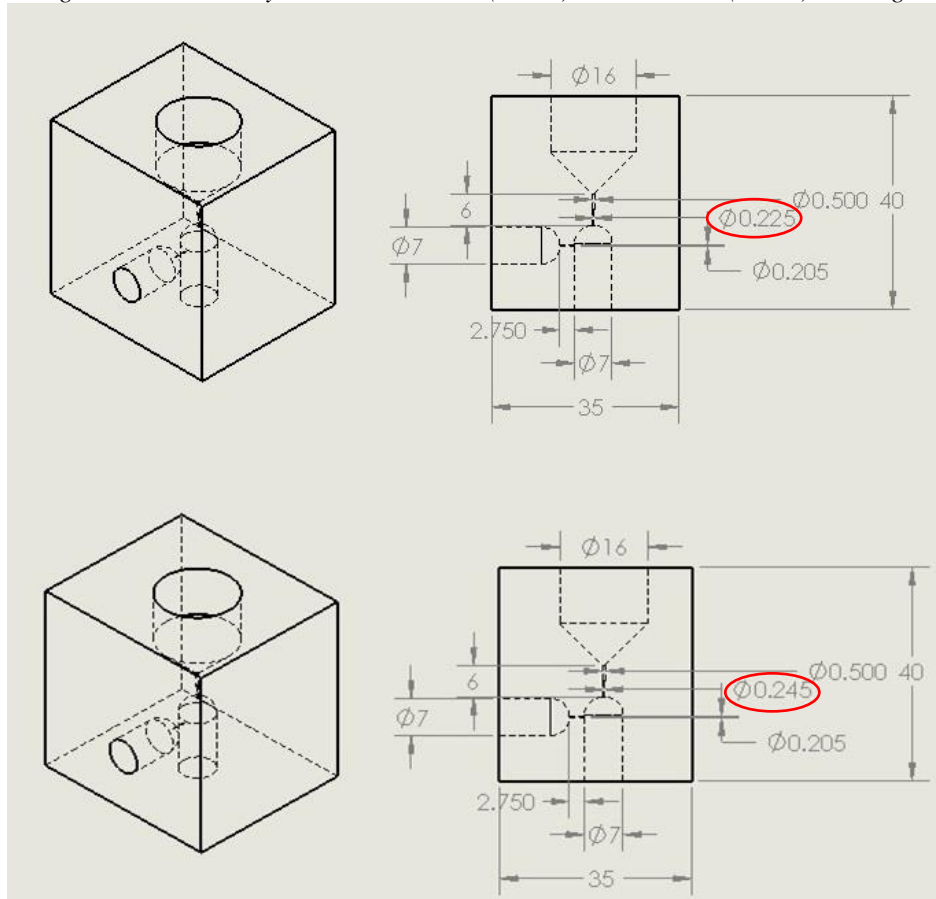
In version 1, the outlet diameter was designed to be Ø225µm, while in version 2 Ø245µm. The outlet to inlet diameter ratios are respectively 45:41 and 49:41. A closer look to the acrylic models shown in Figure 3.2.6 provides the dimensions of the block which are 400mm x 350mm x 350mm. The side passage represents the inlet of the fuel flow, with a Ø7mm bore, the lower channel represents the intermediate valve control chamber that is sealed to avoid leaking – see Figure 3.2.4 – and the upper passage represents the outlet of the fuel flow, with a Ø16mm bore. The functionality of the return valve is dependent on the micro passages, made up of the inlet throttle on the side connecting the inlet passage and the valve control chamber, and the stepped outlet throttle connecting the valve control chamber and the outlet passage. The inlet throttle is manufactured with a Ø205µm, while the outlet throttle with a Ø225µm/Ø245µm and a step of Ø500µm. By having the two throttles, it is possible to separate the fuel lines reaching the nozzle holes at high pressure and the fuel lines returning to the fuel tank at lower pressure.

3.2.2   Fused Silica Assembly

The disadvantage of using the acrylic model is that it would not be able to sustain higher pressure – above 100bar. Especially in the outlet and inlet throttles, which are micro passages, fracture and failures at high pressures would be inevitable. For this reason it was necessary to research a different material able to give optical accessibility and strength at the same time.

The material selected was Spectrosil® 2000 fused silica, which presents the following properties specifications:

Properties	
Density [gcm^{-3}]	2.2
Modulus of elasticity [Nmm^{-2}]	7.0×10^4
Tensile strength [Nmm^{-2}]	50
Flexural strength [Nmm^{-2}]	67

Table 3.2.2   Spectrosil® 2000 Fused Silica properties specifications [85]

However, the challenge of using this material was to replicate the same design as the one used in the acrylic assembly as shown in Figure 3.2.1. The complexity of manufacturing consisted not only in drilling micro-passages, but also in creating an inlet horizontal passage from the side of the block and outlet vertical passage meaning that the drilling instruments would have been small and at the same

time long enough to reach the inside of the block without fracturing the whole assembly. After contacting a large number of laser and glass manufacturing companies in the United Kingdom, it was obvious that this kind of work would require high levels of skills and knowledge. However, a company in Aachen, Germany named *LightFab*, specialised in subtractive 3D printing process of fused silica called SLE – selective laser etching – agreed on pursuing this commission using their technology. The SLE process consists in a two-step process: a first step consists in modifying internally the fused silica material by radiating laser to increase the chemical etchability locally to avoid formation of cracks whilst manufacturing; a second step consists in removing the modified material by wet chemical etching and giving a nice end product with high precision (~1μm). [86] Nevertheless, the issue of using this state-of-the-art technique is that of the positioning of the passages in the geometry, which would require an even more advanced equipment to able to machine within a block from two directions.

The compromise was to modify the drawing so that the inlet and outlet passages would be inline, not normal to each other as in Figure 3.2.1. From these considerations, the following 3D sketches in Solidworks show the modified spill valve geometric model with inline passages:

Figure 3.2.7   3D and cross-sectional view of modified spill valve model
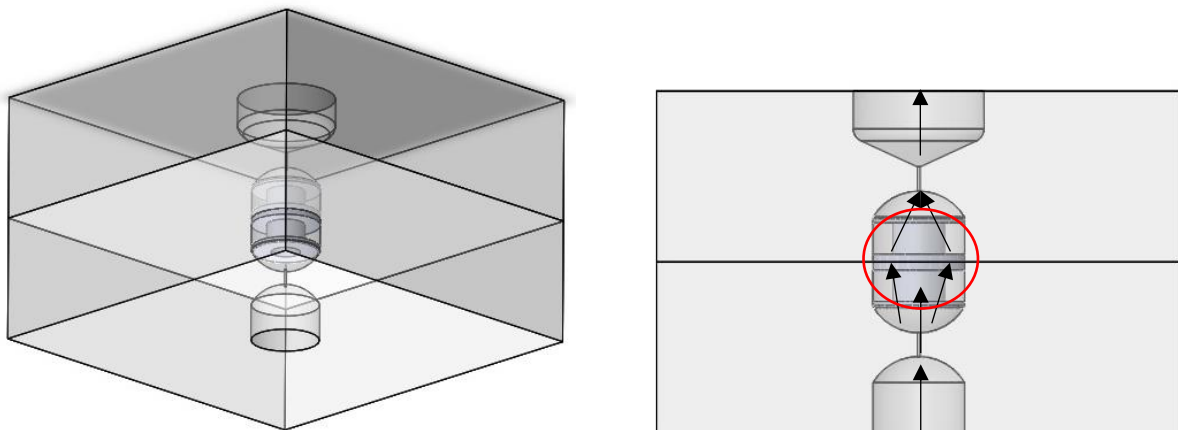
The three necessary regions for the spill valve system are preserved in the new design in Figure 3.2.7, the inlet volume below, the valve control chamber in the middle and the outlet volume above. Apart from the inline design required from LightFab to facilitate manufacturing, it was also essential to break the model into two parts, as it would have not been possible to recreate the important middle region of the valve control chamber by using the SLE from the outer surface.

A finite element analysis stress analysis was performed in Solidworks on the model block, for 100bar and 300bar upstream pressure from the inlet port to the needle sealing point and 1bar downstream pressure for the outlet port, to find the weakest points at operating pressures:

*Figure 3.2.8   FEM analysis on fused silica model block at 100bar*

Figure 3.2.9   FEM analysis on fused silica model block at 300bar
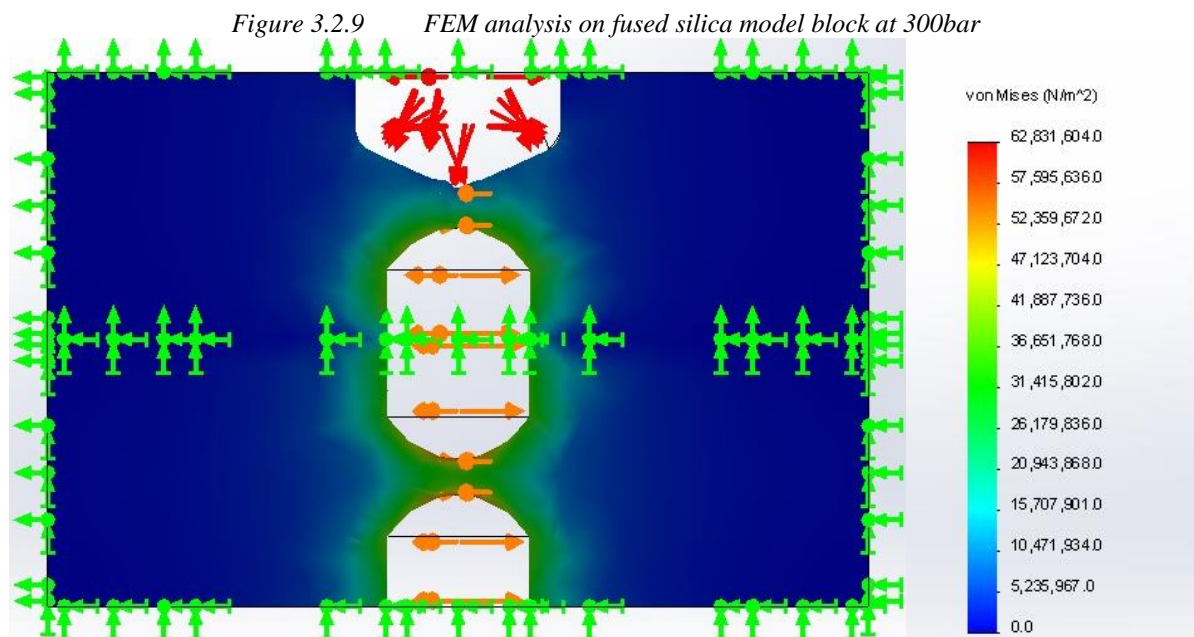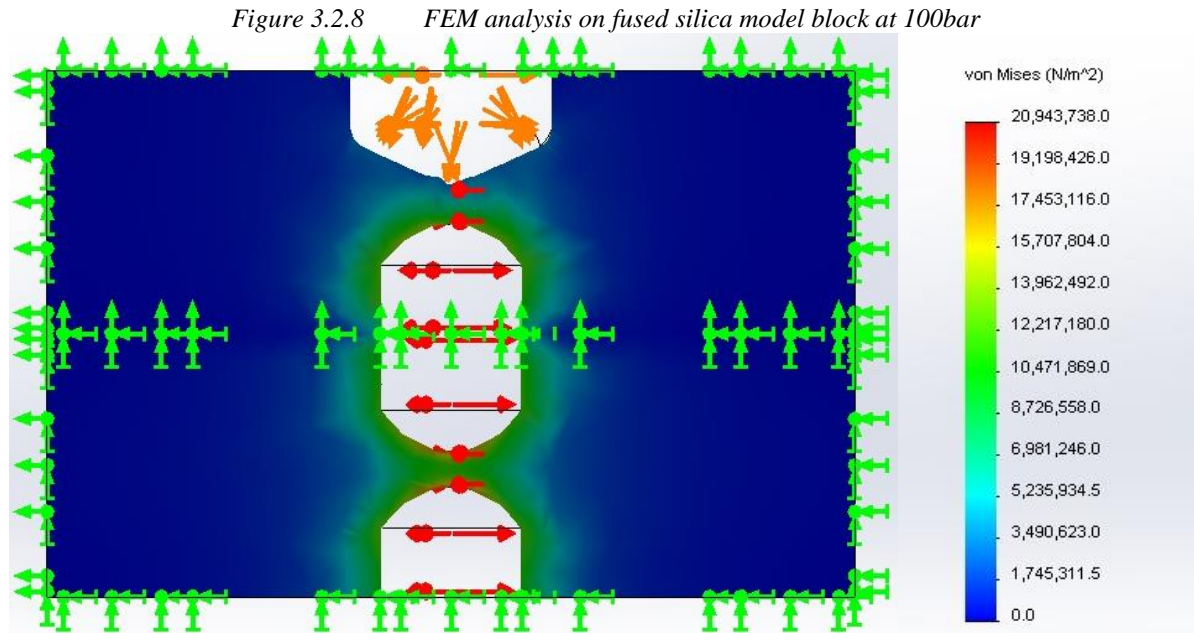
Von Mises stresses shown in Figure 3.2.8 and Figure 3.2.9 present intensified areas along the inlet throttle, the valve control chamber and the inlet of the outlet throttle. It was assumed that the interface between the upstream and upstream blocks acted as rigid faces.

The two blocks would then be linked together using an intermediate stainless steel fitting encircled in red in Figure 3.2.7 with three O-rings (top edge, middle edge and lower edge), avoiding therefore any leaks from the valve control chamber volume. Hence the two separate blocks were designed as follows:

Figure 3.2.10   Fused silica model downstream block (above) and upstream block (below) drawings
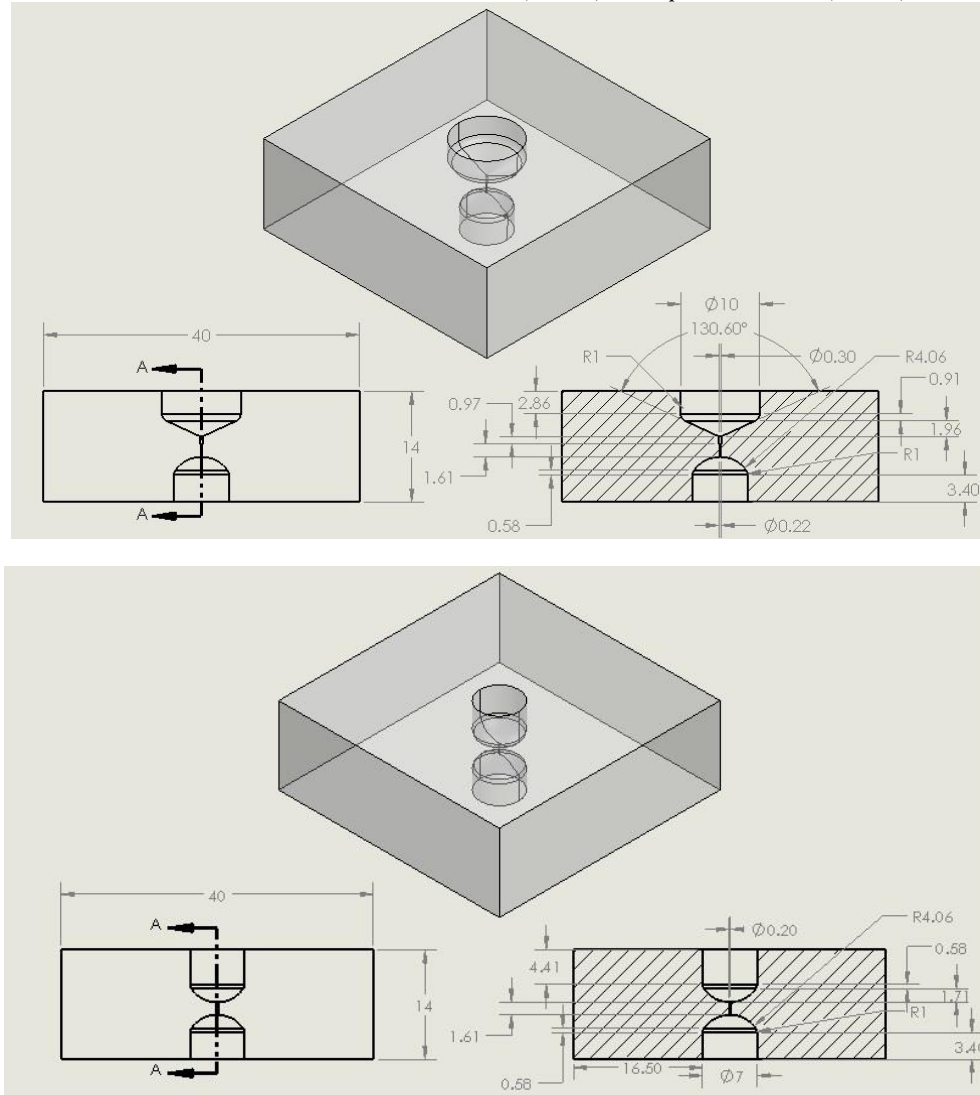
It can be noticed how the two blocks in Figure 3.2.10 are similar in dimensions to the acrylic model version 1 model in Figure 3.2.6. The upstream block consists of the inlet volume for the high pressure fuel, the inlet throttle with diameter Ø200μm and half of the valve control chamber (see geometry in Figure 3.2.10). While the downstream block consists of the other half of the valve control chamber, the outlet throttle with diameter Ø220μm and stepped to Ø300μm, and outlet volume with conical shape to allow the needle sealing during experiment.

As for the acrylic model, the whole fused silica model is sealed properly during experimental work using an external structure made of stainless steel, along with the plunger system needed to simulate the opening/sealing of the outlet throttle.

Figure 3.2.11   3D and frontal view of fused silica model with cage assembly
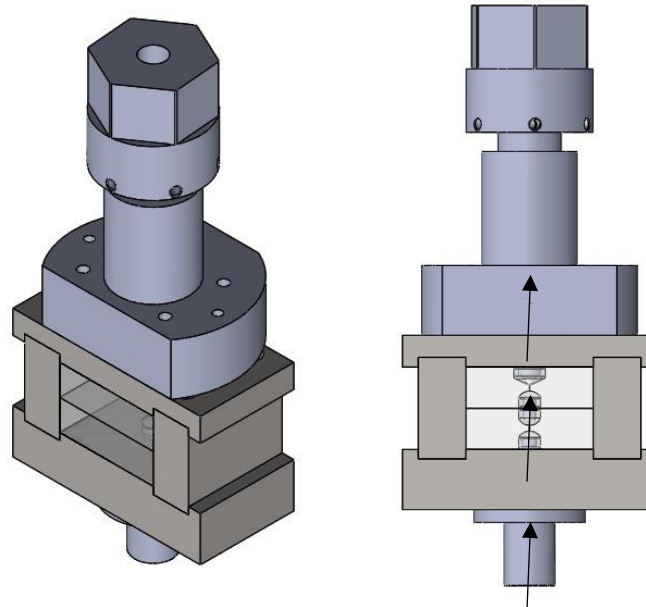
The cage structure as depicted in Figure 3.2.11 shows four metal plates that surround four faces of the fused silica shape giving optical access to the front view and the whole fuel flow across the model – apart from the intermediate fitting which shades part of the flow in the valve control chamber. The inlet and outlet volumes adjacent to the metal plates have stainless steel metal fittings with radial O-ring seals in order to prevent high pressure fuel to hazardously escape and damage the equipment. Following the black arrows in Figure 3.2.11 it is possible to track the fuel flow across the model. The plunger system is designed with a needle screwing mechanism, so it initially seals the outlet valve passage and then it lifts by rotating manually the tope in order to create a gap and allowing the fuel to spill in the return valve. The final manufactured product of the fused silica spill valve model is shown in Figure 3.2.12.

Figure 3.2.12   Fused silica model assembly
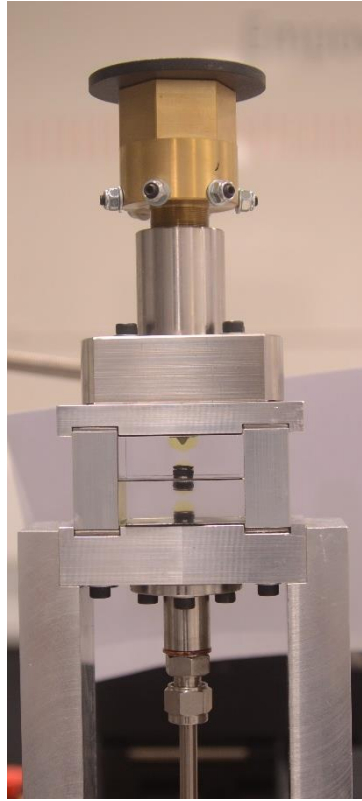
3.3   Experimental Setup

In order to analyse the cavitating flow inside the return valve of a diesel injector, a custom made mechanical flow rig was utilised as used by Lockett et al. where an acrylic replica of the spill mechanism was attached to it [87].

The whole assembly and pressure lines are shown in Figure 3.3.1 where the pressure in the system is generated by the nitrogen cylinder (on the left in Figure 3.3.1). Initially the nitrogen cylinder pressurises the tank containing the fuel with low pressure (~2bar) to be utilised in the experiment so that the fuel can then be transferred to three high pressure fuel cylinders – with a total capacity of ~10.5 l – as shown with the red arrows. Once the fuel bottles are filled (on the bottom in Figure 3.3.1) and the storage tank has been depressurised, the nitrogen cylinder can then be utilised to pressurise the fuel in the three bottles with high pressure according to the requirement for the experiment. The blue arrows in the diagram indicate the higher pressure lines all the way from the nitrogen cylinder to the acrylic model (on the right in Figure 3.3.1), where the flow is expected to generate cavitation as it passes through the narrow passages of the return valve regulated by a manually controlled needle, to then flow back to the

storage tank ready for the next cycle. Pressure gauges are located upstream and downstream the acrylic model in order to control the pressure ratio occurring before/after passing through the return valve. The upstream pressure gauge is set by manually adjusting the nitrogen bottle knob so that the fuel contained in the three fuel bottles is then pressurised by the nitrogen, while the downstream pressure gauge is regulated by manually adjusting a knob to a maximum gauge pressure of 10 bar (all measurements are therefore limited from ambient pressure to 10 bar). A high speed optical camera is shown in Figure 3.3.1, which allows to visualise the flow across the model.

The advantage of this setup is that it is possible to manually control the pressure difference to be created between inlet and outlet of the return valve model, hence to alter the cavitation position and strength according to the experimentalist needs.

The priming of the rig procedure is explained in Appendix A

Figure 3.3.1   Schematic diagram of the test rig utilised for cavitation experiment in the acrylic model
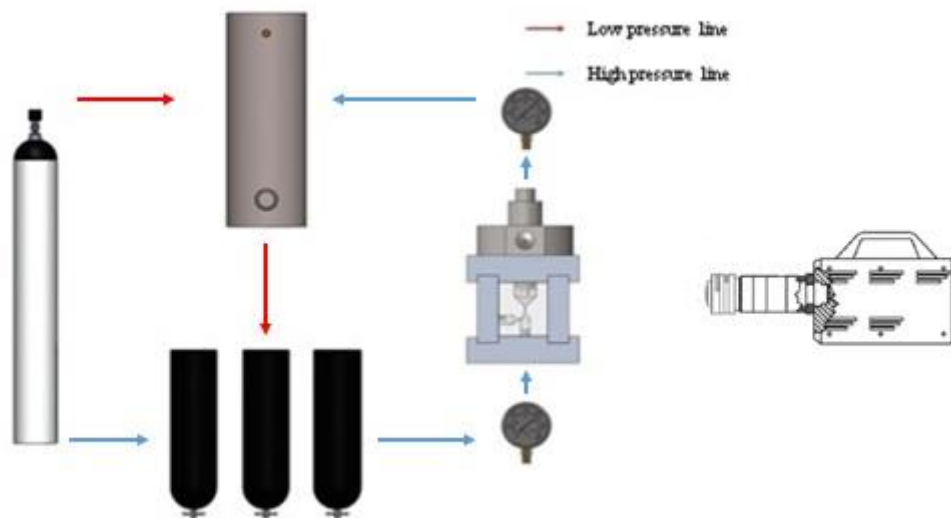
For the camera to capture white light scattering from the cavitated fuel, an ARRILUX Pocket PAR 200W lamp was utilised along with a concave lens to collimate the beam of light directly to the area of interest. The whole setup described in Figure 3.3.1 along with the lamp and lens is shown in Figure 3.3.2 below.

Figure 3.3.2   Experimental setup of low pressure characterisation test

3.4   Experimental Methods

A stainless steel needle seals the outlet throttle to allow the fuel entering to gather in the valve control chamber after passing through the inlet throttle. This needle, shown in Figure 3.2.4, is manually controlled by a rotating movement, where every fifth of a rotation corresponds to a 50μm needle lift. Hence, to allow the fuel to flow through the outlet passage, the needle is lifted from its sitting position.

The fuel is initially gathered in the fuel tank, and then transferred using low pressure nitrogen to the three fuel bottles as previously depicted in Figure 3.3.1. The upstream pressure was then setup from the nitrogen bottle starting from as low as 10bar absolute pressure, and then increasing in steps of 5bar. Ball valves were utilised to manually control when to allow fuel to flow or not. Once the pressurised fuel would enter the model through the inlet passage, it would collect all the way until the needle sealing of the outlet throttle. The moment the needle was lifted, the pressurised fuel would escape in the outlet passage and return to the ambient pressure fuel storage tank, after passing through a second pressure gauge. The needle lift was varied in steps of 50μm from 50μm to 250μm for the acrylic model, while for the fused silica model a more refined needle was used which varied in steps of 10μm from 10μm to 100μm.

An optical Photron APX-RS high speed camera operated at 15 kHz and 3.63x optical magnification would capture the flow crossing the throttle passages, visualising with a magnification factor of 5.5 μm/pixel the cavitation occurring. By means of the downstream pressure gauge, it is possible to control the strength of the cavitation, and determine the pressure ratio necessary for incipient cavitation.

Fuels	Acrylic Model Version 1		Acrylic Model Version 2		Fused Silica Model	
	Upstream Pressure range (bar)	Needle lift range (μm)	Upstream Pressure range (bar)	Needle lift range (μm)	Upstream Pressure range (bar)	Needle lift range (μm)
Paraffinic Model Diesel	$15-20-25-30-35-40$	$50-100-150-200-250$	$25-30-35-40-45-50-55-60-65-70$	$50-100-150-200-250$	$15-20-25-30-35-40$	$10-20-30-40-50-60-70-80-90-100$
Mixture 1 (80% C_{16}, 20% C_8)	$10-15-20-25-30$		$25-30-35-40-45-50-55$			
Mixture 2 (95% C_{16}, 5%C_8)	$10-15-20-25-30$		$25-30-35-40-45-50-55$			

Table 3.4.1   Experimental methods for acrylic and fused silica models

As mentioned in Sec. 3.2.1 for the acrylic assembly, the experiment was conducted using two different acrylic blocks with altered outlet throttle diameters: one with Ø225μm and the other with Ø245μm, and additionally using three different fuels, a paraffinic model diesel fuel (GTL) and fuel mixtures n-hexadecane and n-octane in 80:20 v/v and 95:5 v/v proportions. For each fuel, each model block and each upstream pressure setting, 25 different readings of downstream pressures for incipient cavitation was taken for a fixed needle lift. The incipient cavitation pressure ratio was recorded *'from below'* meaning that the downstream pressure was increased until the cavitation disappeared, and *'from above'* meaning that the downstream pressure was decreased until the cavitation would appear. The mean and standard deviation for each set of measurements was then calculated. Table 3.4.1 above summarises the different conditions at which the experiments were setup, while Table 3.4.2 below presents the saturation vapour pressures and viscosities of the fuels utilised in the experiment. [88], [89]

For the fused silica assembly, as mentioned in Sec. 3.2.2, the same experiment was conducted using only the paraffinic model diesel fuel (GTL). As shown in Table 3.4.1, the range of needle lift was more detailed due to smaller division of 10μm compared to the 50μm step of the acrylic model. Again, for each upstream pressure, 25 different readings of downstream pressures for incipient cavitation was taken for a fixed needle lift (both *'from above'* and *'from below'*). The mean and standard deviation for each set of measurements was then calculated.

	Saturation vapour pressure (kPa)	Viscosity (Ns/m²)
Paraffinic model diesel	<0.0054 @ 25°C	0.00153
Mixture 1 (80% C_{16}, 20% C_8)	0.470 @ 23°C	0.0027
Mixture 2 (95% C_{16}, 5% C_8)	0.15 @ 23°C	0.00323

Table 3.4.2   Experimental fuel properties

Chapter 4 Results and Analysis – Low Pressure

4.1   Experimental Results and Discussion

The following paragraphs will focus on the experimental results obtained following the setup and methods explained in Sec. 3.3 and in Sec. 3.4. In particular, this chapter will present the findings of incipient cavitation in the return valve for acrylic models version 1 and version 2 and for the fused silica, focusing on the effects of needle lift, upstream to downstream pressure ratios, fuels and geometry.

Initially the results will be presented for the three different models separately. Subsequently it will be possible to compare the similarities and differences occurring in the three models and finally conclude with the implications of these results to modern DIE.

4.1.1   Version one of acrylic model

Details of the geometry of the acrylic model version 1 are found in Figure 3.2.6. In particular, it corresponds to the model having an outlet to inlet diameter ratio of 15:14. The fuels, upstream pressures and needle lift range for this model are specified in Table 3.4.1 following the methods explained in Sec. 3.4.

Firstly, the results presented are for the paraffinic model diesel (GTL). It was noticed that for every upstream pressure and needle lift setting, the incipient cavitation would always only occur at the entrance of the outlet throttle. The images below were taken for the case of upstream pressure 40bar, needle lift 250μm, at a shutter speed of 1/100000 sec and a frame rate of 15000 fps.

Figure 4.1.1   *Incipient cavitation (left) and fully cavitating flow (right) for paraffinic model diesel in acrylic model version 1 at the entrance of outlet throttle*
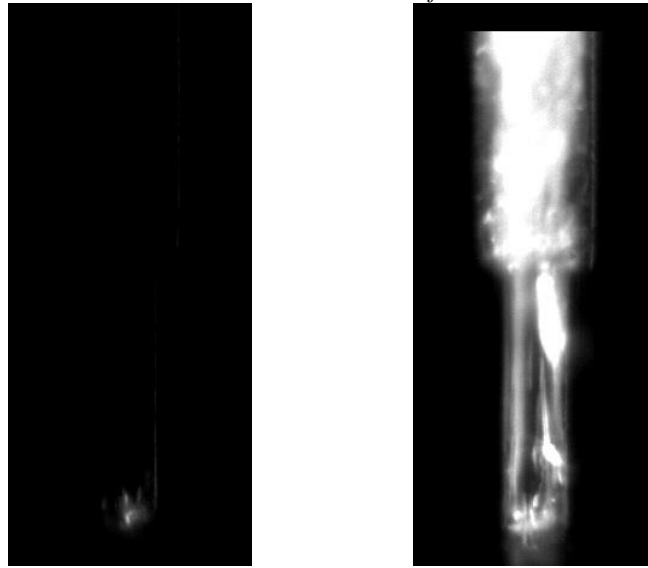
The white light scattered in Figure 4.1.1 represents the cavitating flow. When setting the upstream pressure at 40bar and leaving the downstream pressure at ambient conditions, the flow is fully cavitating throughout the outlet throttle, allowing to visualise clearly also the intermediate step in the outlet throttle (image on the right in Figure 4.1.1). At this point, in order to determine the incipient cavitation, it is necessary to increase the downstream pressure until it is at its minimum and slowly killing the cavitation (image on the left in Figure 4.1.1). The process of increasing the downstream pressure was noted as 'from below', since the incipient cavitation downstream pressure is reached from the lower ambient pressure; while if the downstream pressure is above the incipient cavitation pressure, then no cavitation would appear, and therefore the process of decreasing the downstream pressure in order to achieve incipient cavitation was noted as 'from above' (See Sec. 3.4).

After taking 25 readings 'from above' and 25 readings 'from below' for each of the upstream pressures and needle lifts mentioned in Table 3.4.1, it was possible to observe the trends of upstream to downstream pressure ratios, as shown in the plots below:

Figure 4.1.2   Above and below measurements for acrylic model version 1 with paraffinic model diesel
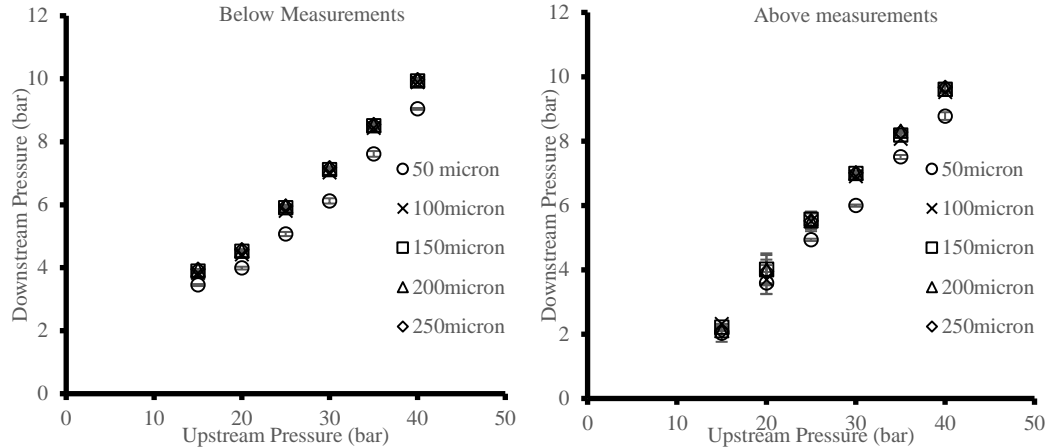
Each data point in Figure 4.1.2 represents the mean of the 25 readings, along with the bars representing the standard deviation. First of all it can be noticed how the measurements in the below chart are more consistent compared to the above chart. The reason of this dissimilarity lays on the fact that while from below the cavitation is slowly reducing until it reaches its minimum, from above incipient cavitation would occur more abruptly. A hysteresis effect was therefore observed to occur, causing irregularity in the readings for downstream pressures from above.

Another important effect is the difference in incipient pressure ratio between the 50μm needle lift and 100μm needle lift. While for needle lift settings of 100μm above, the upstream to downstream pressure ratio remains constant. This implies that the needle also has an effect on cavitation inception: the low needle lift produces a pressure gradient in the annulus around the needle, between the conical surface and the needle itself, thereby reducing the pressure gradient developing across the nozzles. This explains why a larger pressure difference across the nozzles is required to produce cavitation inception. For example, at 30 bar upstream pressure in the below measurements, the corresponding downstream pressure for cavitation inception was found to be 6.122 bar at 50μm, opposed to 7.022 bar at 100μm. The former upstream to downstream pressure ratio is 4.9, while the latter is 4.27.

Upstream and downstream pressure plots at different needle lifts for the paraffinic model diesel in the acrylic model version 1 are presented in Appendix B.1.

The following results are using mixture 1 (n-hexadecane and n-octane in 80:20 v/v proportions) and mixture 2 (n-hexadecane and n-octane in 95:5 v/v proportions) as the working fuels.

Figure 4.1.3   *Above and below measurements for acrylic model version 1 with mixture 1(80%C$_{16}$, 20% C$_8$)*
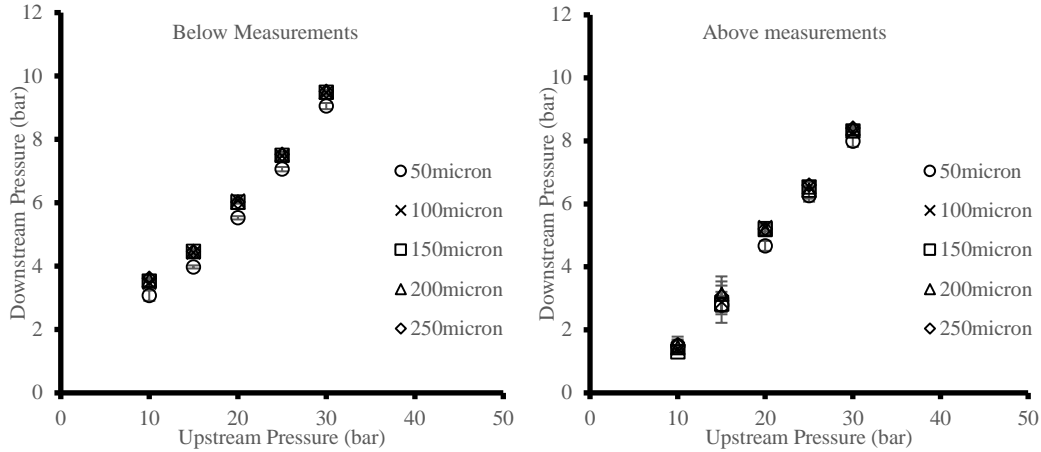
Figure 4.1.4   *Above and below measurements for acrylic model version 1 with mixture 2(95%C$_{16}$, 5% C$_8$)*
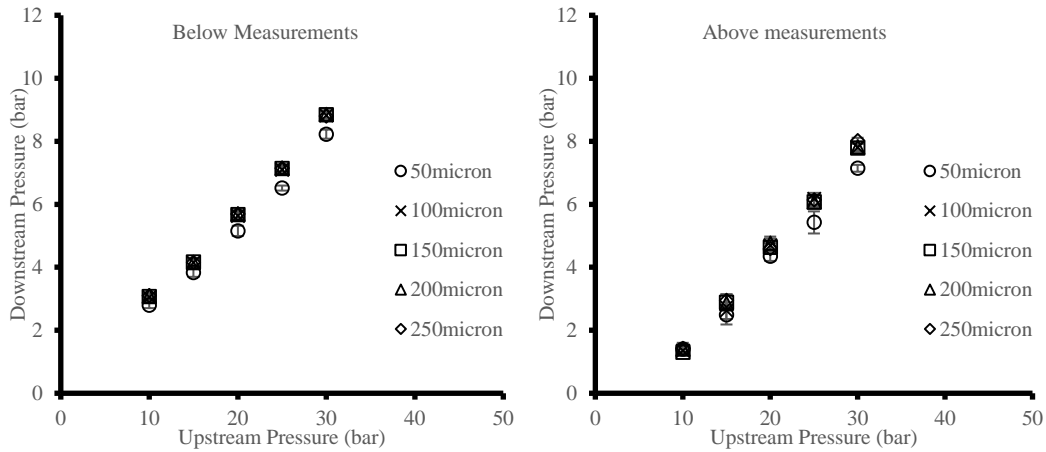
In both Figure 4.1.3 and Figure 4.1.4, the same observations can be made as in Figure 4.1.2 in terms of the difference between above and below measurements and the needle effect at 50μm compared to 100μm and above. The above measurements, apart from being less consistent due to the abrupt cavitation inception, present also higher upstream to downstream pressure ratios compared to the corresponding below measurements. This can be linked to the fact that both mixtures have greater saturated vapour pressure compared to the paraffinic model diesel, as shown in Table 3.4.2. A greater saturated vapour pressure would require therefore a larger pressure difference across the nozzles to produce cavitation inception.

Upstream and downstream pressure plots at different needle lifts for the mixture 1 in the acrylic model version 1 are presented in Appendix 180B.2, while for mixture 2 in the acrylic model version 1 are presented in Appendix B.3. Also to be noted is that the threshold of 10 bar downstream pressure

imposed by the pressure gauge (See Sec.3.3) meant that the upstream pressures could go as far as 30bar in order to determine the incipient cavitation.

The fuel effect on cavitation inception can be thoroughly understood by plotting the upstream and downstream pressures for all three fuels in the same graph. below is the 50μm needle lift case (See Appendix B.4 for all the other needle lift settings) taken for the below measurements:

Figure 4.1.5   *Below measurements for all three fuels at 50μm needle lift – acrylic model version 1*
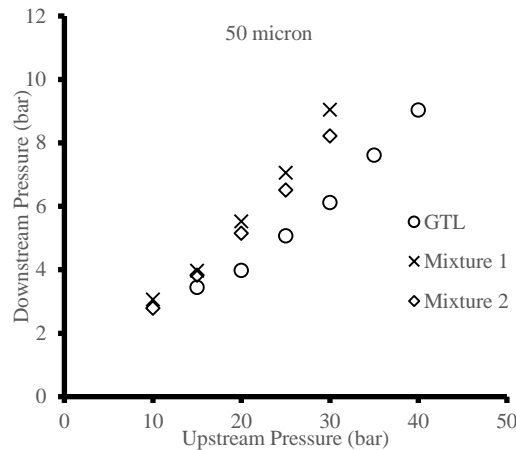
The upstream to downstream pressure ratios for the three fuels are evidently different for the three different fuels, as seen in Figure 4.1.5. The paraffinic model diesel fuel presents the greatest upstream to downstream pressure ratio, followed by mixture 2 and then mixture 1, with the lowest upstream to downstream pressure ratio. For example, at 30 bar upstream pressure, the corresponding downstream pressure for incipient cavitation for the paraffinic model diesel is 6.122, for mixture 2 is 8.226 and for mixture 1 is 9.05, meaning an upstream to downstream pressure ratios of respectively of 4.9, 3.6 and 3.3. This relates once again to the saturated vapour pressure of the three fuels, being the lowest for the paraffinic model diesel and the highest for mixture 1. Using the definition of incipient cavitation shown in Eq. 2.3.2, the values of saturated vapour pressures shown in Table 3.4.2 and the upstream and downstream pressure range shown in Table 3.4.1, it was possible to calculate the incipient cavitation number for the three fuels in the plot below.

Figure 4.1.6   Incipient cavitation number for all three fuels at 50μm needle lift – acrylic model version 1
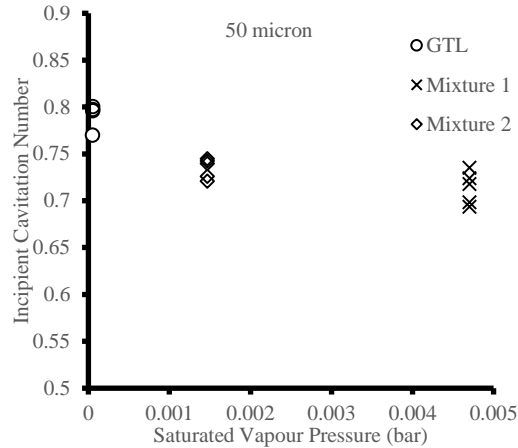
Cavitation inception obtained for the paraffinic rich model diesel occurs at the largest cavitation number and lowest saturated vapour pressure when compared with the two hexadecane-octane mixtures. This indicates a reduced inclination to cavitate for the paraffinic model compared to mixture 2, which in turn shows a reduced inclination to cavitate compared to mixture 1, which exhibits cavitation inception at lower critical cavitation number and largest saturated vapour pressure. The same trend occurs for the remainder needle lift settings presented in Appendix B.5.

It is possible moreover to estimate the intermediate valve control chamber pressure by dividing the fuel flow in the model in three stages as shown in Figure 4.1.7:

Figure 4.1.7   Estimation of intermediate valve control chamber pressure in acrylic model
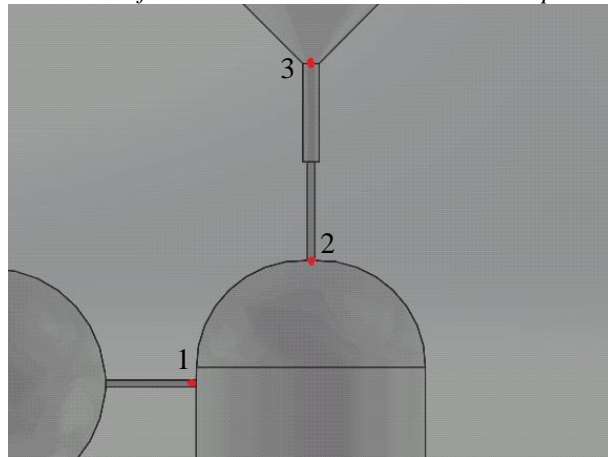
There are three points in the figure above. In particular, point 1 for the inlet throttle, 2 for the entrance of outlet throttle and 3 for the exit of the outlet throttle. While point 1 represents the fuel at the upstream pressure and point 3 the fuel at the downstream pressure, point 2 instead represents the intermediate

pressure in the valve control chamber. The estimation for the intermediate pressure at point 2 can be calculated using Bernoulli's equation for incompressible, inviscid and steady flow:

$$\begin{cases} p_1 + \dfrac{1}{2}\rho v_1^2 = p_2 + \dfrac{1}{2}\rho v_2^2 \\ p_2 + \dfrac{1}{2}\rho v_2^2 = p_3 + \dfrac{1}{2}\rho v_3^2 \end{cases}$$

4.1.1

where p is the static pressure, ρ is the density (in kg/m^3) and v is the fluid velocity (in m/s).[90] Eq.4.1.1 applies the Bernoulli's equation between points 1 and 2 and points 2 and 3 – neglecting the change in height due to micro dimensions – where it is possible to compute the intermediate pressure p_2 knowing the upstream and downstream pressures and the diameters of all three throttles in Figure 4.1.7. The plot in Figure 4.1.2 for the below measurements of the paraffinic model fuel can be modified using the intermediate pressure instead of the upstream pressure, as shown below:

Figure 4.1.8   *Below measurements for acrylic model version 1 with paraffinic model diesel using estimated intermediate pressure*
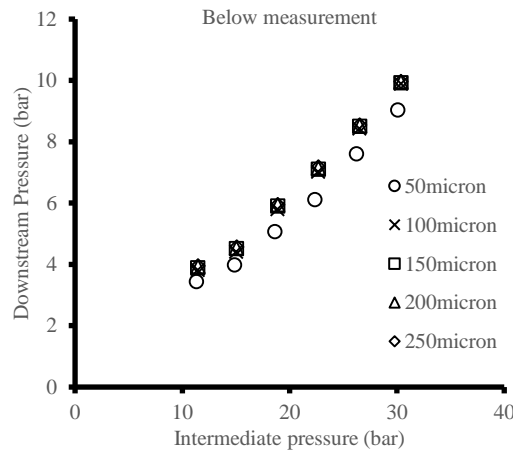
It can be noticed how the intermediate-to-downstream pressure ratios show the same results as for the upstream-to-downstream pressure ratios in terms of needle lift effect. However while in Figure 4.1.2 the upstream pressure is the same as the needle lift increases, in Figure 4.1.8 the intermediate pressure is increasing as the needle lift increases, visible by the slight shift between the 50µm and 100µm markers.

4.1.2 Version two of acrylic model

Details of the geometry of the acrylic model version 2 are found in Figure 3.2.6. In particular, it corresponds to the model having an outlet to inlet diameter ratio of 7:6, hence a larger outlet throttle diameter. The fuels, upstream pressures and needle lift range for this model are specified in Table 3.4.1 following the methods explained in Sec. 3.4.

Firstly, the results presented are for the paraffinic model diesel (GTL). In the same way as in version 1, it was noticed that for every upstream pressure and needle lift setting, the incipient cavitation would always only occur at the entrance of the outlet throttle. The images below were taken for the case of upstream pressure 40bar, needle lift 250μm, at a shutter speed of 1/100000 sec and a frame rate of 15000 fps.

Figure 4.1.9   Incipient cavitation (left) and fully cavitating flow (right) for paraffinic model diesel in acrylic model version 2 at the entrance of outlet throttle
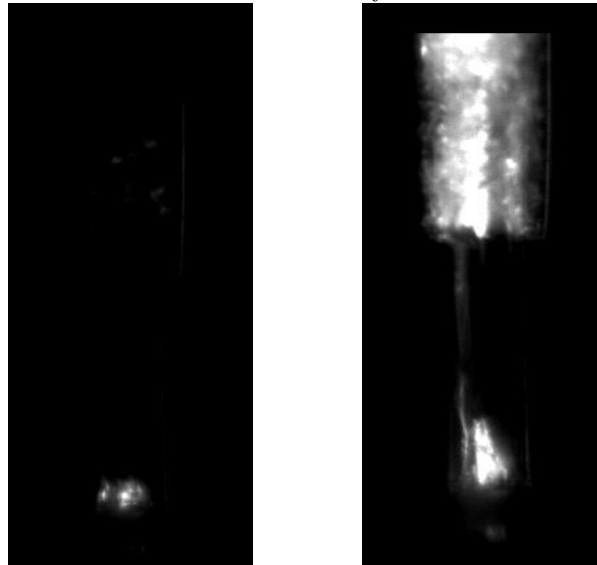
The white light scattered in Figure 4.1.9 represents the cavitating flow. When setting the upstream pressure at 40bar and leaving the downstream pressure at ambient conditions, the flow is cavitating only for a third of the smaller passage and then fully cavitating from the step onwards, allowing to visualise clearly the intermediate step (image on the right in Figure 4.1.9). The variation in geometry has had therefore an influence in the pressure gradient across the nozzle. The incipient cavitation image at the entrance of the outlet throttle is shown on the left in Figure 4.1.9.

After taking 25 readings 'from above' and 25 readings 'from below' for each of the upstream pressures and needle lifts mentioned in Table 3.4.1, it was possible to observe the trends of upstream to downstream pressure ratios, as shown in the plots below:

Figure 4.1.10   Above and below measurements for acrylic model version 2 with paraffinic model diesel
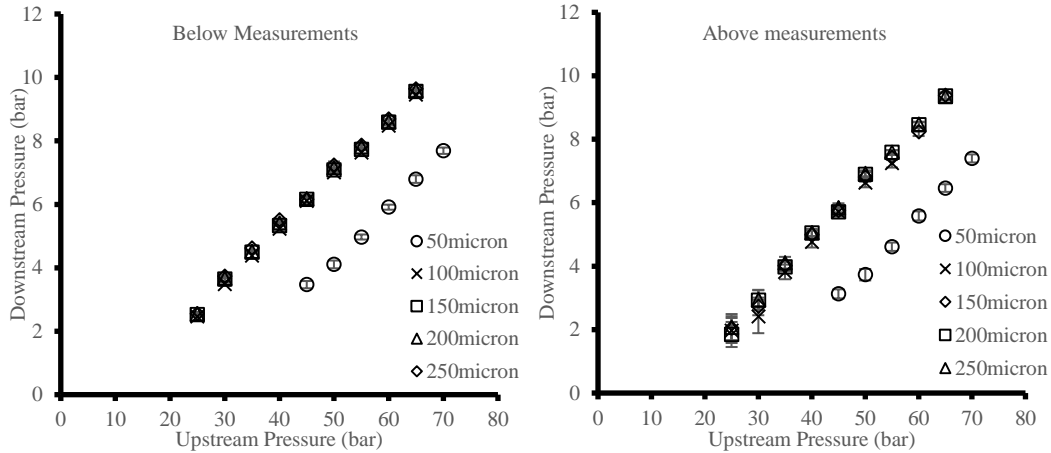
Each data point in Figure 4.1.10 represents the mean of the 25 readings, along with the bars representing the standard deviation. As explained in Sec. 4.1.1 for the acrylic model version 1, the same hysteresis effect occurred in version 2, causing irregularity in the readings for the above measurements of the downstream pressures.

Also very noticeable in the acrylic model version 2 is the difference in incipient pressure ratio between the 50μm needle lift and 100μm needle lift. Therefore the needle keeps having an effect on cavitation inception at low settings due to the pressure gradient generated in the annulus around the needle. A larger pressure difference across the nozzles is therefore required to produce cavitation inception. For example, at 45 bar upstream pressure in the below measurements, the corresponding downstream pressure for cavitation inception was found to be 3.468 bar at 50μm, opposed to 6.104 bar at 100μm. The former upstream to downstream pressure ratio is 12.98, while the latter is 7.37. For needle lift settings of 100μm and above, the upstream to downstream pressure ratio remains constant.

Upstream and downstream pressure plots at different needle lifts for the paraffinic model diesel in the acrylic model version 2 are presented in Appendix C.1.

The following results are using mixture 1 (n-hexadecane and n-octane in 80:20 v/v proportions) and mixture 2 (n-hexadecane and n-octane in 95:5 v/v proportions) as the working fuels.

Figure 4.1.11   Above and below measurements for acrylic model version 2 with mixture 1(80%C$_{16}$, 20% C$_8$)
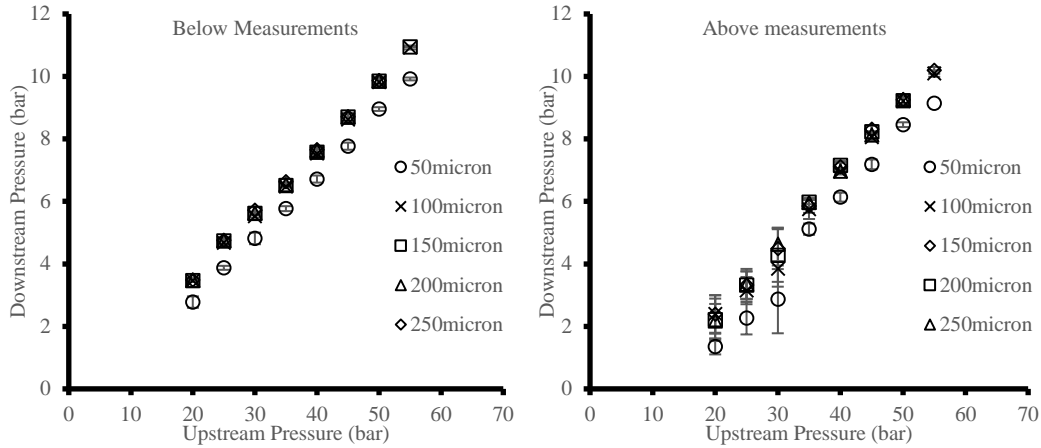
Figure 4.1.12   Above and below measurements for acrylic model version 2 with mixture 2(95%C$_{16}$, 5% C$_8$)
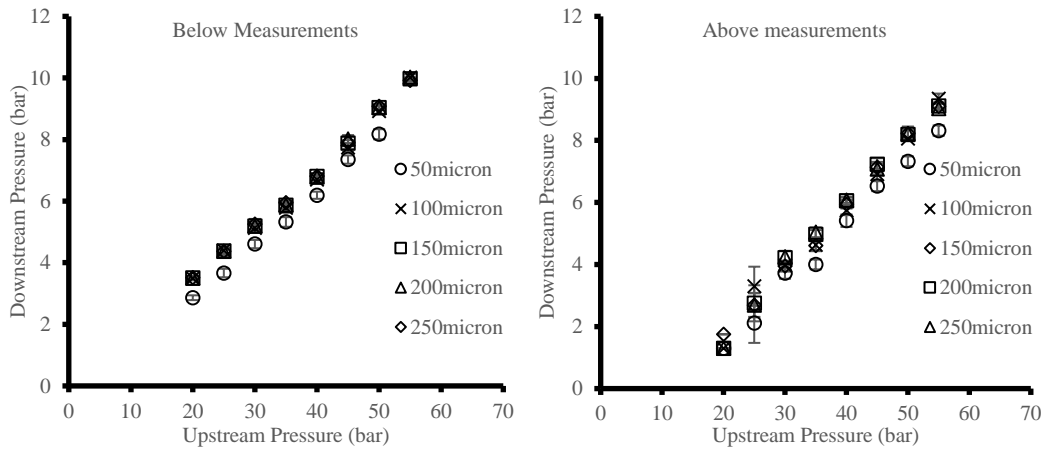
Both Figure 4.1.11 and Figure 4.1.12 once again confirm the difference between the above and below measurements and the needle effect at 50μm compared to 100μm and above. Also as noticed for the acrylic block version 1 in Sec. 4.1.1, the above measurements present higher upstream to downstream pressure ratios compared to the corresponding below measurements due to the fact that both mixtures have greater saturated vapour pressure compared to the paraffinic model diesel, as shown in Table 3.4.2. A greater saturated vapour pressure would require therefore a larger pressure difference across the nozzles to produce cavitation inception.

Upstream and downstream pressure plots at different needle lifts for the mixture 1 in the acrylic model version 2 are presented in Appendix C.2, while for mixture 2 in the acrylic model version 2 are presented in Appendix C.3.

The fuel effect on cavitation inception discussed in Sec. 4.1.1 is confirmed once again for the acrylic model version 2. below is the 50μm needle lift case of all three fuels (See Appendix C.4 for all the other needle lift settings) taken for the below measurements:

Figure 4.1.13   Below measurements for all three fuels at 50μm needle lift – acrylic model version 2
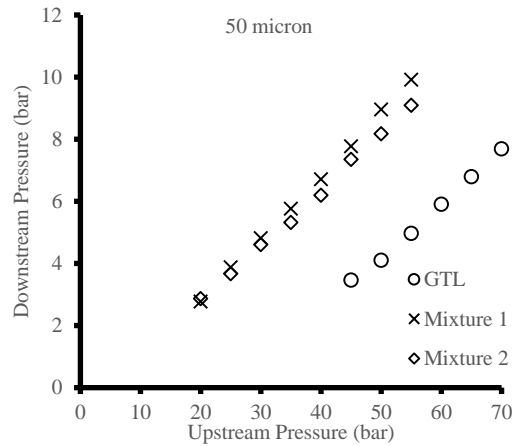
The saturated vapour pressure of the three fuels, being the lowest for the paraffinic model diesel and the highest for mixture 1, as shown in Table 3.4.2, is once again reflected in the results in Figure 4.1.13. In fact the paraffinic model diesel fuel, with the lowest saturated vapour pressure, presents the greatest upstream to downstream pressure ratio, followed by mixture 2 and then mixture 1, with the lowest saturated vapour pressure. For example, at 45 bar upstream pressure, the corresponding downstream pressure for incipient cavitation for the paraffinic model diesel is 3.468, for mixture 2 is 7.35 and for mixture 1 is 7.768, meaning an upstream to downstream pressure ratios of respectively of 12.98, 6.12 and 5.79. Using the definition of incipient cavitation shown in Eq. 2.3.2, the values of saturated vapour pressures shown in Table 3.4.2 and the upstream and downstream pressure range shown in Table 3.4.1, it was possible to calculate the incipient cavitation number for the three fuels in the plot below.

Figure 4.1.14   Incipient cavitation number for all three fuels at 50μm needle lift – acrylic model version 2
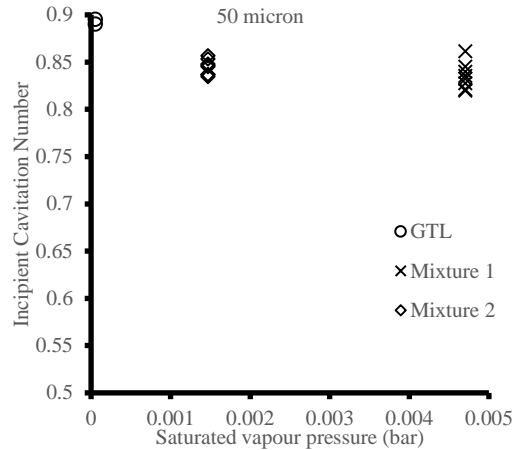
As expected, cavitation inception obtained for the paraffinic rich model diesel occurs at the largest cavitation number and lowest saturated vapour pressure when compared with the two hexadecane-octane mixtures. This result confirms once again that the paraffinic model fuel is less inclined to cavitate compared to mixture 2, which in turn is less inclined to cavitate compared to mixture 1 (the latter in fact exhibits cavitation inception at lower critical cavitation number and largest saturated vapour pressure). The same trend occurs for the remainder needle lift settings presented in Appendix C.5.

Following the same estimation for intermediate pressure as explained in Sec.4.1.1, it was possible to plot the variation of intermediate-to-downstream pressures for incipient cavitation for the acrylic model version 2:

Figure 4.1.15   Below measurements for acrylic model version 2 with paraffinic model diesel using estimated intermediate pressure
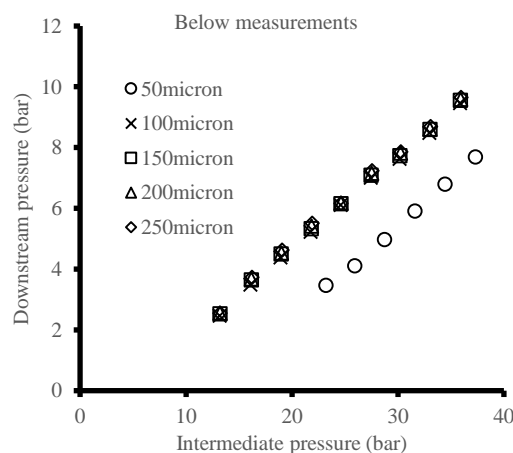
Again it can be noticed how the intermediate-to-downstream pressure ratios show the same results as for the upstream-to-downstream pressure ratios in terms of needle lift effect. However while in Figure

4.1.10 the upstream pressure is the same as the needle lift increases, in Figure 4.1.15 the intermediate pressure is increasing as the needle lift increases, visible by the slight shift between the 50μm and 100μm markers.

4.1.3   Fused Silica model

Details of the geometry of the fused silica model are found in Figure 3.2.10. In particular, it corresponds to the model having an outlet to inlet diameter ratio of 11:10, with the upstream and downstream blocks links together by a metal fitting. The upstream pressures and needle lift range for this model are specified in Table 3.4.1 following the methods explained in Sec. 3.4. The model was tested using the paraffinic model diesel as the working fluid.

From the results of the acrylic models described in Sec.4.1.1 and in Sec.4.1.2, it was highlighted that a big pressure ratio difference occurred between the 50μm and 100μm needle lifts settings. Therefore, in the fused silica assembly, a more refined needle was used with a 10μm step, allowing to focus in the lower needle lift settings.

It was observed that for every upstream pressure and needle lift setting, the incipient cavitation would again only occur at the entrance of the outlet throttle. The images below were taken for the case of upstream pressure 40bar, needle lift 80μm, at a shutter speed of 1/frame sec and a frame rate of 21600 fps.

Figure 4.1.16   Incipient cavitation (left) and fully cavitating flow (right) for paraffinic model diesel in fused silica model at the entrance of outlet throttle
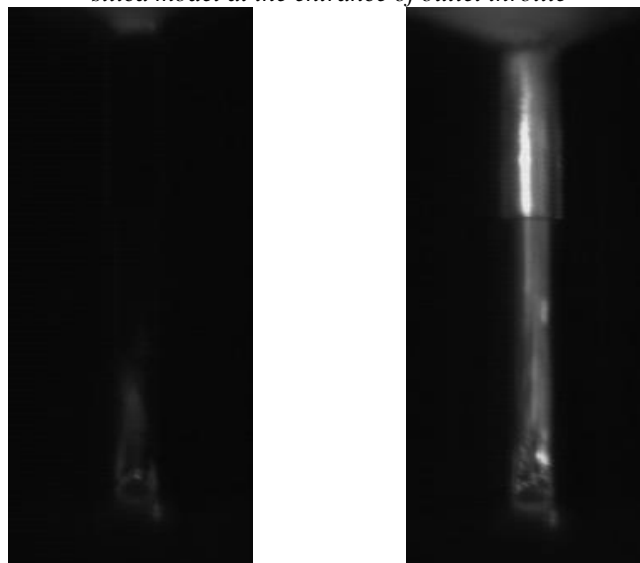
The white light scattered in Figure 4.1.16 represents the cavitating flow. When setting the upstream pressure at 40bar and leaving the downstream pressure at ambient conditions, the flow is cavitating throughout the throttle, allowing to visualise clearly the intermediate step (image on the right inFigure 4.1.16). The incipient cavitation image at the entrance of the outlet throttle is shown on the left in Figure 4.1.16. Moreover the entrance to the conical return volume is visible, where the flow is cavitating around the needle.

Starting from as low as 10μm needle lift setting all the way to 100μm in 10μm steps, it was possible to take 25 readings 'from above' and 25 readings 'from below' for upstream pressures from as low as 15bar where it was possible to capture incipient cavitation as mentioned in Table 3.4.1. The trends of upstream to downstream pressure ratios are shown in the plots below:

Figure 4.1.17   Above and below measurements for fused silica model with paraffinic model diesel
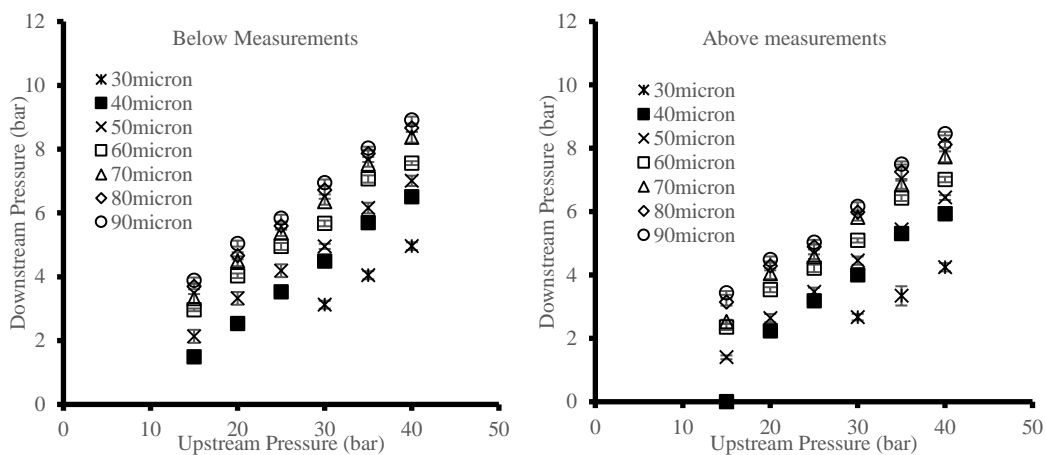
An obvious difference comparing the results in Figure 4.1.17 with the ones of the acrylics in Figure 4.1.2 and Figure 4.1.10 is that all needle lifts present different upstream to downstream pressure ratios. It was found that incipient cavitation starting occurring for as low as 30μm lift and 30 bar upstream pressure, and as low as 15bar upstream pressure and 50μm lift. A larger interval in the pressure ratio was found between 30μm and 40μm, while as the needle lift increased, the pressure ratio became more constant towards 100μm. The results in Figure 4.1.17 confirm the needle effect on cavitation inception at low settings due to the pressure gradient generated in the annulus around the needle. Hysteresis effect is still present in the above measurement, although a clearer relationship between upstream and downstream pressures is visible.

Upstream and downstream pressure plots at different needle lifts for the paraffinic model diesel in the fused silica model are presented in Appendix D.1.

Even for the fused silica model, it is possible to estimate the intermediate valve control chamber pressure by dividing the fuel flow in the model in three stages as shown in Figure 4.1.18:

Figure 4.1.18   Estimation of intermediate valve control chamber pressure in fused silica model
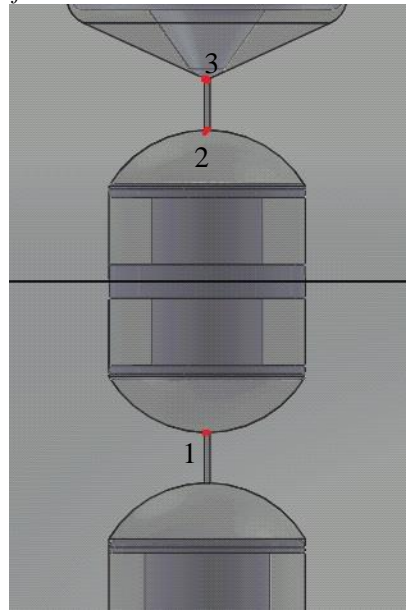
Using again Bernoulli's equation in Eq.4.1.1 to find the intermediate pressure p_2, it was possible to plot the variation of intermediate-to-downstream pressures for incipient cavitation for the fused silica model:

Figure 4.1.19   Below measurements for fused silica model with paraffinic model diesel using estimated intermediate pressure
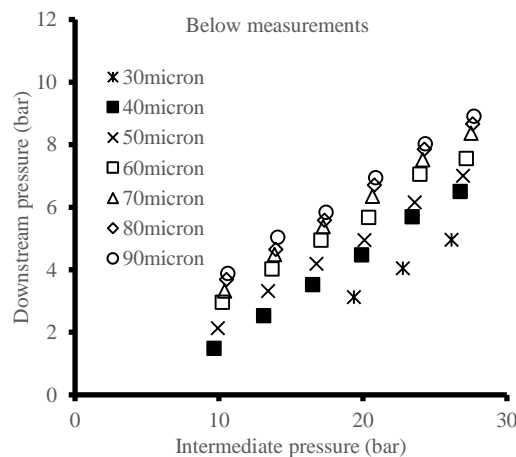
Once again it can be noticed how the intermediate-to-downstream pressure ratios show the same results as for the upstream-to-downstream pressure ratios in terms of needle lift effect. However while in Figure

4.1.17 the upstream pressure is the same as the needle lift increases, in Figure 4.1.19 the intermediate pressure is increasing as the needle lift increases, visible by the slight shift between the full range of 30μm to 90μm marker.

4.2   Discussion Arising on Comparison of Optical Accessible Models

As from the results presented in Sec. 4.1, a various number of conclusions can be identified in the characterisation of the return valve system.

Cavitation inception was found to be dependent on fuel type, cavitation number, saturated vapour pressure and needle lift. The paraffinic model diesel for instance was the working fuel utilised having the lowest saturated vapour pressure, however it gave rise to the largest cavitation number. This outcome explained the reason why the experiments with paraffinic model diesel presented the highest upstream to downstream pressure ratios, whereby the lower saturated vapour pressure increased the pressure difference across the outlet nozzle resulting in a lower downstream pressure for cavitation inception. On the other hand, mixture 1(n-hexadecane and n-octane 80:20 v/v proportions) presented the highest saturated vapour pressure along with the lowest cavitation number, hence the lowest upstream to downstream pressure ratio. This finding is consistent with the results obtained by Ndamuso [88], where different fuels with different saturated vapour pressures were tested under similar conditions in optical accessible models of diesel nozzle injectors. Independently by the type of nozzle geometry, the greater the saturated vapour pressure of the fuel utilised was, the lower the incipient cavitation number was found. Diesel fuels, for example, contain various paraffinic and aromatic compounds (See Sec.2.1), leading to a saturation vapour pressure greater than the paraffinic model diesel, but lower than the two mixtures studied above (less than 0.1kPa [91] – compared to values in Table 3.4.2). As a consequence, it is expected that diesel fuel will have a greater upstream-to-downstream incipient cavitation pressure ratio than the two mixture, but lower compared to the paraffinic model fuel.

When testing the acrylic blocks, it was found that the upstream to downstream pressure ratios were constant for needle lift settings of 100μm and higher, whilst it was noticed that between 50μm and 100μm there was a substantial difference. Setting up the fused silica block with a new cage assembly, it was possible to investigate the lower needle lift region by employing a needle with 10μm steps. As a

result, the region of interest below 100μm was studied, and the results proved that needle lift setting would vary the upstream to downstream pressure ratios almost linearly. Hence the very initial stage of opening the outlet throttle to allow the fuel to return in the tank follows the generation of a pressure gradient in the annulus between the outlet volume and the needle, which in turn will increase the pressure difference across the nozzle required for the onset of cavitation. The needle effect becomes negligible once it has reached the 100μm threshold. The images below in Figure 4.2.1 show the development of the cavitating flow in the fused silica model for upstream pressure of 40bar and ambient downstream pressure when varying the needle lift. The lower needle lift setting displays closer conditions to incipient cavitation due to the additional pressure gradient, while higher needle lift settings display a fully cavitating flow.

Figure 4.2.1   Development of cavitating flow at 40bar upstream, paraffinic model diesel in fused silica model for different needle lift settings
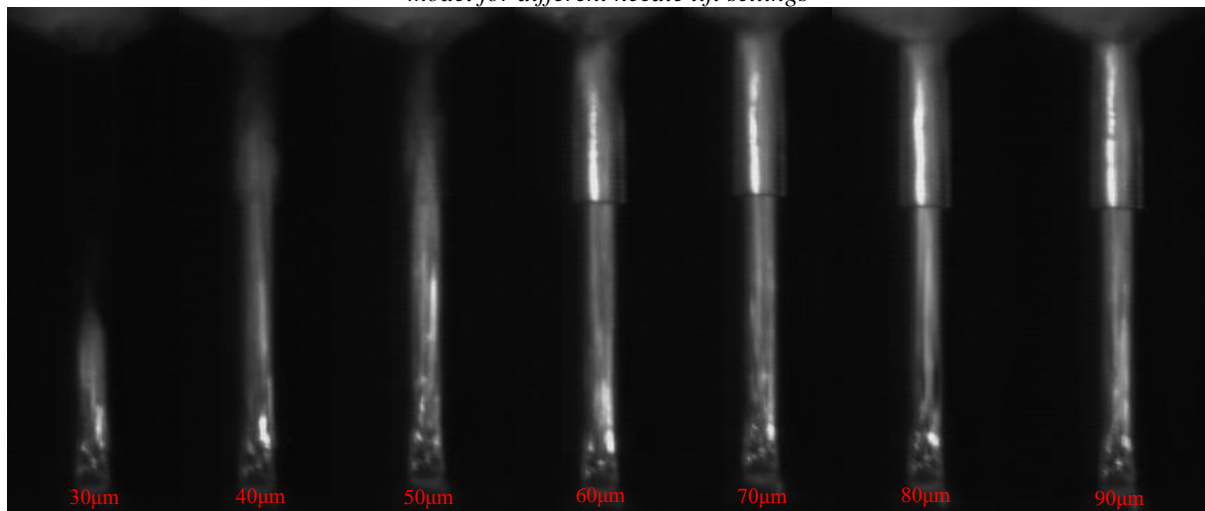
From a geometric point of view, a dependence of the upstream to downstream pressure ratio with the outlet to inlet diameter ratio was noticed. For instance, the two acrylic blocks were designed exactly the same, only with different outlet diameters. Comparing the upstream to downstream pressure ratio results of the two models, the following result is obtained:

Figure 4.2.2   *Comparison of incipient cavitation pressure ratio of acrylic models for 100μm needle lift and paraffinic model diesel*
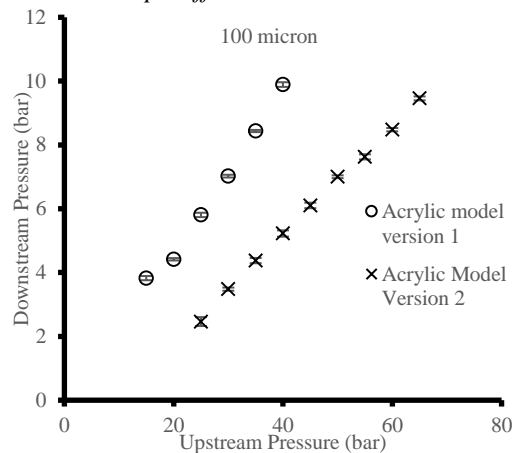
The plot above was obtained combining the incipient cavitation pressure results from the acrylic model version 1 and version 2 at needle lift of 100μm and paraffinic model diesel as working fuel. Despite having the same geometry, a different result was obtained due to the outlet diameter difference. For example, at 40bar upstream pressure, the corresponding downstream pressure for incipient cavitation for model 1 was 9.892bar, while for model 2 was 5.224bar. Hence the pressure ratios were respectively 4 and 7.7, almost double the difference. It can be deduced therefore that increasing the outlet diameter will not change the location of the cavitation onset, but only the required pressure difference. The greater the outlet diameter, the greater will be the pressure difference across the nozzle for cavitation inception. This is also manifested in Figure 4.2.3, where for version 1 on the left the fuel is cavitating throughout the nozzle, while in version 2 on the right is only partially cavitating.

Figure 4.2.3   *Comparison of fully cavitating flows at 40bar upstream pressure, 100μm needle lift, paraffinic model diesel for acrylic block version 1 (left) and version 2 (right)*
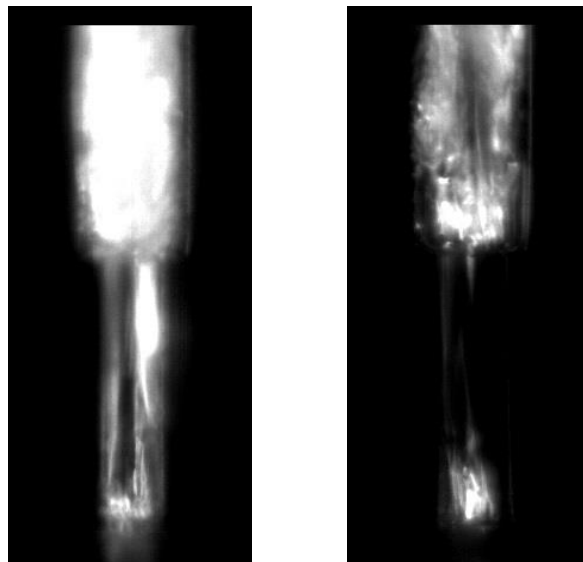
When comparing the fused silica model with the acrylic model version 1, having the closest outlet to inlet diameter ratio of ~1.1, very similar upstream to downstream pressure ratios were obtained, as shown in the plot below.

Figure 4.2.4   Comparison of incipient cavitation pressure ratio of acrylic model version 1 and fused silica model for 100μm needle lift and paraffinic model diesel
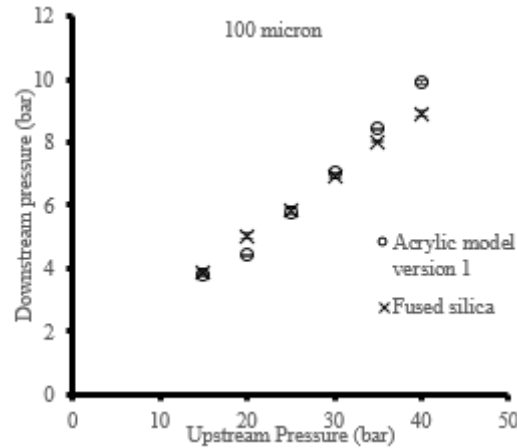
4.3   Implications for Modern Diesel Injection Systems

From the analysis of the three models an important observation was emphasised in regards to the design of modern diesel injection return valves. As noticed in Figure 4.2.2, the pressure ratio for incipient cavitation almost doubled when increasing the size of the outlet diameter, and Figure 4.2.3 illustrates how the additional pressure gradient is present in the latter circumstance. This leads to the question of whether the intermediate valve control chamber pressure is also changing to compensate the difference in pressure ratio.

The pressure in the valve control chamber has to decrease whilst the solenoid armature is opening the outlet throttle to allow the fuel to return back to the fuel tank. By decreasing the pressure, the needle injector is lifted consenting fuel injection in the combustion chamber (See Sec. 2.2.5). In the example presented in Figure 4.2.2, since the upstream pressures in the two models were the same while the downstream pressures were dissimilar, the intermediate valve control chamber pressure would most likely have to be dissimilar. This was confirmed when comparing the upstream-to-intermediate pressure ratios for incipient cavitation for acrylic models version 1 and version 2:

Figure 4.3.1   Comparison of incipient cavitation upstream-to-intermediate pressure ration of acrylic models version 1 and version 2 for 100μm needle lift and paraffinic model fuel
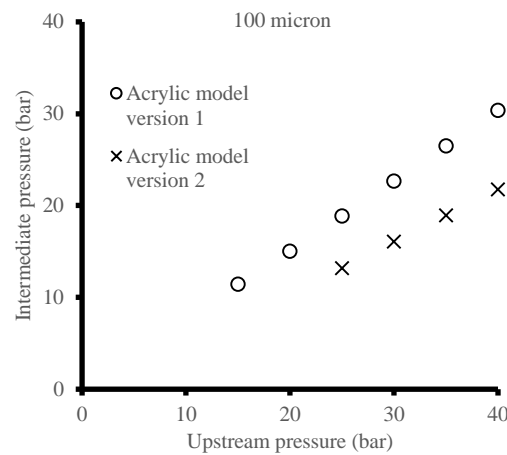
As expected in Figure 4.3.1, the intermediate pressure almost halved from acrylic model version 1 to version 2 (for example from ~19bar down to ~13bar respectively at 25bar upstream pressure). The intermediate pressure is therefore dependent on the outlet throttle diameter, reducing faster as the diameter increases for the same inlet throttle diameter.

Once the needle is lifted, the cavitation inception always and uniquely occurs at the entrance of the outlet throttle and almost instantaneously at the intermediate step along the throttle (See Figure 4.2.3). The inlet throttle never presents any form of cavitation, despite being a similar size to the outlet throttle. The pressure difference between the inlet volume and the valve control chamber is insignificant compared to the pressure difference between the valve control chamber and the outlet volume. It is believed therefore that the design of the return valve system has been developed not only to allow the valve control chamber to reduce its pressure to start injection, but also to shift the cavitation inception exclusively to the outlet throttle. If the fuel would start cavitating earlier in the inlet throttle, it would compromise the pressure in the valve control chamber, disturbing the injection process; whereas cavitation occurring in the outlet throttle would not affect at all the valve control chamber. The two stage pressure control system in the return valve plays a very important role therefore in making sure the correct amount of fuel is returned to the tank while simultaneously allowing fuel injection at the common rail pressure with no disturbance from the cavitating flow occurring in the spill valve.

Chapter 5 High Pressure Recirculation Test with Fused Silica Assembly

5.1 Experimental Setup

The high pressure recirculation experiment consisted of three principal set of equipment: the high pressure flow test rig, where the diesel fuel was allowed to flow through the fused silica return valve model; the in-situ laser extinction apparatus, where the change of the fuel properties were tracked throughout the length of the experiment by means of spectra measurements; the ultraviolet-visible spectroscopy apparatus, where samples of cavitated diesel fuel taken at different times during the experiments were used to take absorbance and transmittance spectra measurement.

The purpose of this experiment was to understand the change in properties of diesel fuel due to cavitation at high pressure when flowing across the return valve in a diesel injector over a long period of time. Using a test rig running the fuel at high pressure across a model return valve, and two optical equipment – the laser extinction equipment and the uv-vis spectroscopy – it was possible to track the changes of a diesel fuel over time.

The three different apparatus are described in more detail in Sec. 5.1.1, Sec. 5.1.2 and Sec. 5.1.3 below.

5.1.1 Flow Test Rig

This section of the experimental project is aimed to study the effect of recirculating cavitating flow on the chemical stability over long durations of diesel fuel as it goes through the spill valve model. Over time, some components in diesel fuel start to form deposits, hence this kind of experiment will allow to evaluate the change in the chemistry of the fuel over a long period of continuous recirculation due to the hydrodynamic cavitation caused by the geometry and the great pressure difference.

The apparatus that was utilised for this test is a custom made mechanical flow rig utilised firstly by Lockett and Jeshani [15], followed by Lockett and Fatmi [16] where the fused silica replica of the spill valve mechanism was attached to it. The whole assembly schematic is shown in Figure 5.1.1 below.

Figure 5.1.1   Schematic diagram of the test rig utilised for recirculation experiment in the fused silica model [16]
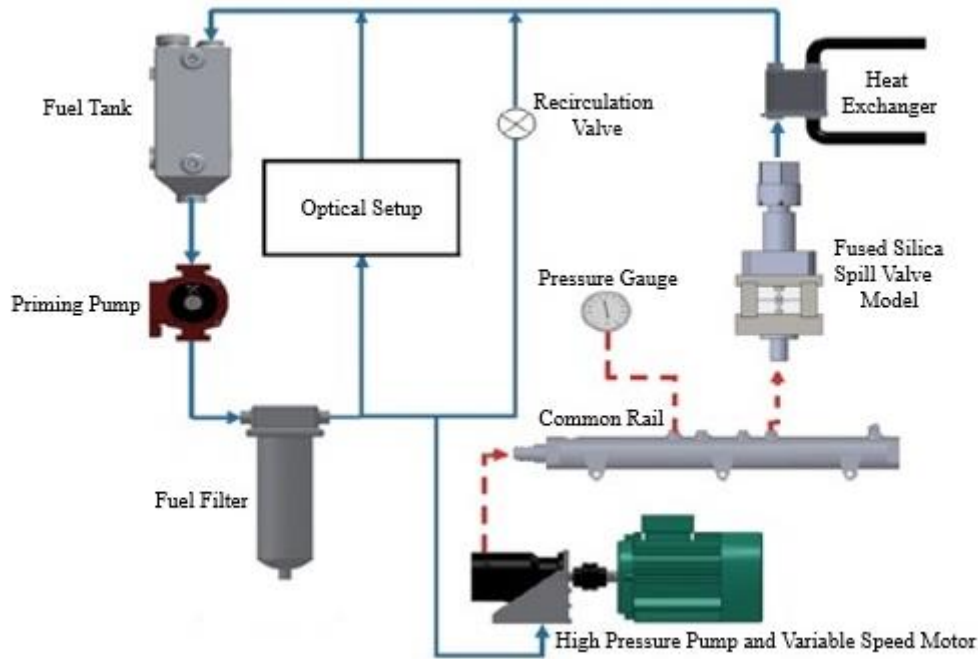
The rig works in a similar way to a typical FIE in diesel engines. Fuel is stored initially in a 3.7 litre capacity fuel tank and starts moving through a fuel line by means of a low pressure pump and reaches the high pressure pump after going through a fuel filter to eliminate large sediments to obstruct the rig. A 7kW variable speed motor would allow the Denso Mark-2 high pressure diesel pump (Part number DCRP200010) to reach the set testing pressure, so that the pressurised fuel would then flow to the common rail followed by the fused silica return valve model, where the fuel would cavitate. Finally the fuel would return to the fuel tank after cooling down by means of a counter-flow shell-and-tube heat exchanger. The recirculation of the fuel would continue as long as the motor kept running, keeping the high pressure pump at the set pressure.

For the purpose of the experiment, two deviations to the fuel line between the fuel filter and the high pressure pump occurred: one that allowed the fuel to run through an optical absorption setup and then back to the fuel tank; the other allowed the excess fuel to return back to the fuel tank through a recirculation valve. The blue lines in Figure 5.1.1 represent the low pressure lines, while the red dashed

line represent the high pressure lines. For health and safety, the rig was activated by means of an external apparatus, located in a room adjacent to the test lab. Both low pressure and high pressure pumps are activated with this apparatus, along a temperature reading to keep track of any raise in fuel temperature.

In order to drain the rig, two drainage points were allocated: a first drainage point was located under the heat exchanger, which emptied the fuel in the heat exchanger and return line from the receiver; a second drainage point was located under the fuel filter, which emptied the fuel from the tank, the fuel filter, the optical equipment and the rest of the fuel lines.

5.1.2   Extinction Measurement System

To study the change of the chemical properties of diesel fuel with time whilst running at high pressures through the return valve model as explained in Sec. 5.1.1, an extinction measurement system was setup. The objective of this apparatus is to capture the change of the fuel optical properties, in particular measuring its spectral extinction coefficient during the whole length of the long run of the experiment.

The setup of this equipment, located in between the fuel filter and the high pressure pump as shown in Figure 5.1.1, is a replica of that utilised by Mahesh [92]. It consists of a 405nm laser diode, an optical viewing cylinder, two photo-detectors and a beam splitter, as shown in Figure 5.1.2. The filtered fuel coming from the test rig enters the optical viewing cylinder from below and exit from above to return back to the fuel tank.

Figure 5.1.2   Laser and optics schematic setup [92]
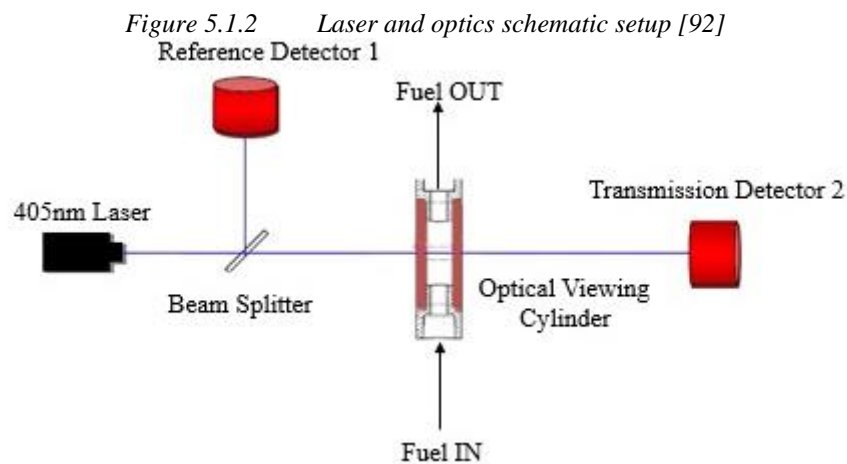
A 35 mW CW (Laser 2000) 405 nm diode laser was utilised to carry out these optical measurements, following previous experiments showing absorbance peaks at 405nm. The laser was directed towards

an optical viewing cylinder, made of a 30mm thick steel cylinder body, a 10mm x 40mm optical chamber with two optical grade fused silica windows of 6mm thickness each on two sides of the cylinder, to allow optical access to the working fuel. The laser would therefore cross the first fused silica window, followed by the optical chamber containing the recirculating diesel fuel, and then exit the cylinder through the second fused silica window. As the laser light crossed this assembly containing the fuel, it would transmit light, which would then reach the transmission detector at the end.

As noticeable in Figure 5.1.2, the laser encounters a deviation through its course in between the module and the optical cylinder due to the presence of a beam splitter. This was a ND0.03 neutral density filter, placed at 45˚ angle from the incident laser beam. The purpose of the filter was to split the laser beam, so that 90% of the beam would continue towards the optical cylinder, while 10% would reflect and deviate at 90˚ angle towards a second photo-detector, this time a reference detector.

The photo-detectors utilised were Laserpoint (A-02-D12-BBF) thermal low power sensors. Thermopile sensors, having a power resolution of 10μW, detect the laser coming from the module and measure its power from the temperature difference between the temperature inside the sensor and the ambient temperature. The laser power measurements were then recorded and averaged every 15s by a computer based software called Leonardo, which allowed to keep track throughout the running of the test rig the change of the laser power.

The reference detector is located in this apparatus so that it measures the laser beam intensity without passing through the cavitated diesel, whilst on the other hand the transmission detector measures the laser beam intensity after passing through the optical cylinder. In this way, it was possible to normalise the beam-transmitted intensity with the reference intensity. Moreover, to avoid influences by external light, an outer box covered the whole optical arrangement.

Figure 5.1.3 below is an image taken of the laser and optic setup contained in the box.

Figure 5.1.3   Laser and optics experimental setup
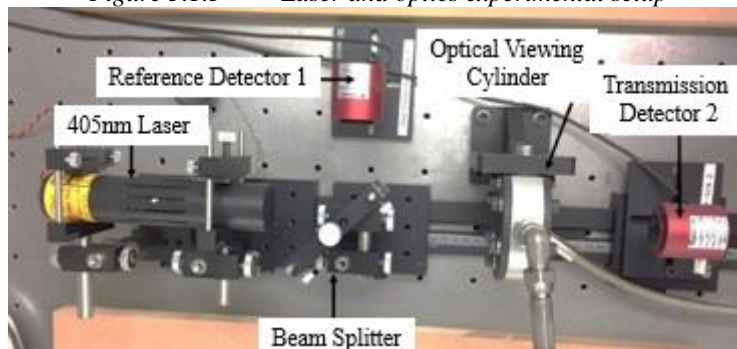
5.1.3   UV-VIS Absorption Spectrophotometer System

Similarly to the extinction measurement equipment described in Sec. 5.1.2, the ultraviolet-visible spectroscopy equipment was utilised to capture the change of chemical properties of diesel fuel over time. In particular, the UV-VIS analyses both spectra and photometric measurements of diesel samples taken at different intervals during the length of the experiment.

The main difference with the laser equipment is that the spectra measurements are taken for a range of wavelengths rather than a fixed one, from 190nm to 1100nm, hence including near infrared region (NIR), the visible region (390nm to 700nm) and the near ultraviolet region. This was obtained using a Shimadzu UV-1800 UV-Visible spectrophotometer, by means of a halogen lamp and a deuterium lamp and a set of mirrors and lens as shown in the schematic below.

Figure 5.1.4   Spectrophotometer schematic setup [93]
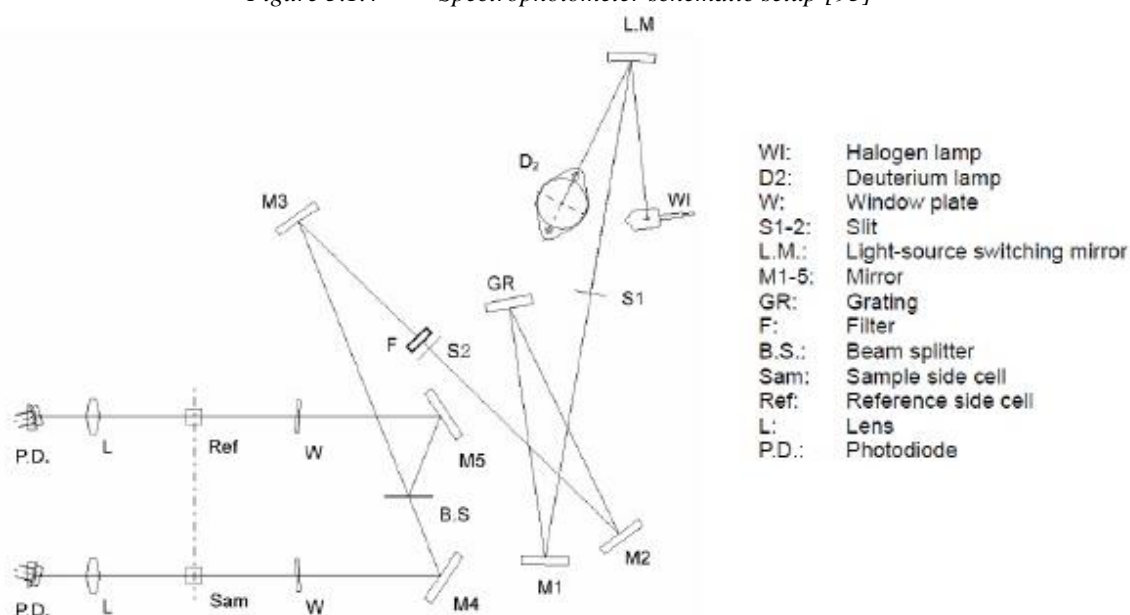
By means of the halogen and deuterium lamp, a double beam would generate from the beam splitter and reflected by M4 and M5 as shown in Figure 5.1.4. From M4, the beam would then cross a sample cell and reach thereafter the photodiode which will store the spectra information, while from M5 the beam would cross a reference cell and reach another photodiode. Similarly to the extinction laser equipment, the purpose of the reference beam is to create a baseline measurement in order to normalise the result obtained from the sample fuel.

For the photometric analysis, the sample and reference cells were occupied by Starna Scientific square cells cuvettes made of UV quartz with a sample path length of 10mm. A fixed wavelength would then be allowed to cross these cuvettes containing n-heptane for the reference cell and a diluted liquid containing the test fuel in the sample cell.

Finally the results gathered from the photodiode in the UV-Vis spectrophotometer would then be saved on a computer using a USB interface in a software called UV Probe, therefore allowing the user to view, manipulate and post-process the results for the required wavelength. The resolution of the wavelength could be as low as 0.01 nm, while the absorption measurement could vary from zero to four on a logarithmic scale.

5.2   Experimental Methods

5.2.1   Description of High Pressure Rig Recirculation Test Methods

Conversely to the flow characterisation of optical accessible model of modern return valve at low pressure described in Chapter 3, the high pressure recirculation test consisted on longer hours testing in order to observe the changes in fuel properties with time due to cavitation. In order to reach higher pressures, the fused silica model was used for this purpose being designed for higher pressure experiments.

The high pressure recirculation test were carried out in three stages. Each stage consisted in a weeklong of experiments during working hours, more specifically one day of flushing and priming the rig, and four days of experimenting. A summary of the experimental breakdown is shown in Table 5.2.1.

	Fuel	Duration	Number of Samples	Pressures
Week 1	Mixture of Fuel 1 (BDN) + previously cavitated Fuel 1 (BDN)	38 hours	5	200 bar
Week 2	Fuel 1 (BDN)	32 hours	4	200 bar
Week 3	Fuel 1 (BDN)	20 hours	2	250 bar
		12 hours	2	300 bar

Table 5.2.1   Experimental methods for high pressure recirculation test of fused silica model

The first batch of fuel utilised for week 1 experiment was a mixture of 0.95l of previously cavitated Fuel 1 (BDN) – the new conventional base diesel fuel consisting in a composition by mass of 38 % paraffins, 37 % naphthenes, 20 % mono-aromatics, 4.5 % di-aromatics, and less than 0.5 % tri- and poly-aromatics – from Lockett et al. [16] long duration test, with an additional 1.55l of fresh Fuel 1 (BDN). Whilst the following batches for week 2 and week 3 were fresh Fuel 1 (BDN), each of 2.5l.

The duration of the tests varied each week. For week 1, since the flushing and priming took place the previous week, the experiment was distributed as 6 hours on Day 1 and 8 hours for the following days, for a total of 38 hours at 200bar upstream pressure. For week 2, the experiment was distributed in 8 hours for four days, for a total of 32 hours at 200bar upstream pressure. For week 3, the experiment was distributed in 8 hours for four days, the first two days at 250 bar, on day 3, 4 hours were at 250bar and the remainder 4 hours at 300 bar, and on Day 4 at 300bar, for a total of 32 hours (20 hours at 250bar and 12 hours at 300bar). In addition to these hours there was also a warm up period at the beginning of each day at 100bar for 30minutes, to avoid the fused silica model failing due to the sudden jump at high pressure. A control temperature of 55˚C ensured the test rig to operate within safety conditions, using cooling water to keep the temperature below the control temperature. For the purpose of the experiment, a 3μm polypropylene fibre matrix filter was utilised throughout the duration of the tests.

Samples of diesel fuel were taken daily at the end of each working day and analysed in the UV-Vis absorption spectrometer. Meaning that in week 1, a total of 5 samples were taken, while for the other two weeks a total of 4 samples per week were taken.

Before starting each week of experimental testing, it was necessary to drain, flush and refill the test rig with the appropriate fuel. Through two available drainage points in the test rig, it was possible to remove the fuel from the previous experiment and collect in suitable beakers. Once the drainage of the old fuel was completed, it was necessary to flush the rig, i.e. fill and allow to recirculate the new test fuel at low pressures inside the rig and in the optical setup in order to clean it as much as possible from the previous fuel and prepare it for the new fuel without too much contamination. Two flushing cycles were effected, each time with 2.5l of the new test fuel (a total of 5l of fuel utilised for flushing), so that by the end of the second cycled and the filling of the new and final 2.5l the contamination was reduced to approximately 0.1%. For each flushing cycle, a total of 50 minutes of the operating rig was required, where for the first 4-5minutes the new fuel in the tank was allowed to recirculate using the low pressure pump to remove the trapped air inside the rig. For the remainder 45minutes, the high pressure pump was activated at an operating pressure of 100bar to ensure the fuel got recirculated throughout the apparatus, including the fused silica model.

The detailed methods for draining, flushing and refilling of the high pressure test rig is presented in Appendix E.1.

The experimental daily methods consisted in the following steps:

- Turn on the low pressure pump for 4-5minutes

- Turn on the high pressure pump and set the operating pressure at 100bar for 30 mins

- Turn on the in-situ laser transmission and increase the pressure to the required experimental pressure and run for the rest of the day as specified in Table 5.2.1, keeping an eye on the rig and the assembly in case of failure and on the laser transmission.

- At the end of the day, a 5ml sample of the diesel was taken from the fuel filter draining valve, and taken straight away for the UV-Vis absorption spectrometer

The detailed methods for the operation and procedure for running the high pressure test rig is presented in Appendix E.2.

5.2.2 Spectral Attenuation Data Analysis

During the high pressure recirculation experiment, an in-situ laser extinction measurement equipment was utilised in order to track the diesel's spectral attenuation. As the diesel fuel cavitates for a long period of time, carbon-rich species are expected to be produced which increase the spectral attenuation in the long run. The spectral attenuation can be measured by means of the transmitted laser signal passing through the diesel in the optical setup, expected to decrease as the spectral attenuation increases.

As the 405nm laser beam transmitted goes through the diesel sample, it goes through absorption and scattering. To measure the transmitted laser power, it is possible to apply the Beer-Lambert-Bouguer Law for optical extinction:

$$I_t(x) = I_o e^{-\alpha x} \qquad\qquad 5.2.1$$

where I_t represents the transmitted laser power (W) , I_o is the initial laser power incident to the absorptive sample (W) , α is the spectral attenuation coefficient (m^{-1}) and x is the distance of the laser beam through the sample (m). The absorption and scattering of the laser beam is identified in the spectral attenuation coefficient as:

$$\alpha = \alpha_{sc} + \alpha_{abs} \qquad\qquad 5.2.2$$

where α_{sc} is the scattering coefficient and α_{abs} is the absorption coefficient. Following the derivation by Lockett et al. [15], [92] to relate the Beer-Lambert-Bouguer law to the in-situ laser extinction setup, it is possible therefore to rearrange Eq.5.2.1 for α as follows:

$$\alpha = \frac{ln\frac{I_o}{I_t(x)}}{x} \qquad\qquad 5.2.3$$

The term in the numerator of Eq.5.2.3, $\frac{I_o}{I_t(x)}$, represents the absorbance *Abs*, while the transmittance *Tr* is given by the ratio:

$$Tr = \frac{I_t(x)}{I_o} \qquad\qquad 5.2.4$$

In the in-situ laser extinction equipment, I_o is the initial laser power incident to the diesel sample. Before reaching the diesel sample, it has to pass through the ND0.03 neutral density beam filter at 45˚ incidence and the fused silica window, thus:

$$I_o = t_f t_{fs} I_l \qquad\qquad 5.2.5$$

where t_f is the transmission coefficient through the neutral density filter and t_{fs} is the transmission coefficient through the fused silica cell window. Since the neutral density beam filter reflects the laser beam to a reference laser power detector, I_o can be rewritten from Eq.5.2.5 as:

$$I_o = \frac{t_{fs}(1 - r_f)}{r_f} I_{ref} \qquad\qquad 5.2.6$$

where r_f is the reflectivity of the ND0.03 neutral density beam filter and I_{ref} is the reference detector laser power. The laser power exiting the diesel sample (the transmitted laser power I_t) will have to go through a further fused silica glass before reaching the final detector, giving rise to the next equation:

$$I_P = t_{fs} I_t \qquad\qquad 5.2.7$$

where I_P is the laser power measured by the detector.

Finally, combining Eq.5.2.3 with Eq.5.2.6 and Eq.5.2.7, the following equation for spectral attenuation coefficient can be obtained:

$$\alpha = \frac{ln \dfrac{t_{fs}^2 (1 - r_f) I_{ref}}{r_f I_P}}{x} \qquad\qquad 5.2.8$$

The values of t_{fs}^2, r_f and x were calculated through a series of calibration tests by Lockett et al. [15], [92] as respectively 0.945, 0.16 and 1.03cm.

The presence of a reference photo-detector for the experiment was essential due to the diode laser warming in time during the long duration of the experiment. Having a reference detector would allow therefore to normalise the value of the laser power measured by the transmission detector against the value of the laser power measured by the reference detector, keeping track therefore on the performance of the laser throughout the experiment.

As explained in Sec.5.1.2, the software that would record the laser power from the transmission and reference detectors was called Leonardo. Once the laser system was turned on, as explained in Sec.5.2.1, the software would record a 15s average laser power from the two detectors separately throughout the whole duration of the daily experiment. To process the data, the recorded laser powers were then

grouped in 15mins average laser powers to reduce the number of signals to analyse. The values of the 15mins average transmitted laser power I_P were then normalised by dividing them by the values of the same 15mins average reference laser power I_{ref}. Ultimately Eq.5.2.8 could be used to calculate the value of the spectral attenuation coefficient as a function of time.

5.2.3 Discrete Samples for UV-VIS Data Analysis

The purpose of the UV-Visible Spectrophotomer was to analyse the Fuel 1 (BDN) diesel samples collected at the end of each experimental day, in particular to track the absorption spectra of the samples at different interval of time and thereby establish the change in fuel properties as it cavitates for a long period of time. From the variation of spectral absorption with time it is possible to understand how the fuel properties are changing.

Figure 5.2.1   Fuel samples taken in week 1 of high pressure recirculation test for UV-Vis analysis

In order to analyse the full range of the spectra absorption in more detail, it was decided to proceed in the UV-Vis spectral analysis in three different steps:

1. A first analysis would consist in measuring the absorbance in the wavelength range between 350nm – 500 nm of the fuel samples;

2. A second analysis would consist in measuring the absorbance in the wavelength range between 240nm – 305 nm;

3. A third analysis would consist in measuring the absorbance in the wavelength range between 190nm – 405nm.

The Shimadzu UV-1800 UV-Visible spectrophotometer has a dynamic absorption measurement range between 0 and 4, but in order to gain accurate and more precise results for the absorbance spectra of the diesel samples, it was necessary to establish an upper threshold of 2.7 absorbance. To do so, a dilution

process was essential, and n-heptane was used as the diluent (also used as background solution in the reference cell, see Sec.5.1.3).

For the first subrange, 350nm – 500nm, no dilution was necessary since the absorbance remained below 2.7 in the specified wavelength. However in both the other subranges dilution was required.

In the second subrange, 240nm – 305nm, a dilution ratio of 1:520 was adopted, where 5μl of the cavitated fuel sample was diluted in 2.6ml of n-heptane. Whilst in the third subrange, 190nm – 405nm, a dilution ratio of 1:10000 was adopted, where 140μl of the 1:520 diluted sample was furthe diluted in 2.6ml of n-heptane. For the n-heptane, a Socorex Swiss glass syringe was utilised, while for the first dilution a 5μl Drummond micro-dispenser was utilised, and for the second dilution a 20μl and a 100μl Drummond micro-dispensers were utilised.

For the first analysis, 3ml of the fuel sample was poured into a 4ml glass cuvette and placed in the test cell in the spectrometer along with the n-heptane cuvette positioned in the reference cell for background solution. The sample would then be scanned three times in the wavelength region of 350nm – 500nm, and then averaged to give a mean absorbance spectrum solution.

For the second analysis, the dilution 1:520 sample would be poured in another 4ml glass cuvette and placed in the test cell in the spectrometer along with the n-heptane cuvette positioned in the reference cell for background solution. The sample would be again scanned three times in the wavelength region of 240nm – 305nm, and then averaged to give a mean absorption spectrum solution. Due to the fact a dilution process was incurred, three other 1:520 samples were scanned in the same way to ensure dilution repeatability. All four absorption spectra would have to be as precise and close as possible to consider the diluted solution spectrum reliable. Therefore for each of the four averaged absorption spectra, the ratio of 1σ standard deviation over the mean absorbance of the four spectra was calculated, i.e. the coefficient of variation, and established to be less than 2%. In order for this condition to be valid, the final absorption spectrum for the diluted sample in the 240nm – 305nm wavelength range was the mean of the four averaged absorption spectra.

For the third analysis, the dilution 1:10000 sample would be poured into another 4ml glass cuvette and placed in the test cell in the spectrometer along with the n-heptane cuvette positioned in the reference

cell for background solution. The sample would be scanned three times again in the wavelength region of 190nm – 405nm, and then averaged to give a mean absorption spectrum solution. As in the second analysis, three other 1:10000 samples were scanned to ensure dilution repeatability. If the coefficient of variation would still be less than 2% also for the new four averaged absorption spectra, then the final absorption spectrum for the diluted sample in the 190nm – 405nm wavelength range would be the mean of the four averaged absorption spectra.

The detailed methods for the operation of the UV-Vis absorption spectrum of the three wavelength ranges is presented in Appendix E.3.

5.3   Final Design Modification of Fused Silica Assembly at High Pressure

In addition to the challenges in finding a manufacturing company able to recreate the return valve system in fused silica, and the further modifications to the design explained in Sec.4.1.3, further issues were encountered during the experiment in the high pressure recirculation rig.

While for the low pressure test rig experiment the fused silica model worked just fine, when it came to the high pressure recirculation rig the model failed numerous times, causing delays. For safety reason, an aluminium cage was positioned around the fused silica assembly in order to avoid high pressure fuel jets or glass shards to disperse around the experimental equipment causing hazardous damage. The needle apparatus was kept in the assembly, only lifted at 300μm to avoid generating further pressure gradients.

The block would not fail when setting the upstream pressure at 100bar, but a few minutes after setting the pressure at 200bar it would suddenly shatter into small shards. The first time only the upstream block failed. It was therefore decided to insert a viton sheet in between the two blocks, since the failure was thought to have occurred due to the strain between the two glass surfaces.

Subsequently, another failure occurred again at 200bar upstream pressure after the 100bar 30minutes priming, only this time the downstream block failed. Conversely to the first failure which resulted in the block shattering into small shards, this time the failure presented itself as a crack, as shown in Figure 5.3.1 below.

Figure 5.3.1   Downstream block of the fused silica assembly failing at 200bar upstream pressure

It was suspected after closer inspection that the stainless steel intermediate fitting might have caused the fracture by etching the top spherical corner of the valve control chamber, as shown in Figure 5.3.1 above. For this reason, a viton sheet in the shape of a ring was positioned around the metal fitting, to avoid the fracture to re-occur in the following spare downstream block.

Following these modifications, the fused silica assembly managed to resist higher pressures all the way up to 300bar, without resulting in failures or fuel leakages. below is the final assembly after the modifications were made.

Figure 5.3.2   Fused silica assembly in high pressure recirculation rig after the appropriate modifications
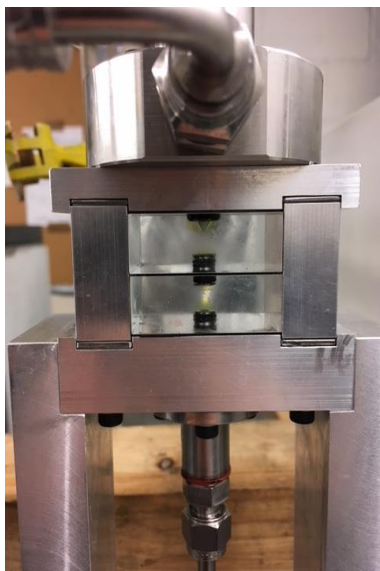
Chapter 6 Results and Analysis – High Pressure

The following paragraphs will focus on the experimental results obtained following the setup and methods explained in Sec.5.1 and in Sec.5.2. In particular, this chapter will present the findings of high pressure recirculation experiments for the fused silica model, focusing on the effects of long duration cavitation effects on diesel fuel properties whilst passing through the return valve.

Initially there will be a description of how the repeatability of the dilutions were attained, explaining the steps required in order to be satisfied with accurate dilution samples. Then the results will be presented for the in-situ laser extinction measurements taken during the experiment, whereby the spectral properties of the fuel will be analysed for the 405nm absorbance. The UV-Visible spectrophotometer results will also be presented, whereby the spectral attenuation of the fuel for a greater wavelength range will be analysed using the samples taken periodically during the experiment. Finally all these results will be compared with previous work done on long duration cavitation analysis in modern DIE.

6.1   Repeatability of Dilutions

The dilution methods explained in Sec.5.2.3 was tested on a cavitated sample of Fuel 1 (BDN) from Zeeshan's [94] experiments in order to outline the steps carefully and master the techniques required to accurately dilute the fuel in n-heptane. The time at which the repeatability test was taken is earlier than the time at which the experiments were carried out in Sec.6.2.2. For the dilution process to be accurate, repeatability needs to be valid. Therefore 40 diluted samples were prepared in both dilution ratios 1:520 and 1:10000 (See Sec.5.2.3). The repeatability test followed the same steps outlined by Zeeshan in [94].

For the first dilution ratio 1:520, 40 samples were prepared with 2.6ml of n-heptane and 5μl of fuel sample in each cuvette. Each cuvette was then positioned one at the time in the test cell inside the spectrophotometer alongside the n-heptane cuvette in the reference cell, and scanned over the wavelength range of 240nm-285nm. below in Figure 6.1.1 is the mean absorption spectrum of the 40 diluted samples with dilution ratio 1:520, along with error bars representing 2σ standard deviation. While in Figure 6.1.2 it is displayed the distribution of the absorbance bins amongst the diluted samples

in the wavelength of 260nm, where the mean absorption was calculated to be 2.09. It can be noticed how the repeatability shows good agreement with the mean value.

Figure 6.1.1   Mean absorption spectrum of Fuel 1 (BDN) diluted sample in the ratio of 1:520 with 2σ error bars
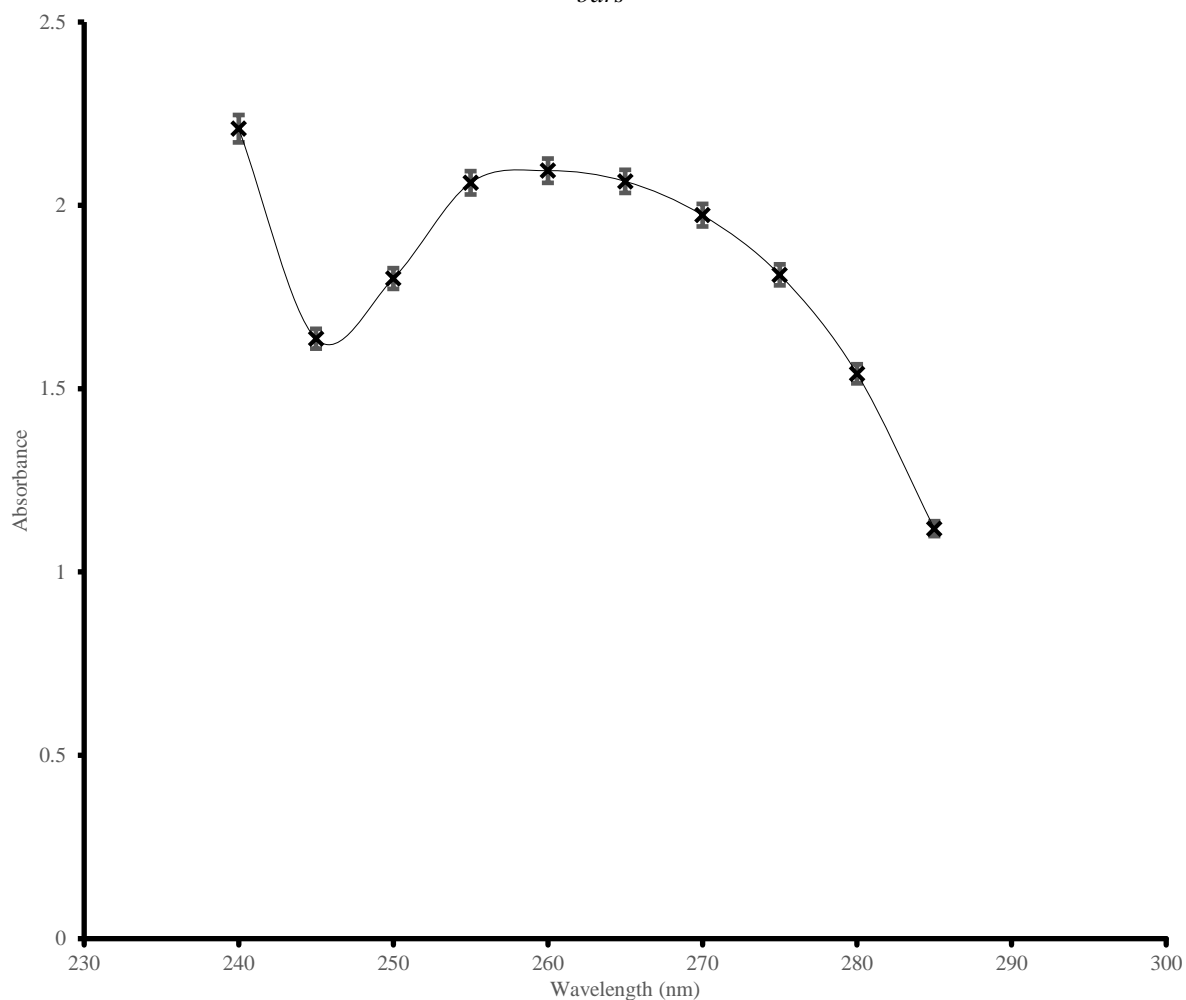
Figure 6.1.2   Distribution of absorbance bins amongst the 1:520 dilution ratio samples in the 260nm wavelength
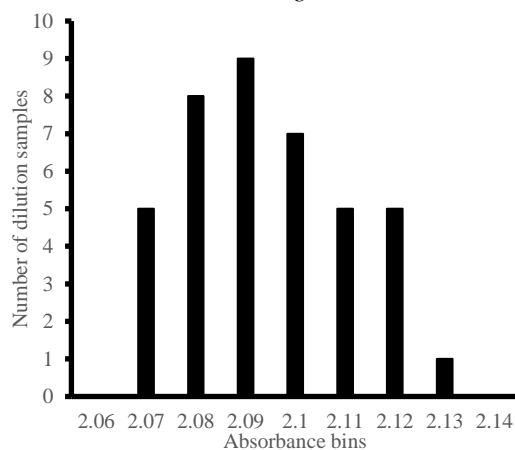
For the second dilution ratio 1:10000, 40 samples were prepared with 2.6ml of n-heptane and 140µl of the first diluted sample (1:520) in each cuvette. Each cuvette was then positioned one at the time in the test cell inside the spectrophotometer alongside the n-heptane cuvette in the reference cell, and scanned over the wavelength range of 195nm-250nm. below in Figure 6.1.3 is the mean absorption spectrum of the 40 diluted samples with dilution ratio 1:10000, along with error bars representing 2σ standard deviation. While in Figure 6.1.4 it is displayed the distribution of the absorbance bins amongst the diluted samples in the wavelength of 205nm, where the mean absorption was calculated to be 2.18. It can be noticed how the repeatability shows good agreement with the mean value. The lower wavelengths of 195nm and 200nm are less accurate due to the spectrophotometer limitations at those wavelengths.

Figure 6.1.3   Mean absorption spectrum of Fuel 1 (BDN) diluted sample in the ratio of 1:10000 with 2σ error bars
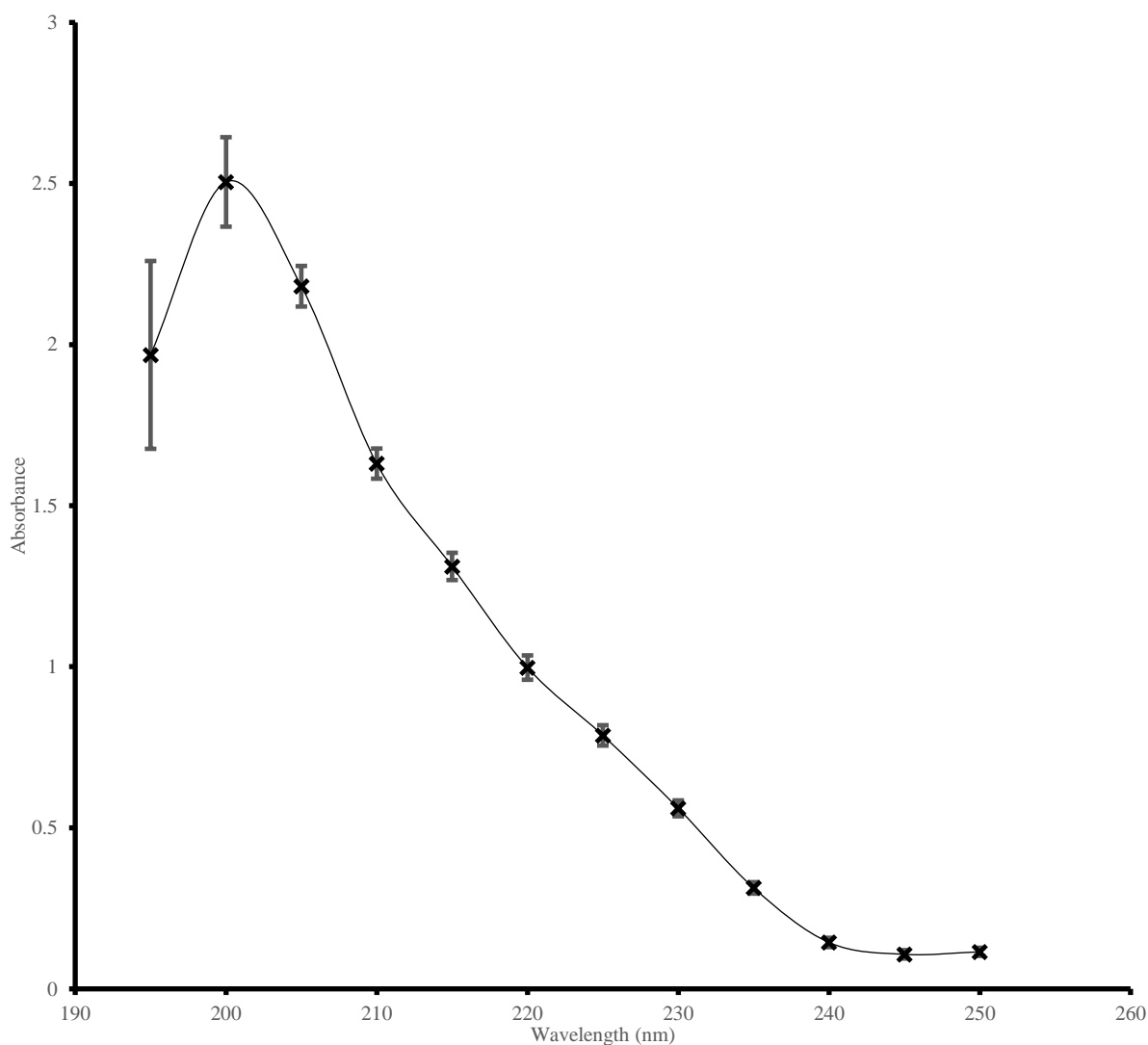
Figure 6.1.4   Distribution of absorbance bins amongst the 1:10000 dilution ratio samples in the 205nm wavelength
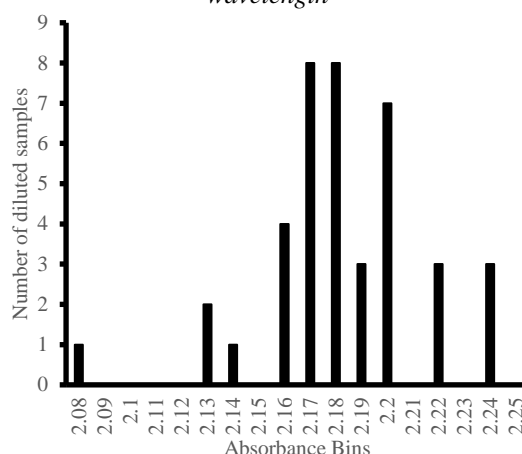
As a means to decide whether the dilutions are precise or not, the coefficient of variation was adopted, which represents the ratio of 1σ standard deviation over the mean. This value had to be below 2% in order for the diluted samples to be agreeable.

Figure 6.1.5   Coefficient of variation for the wavelength ranges of the two dilution ratios, 1:520 (left) and 1:10000 (right)
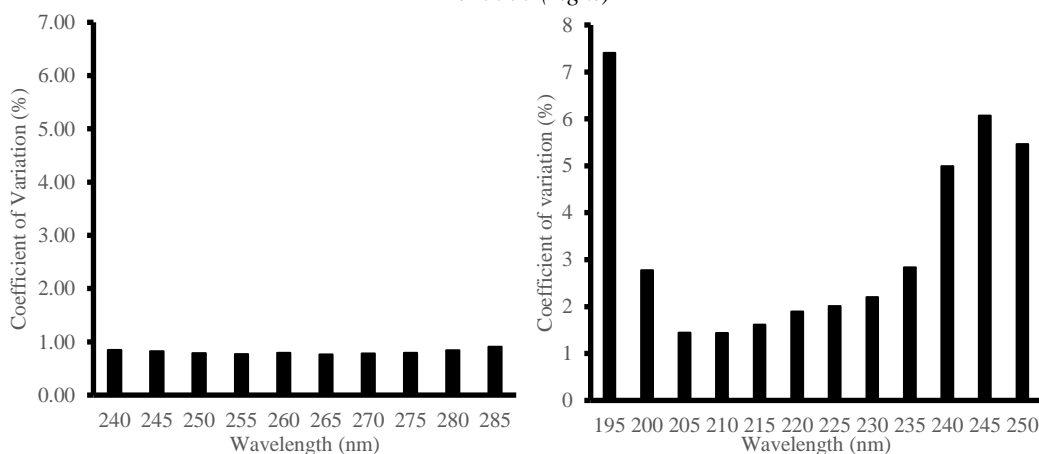
For the first dilution ratio 1:520, the 40 samples presented a coefficient of variation below 2% throughout the wavelength range tested, showing therefore a great agreement. For the second dilution ratio 1:10000, the 40 samples presented a coefficient of variation below 2% in the wavelength range between 205nm – 230nm. The wavelength range above 230nm showed higher values of coefficient of performance since the absorption values calculated were close to 0, hence the ratio of coefficient of performance would give rise to a greater value.

6.2   Experimental Results and Discussion

6.2.1   Spectral Attenuation Data Analysis

The first part in investigating the pyrolytic reactions occurring in the diesel fuel whilst cavitating in the outlet throttle of the return valve system, was to utilise a 405nm diode laser in the optical setup described in Sec.5.1.2 and measure the change in the spectral attenuation of the fuel with time.

When molecules are exposed to light with an energy level able to excite the electrons within the molecule to a different orbital, it will allow the light energy to be absorbed in the molecule. The molar absorptivity ε ($1 \cdot$ mol$^{-1} \cdot$ cm^{-1}) can be determined from the Beer's law as:

$$\varepsilon = \frac{Abs}{bc} \qquad\qquad 6.2.1$$

where b is the length of light path through the sample (cm) and c is the concentration of the chromophores (mol/l).[95], [96] A chromophore is the part of the molecule which is responsible for its colour and when hit by light it absorbs the latter by exciting electrons from ground to higher energy states. [97] From Eq.6.2.1 it can be seen that the absorption is directly proportional to the concentration of the chromophores in the sample. The relationship is generally valid for a specific wavelength λ, and it is of great importance as it allows to track the variation of fuel chemical properties with time by analysing its absorbance and the change in concentration of the fuel chromophores.

In the in-situ laser extinction equipment setup, the laser power was recorded in 15s averages for both transmission and reference signals (See Sec.5.2.2). However, the issue in recording signal data in 15s averages is that it takes account of any slight variation of experimental condition, such as the cooling of the fuel with water in the heat exchanger when reaching control temperature (See Sec.5.1.1), the pressure of the pump to the fuel and the same air temperature inside the experimental cell.

Figure 6.2.1   *Comparison of signal data when averaging seconds and minutes*
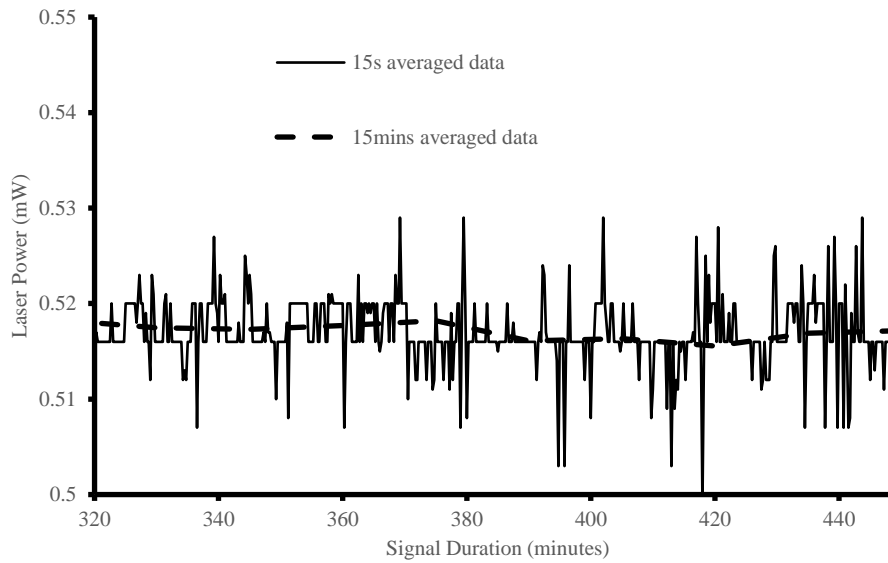
By averaging the 15s signal data in 15minutes average signal data, it was possible to eliminate some of these variations. Figure 6.2.1 illustrates an example of the 15s signal data laser power recorded by one of the detectors compared to the corresponding average of the 15minutes signal data laser power. The seconds-average data is much more irregular, due to the change of fuel temperature conditions. On the other hand the minutes-average data removes for example the cooling of the fuel due to the heat exchanger and water cooling, allowing a more regular variation and eliminating the pulsating variation illustrated in the plot above. Therefore, the processing of the signal data from the detectors consisted in first of all averaging the laser powers in 15minutes averaged data for both transmission and reference signal. It then involved in normalising the transmission signal by dividing the transmission averaged data with the reference averaged data, in order to eliminate any variation during the experiment such as the heating of the diode laser over time. Finally, the spectral attenuation coefficient would be calculated using Eq.5.2.8 explained in full detail in Sec.5.2.2.

Following the experimental methods in Table 5.2.1, the high pressure recirculation experiment was executed in three separate weeks, each with a different duration, different pressure and different fuel.

In Week 1, the fuel utilised was a mixture of Fuel 1 (BDN) and of Fuel 1(BDN) previously cavitated (See Sec. 5.2.1) in a 62:38 v/v proportion. Each experimental day, the rig would be left to run for 30mins at 100bar, after which the upstream pressure was increased to 200bar; at which point the laser extinction

equipment was turned on and the signal data started recording for the rest of the day. The working schedule for Week 1 explained in Sec.5.2.2 is presented in Table 6.2.1.

Day	Pressure (bar)	Maximum Temperature (°C)	Duration (hours)
1	100	45.2	0.5
	200		6
2	100	45.4	0.5
	200		8
3	100	46.2	0.5
	200		8
4	100	46.4	0.5
	200		8
5	100	46.5	0.5
	200		8

Table 6.2.1   Experimental schedule for Week 1

Once the whole data was collected at the end of the week, the post-processing of the results – meaning the 15mins averaging of data, normalising the transmission laser power signal and calculating the attenuation coefficient – resulted in the following plot.

Figure 6.2.2   Normalised laser transmission (left) and attenuation coefficient (right) at 405nm for Week 1 experiments
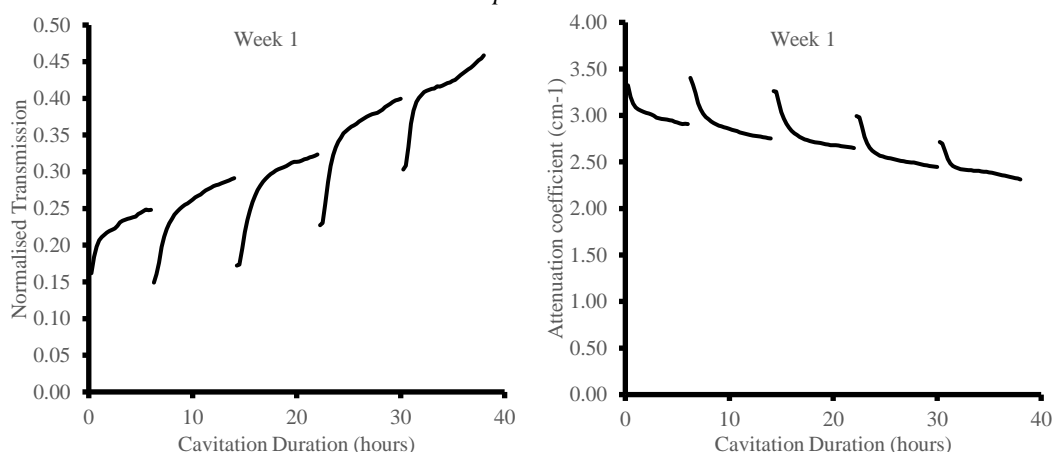
From the normalised transmission measurement plotted in Figure 6.2.2, there are two aspects that can be highlighted. First of all, each day results in a separate line having the similar trend of starting at low normalised transmission, followed by a rapid increase occurring in a length of time of ~1 hour and then a steady lower increase rate. Thus, at the beginning of each working day, there would be an interruption in the normalised transmission data, due to the ~1 hour delay for the data to stabilise. This phenomenon can be referred to the fact that overnight, the rig would cool down during non-operating hours, allowing

similarly the fuel to cool down; consequently at the start of the following working day, the test rig and likewise the fuel need to warm up and reach the same conditions of the previous day to allow the transmission measurements to continue smoothly.

The other aspect that can be highlighted is that the normalised transmission is steadily increasing with time throughout the week. The starting value of normalised transmission calculated was 0.21, and it increased all the way up to 2.31 by the end of the week. This result would suggest that there is a change in the chemical properties of fuel, in particular in the 405nm wavelength of the beam, confirming the pyrolytic type reactions occurring in a cavitating diesel flow.

The attenuation coefficient was calculated using values of t_{fs}^2, r_f and x shown in Sec.5.2.2. The trend as expected is the exact opposite, ranging from 3.12cm^{-1} to 2.31cm^{-1}, i.e. decreasing due to the change of chemical properties and formation of larger particles.

In Week 2, the fuel utilised was a fresh batch of 2.5l of Fuel 1 (BDN) (See Sec. 5.2.1). Once again on each experimental day, the rig would be left to run for 30mins at 100bar, after which the upstream pressure was increased to 200bar; at which point the laser extinction equipment was turned on and the signal data started recording for the remainder of the day. The working schedule for Week 2 explained in Sec.5.2.2 is presented in Table 6.2.2.

Day	Pressure (bar)	Maximum Temperature (°C)	Duration (hours)
1	100	46.6	0.5
	200		8
2	100	46.9	0.5
	200		8
3	100	46	0.5
	200		8
4	100	45.9	0.5
	200		8

Table 6.2.2   Experimental schedule for Week 2

On the contrary to Week 1, Week 2 was spread over the course of four days, since one day was needed to drain and flush the rig in preparation of the new test (in Week 1, the draining and flushing was executed the previous week).

Once the whole data was collected at the end of the week, the post-processing of the results – meaning the 15mins averaging of data, normalising the transmission laser power signal and calculating the attenuation coefficient – resulted in the following plot.

Figure 6.2.3   Normalised laser transmission (left) and attenuation coefficient (right) at 405nm for Week 2 experiments
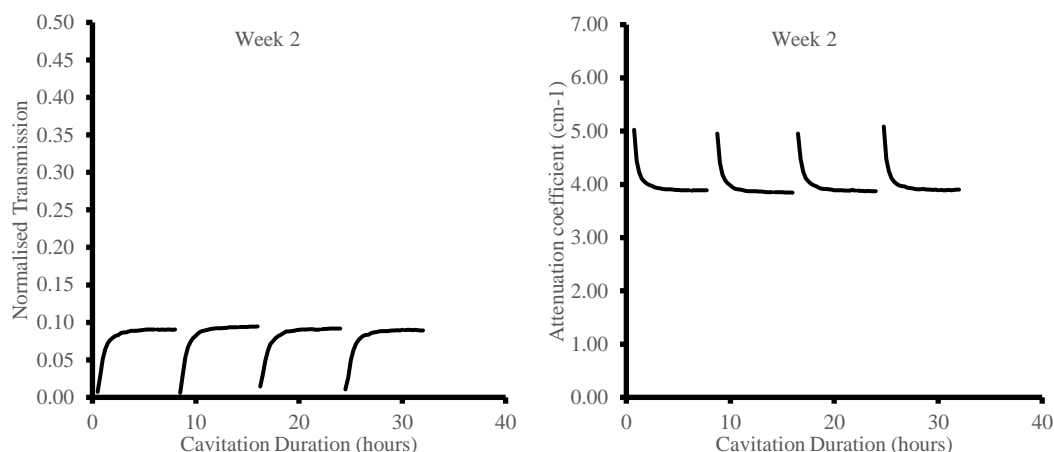
From the normalised transmission measurement plotted in Figure 6.2.3, there are again two aspects that can be highlighted. The first aspect is the same as the one highlighted for Week 1, which is the interruption of the normalised transmission measurements between the end of one day and the beginning of the following day. As explained before, this is a consequence of the settling time for the fuel to readjust to the working temperatures of the previous day, as it cooled off overnight while non-operating.

The second aspect, which differentiates Week 2 experiments with Week 1 experiments, is the lack of increase in the normalised transmission measurements over the length of the test. In fact, the plateau value of normalised transmission was calculated ~0.09. This phenomenon can be linked to the chemical properties of the working fuel. While in Week 1 the mixture utilised was one that already cavitated at 1650bar upstream pressure, meaning that some new particles were already present from the beginning, in Week 2 the fuel was a fresh Fuel 1 (BDN), which despite cavitating at 200bar upstream pressure, it has not reached the conditions to initiate a pyrolytic type chemical reaction. The constant normalised transmission signal meant that no change occurred in the chemical properties of fuel over time, in particular in the 405nm wavelength of the beam.

The attenuation coefficient was calculated using values of t_{fs}^{2}, r_f and x shown in Sec.5.2.2. Similarly to the normalised transmission, the attenuation coefficient remains constant at 3.98cm^{-1} throughout the duration of the weekly experiment.

In Week 3, the fuel utilised was a fresh batch of 2.5l of Fuel 1 (BDN) (See Sec. 5.2.1). Once again on each experimental day, the rig would be left to run for 30mins at 100bar, after which the upstream pressure was increased to 250bar for the first three days; then halfway on the third day, the upstream pressure was increased to 300bar and after the 100bar warm up on the fourth day the pressure was increased directly to 300bar. The laser extinction equipment was turned on at the end of the 100bar warm up period on each day and the signal data started recording for the remainder of the day. The working schedule for Week 3 explained in Sec.5.2.2 is presented in Table 6.2.3.

Day	Pressure (bar)	Maximum Temperature (°C)	Duration (hours)
1	100	47.4	0.5
	250		8
2	100	47	0.5
	250		8
3	100	49.5	0.5
	250		4
	300		4
4	100	49.6	0.5
	300		8

Table 6.2.3   Experimental schedule for Week 3

Week 3 was spread over the course of four days as in Week 2, using the first day of the week for draining and flushing purposes.

Once the whole data was collected at the end of the week, the post-processing of the results – meaning the 15mins averaging of data, normalising the transmission laser power signal and calculating the attenuation coefficient – resulted in the following plot.

Figure 6.2.4   *Normalised laser transmission (left) and attenuation coefficient (right) at 405nm for Week 3 experiments*
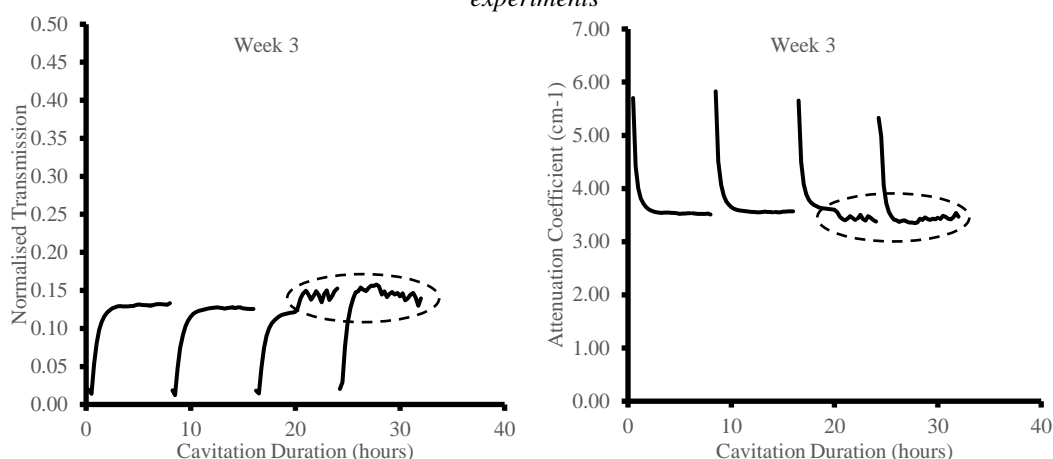
From Figure 6.2.4, apart from the interruption of the normalised transmission measurements between the end of one day and the beginning of the following day discussed before, another two aspects can be highlighted.

Firstly there is the lack of increase in the normalised transmission measurements over the length of the test. In fact, the plateau value of normalised transmission was calculated ~0.13. This phenomenon recurred similarly in Week 2, and can be linked to the fact that using fresh Fuel 1 (BDN) does not reach the conditions to initiate a pyrolytic type chemical reaction despite cavitating at 250bar/300bar. The constant normalised transmission signal meant that no change occurred in the chemical properties of fuel over time, in particular in the 405nm wavelength of the beam.

Secondly is the sudden irregularity shown in the encircled region on day 3 and day 4 in Figure 6.2.4. The increase in normalised transmission from ~0.13 to ~0.15 is expected due to the increase in upstream pressure from 250bar to 300bar. The irregularities on the other hand are a result of a 30minute modification on day 3 whilst running the rig at 300bar, where the pressure was lowered to 250bar to observe a sonoluminescence phenomenon occurring in the outlet throttle (See 6.3). The same occurred on day 4, only for a shorter interval of time.

The attenuation coefficient was calculated using values of t_{fs}^2, r_f and x shown in Sec.5.2.2. Similarly to the normalised transmission, the attenuation coefficient remains constant at 3.55cm^{-1} whilst operating at 250bar upstream pressure, and decreasing to ~3.4cm^{-1} whilst operating at 300bar upstream pressure.

6.2.2 Discrete Sample for UV-Vis Data Analysis

To better understand the change in chemical properties aroused while running the high pressure recirculation rig, the UV-Visible Spectrophotometer allowed to analyse the spectra in the ultraviolet region where the fuel chromophores absorbing the light would facilitate identifying the species characterising the chemical properties of the fuel when cavitating for long hours.

Discrete samples were collected at the end of each experimental day, as explained in Sec.5.2.3. These samples where then used in order to carry out the three step analysis to measure absorbance in the wavelength ranges of 350nm-500nm, 240nm-305nm and 190nm-405nm with the appropriate dilutions with n-heptane, as explained in Sec.5.2.3.

A first investigation consisted in tracking the absorbance of the samples at 405nm, which coincides with the diode laser results in Sec.6.2.1. While the spectral attenuation – which is proportional to absorbance (See Eq.5.2.3) – was measured for the whole duration of time in the three week experiments using the in-situ laser extinction equipment, the UV-Visible spectrophotometer results would only provide values of absorbance at the time the samples were taken (the UV-Vis measurements were taken directly after collecting the sample at the end of the experimental day). below in Figure 6.2.5 is the spectral absorbance calculated for the five fuel samples collected at the end of each day of Week 1, which presented a variation in transmission according to the results in Figure 6.2.2.

Figure 6.2.5   Spectral absorbance at 405nm for diesel samples in Week 1
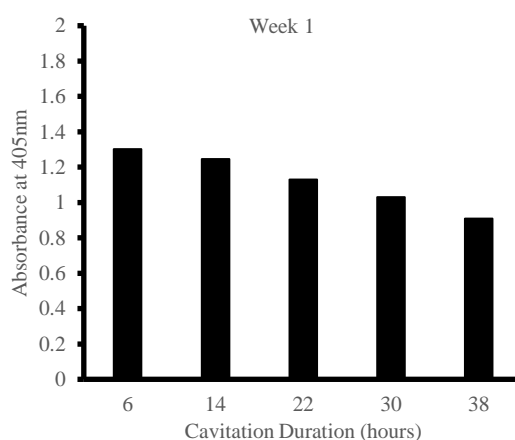
The absorbance measurements in Figure 6.2.5 obtained from the mixture fuel in Week 1 (See Table 5.2.1) were consistent with the trends showed in the normalised transmission and spectral attenuation

measurements in Figure 6.2.2. As a matter of fact, a decrease in absorbance with time was expected if the spectral attenuation results in the laser extinction measurement exhibited also a reduction. It has to be mentioned however that while the laser extinction measurements were taken place during the experiment at high temperatures (See Table 6.2.1), the UV-Vis measurements were taken at room temperature shortly after the end of the experimental day.

The UV-Visible spectrophotometer analysis was carried out following the steps outlined in Sec.5.2.3. Initially, the pure fuel samples were used to obtain spectra measurements in the wavelength range of 350nm – 500nm. below is the plot of the spectra analysis in the latter wavelength range for Week 1 experiment, following the averaging method explained in Sec. 5.2.3.

Figure 6.2.6   Discrete sample spectra in the 350nm-500nm wavelength range in Week 1
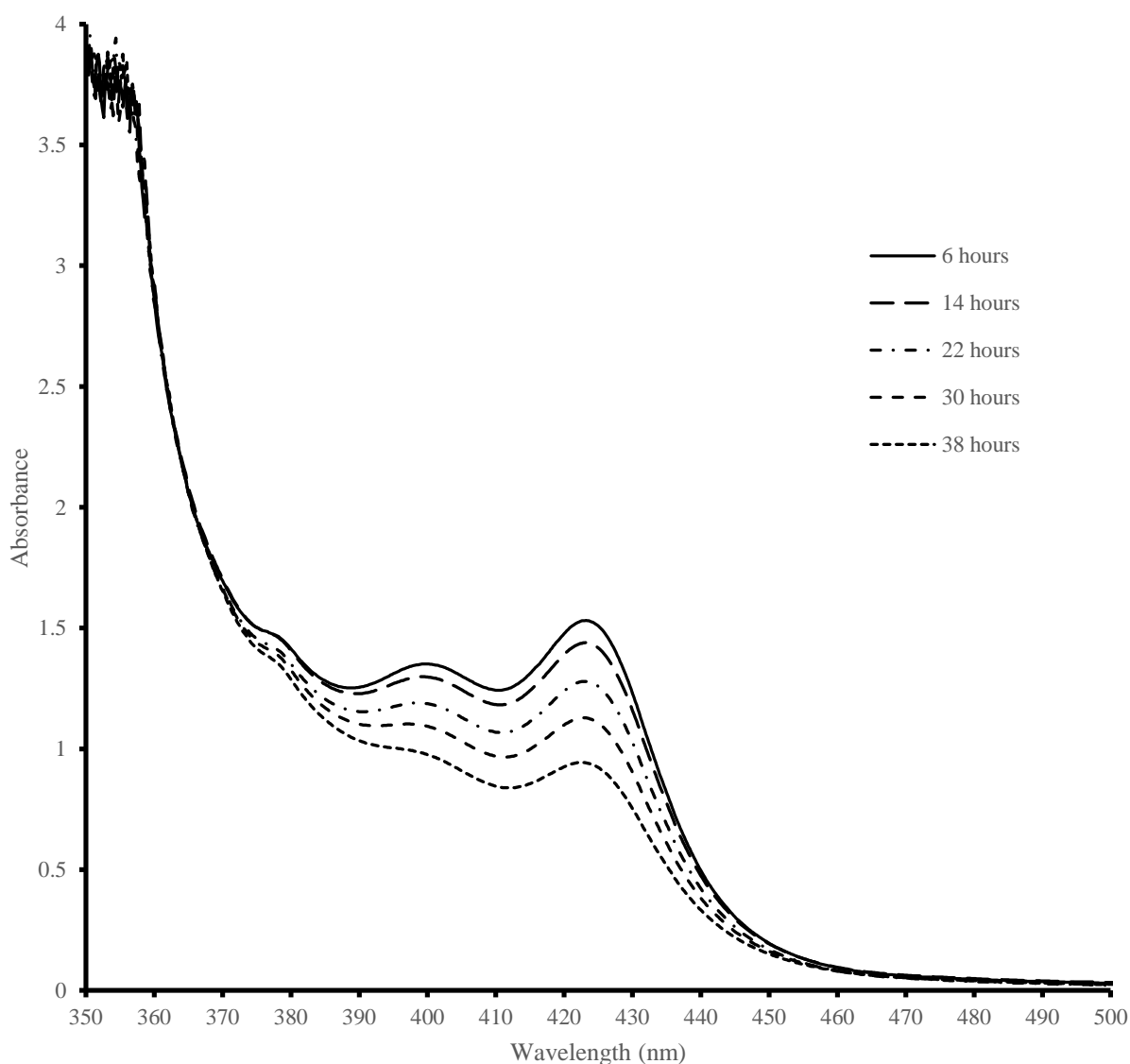
From Figure 6.2.6 a broad-band absorbance decrease can be noticed with cavitation time in the wavelength range between ~370nm and ~450nm. In particular, the 6 hours absorbance spectrum showed in the latter wavelength range the maximum absorbance throughout, followed by 14 hours and so on, until the 38 hours with the minimum absorbance, but following the same trend. In the wavelength range outside the 370nm-450nm the absorbance spectra are almost identical for the different cavitation times.

It was already established in Figure 6.2.5 that the absorbance was decaying at 405nm with cavitating time. Although now in Figure 6.2.6 the presence of a peak absorbance at ~425nm where the absorbance band is the broadest is noticeable. This can be explained by the fact that in poly-aromatics hydrocarbons (PAHs), as the number of fused rings increases, the long wavelength absorption shifts to higher values – also called a red shift. This is valid from three rings above, such as anthracene (λ_{max}=357nm), tetracene (λ_{max}=471nm), pyrene (λ_{max}=370nm), etc.[98]. The decrease of absorbance with cavitation time means that also the concentration of this particulates is decreasing with cavitation time. A spectral attenuation analysis could have been therefore performed also at 425nm, corresponding to the maximum absorbance peak, compared to the lower peak at 405nm.

Further on, the pure fuel samples were diluted with n-heptane as explained in Sec.6.1 to obtain spectra measurements in the wavelength range of 240nm – 305nm. This region of wavelength is of particular importance in the study of chemical properties of fuel since it constitutes the *benzenoid band*, a unique band characterised by low intensity and under high resolution there are several narrow peaks. The benzenoid band corresponds to a low-energy $\pi \rightarrow \pi^*$ transition of the benzene molecules. The absorption intensity is weak because the π^* state involved has the same electronic symmetry as the ground state of benzene, and transitions between symmetrical states usually are forbidden. [99]

Figure 6.2.7   Benzenoid band absorption spectra [99]

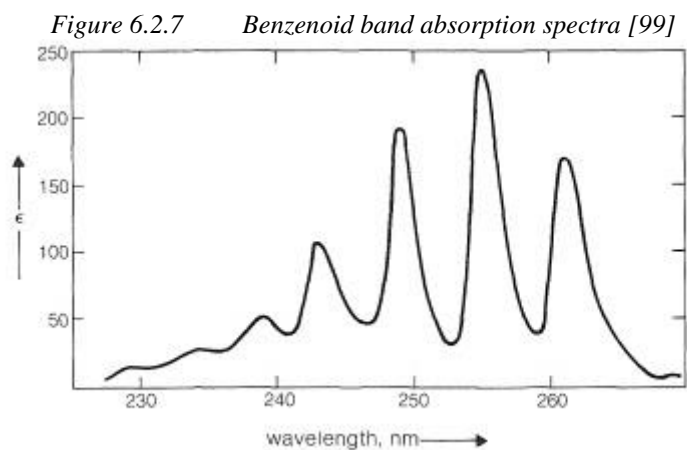below is the plot of the spectra analysis in the latter wavelength range for Week 1 experiment, following the averaging method explained in Sec. 5.2.3 and the coefficient of variation below 2% as explained in Sec.6.1.

Figure 6.2.8   Discrete sample spectra in the 240nm-305nm wavelength range in Week 1
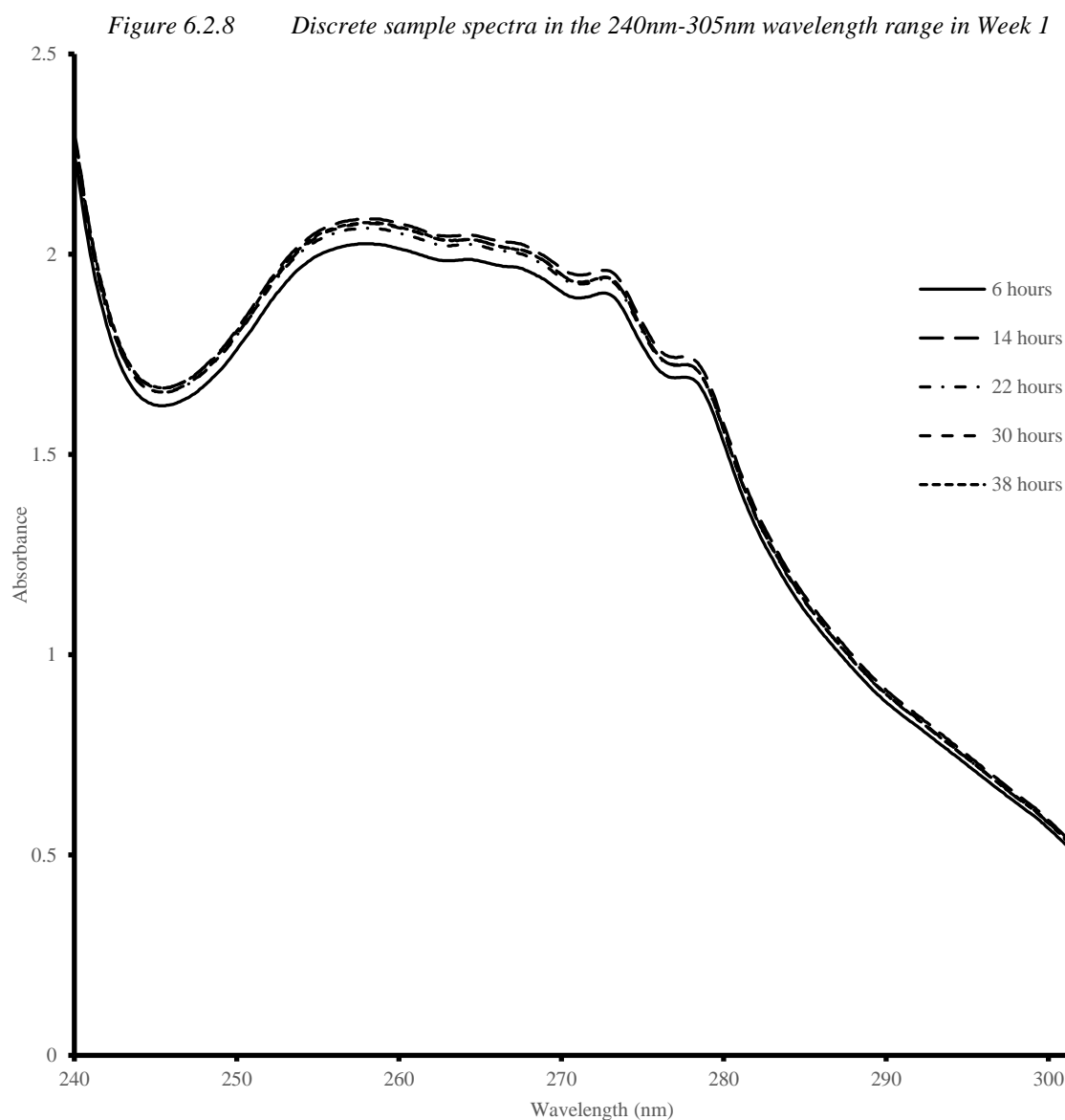
Comparing the spectra in Figure 6.2.7 and in Figure 6.2.8 shows that the first trough in the former corresponds at a wavelength lower than 230nm, while the first trough in the latter corresponds at a wavelength of 245nm. The shift of the trough in the benzenoid band suggests that there is a presence of naphthenic mono-aromatic hydrocarbons, as observed by Zeeshan in [94] with a similar absorbance spectrum.

Another observation to be done in Figure 6.2.8 is the broad-band absorbance spectra between 6 hours cavitating time and beyond. In fact, there seems to be an increase in absorbance with cavitating time in between 6 and 14 hours, after which the absorbance stays almost constant. The increase in absorbance justifies an increase in concentration in the benzenoid band.

For Week 2 and Week 3, it was observed that some absorptions for wavelength range of 350nm-500nm were above the threshold of 2.7, meaning that the results are not conclusive. These are shown in Appendix F.1. For wavelength range of 240nm – 305nm, the absorption spectra was normalised at the 245nm trough, i.e. shifting all the spectra towards one of them in order to have the same absorbance at the 245nm trough. This was done in order to understand better the relationship between the different spectra.

below in Figure 6.2.9 and in Figure 6.2.10 are the normalised absorption spectra for in Week 2 and Week 3.

Figure 6.2.9   Discrete sample normalised spectra in the 240nm-305nm wavelength range in Week 2
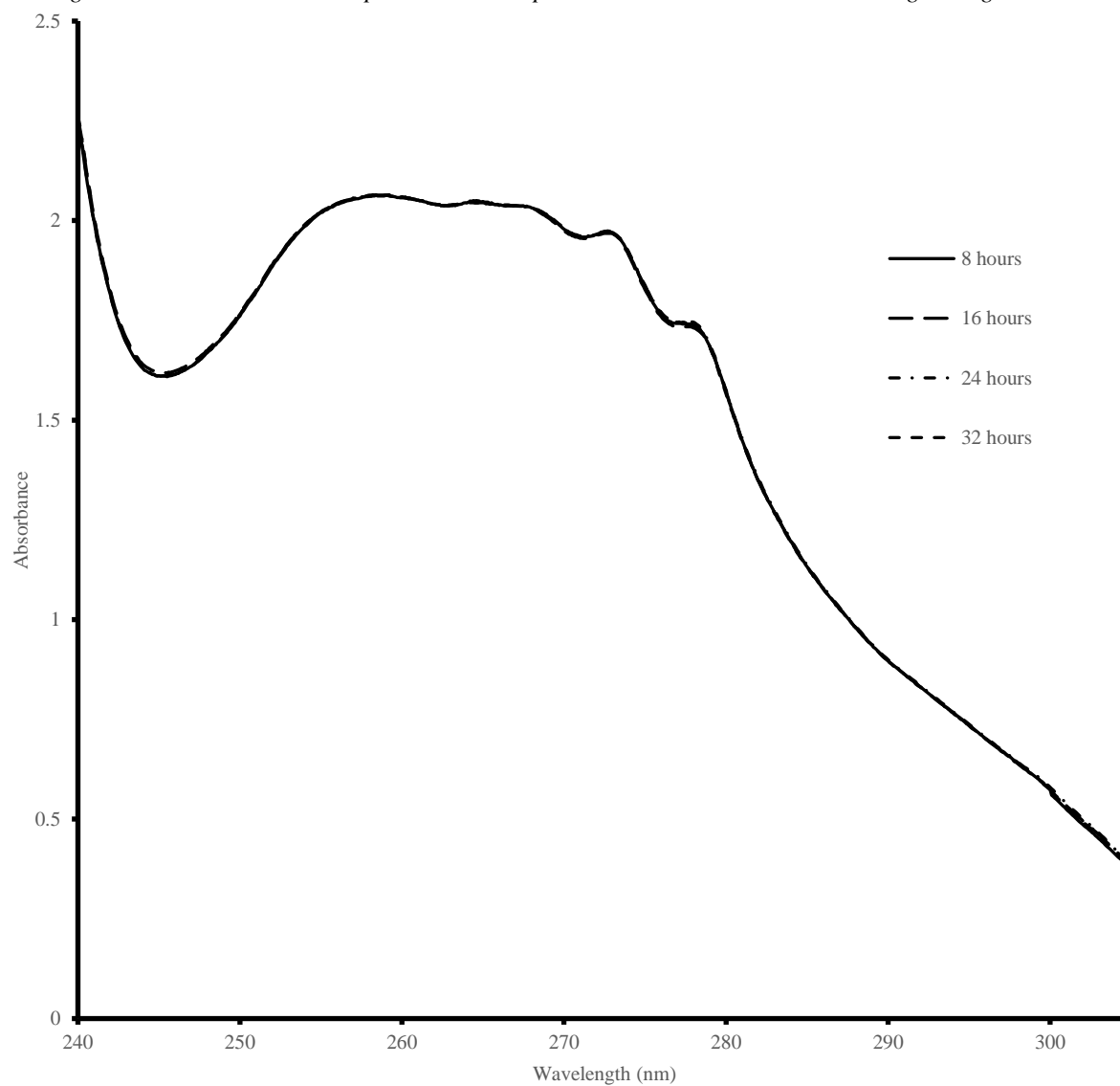
Figure 6.2.10   Discrete sample normalised spectra in the 240nm-305nm wavelength range in Week 3
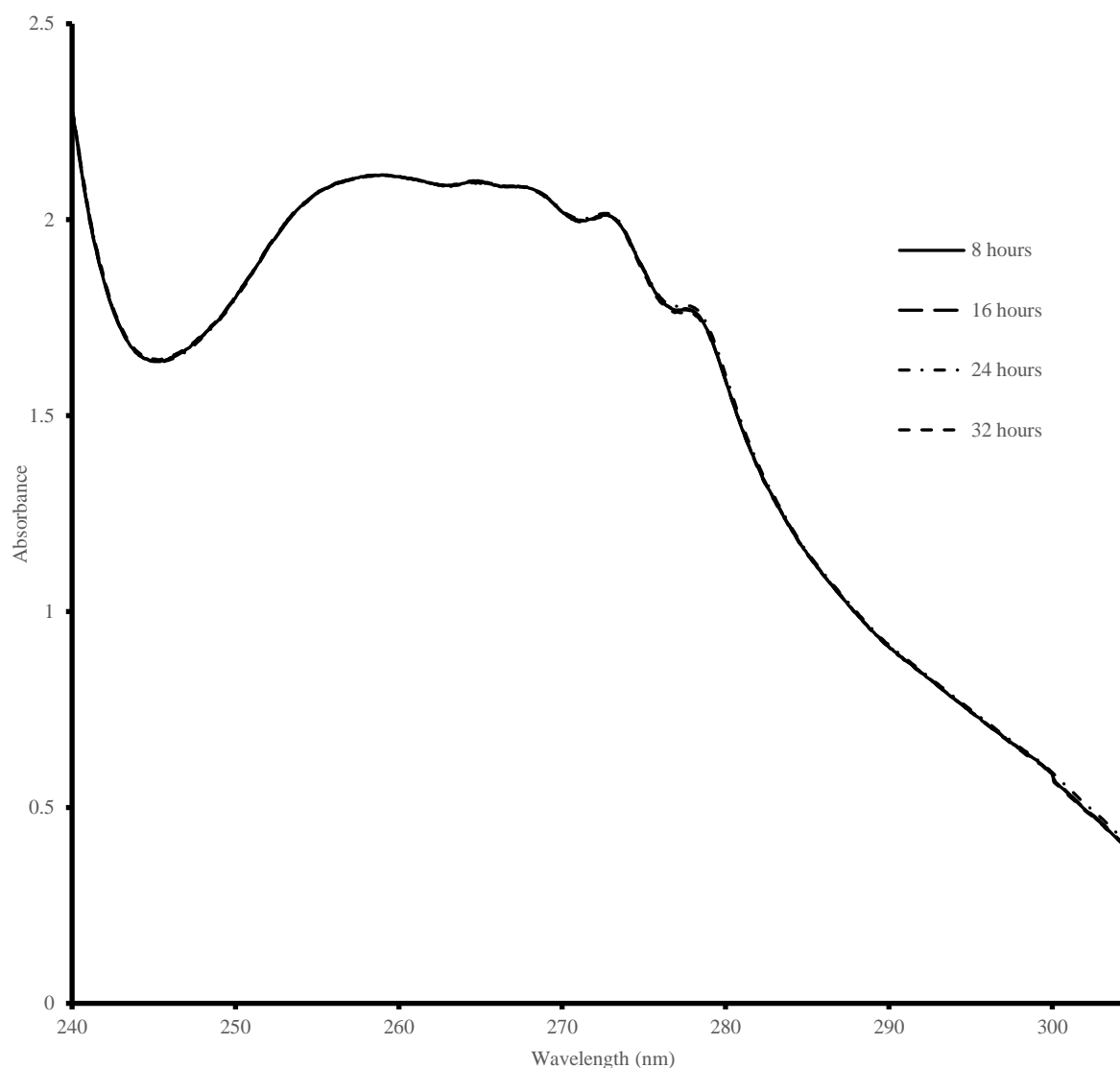
It can be noticed how there is no variation in the cavitating time, confirming the assumption made in Sec.6.2.1 where the fresh Fuel 1 (BDN) batch at the testing pressures does not experience the pyrolytic reaction observed instead in Week 1, with the mixture fuel.

Finally, the pure fuel samples were furthermore diluted as explained in Sec. 6.1 to obtain spectra measurements in the wavelength range of 190nm – 405nm. Due to malfunctions of the spectrophotometer at lower wavelengths, the absorption spectrum plotted in Figure 6.2.11 only shows the range between 220nm and 250nm, showing a 'shoulder-like' structure around the 225nm. It can be noticed once again that the absorbance is increasing with cavitating time, confirming the increase in concentration of particulates.

Figure 6.2.11   Discrete sample spectra in the 220nm-250nm wavelength range in Week 1
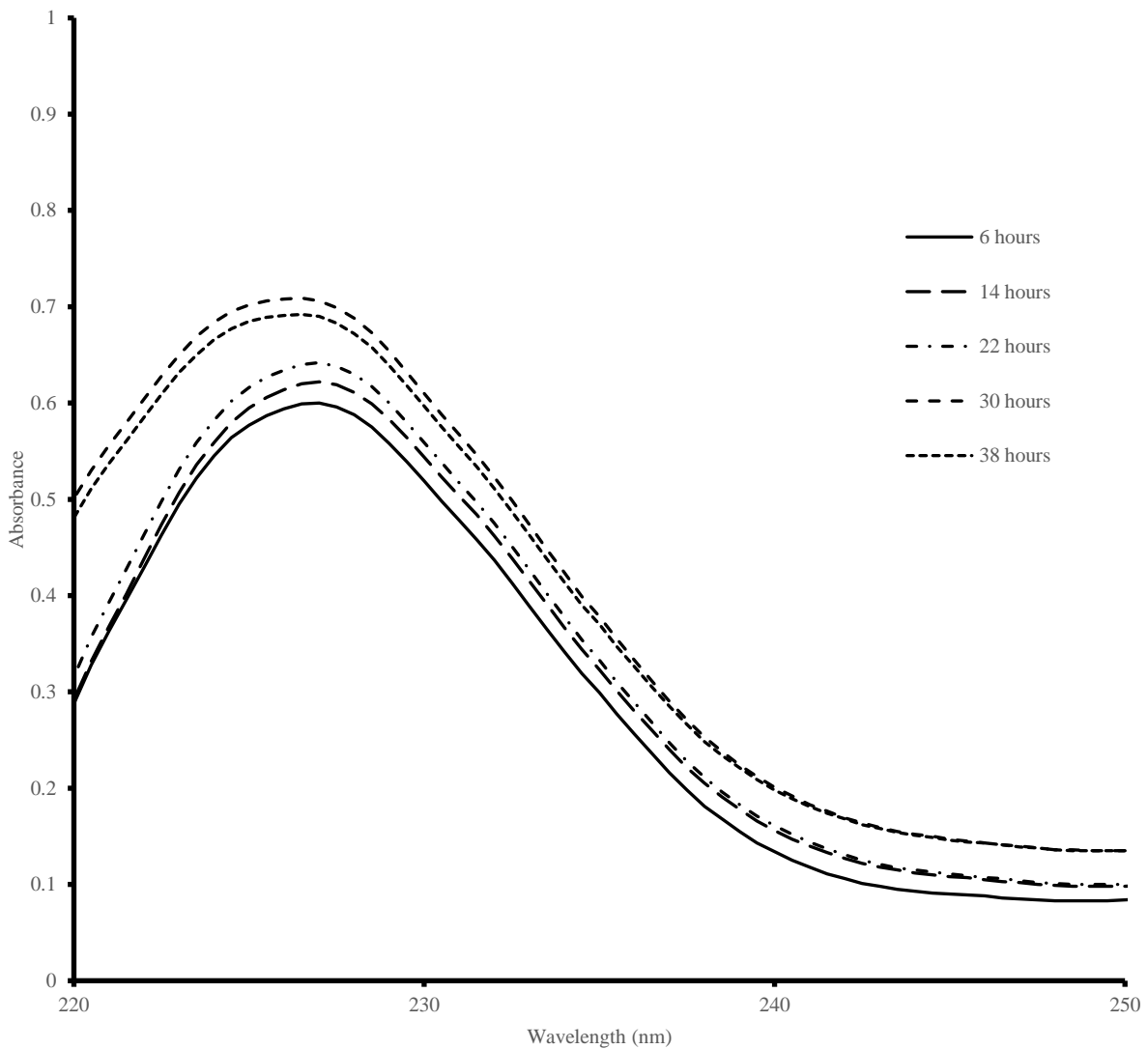
The full results for the wavelength range of 190nm-405nm of the three Weeks experiments are shown in Appendix F.2.

6.3   Discussion Arising on Comparison at Different Pressures

Comparing the results presented in Sec.6.2.1 and Sec.6.2.2 with the results presented by Zeeshan [94] for the high pressure cavitation test in the same recirculation test rig using injector nozzle instead of the model return valve and upstream pressure of 1650bar, some similarities were observed.

For the wavelength range of 350nm-500nm, Zeeshan's initial tests results of spectral attenuation coefficient and UV-Vis absorbance spectra of fresh Fuel 1 (BDN) show similar characteristics as the ones presented in Figure 6.2.2 and Figure 6.2.6 respectively for the fuel mixture. The spectral attenuation coefficient at 405nm was decaying in both cases with cavitating time, and the UV-Vis

absorbance spectra presented a decay in the broad-band absorbance for wavelengths above 380nm. However the absorbance in the wavelength range below 380nm, results in Figure 6.2.6 do not present any variation, compared to Zeeshan's result which instead presented a broad-band absorbance that increased with cavitation time. Figure 6.2.8 for the wavelength 240nm-305nm show however an increase in absorption spectra with cavitation time, meaning that smaller PAH formation is undergoing indeed, as concluded by Zeeshan [94].

The results presented however with the fresh batch of Fuel 1 (BDN) in Figure 6.2.3 and Figure 6.2.4 for spectral attenuation coefficient and Figure 6.2.9 and Figure 6.2.10 for UV-Vis absorbance spectra, show no variation with time. Even though not all the UV-Vis analyses results allowed to give a full range of absorbance spectra, it can be concluded that for a fresh batch of Fuel 1 (BDN) soot particles start forming at high pressures. For a fuel already containing dissolved gases, the pressure of 200bar is high enough to continue the pyrolytic reactions.

Chapter 7 Optical Measurement of Fluorescence Phenomenon in High Pressure Recirculation Rig

From the high pressure recirculation test, it was noticed that at ~150bar upstream pressure, a fluorescence phenomenon was occurring in the outlet throttle of the fused silica model, where normally cavitation would occur. The experimental setup explained in Chapter 5 was not equipped to investigate this unexpected phenomenon. Therefore a new setup was prepared in order to characterise better this flow condition.

The same high pressure rig in Chapter 5 was utilised to pressurise the upstream fuel, with the exception of the in-situ laser extinction apparatus which would not be needed for this part of the experiment. To focus on the section of the return valve model where the fluorescence was occurring, a digital camera was setup to take zoomed pictures. Moreover, the same Photron APX-RS video camera utilised in the low pressure test rig as shown in Chapter 3 was operated to take videos as the phenomenon would take place. Finally an Oriel 77400 spectrometer 125mm lens was utilised to analyse the fluorescence spectra.

In this chapter, there will be an explanation of the apparatus employed in Sec.7.1 along with the presentation and discussion of main results in Sec.7.2.

7.1 Experimental Setup and Methods

7.1.1 Photographic Setup and Methods

In order to take a closer look at the fluorescent phenomenon occurring at the entrance of the outlet throttle in the fused silica return valve model, two photographic setups were adopted. A first photographic setup consisted in a Nikon D7000 photo-camera, allowing to take close-up photographic images of the outlet throttle containing the fluorescence. A second photographic setup consisted in a Photron APX-RS high speed camera, allowing to take close-up videos as the fluorescent fuel would flicker inside the outlet throttle passage.

The Nikon NIKKOR D7000 was setup using a 50mm f/1.2 aperture camera lens and an 86mm extension length tube, allowing therefore a faster shutter speed for the same exposure. Using a tripod to elevate

the camera at the same height of the entrance of the outlet throttle, it was necessary to position the camera at the right distance from the object to allow a focused image. The optimal object to image distance was measured to be ~320mm, which corresponded to an image distance of ~250mm and an object distance of ~70mm. The camera magnification resulting from this setup would therefore be the ratio of image distance over the object distance, which is approximately 3.6. The image below shows the setup of the camera during the experiment.

Figure 7.1.1   Nikon NIKKOR D7000 setup for photographic imaging of fluorescence phenomenon

The images were taken initially with no lights on in the laboratory test cell, and then with lights on, using a white sheet of A4 paper as a background. The test rig was operated following the procedure outlined in Appendix E.2. The upstream pressure was set at 200bar and 250bar, to observe any variation in the intensity of the fluorescence when modifying the upstream pressure. Also, the shutter speed was varied from as low as $\frac{1}{80}$s to as high as $\frac{1}{1000}$s.

The Photron APX-RS 2kHz high speed camera was setup using again a 50mm f/1.2 aperture camera lens and an 86mm extension length tube. The camera was positioned on an optical table and elevated with translating mounting platforms in order to be aligned with the entrance of the outlet throttle. The

same distances were replicated, for a camera magnification of ~3.6. The image below shows the setup of the camera during the experiment.

Figure 7.1.2   Photron APX-RS high speed camera setup for video imaging of fluorescence phenomenon
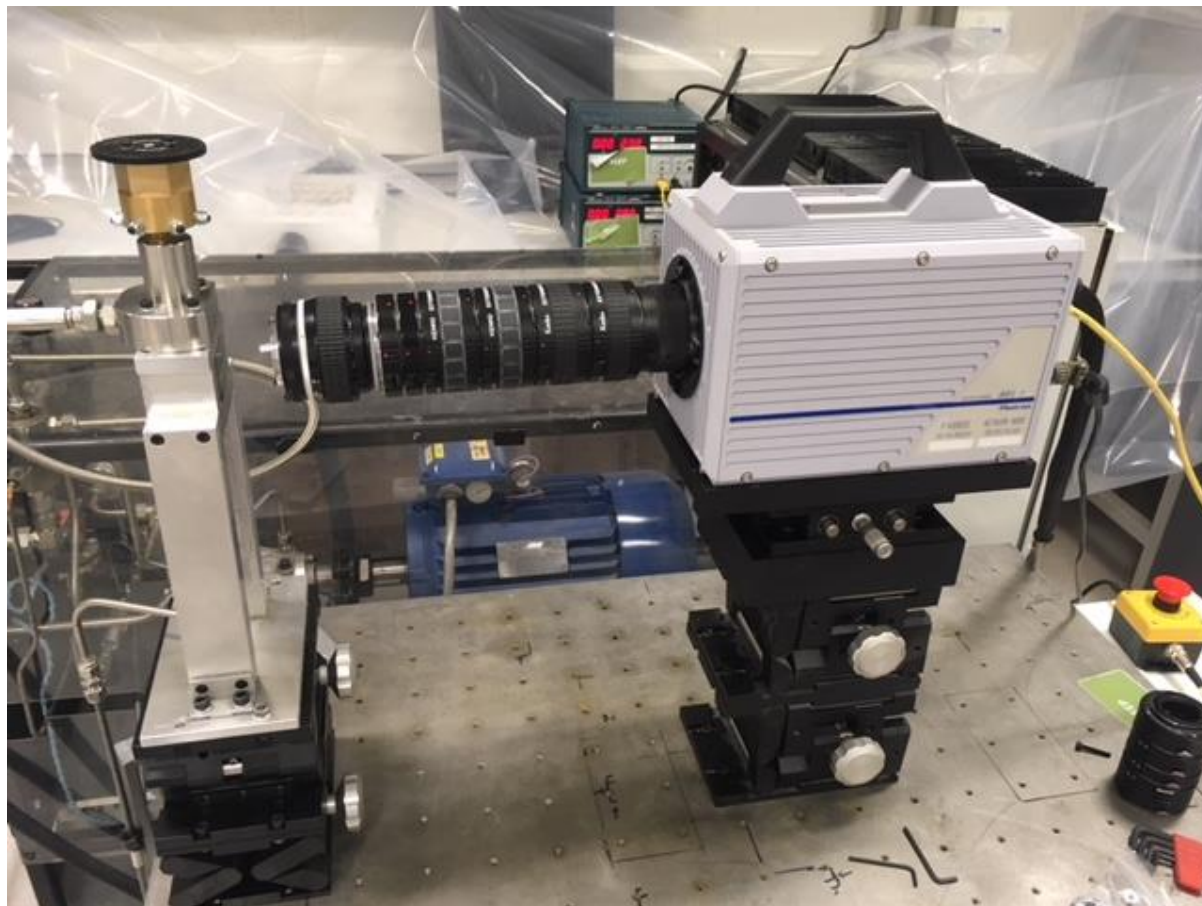
The videos recorded with the Photron APX-RS high speed camera had a resolution of 1024 x 1024, a frame rate of 2000fps and a shutter speed of 1/frame of a second. The videos were recorded with light off in the laboratory test cell. The test rig was operated following the procedure outlined in Appendix E.2 and the upstream pressure was set at 200bar.

7.1.2   Spectrometer Setup and Methods

Analysis of the absorbance spectrum from the light emitted by the diesel fuel while cavitating in the outlet throttle of the return valve is a means to identify the species responsible for the fluorescence. Fluorescence spectroscopy is becoming popular in the petroleum industry since it allows to provide information of the chemical and physical composition of an oil by simply analysing the wavelength and emission intensity of the light. Heavy oils are expected to present broad spectrum whilst light oils have narrow and intense spectrum.[100] While fluorescence spectroscopy techniques requires

using a various number of different solvents to transmit light, the phenomenon observed with the high pressure recirculation rig (See Chapter 5) emitted light on its own.

The spectrometer utilised to take measurements was an Oriel Model 77400 125mm spectrograph [101], with 120mm focal length. For the functioning of the spectrograph, a slit model 77730 (200µm width and 10mm height) was required at the input port to ensure the resolution of the spectrum, along with a grating allowing to spatially separate light of different wavelength of interest to analyse, and a LineSpec detector to record the light intensity onto the computer software. The spectrometer was positioned on an optical table and elevated with translating mounting platforms in order to be aligned with the entrance of the outlet throttle. The object to image distance was 40cm, with an intermediate collimating lens at 16cm from the model. The image below shows the setup of the spectrometer during the experiment.

Figure 7.1.3   Oriel 77400 MS125 spectrometer setup for spectrum analysis of fluorescence phenomenon

The slit is fitted at in the holder at the input port, adjusted externally using a micrometer (each step in the micrometer corresponds to 50nm), while the grating is inserted internally and the detector is mounted externally, as shown in Figure 7.1.4.

Figure 7.1.4   MS125 spectrometer dimensional drawing [101]
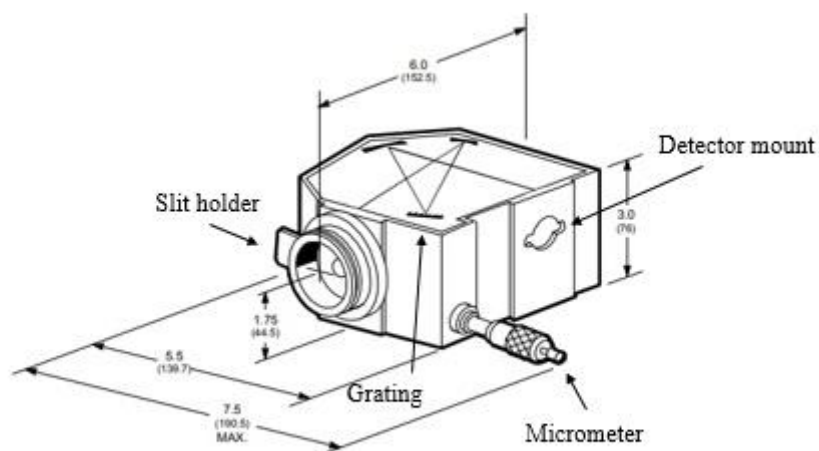
The alignment of light through the slit all the way to the detector was calibrated using a green helium-neon 543.5nm laser. Once the laser hit the middle of the slit, it would reach a mirror inside the spectrometer and reflect onto the grating, adjusted using the precision holder shown in Figure 7.1.4. From the grating, the laser light bounced off to another mirror, which finally reflected it towards the detector. The image below shows the equipment calibration using green helium-neon laser.

Figure 7.1.5   Spectrometer calibration using green helium-neon laser
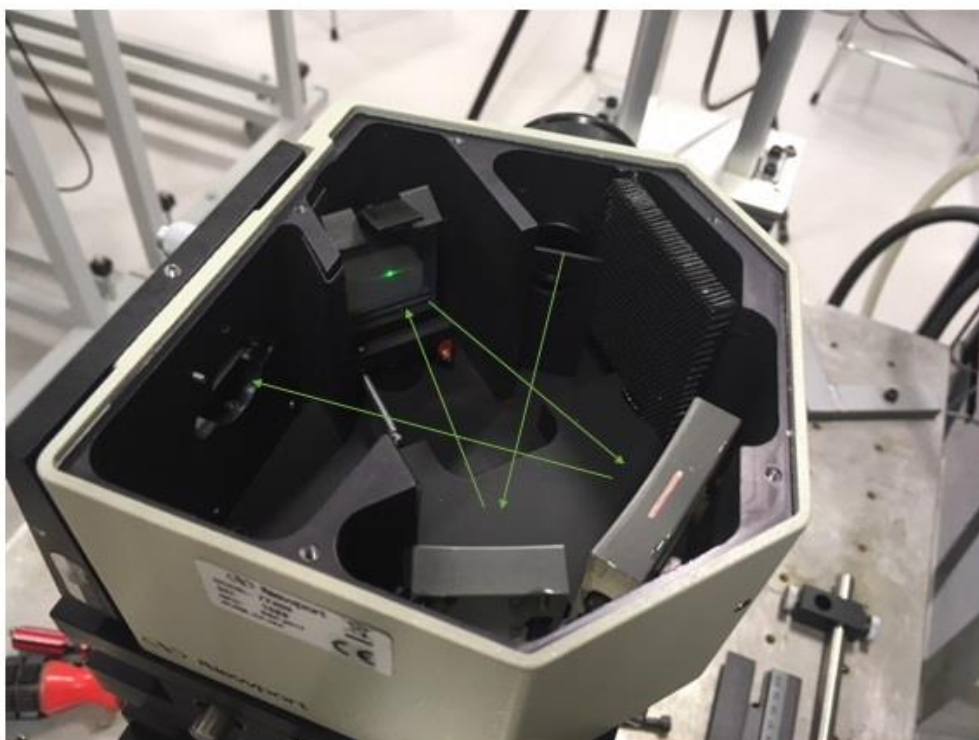
The detector consisted of a CCD sensor, able to convert the signal measurement into intensity (counts) using LineSpec. The user can therefore track the absorption of light using the adjustable micrometer slit to pick the wavelength of interest.

The methodology of the spectrum analysis consisted in taking background spectra, calibration spectra and the actual light spectra. The background spectra signal was subtracted from all other signal measurements in order to eliminate all other spectral absorption present in between the light source and the spectrometer. The calibration spectra signal was used as reference signal in order to normalise the geometric gain of the instrument, included in the actual light spectrum signal. Each orientation would produce a spectrum gain, which needs to be normalised against the maximum peak in order to get a true signal. Three sets of spectral measurements were taken each time and averaged to get the final signal spectrum.

The bandwidth of interest was in the wavelength region of 300nm and 500nm, corresponding to the blue colour shown in the glowing fuel. Each spectral measurement would capture the spectral signal in 2047pixels corresponding to a bandwidth of 70.75nm, hence a density of ~0.035nm/pixel. The micrometer reading would determine the 1085 pixel out of the 2047 pixels. For example, a reading of 7 in the micrometer would correspond to $7 \times 50nm = 350nm$ wavelength. For the calibration spectra, measurements were taken with micrometer setting at 7.25, 7.5, 7.75, 8, 8.25 and 8.5, corresponding respectively to wavelengths 362.5nm, 375nm, 387.5nm, 400nm, 412.5nm and 425nm. While for the actual light spectra, measurements were taken with micrometer setting of 7, 7.5, 8, 8.5 and 9, corresponding respectively to wavelengths 350nm, 375nm, 400nm, 425nm and 450nm.

7.2   Experimental Results and Discussion

7.2.1   Imaging analysis

Photographs taken using the Nikon NIKKOR D7000 camera (See Sec.7.1.1) are illustrated in Appendix G.1 for 200 bar upstream pressure and Appendix G.2 for 250 bar upstream pressure for shutter speeds of $\frac{1}{125}$s, $\frac{1}{160}$s, $\frac{1}{200}$s, $\frac{1}{250}$s, $\frac{1}{500}$s and $\frac{1}{1000}$s. Figure 7.2.1 shows a photograph taken at $\frac{1}{80}$s shutter speeds and 200bar upstream pressure:

Figure 7.2.1   Fluorescent diesel flow at 200bar upstream pressure image taken at $\frac{1}{80}$s shutter speed using Nikon NIKKOR D7000 camera
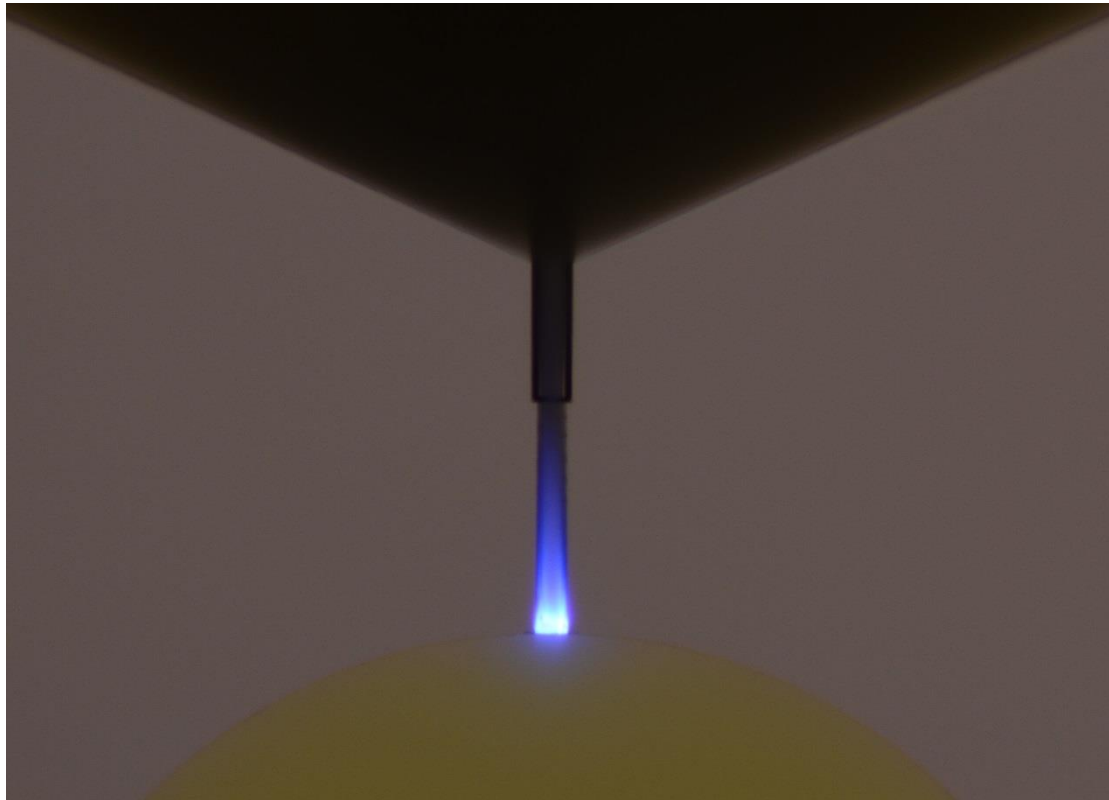
Using a shutter speed of $\frac{1}{80}$s allowed to fully visualise   the entire outlet throttle, including a section of the valve control chamber and the conical outlet volume. The fluorescent flow appeared at the entrance of the outlet throttle, developing in the Ø220μm hole passage, resembling to a flame. Closer to the entrance the flow is glowing brighter, and reducing in intensity as it develops towards the outlet throttle step. Using a lower shutter speed allowed to clearly visualise the diesel flow in the valve control chamber, yellow in colour, and the cavitating diesel flow in the return volume, cloudy and dark in colour. Greater shutter speeds shown in Appendix G.1 and Appendix G.2 allow to visualise better the colours of the fluorescence at the entrance of the outlet throttle. No significant difference was noticed between 200bar and 250bar upstream pressure in terms of characterisation of the fluorescent phenomenon.

Videos capturing white-light scattering of the fluorescent flow from the Photron APX-RS high speed camera allowed to visualise the flickering of the flame-like flow with time. A screenshot taken from a 200bar upstream pressure case scenario shows the white-light scattering from the flow as it cavitates at the entrance of the outlet throttle where fluorescence is occurring:

Figure 7.2.2   Fluorescent diesel flow at 200bar upstream pressure image taken at $\frac{1}{frame}s$ shutter speed using Photron APX-RS high speed camera

While in Figure 4.1.16 the white-light scattering was representing the cavitating flow development, Figure 7.2.2   the white-light scattering is showing the region where fluorescence is occurring. The emission of light shown in Figure 7.2.1 comes as a result of complex chemical reactions of the fuel visualised in Figure 7.2.2 where the high temperatures developed are leading to formation of ionised gases, i.e. plasma.[102] The glowing effect of the plasma flow was thought therefore to be either a consequence of sonoluminescence, i.e. produced by ultrasonic waves, or of electroluminescence, i.e. produced by AC or DC voltage applied to the flow. [103] It is more likely for the latter to be the case, since the model was not earthed, allowing therefore the plasma flow developed to start glowing.

7.2.2   Spectral analysis

The spectral analysis of the light source consisted in first of all determining the gain of the instrument. Initially, all the background signals were subtracted from both calibration and actual light spectra signal. The calibration spectra signals were then plotted, once converting all the pixels in wavelengths according to the pixel density and the micrometer setting, as explained in Sec.7.1.2.

Figure 7.2.3   Calibration spectrum signal before normalisation
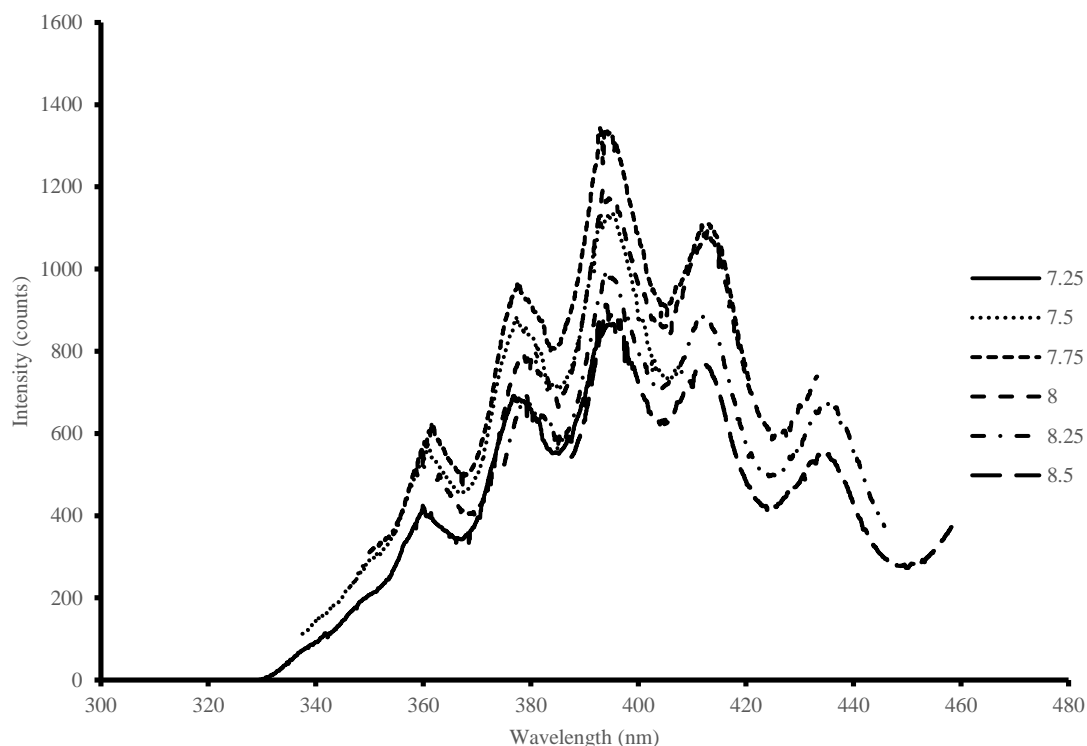
Each different line in Figure 7.2.3 corresponds to the micrometer setting (each turn of the micrometer corresponds to 50nm as explained in Sec. 7.1.2) with a bandwidth of 70.75nm. Each line has a peak at different intensity, due to the gain of the instrument. The normalisation consists therefore in finding the maximum peak of each line, and then using the highest value of the maximum peaks as the reference value. The ratio of the highest value of the maximum peak with the other values corresponds to the gain of the instrument. The normalisation consists therefore in dividing each bandwidth by the gain, allowing therefore an adjustment of the spectra to eliminate this error. The calculated gain was therefore utilised to normalise the actual light spectra signal for the micrometer settings shown in Sec. 7.1.2. It was possible therefore to combine the different bandwidths to finally obtain the final spectrum, as shown in Figure 7.2.4.

Figure 7.2.4   Fluorescent spectrum after calibration normalisation
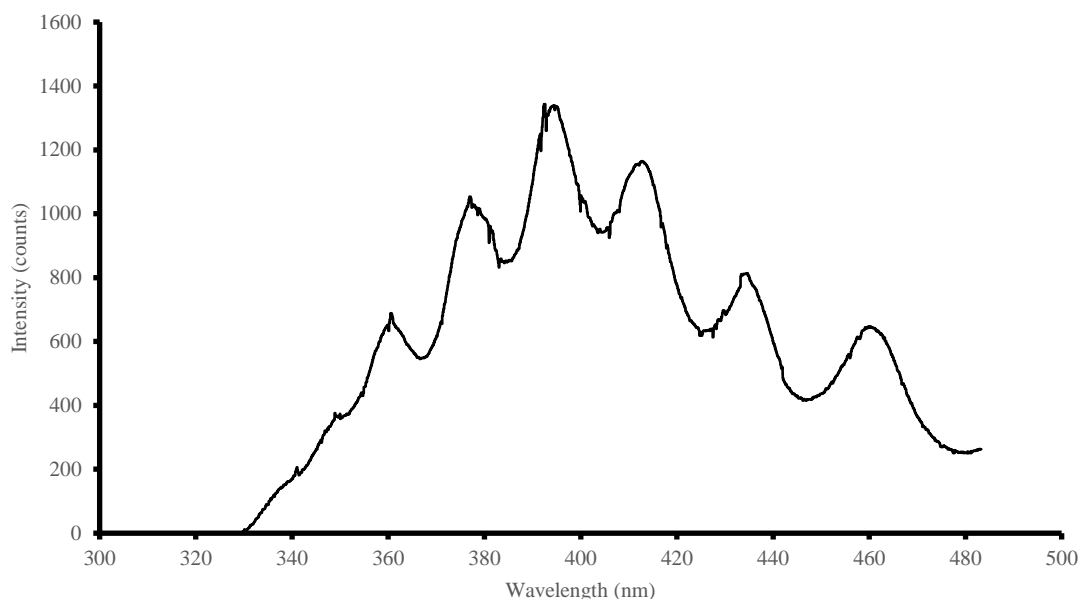
The obtained spectrum in Figure 7.2.4 shows the presence of 6 peaks. The highest peak occurred at a wavelength of 392.2nm. It was thought that this peak signal corresponded to a CH $B^2\sum \rightarrow X^2\Pi$ transition, which normally lies at 387nm.[104] A systematic shift of the spectrum was therefore caused by the diode laser utilised for calibration. This was then confirmed at a later stage once the calibration was corrected.

A modification of the spectrum in Figure 7.2.4 consisted in shifting the whole spectrum in order to match the highest peak to the 387nm wavelength, as shown in Figure 7.2.5. Some of the other peaks that can be found in the literature are the ones corresponding to 357nm to H_2 [105]and 431.5nm to a CH $A^2\Delta \rightarrow X^2\Pi$ transition [104].

Figure 7.2.5   Fluorescent spectrum modified after shifting wavelength
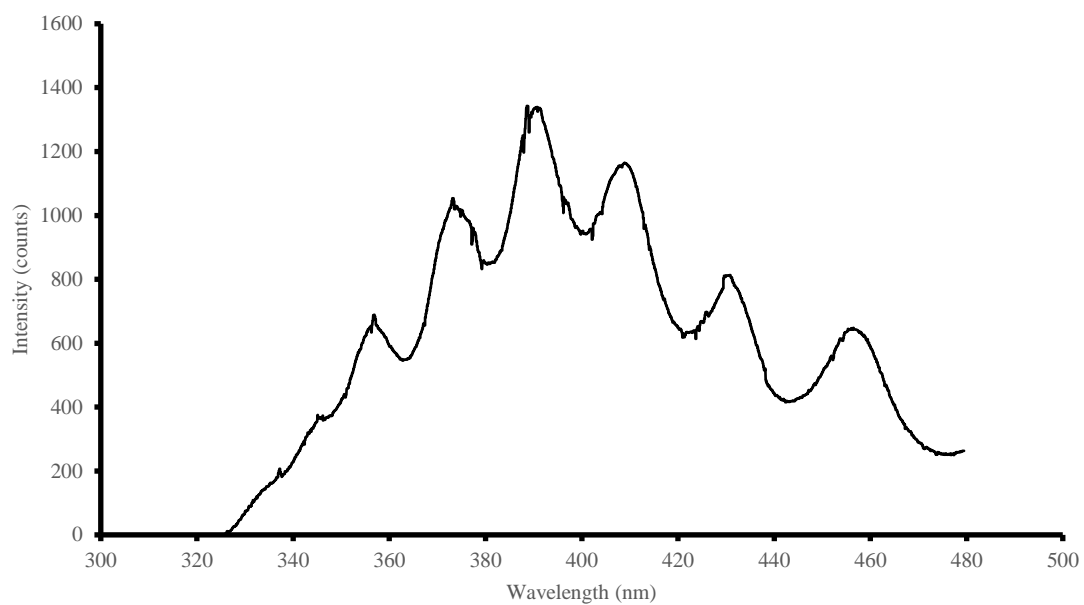
Chapter 8 Chemical Kinetic Model of Cavitation Pyrolysis

Fuels utilised in means of transport are composed of complex mixtures which could often add up to thousands of different species. It is easier therefore to classify these fuels in groups of species which are known as "surrogate" mixtures of fuels. Surrogates are therefore defined according to the classes of compounds that exist, such *n*-alkanes, *iso*-alkanes, aromatics, polycyclic alkanes, olefins, naphthenes and oxygenated hydrocarbons. Each fuel also have species that behave differently according to the temperature of reaction, igniting earlier than others. By means of a comprehensive reaction mechanism, it is possible to simulate chemical reactions occurring in the surrogate fuels which can be validated through experimental work. [106]

There have been many developments and application of these surrogate mechanisms over years, some of which can be listed as follow:

- Chevalier et al. [107] created a n-hexadecane mechanism containing 1200 species and 7000 elementary reactions to simulate engine knock phenomena and followed specific rules for the formulation of rates of reaction;

- Nehse et al. [108] developed a mechanism for *n*-decane and *n*-heptane to simulate shock tube experiments at intermediate temperature for both fuels;

- Degaut et al. [109] used *n*-decane as a surrogate for kinetic mechanism developments of kerosene of jet engine simulations, and later on [110] extended the work on *n*-hexadecane to simulate oxidation of rapeseed oil methyl ester;

- Olchanski and Burcat [111] developed a reduced high temperature mechanism for *n*-decane and oxygen diluted in argon to analyse reflected shock wave ignition delay experiments;

- Bikas and Peters [112] developed a full temperature range mechanism to analyse *n*-decane combustion simulations in laminar flames, jet-stirred reactors and shock tubes;

- Zeppieri et al. [113] developed a high and intermediate temperature mechanism for *n*-decane oxidation, without the inclusion of low temperature reaction pathways;

- Lindstedt and Maurice [114] have developed *n*-heptane and *n*-decane reaction mechanisms to analyse combustion of jet fuels;

- Dagaut and Cathonnet [115] have showed how surrogate fuel mechanisms, including *n*-decane, aromatic and other species, are able to predict quite accurately the development of soot particles, thus without using robust surrogate mixtures;

- Buda et al. [116] have developed a unified kinetic mechanisms for modelling the autoignition delay times of a various number of alkanes in a temperature range of 600K to 1200K, a pressure range of 1 to 50 bar and equivalence ratio range of 0.5 to 2;

- Ranzi et al. [117] have developed a lumped model semidetailed kinetic scheme of hydrocarbon oxidation of heavy fuels applied to *n*-decane, *n*-dodecane and *n*-hexadecane in a large variety of measurements, showing a general agreement with experimental results, despite reducing the size of each mechanism.

Cavitation occurring in diesel fuel lead to the formation of larger particulates with time. Polycyclic aromatic hydrocarbons (PAHs) and soot particle are an important issue in regards of the environment pollution and damages to injection system, which is why a qualitative and quantitative understanding of the chemical processes occurring during hydrocarbon oxidation, formation and depletion of PAHs and soot are crucial. [118]

The following steps for soot formation are widely accepted:

- *Particle nucleation:* PAHs are formed by reaction of radicals of smaller PAHs with acetylene (C_2H_2), PAH or other PAH radicals. PAHs may react with each other or continue growing independently (particle inception or nucleation occurs);

- *Surface growth:* reactions at the surface are similar to those of PAH, where hydrogen abstraction and oxidation by O_2, OH and O take place. As the particle grows, surface growth rate reduces, in the same way as H-to-C ratio;

- *Particle coagulation:* further growth is obtained by collision of growing soot particles into aggregates.

For a quantitative understanding, detailed reaction mechanisms have been developed for particle formation following similarly the formation and depletion of PAHs (assumption of PAH of a certain size to be soot nuclei). Richter et al. [118] for example divided the soot particles into classes called

BINs according to properties such as mass, number of carbon and hydrogen atoms. Their mechanism consisted of 295 species, 1102 conventional gas phase and 5552 reactions. BINs were classified in 20 groups, where BINs 1 to 4 were conceptually treated as "large PAHs" since their mass is less than 2000amu, while BINs 5 and larger were considered as "particles". For each class, the corresponding class of radicals were also determined – e.g. BIN 1J is the corresponding radical class to BIN 1 – hence 40 groups of BINs in total. Each BIN class doubles the number of carbon and hydrogen, for example BIN 1 is $C_{24}H_{12}$, BIN 2 is $C_{48}H_{24}$ and so on. BIN 1 and BIN 2 for instance were described by 609 reactions between PAH and their radicals and between PAH radicals. All reactions were treated as irreversible. As the BIN class gets higher, the H-to-C ratio decreases due to the five-membered ring structural units of PAHs. All the BINs are then activated by hydrogen abstraction with H and OH radicals as well as unimolecular hydrogen loss, utilising available kinetic data from literature for benzene and phenyl as starting point for the increased BIN size. Also included in the mechanism were all other reactions of parent BINs with PAH radicals, all radical BINs with acetylene, BINs with radical BINS and between radical BINs (stoichiometric coefficients were calculated from H and C, while rate constants were scaled corresponding to the increase of collision efficiencies).

There are three major approaches adopted in literature for the development of mechanisms for soot formation, i.e. the method of moment, the stochastic approach and the discrete section method. The method of moment, used for example by Frenklach [119] to analyse the chemical reactions and physical processes that lead to the formation of PAHs and soot in hydrocarbon flames, consists of describing in detail each particle dynamics using moments of the particle size distribution function (PSDF). By knowing just the first few PSDF moments will allow to gather all essential properties of a particle cloud, using interpolation to close the system of equations for the moments. The stochastic approach, used for example by Balthasar and Kraft [120] to calculate the PSDF of soot particles in laminar premixed flames, consists of a stochastic particle system instead of solving the equations of moments where all processes are treated probabilistically using Monte-Carlo techniques, allowing to converge to the exact solution of the particle cloud. Finally the discrete section method, used by Saggese et al. [121], [122] to construct a soot model coupling a gas-phase chemical kinetic model of hydrocarbon fuel pyrolysis and oxidation with the fundamental processes of soot nucleation and mass/size growth, consists of

separating the particle size spectrum into a set of size classes each with its own transport equation. Despite being with the highest computational cost, it is the most accurate and detailed.

Sec.8.1 will describe the development of a new comprehensive soot-formation kinetic model while Sec.8.2 will validate this model with auto-ignition delay measurements and soot formation measurements.

8.1 Development of Kinetic Model using Distinct Mechanisms

A comprehensive kinetic model was constructed with the purpose of allowing a more detailed analysis of soot particle formation. As mentioned earlier, there have been different approaches in modelling soot formation, but the general limitations were the size of equations and computational cost. In this new approach, the focus was to create a more robust soot formation model that included also paraffinic reactions to PAH formation. In order to do so, it was necessary to carry out research on previous kinetic mechanisms and combine them accordingly.

The kinetic model constructed consisted of the combination of three mechanisms:

- C_1-C_4 mechanism with PAH formation, from Lawrence Livermore National Laboratory; [123]

- C_8-C_{16} n-Alkanes pyrolysis and oxidation, from Lawrence Livermore National Laboratory; [124]

- Soot kinetic mechanism, from CRECK Modelling Group. [125]

The first mechanism, the C_1-C_4 mechanism from Lawrence Livermore National Laboratory, was developed by Marinov et al. [126] to investigate aromatic and two-ring/three-ring PAH formation pathways in a premixed, rich, sooting, n-butane-oxygen-argon burner stabilised flame. It consists of 680 reaction and 156 species, obtained by the combination of other sub-mechanisms specified in [126].

The second mechanism, the C_8-C_{16} mechanism from Lawrence Livermore National Laboratory, was developed by Westbrook et al. [106] to describe the pyrolysis and oxidation of nine n-alkanes larger than n-heptane, including n-octane (n-C_8H_{18}), n-nonane (n-C_9H_{20}), n-decane (n-$C_{10}H_{22}$), n-undecane (n-$C_{11}H_{24}$), n-dodecane (n-$C_{12}H_{26}$), n-tridecane (n-$C_{13}H_{28}$), n-tetradecane (n-$C_{14}H_{30}$), n-pentadecane (n-$C_{15}H_{32}$), and n-hexadecane (n-$C_{16}H_{34}$). The mechanism was divided into the primarily high temperature

one where the major alkyl radicals decompose thermally into smaller radicals and olefin species, and the lower temperature one initiated by the addition of molecular oxygen to the major alkyl radicals. It consists of 8130 reactions and 2116 species, obtained by the combination of other sub-mechanisms specified in [106].

The third mechanism, the soot kinetic mechanism from CRECK Modeling Group, was developed by Saggese et al. [121] to analyse the aerosol dynamics using the discrete sectional method, the coagulation and the surface reactions governing soot nucleation and mass/size growth. It consists of 6300 reactions and 200 species, obtained from previously developed gas-phase model in the same CRECK Modeling group, only that it included the chemistry of PAHs of up to four-to-five rings.

The soot particles were discretised in 20 classes of pseudo-species, called "BIN", with masses doubled from one class to the next. From BIN 1 to BIN 10, there are three ulterior subclasses, named A, B and C, with different H-to-C ratios, while from BIN 11 to BIN 20 there are two ulterior subclasses A and B. Since each of the subclasses has a corresponding radical subclass BIN_j, a total of 100 lumped pseudo-species in 20 BINs are gathered. Moreover, BIN 1 to BIN 4 are considered as "heavy PAHs", BIN 5 to BIN 12 are considered as "particles", and BIN 13 to BIN 20 are considered as monodisperse "aggregates" with BIN_{12} particles. below are classified the properties of these BINs, divided in Table 8.1.1 for the heavy PAHs, Table 8.1.2 for the particles and Table 8.1.3 for the aggregates. Included in the list of properties shown are the number of carbon atoms, the median mass, the diameter (collision diameter for the aggregates, since it is obtained from the radius of gyration, dependant on the number of particles), the H-to-C ratios and the number of primary particles (N_P) for the aggregates. The values derivation are specified in [121].

BIN_i	Number of C	Median mass (amu)	Diameter (nm)	H/C		
				A	B	C
1	20	250	0.81	0.8	0.5	0.3
2	40	500	1.02	0.8	0.5	0.3
3	80	1000	1.28	0.75	0.45	0.3
4	160	2000	1.62	0.7	0.4	0.3

Table 8.1.1   Properties of BINs 1 to 4 (heavy PAHs) [121]

BIN$_i$	Number of C	Median mass (amu)	Diameter (nm)	H/C		
				A	B	C
5	320	4×10^3	2.04	0.65	0.35	0.2
6	640	8×10^3	2.57	0.6	0.35	0.15
7	1250	1.55×10^4	3.21	0.55	0.3	0.1
8	2500	3×10^4	4.04	0.5	0.25	0.1
9	5000	6×10^4	5.09	0.45	0.2	0.1
10	1×10^4	1.2×10^5	6.4	0.4	0.15	0.1
11	2×10^4	2.45×10^5	8.05	0.35	0.1	
12	4×10^4	4.9×10^5	10.14	0.35	0.1	

Table 8.1.2   Properties of BINs 5 to 12 (Particles) [121]

BIN$_i$	Number of C	Median mass (amu)	Collision Diameter (nm)	H/C		
				N$_p$	B	C
13	8×10^4	9.7×10^5	13.27	2	0.3	0.1
14	1.6×10^5	1.95×10^6	19.5	4	0.3	0.1
15	3.2×10^5	3.9×10^6	28.63	8	0.25	0.1
16	6.4×10^5	7.8×10^6	41.98	16	0.2	0.05
17	1.25×10^6	1.51×10^7	60.89	32	0.2	0.05
18	2.5×10^6	3.02×10^7	89.49	64	0.2	0.05
19	5×10^6	6.02×10^7	131.53	128	0.2	0.05
20	1×10^7	1.21×10^8	193.32	256	0.2	0.05

Table 8.1.3   Properties of BINs 13 to 20 (Aggregates) [121]

The soot mechanism proposed by Saggese et al. [121] was divided in six heterogeneous reaction classes leading to soot, that are:

1. Hydrogen-abstraction-carbon-addition (HACA) mechanism: consists of the mechanisms where first of all H˙ and OH˙ together with BIN species form surface radicals BIN˙. By means of the acetylene addition to the surface radicals BIN˙, the HACA mechanism is then complete;

2. Soot inception: consists of the mechanisms where heavy PAHs (See Table 8.1.1) interact with each other as radical-radical, radical-molecule or molecule-molecule, to form the first particles;

3. Surface growth: consists of the mechanisms where small resonantly stabilised radicals, such as propargyl, interacted with all BINs, contributing to soot growth. These addition reactions also included the PAH radicals interacting with soot particles and aggregates;

4. Dehydrogenation: consists of the mechanisms where heavy PAHs and soot particles undergo dehydrogenation by molecular and radical pathways, varying therefore the H-to-C ratio.

Dehydrogenation is also promoted by H-addition reactions and successive de-methylation, included therefore in this reaction class. When temperatures are very high, a C-H will fission occur;

5. <u>Coalescence and aggregation</u>: consist of the mechanisms where particle-particle interactions (coalescence) and aggregate-aggregate interactions (aggregation) occur. In the case of a particle interacting with an aggregate, a "soft-aggregation" would occur;

6. <u>Oxidation</u>: consists of the mechanisms where BINs reduce in size due to their reaction with $OH^{\cdot}$ radical, $O^{\cdot}$ radical and O^2.

Details of the reaction classes are found in [121].

The software utilised to run the comprehensive kinetic model was ANSYS Chemkin-Pro 17.2.

In order for the model to work on this software, it needed a kinetic mechanism file, a thermodynamic data file and a transport data file. Details of the setting up of these files are found in [127], [128]. The kinetic mechanism corresponds to the ensemble of chemical reactions involving a series of elements named in the element data and species named in the species data. The purpose of the element data is to associate atomic weights of the element with their character symbol, as shown below:

Figure 8.1.1   Example of element data information in the kinetic mechanism file

```
elements h   o    c   ar n    he end
```

The purpose of the species data is to identify the order in which FORTRAN arrays of species information are referenced. Each species must be composed of elements identified in the elements data. The information of each species is defined in the Thermodynamics and Transport data files. Figure 8.1.2 shows an example of a species data.

Figure 8.1.2   Example of species data information in the kinetic mechanism file

```
SPECIES
HE          AR          N2          O2          H2
H2O         H2O2        CO          CO2         CH2O
CH4         CH3OH       CH3OOH      C2H2        CH2CO
C2H2O2      C2H4        C2H4O       CH3CHO      C2H4O2
C2-OQOOH    C2H6        C2H5OH      C2H5OOH     C3H2
PC3H4       AC3H4       C2H3CHO     C3H6        C3H6O
CH3COCH3    C2H5CHO     C3H8        C4H2        C4H4
C4H6        IC3H5CHO    IC4H8       NC4H8       C3H7CHO
END
```

Each line of the kinetic mechanism line is divided into two fields: the first is the symbolic description of the reaction; the second is the Arrhenius rate coefficients. In fact, the rate constant of reaction (k) presented in the Arrhenius form is as follows:

$$k = A_i T^{\beta i} e^{-\frac{E_i}{RT}}$$

8.1.1

where A_i is the pre-exponential factor ($l \cdot mol^{-1} \cdot s^{-1}$) , β_i is the temperature exponent, E_i is the activation energy ($kcal \cdot mol^{-1}$), R is the universal gas constant ($kcal \cdot mol^{-1} \cdot K^{-1}$) and T is the absolute temperature (K). The Arrhenius factors, A_i, β_i and E_i need to be present in the same line as the reaction they are referred to. Figure 8.1.3 shows an example of chemical reactions.

Figure 8.1.3   Example of reaction mechanism in the kinetic mechanism file

```
reactions
!
h+o2=oh+o                                          .2330e+15     .000   16650.0
o+h2=oh+h                                          .4330e+14     .000   10000.0
h+o2(+m)=ho2(+m)                                     .5580e+13    .400            .0
 low/  .8400e+18     -.800         .0/
troe/      .5000           .1000e-29    .1000e+31                  /
h2o/ 18.00/h2/  2.50/n2/  1.26/ar/    .80/he/    .80/o2/    .00/co/  1.20/
h+o2+o2=ho2+o2                                       .8900e+15     .000   -2822.0
oh+ho2=h2o+o2                                       .5000e+14     .000    1000.0
h+ho2=oh+oh                                         .2500e+15     .000    1900.0
o+ho2=o2+oh                                         .3250e+14     .000          .0
oh+oh=o+h2o                                         .3570e+05    2.400   -2110.0
h2+m=h+h+m                                          .2230e+15     .000   96081.0
h2/  2.50/h2o/ 12.00/ar/   .50/he/   .50/co/  1.90/co2/  3.80/
o2+m=o+o+m                                           .1550e+15    .000  115120.0
h2/  2.50/h2o/ 12.00/ar/   .20/he/   .20/co/  1.90/co2/  3.80/
h+oh+m=h2o+m                                         .4500e+23  -2.000           .0
h2o/ 16.00/h2/  2.00/co2/  1.90/
```

The thermodynamic data corresponds to the ensemble of species involved in the reactions presented in the kinetic mechanism file. For each species, there has to be the elemental composition of the species, the temperature range and a series of coefficients necessary to derive the following information:

$$\frac{C^{\circ}_{p_k}}{R} = a_{1k} + a_{2k} T_k + a_{3k} T_k^2 + a_{4k} T_k^3 + a_{5k} T_k^4$$

8.1.2

$$\frac{H^{\circ}_{k}}{RT_k} = a_{1k} + \frac{a_{2k}}{2} T_k + \frac{a_{3k}}{3} T_k^2 + \frac{a_{4k}}{4} T_k^3 + \frac{a_{5k}}{5} T_k^4 + \frac{a_{6k}}{6}$$

8.1.3

$$\frac{S^{\circ}_{k}}{R} = a_{1k} ln T_k + a_{2k} T_k + \frac{a_{3k}}{2} T_k^2 + \frac{a_{4k}}{3} T_k^3 + \frac{a_{5k}}{4} T_k^4 + a_{7k}$$

8.1.4

where C°_{pk} is the standard-state specific heat (ergs· mol⁻¹· K⁻¹), H°_{k} is the standard-state enthalpy (ergs·mol⁻¹), S°_{k} is the standard-state entropy (ergs· mol⁻¹· K⁻¹) and a_k is the polynomial coefficient that varies from 1 to 7. A total of 14 coefficients are present for each species, 7 coefficients to be used for the lower temperature range to find the values in Eq.8.1.2, Eq.8.1.3 and Eq.8.1.4 and the other 7 for the higher temperature range. Figure 8.1.4 shows an example of thermodynamic data.

Figure 8.1.4   Example of thermodynamic data

```
thermo
  300.    1000.    4000.
he                          he  1               g      300.00    4000.00 1000.00        1
 .250000000e+01 .000000000e+00 .000000000e+00 .000000000e+00 .000000000e+00             2
-.745375000e+03 .928723974e+00 .250000000e+01 .000000000e+00 .000000000e+00             3
 .000000000e+00 .000000000e+00-.745375000e+03 .928723974e+00                            4
ar                          ar  1               g      300.00    4000.00 1000.00        1
 .250000000e+01 .000000000e+00 .000000000e+00 .000000000e+00 .000000000e+00             2
-.745375000e+03 .436600000e+01 .250000000e+01 .000000000e+00 .000000000e+00             3
 .000000000e+00 .000000000e+00-.745375000e+03 .436600000e+01                            4
end
```

In Chemkin, a kinetic mechanism file and thermodynamic file are sufficient to operate certain simulations. However, in some instances, it is necessary to introduce also a transport data when further information is needed. The transport data corresponds to the ensemble of coefficients necessary to characterise the molecular transport of species, momentum and energy. For each species involved in the kinetic modelling, it provides values of diffusion coefficients, viscosities, thermal conductivities and thermal diffusion coefficients. In particular, the values presented are a reference to the geometrical configuration (0 for single atom, 1 for liner molecule and 2 for nonlinear molecule), the Lennard-Jones potential well depth (ε/k_B in K), the Lennard-Jones collision diameter (σ_{col} in Å), the dipole moment (μ_d in Debye), the polarizability (α in Å³) and the rotational relaxation collision number (Z_{rot} at 298K). Figure 8.1.5 shows an example of transport data.

Figure 8.1.5   Example of transport data

```
ac3h4       1    252.000    4.760    0.000    0.000    0.000
ch3cooh     2    436.000    3.970    0.000    0.000    2.000
ch3coch3    2    411.000    4.820    0.000    0.000    1.000
c2h3cho     2    443.200    4.120    0.000    0.000    1.000
c2h5cho     2    411.000    4.820    0.000    0.000    1.000
c4h9cho     2    500.000    5.640    0.000    0.000    1.000
ch2chch2    2    316.000    4.220    0.000    0.000    1.000
chchch3     2    316.000    4.220    0.000    0.000    1.000
ch2cch3     2    316.000    4.220    0.000    0.000    1.000
ar          0    136.500    3.330    0.000    0.000    0.000
c6h5ch2oh   2    622.400    5.530    0.000    0.000    1.000
c6h4o2      2    450.000    5.500    0.000    0.000    1.000
c6h6        2    468.500    5.230    0.000   10.30     1.000
```

The merging process of the three mechanisms required a careful observation on how each file was previously setup. Since the new comprehensive mechanism was mainly aimed to be a soot mechanism, the soot kinetic mechanism from CRECK Modelling Group was chosen to be the principal mechanism around which the other mechanisms had to be modified in order to conform in one combined mechanism.

Therefore the first step required was to change all the units of the Arrhenius factors in the Lawrence Livermore National Library files in the units shown in Eq.8.1.1 (Lawrence Livermore National Library used a CGS unit system).

The next step involved eliminating all the duplicate species. This was done using the thermodynamic data files and the species data files, since different naming convention of the same species could be tracked from the composition. Using the CRECK model as the principal model for the naming convention, all the different named species were tracked and modified. For example, the species C3H4-A in the Lawrence Livermore National Library was varied to AC3H4, as presented in the CRECK model, having the same composition. In this way, a combined species data, thermodynamic data and transport data (once the species to be varied were found, the transport data species were varied automatically) were already shaped.

The kinetic mechanism however required even more attention. First of all, all the species were re-named as per the new naming convention. Then all the duplicate reactions had to be eliminated. This process followed the Euler and Venn diagram shown in Figure 8.1.6.

*Figure 8.1.6   Merging scheme diagram of the three mechanisms*
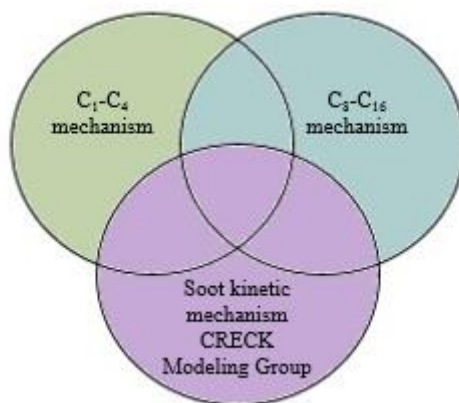
Firstly, all the duplicate reactions present in the C_8-C_{16} model comparing with the CRECK model were eliminated. The same would follow then for all the duplicate reactions present in the C_1-C_4 model comparing with the CRECK model. And finally all the duplicate reactions of the remaining C_1-C_4 model comparing with the modified C_8-C_{16} were also eliminated. The Euler and Venn diagram shown in Figure 8.1.6 is a schematic representation of the final kinetic mechanism, where the CRECK model remained untouched, while the C_8-C_{16} mechanism lost all its duplicates with the CRECK model and the C_1-C_4 lost all its duplicates with both CRECK model and C_8-C_{16} model.

All three files, the kinetic mechanism, thermodynamic data and transport data files, were then tested on the Chemkin software, which would advise on any error found. Before any Chemkin applications, the gas phase chemistry (kinetic mechanism and thermodynamic data) and transport data need to comply with Chemkin's formatting, as shown in Figure 8.1.7.

Figure 8.1.7   Schematic of the relationship between the Gas Phase chemistry data, the Transport data and the Application program [128]
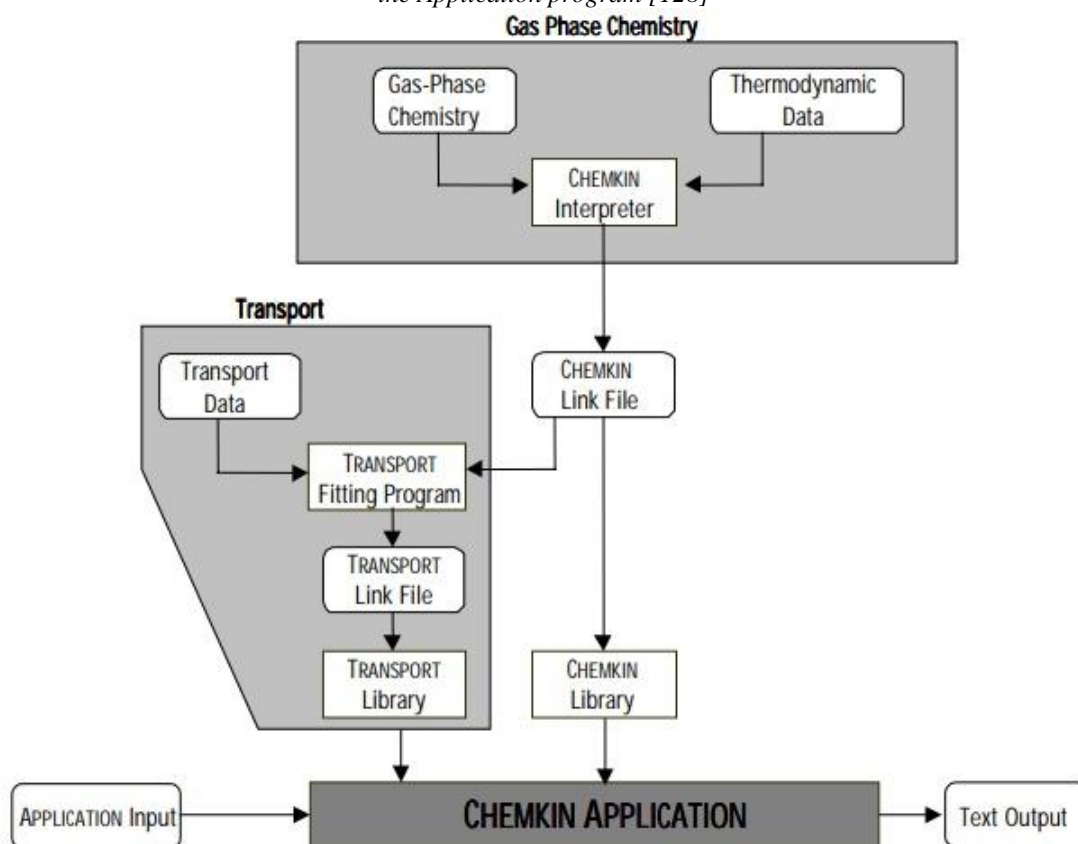
The final kinetic mechanism, thermodynamic data and transport data files are saved in the attached CD-ROM. The final comprehensive soot formation mechanism comprises of 2438 species and 23413 reactions.

8.2   Validation and Methods

In order to be able to use the new comprehensive kinetic model obtained following the steps in Sec.8.1, it was necessary to validate it against previous work results to ensure that no alterations would occur when using the Chemkin software to start simulations. Two validation simulations were chosen, an ignition delay time simulation and a soot particle formation simulation.

Ignition time delay experiments are usually carried out in shock tube, where a mixture composition is allowed to flow through the tube at a certain temperature and pressure. At a certain time, the mixture will auto-ignite inside the shock tube, allowing researchers to determine the conditions necessary for this phenomenon to occur. There are lots of ignition time delay simulations, which corresponds to the measure of the time from initial shock wave heating to a defined ignition point, either a sudden increase in pressure or a sudden change in species population. [129]

Two ignition time delay simulations were carried out, using experimental data found from the literature. A first simulation was of toluene (C_7H_8) in air using sidewall PZT pressure carried out by Vasu et al.[130], who utilised the following range of data in the experiment:

Temperature range (K)	965	1211
Pressure range (atm)	41.5	54.2
Fuel mole fraction (%)	2.28	2.28
Oxygen mole fraction (%)	20.5	20.5
Nitrogen mole fraction (%)	77.24	77.24
Equivalence ratio	1	1

Table 8.2.1   Data range for toluene in air shock tube experiment by Vasu et al. [130]

A second simulation was of n-hexadecane ($C_{16}H_{34}$) in argon from aerosol shock tube experiments using sidewall PZT pressure and CH˙emission near 430nm carried out by Haylett et al. [131], who utilised the following range of data in the experiment:

Temperature range (K)	1159	1355
Pressure range (atm)	1.7	6.8
Fuel mole fraction (%)	0.09	0.18
Oxygen mole fraction (%)	1	4
Argon mole fraction (%)	98.91	95.82
Equivalence ratio	0.56	1.22

Table 8.2.2   Data range for n-hexadecane in argon shock tube experiment by Haylett et al. [131]

On Chemkin, utilising the new comprehensive kinetic mechanism and thermodynamic data, along with the data provided in

Table *8.2.1* and in Table 8.2.2, it was possible to compute ignition time delay based either on inflection point, i.e. the ignition point corresponding to the point at which the rate of change of temperature with respect to time is at its maximum, or on OH species, i.e. the ignition point corresponding to the point with maximum OH concentration.

Figure 8.2.1   Comparison of experimental and computational ignition time delay for toluene [130] (left) and n-hexadecane [131] (right)
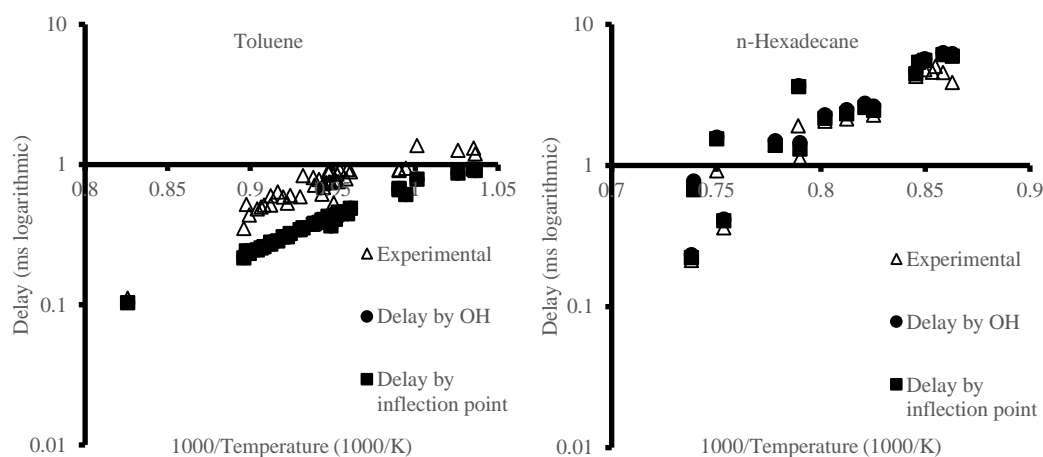

The results in Figure 8.2.1 show that both qualitatively and quantitatively the mechanism captures the trends of the ignition time delay with temperature quite correctly. For the n-hexadecane case, the matching of computational and experimental results is almost completely accurate, for the toluene case there is a very small margin difference. Especially at lower temperatures, the factor of difference

between the experimental and computational results is ~1.5. Even though the small factor of difference is present, the overall agreement in both cases are sufficient as a first validation.

The soot particle formation validation was carried out comparing the soot particles and aggregates distribution obtained by Saggese et al. [121] in the burner-stabilised stagnation (BSS) flame. Saggese et al. [121] utilised OpenSMOKE++ software to run the simulation, where soot was generated in a 16.3% ethylene (C_2H_4)-23.7% oxygen-60% argon at 1 atm pressure and a temperature profile shown in Figure 8.2.2 and a cold gas velocity of 8 cm/s (298 K and 1 atm).
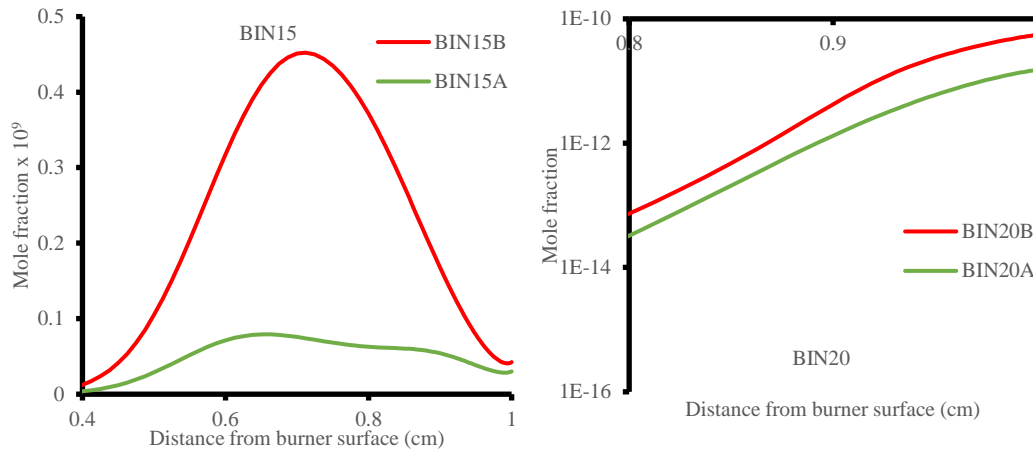
Figure 8.2.2   Temperature profile in the BSS flame simulation [132]
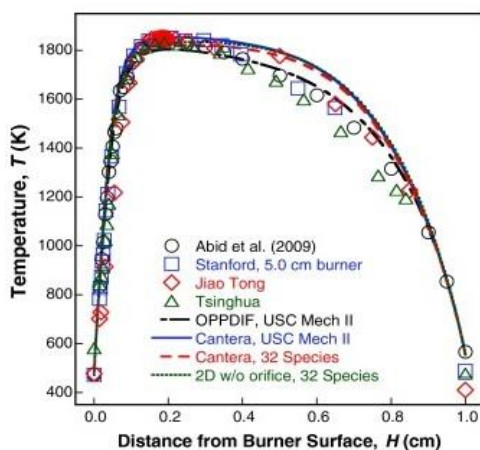
Adopting the same conditions as the ones used by Saggese et al. [121], the following results were obtained for BINs distribution:
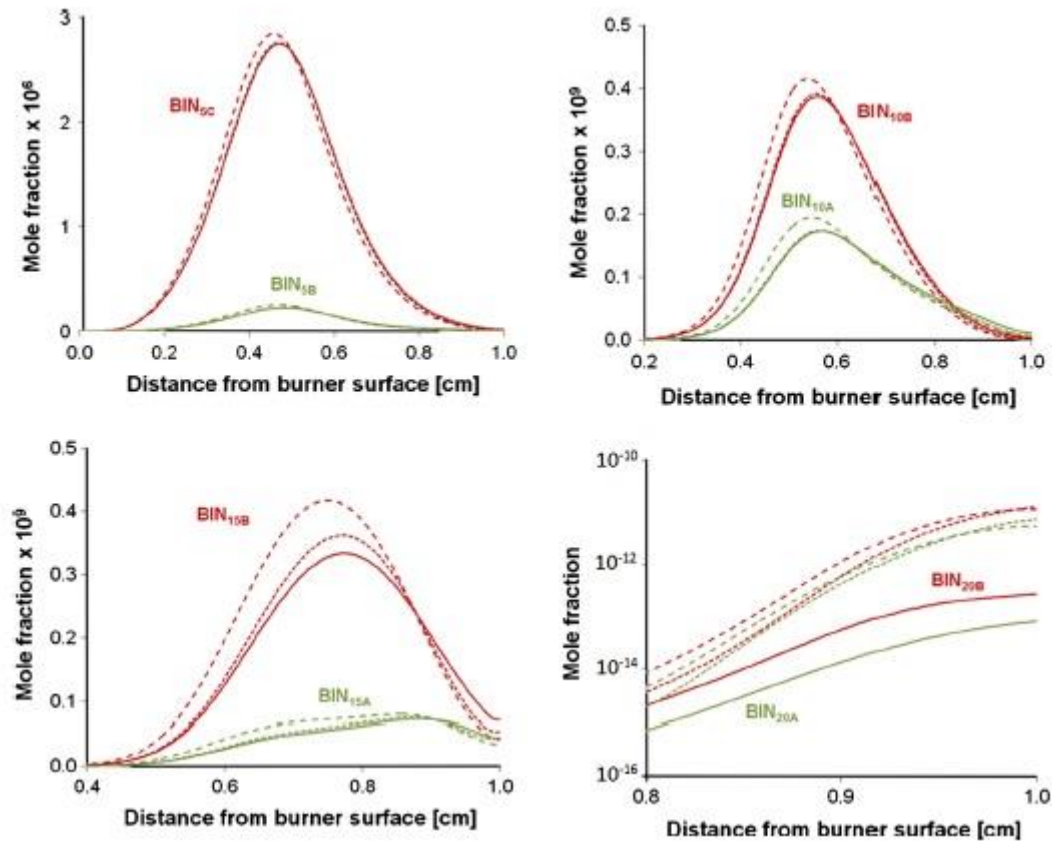
Figure 8.2.3   Mole fraction profile for BIN5, BIN10, BIN15 and BIN20 using Chemkin software
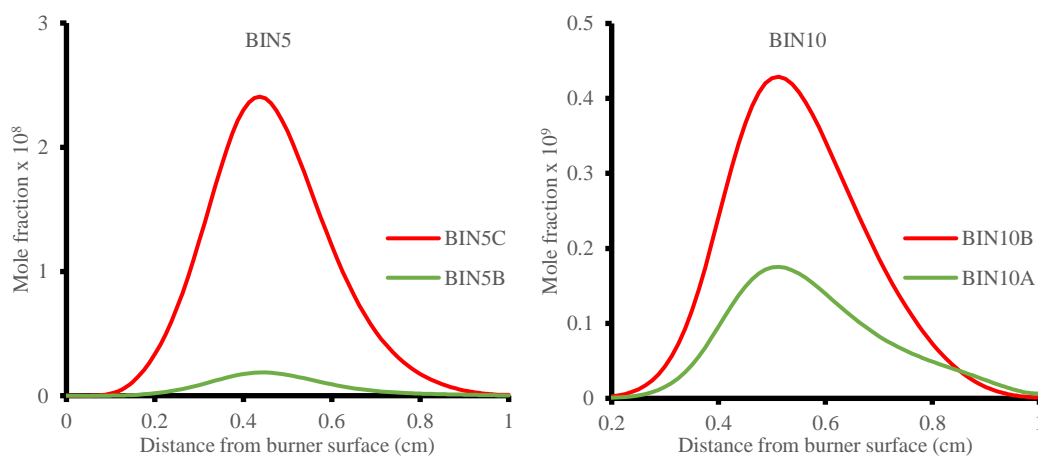
It is possible to compare these results with the ones of Saggese et al. [121] shown below.

Figure 8.2.4   Mole fraction profile for BIN5, BIN10, BIN15 and BIN20 obtained by Saggese et al. [121]

It can be seen that the overall trends and magnitudes of BIN mole fractions are quite accurate, apart

from BIN5, which despite having the same trend, it has a 10^2 order of magnitude difference. It is

believed that the difference might be caused by a misprint in the Saggese et al. [121] paper, since also

other results happen to be accurate, such as the ones shown in Figure 8.2.5 and Figure 8.2.6.

Figure 8.2.5   *Comparison of major species mole fraction profiles for Chemkin (left) and Saggese et al.*
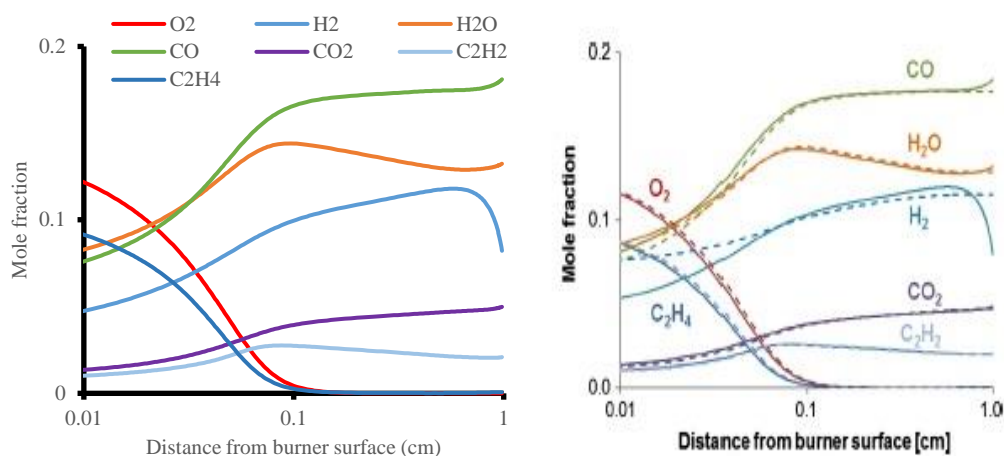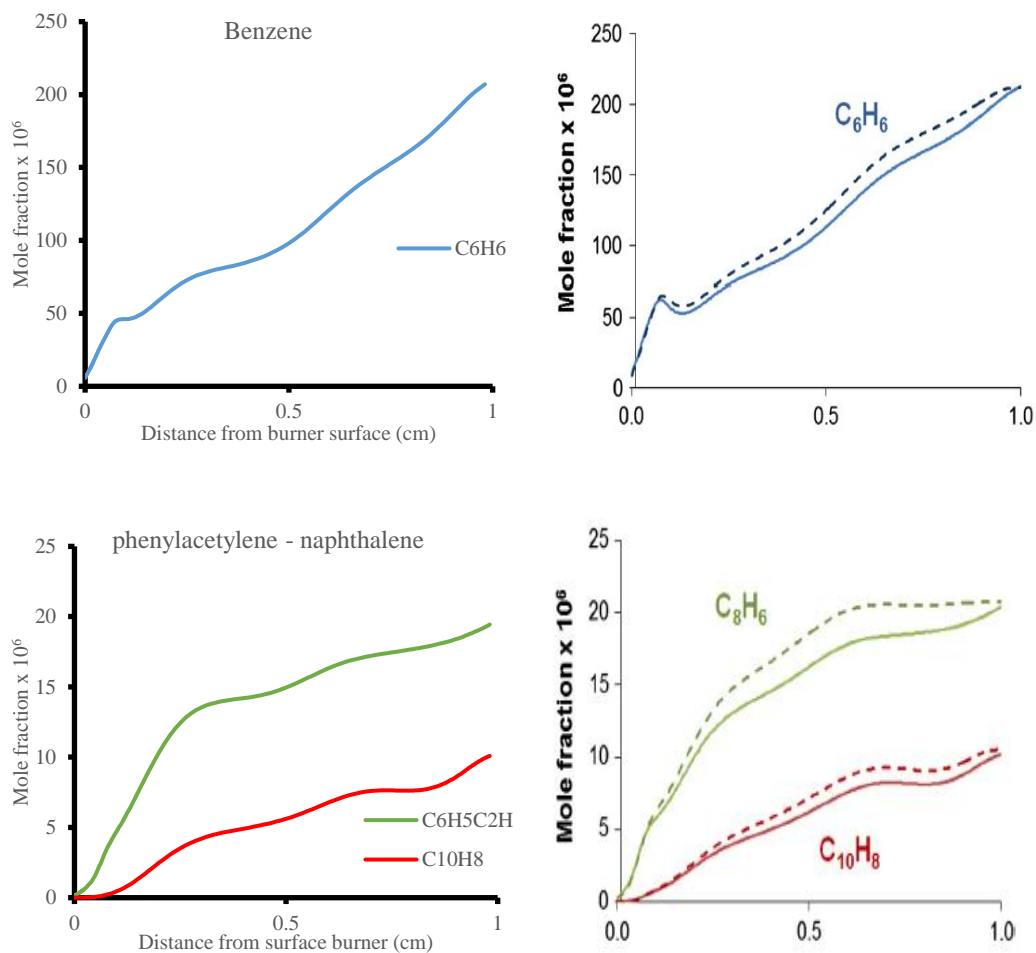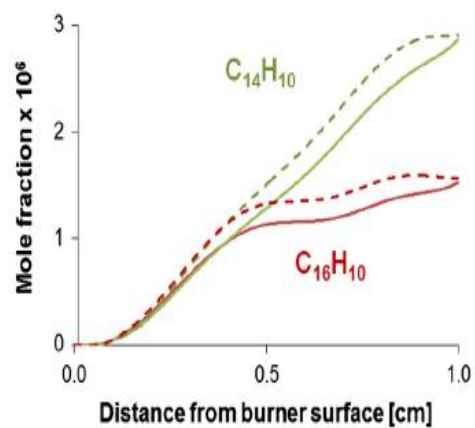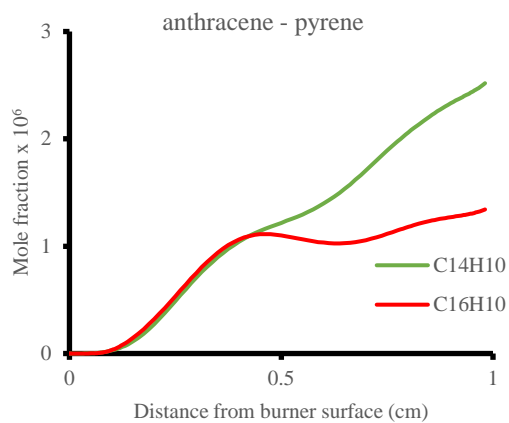*[121]*

Figure 8.2.6   *Comparison of mono-, di- and tri- aromatics mole fraction profiles for Chemkin (left) and*
Saggese et al. [121]

Chapter 9 Simulation of Cavitation Profiles and Analysis of Reaction Paths in Particulate Formation

The purpose of the new comprehensive soot formation mechanism explained in Chapter 8 is to be able to apply it to simulate real life pyrolysis occurring in diesel fuels. In particular, concerning the cavitation occurring in modern return valve DIE, it is possible to utilise this new mechanism to model cavitation collapse of a bubble in a surrogate diesel fuel. The advantage of the new mechanism compared to others presented in Chapter 8, is that it comprises of both paraffins and aromatics species leading to the formation of PAHs and soot particles/aggregates.

The application of the new mechanism will be useful to validate experimental results, in particular when cavitation experiments on diesel fuel show the modification of chemical properties, allowing a comparison between computational and experimental results.

In this chapter, the new comprehensive soot formation mechanism will be proposed to study the effects of bubble collapse in a surrogate diesel fuel, using two different case scenarios. The first case in Sec.9.1 is using an isotropic temperature and pressure profiles to study the effect of increasing the temperature in a bubble on soot formation. The second case in Sec.9.2 is using polytropic temperature and pressure profiles to simulate different bubble collapse scenarios, where pressure and temperature are increasing, and study the reaction paths of some of the major components of the surrogate diesel fuel leading to soot formation. In both cases, the addition of air in the pyrolytic type reaction will be also included in the simulations.

9.1   Isotropic profiles for the kinetics modelling of a collapsing bubble

9.1.1   Simulation without air

The surrogate diesel fuel utilised for these set of measurements are taken from Zeeshan [94] who performed a GC x GC analysis of the same conventional Fuel 1 (BDN), obtaining the following composition results of the diesel fuel:

Hydrocarbon Class	Reactants	Molar fraction
N-Paraffins	$nC_{10}H_{22}$ (n-decane)	0.026
	$nC_{11}H_{24}$ (n-undecane)	0.048
	$nC_{12}H_{26}$ (n-dodecane)	0.037
	$nC_{13}H_{28}$ (n-tridecane)	0.041
	$nC_{14}H_{30}$ (n-tetradecane)	0.029
	$nC_{15}H_{32}$ (n-pentadecane)	0.029
	$nC_{16}H_{34}$ (n-hexadecane)	0.17
Naphthenes + Cycloolefins	cyC_6H_{12} (cyclohexane)	0.123
	cyC_6H_{10} (cyclohexene)	0.123
	$mcyC_8$ (methylcyclohexane)	0.123
Mono-Aromatics	C_6H_6 (benzene)	0.083
	C_7H_8 (toluene)	0.028
Naphthenic Mono-Aromatics	Indene	0.09
Di-Aromatics	$C_{10}H_8$ (naphthalene)	0.001
	$C_{10}H_7CH_3$ (methylnaphthalene)	0.004
	Biphenyl	0.025
	$C_{12}H_8$ (acenaphthalene)	0.01
Tri (+)-Aromatics	$C_{14}H_{10}$ (phenanthrene/anthracene)	0.009
	bz(a)phnthrn (benzo(a)phenanthrene)	0.001

Table 9.1.1   Detailed composition of the surrogate diesel fuel utilised in the Chemkin simulation with the new comprehensive soot formation mechanism

Table 9.1.1 provides the paraffinic and aromatic detailed composition of the surrogate diesel to be utilised in the simulations in Sec.9.1 and in Sec.9.2. It was assumed for the simulation that the components inside the bubble were a homogeneous gas-phase mixture of the species in Table 9.1.1.

The isotropic profile consisted in a 110µs time range parametric study, where the temperature and pressure were set constant throughout the time range, using the following settings in Table 9.1.2:

Temperature (K)	Pressure (bar)
773	1
1273	1
1773	1
2273	1

Table 9.1.2   Isotropic temperature and pressure profiles for the Chemkin simulation with the new comprehensive soot formation mechanism
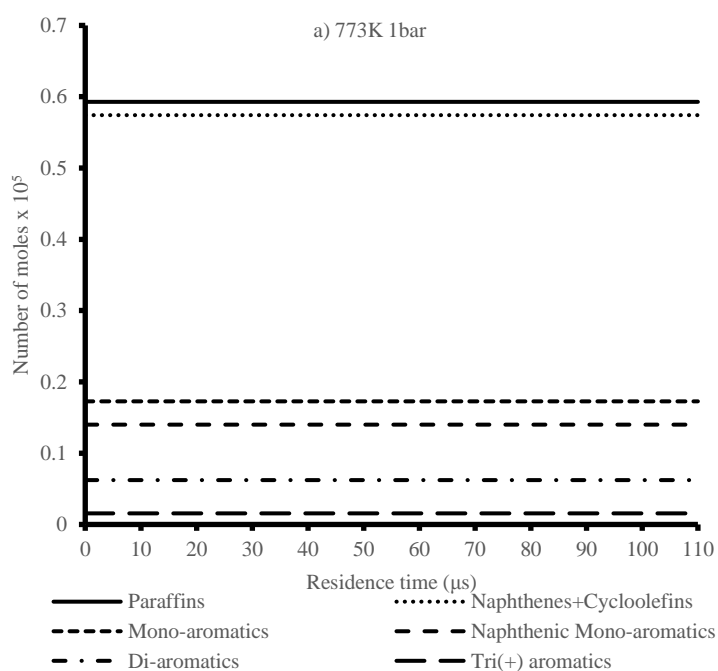
The simulation took place using ANSYS Chemkin-Pro 17.2 (See Sec.8.1), where the new comprehensive soot formation mechanism (kinetic mechanism and thermodynamic data files) was utilised to model the pyrolysis of the surrogate diesel. Under a closed homogeneous reactor, where the

pyrolytic reactions in the bubble were assumed to take place, it was possible to track the change in mole fraction with time of the component of the surrogate diesel fuel in Table 9.1.1. Each mole fraction was then converted to number of moles (m) using the ideal-gal law equation:

$$m_x(t) = f_x(t) \times \frac{p(t) \times V(t)}{R \times T(t)}$$

9.1.1

where f_x is the mole fraction of a species, p is the pressure (bar) and V is the volume (m^3) at a specific time t as obtained from the simulation.

Figure 9.1.1   *Variation in number of moles for isotropic profile of major components in the surrogate diesel fuel*

a) 773K 1bar

b) 1273K 1bar

Legend:
— Paraffins
⋯⋯ Naphthenes+Cycloolefins
- - - Mono-aromatics
– – – Naphthenic Mono-aromatics
–·–·– Di-aromatics
— — Tri(+) aromatics

c) 1773K 1bar

Legend:
— Paraffins
⋯⋯ Naphthenes+Cycloolefins
- - - Mono-aromatics
– – – Naphthenic Mono-aromatics
–·–·– Di-aromatics
— — Tri(+) aromatics
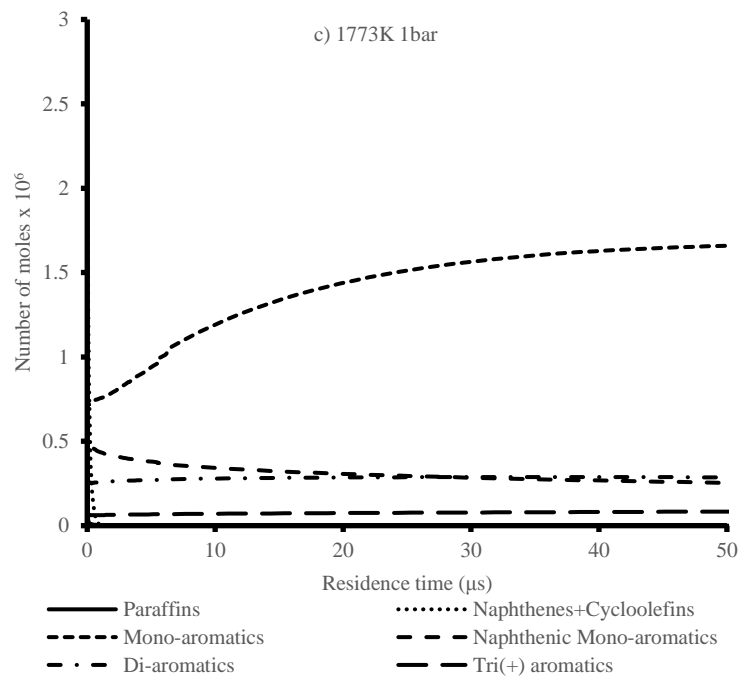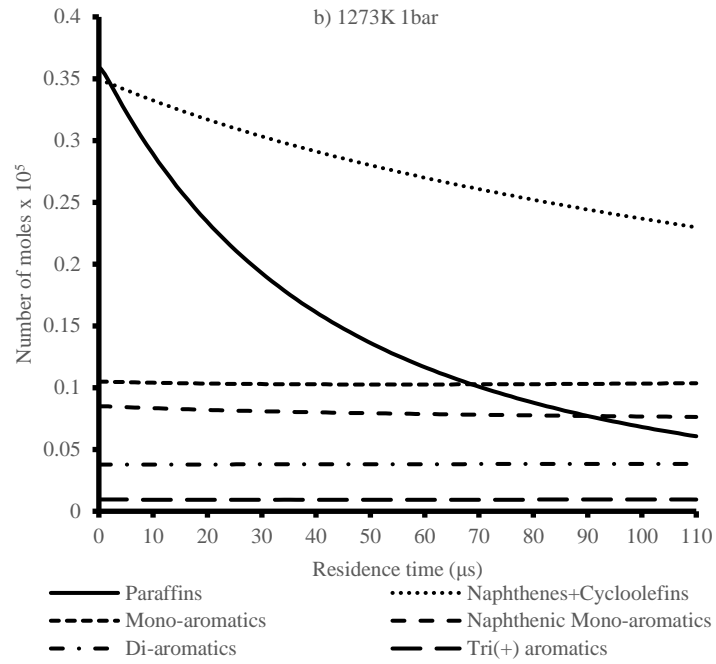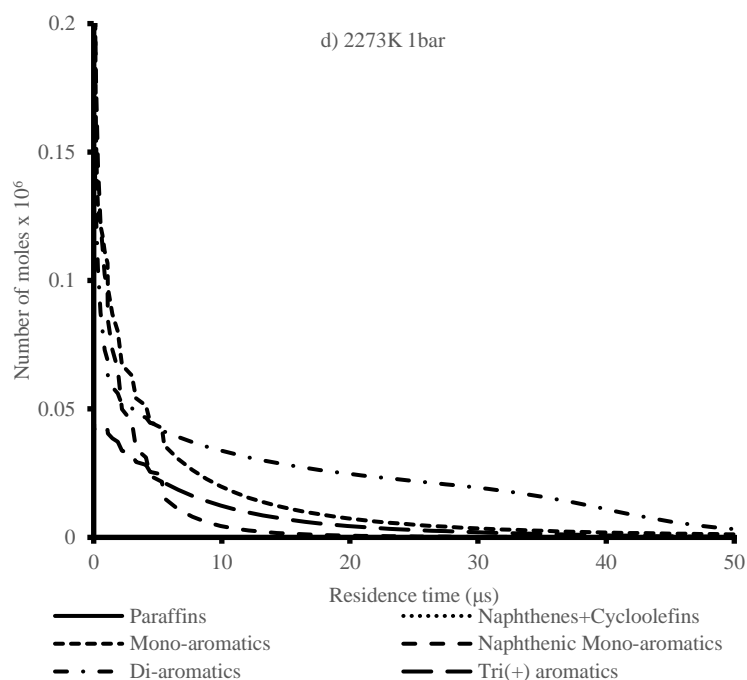
d) 2273K 1bar

From Figure 9.1.1a, it can be noticed that at the lower temperature of 773K – 1bar, there is no change in the number of moles of the major species throughout the time span. In Figure 9.1.1b, at 1273K – 1bar, the only species experiencing a mole reduction are the paraffins and naphthenes+cycloolefins, while all the other species are experiencing insignificant change. In Figure 9.1.1c all the main reactions are occurring in less than 10μs, in particular paraffins, naphthenes+cycloolefins and naphthenic mono-aromatics are reducing in number of moles, while the mono-aromatics are steadily increasing with time. In Figure 9.1.1d all the main reactions are occurring in less than 5μs, this time all species are decreasing in number of moles with time, including larger aromatics.

Following a reaction path analyser included in the Chemkin software, it was found that for the 1273K – 1bar case, the precursor of reactions at the start was indene, the only naphthenic mono-aromatic present in the fuel. The first reaction occurring was in fact producing from two molecules of indene, pyrene ($C_{16}H_{10}$), ethylene (C_2H_4), methyl radical (CH_3) and hydrogen radical:

$$2Indene \rightarrow C_{16}H_{10} + 0.5C_2H_4 + CH_3 + H \qquad\qquad 9.1.2$$
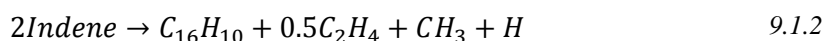
The paraffins experienced a decrease in number of moles throughout the time span, as visible in the reaction path analysis. N-Hexadecane (n-$C_{16}H_{34}$) for instance decomposed in various smaller alkyl radicals, such as heptyl (nC_7H_{15}), and larger alkyl radicals, such as $nC_{16}H_{33}$. These then continued to decompose in methane (CH_4) and ethylene (C_2H_4). The products of the indene reactions, in particular

the methyl radical and hydrogen, would lead to hydrogen abstraction reaction for the paraffins, explaining their reduction with time.

This reduction is accentuated with the increase in temperature, in the 1773K – 1bar results, where most of the major species follow a faster decomposition due to the higher temperature, while the mono-aromatics experienced an increase in number of moles. In particular, close to 10μs, it was possible to track the reaction path of benzene (C_6H_6). Benzene was being produced by reactions of indene, n-hexadecane and methylcyclohexane through attacks of phenyl group and hydrogen radical. This explains why the groups of paraffins, naphthenes+cycloolefins and naphthenic mono-aromatics experience the greatest reduction in number of moles.

At the highest temperature analysed, at 2273K – 1bar, mono-aromatics go back to decreasing in number of moles along the larger aromatics. Benzene for instance was found to be the precursor in producing naphthalene ($C_{10}H_8$), a di-aromatic, which in turn through hydrogen abstraction forms other radicals responsible in decaying paraffins and mono-aromatics even more.

Moreover, the variation of number of moles with time can be explained through soot formation, as shown in the plots below:

Figure 9.1.2   *Variation in number of moles for isotropic profile of BIN1 to BIN10 in the surrogate diesel fuel*

c) 1773K - 1bar

d) 2273K - 1bar
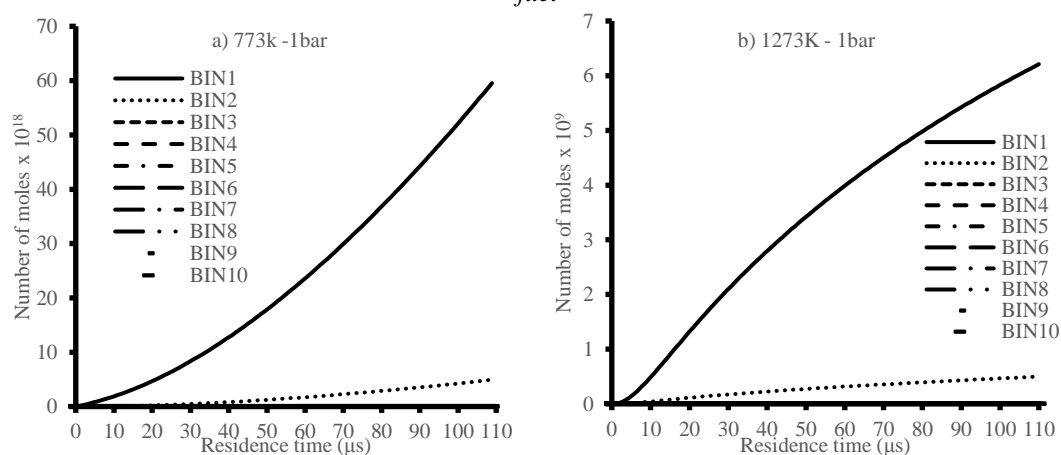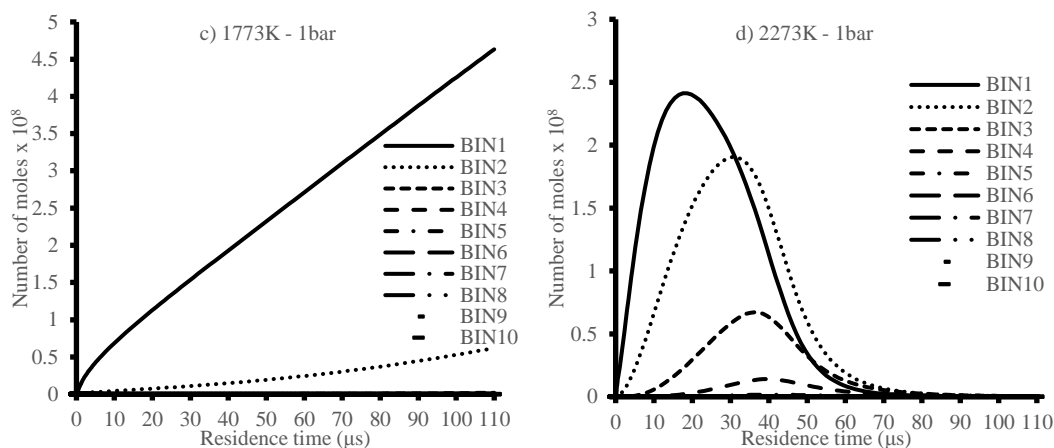
Each BINs shown in Figure 9.1.2 represents the sum of the sub-categories A, B, C (See Sec.8.1). As it can be seen, the higher the BIN size, the lower the number of moles becomes, which is why only the first ten BIN classes are plotted.
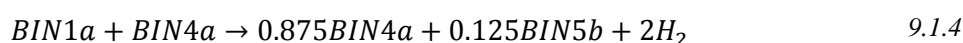
It can be observed in Figure 9.1.2 that the BIN mole magnitude decreases as the BIN class increases. For the temperature profiles of 773K, 1273K and 1773K, it is illustrated how BIN1 and BIN2 are increasing steadily within the time range of 110μs.

From the reaction path analysis, it can be seen how the small BINs are formed as a result of PAH reactions, in particular for BIN1 and BIN2, while larger BINs are formed from the reactions between BINs. The key precursors in the formation of BIN1 were found to be biphenyl and indenyl radicals when reacting with species such as benzene, indene, phenanthrene and anthracene, which were constantly present in the surrogate diesel as shown in Figure 9.1.1. An example of reaction forming BIN1 was:

$$Indene + \ C_{14}H_{10} \rightarrow 0.5BIN1a + 0.6BIN1b + CH_3 + H \qquad 9.1.3$$
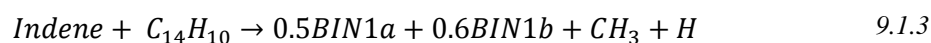
where indene and phenanthrene react to form BIN1 along with the methyl group and hydrogen radical. The latter would then contribute in hydrogen abstraction reactions.

Larger BIN sizes were obtained from the coalescence/aggregation of smaller BIN species, as explained in Sec.8.1. For example, the reaction path analysis illustrated the formation of BIN5 with the following reactions:

$$BIN1a + BIN4a \rightarrow 0.875BIN4a + 0.125BIN5b + 2H_2 \qquad 9.1.4$$

$$rbiphenyl + BIN4a \rightarrow 0.918BIN4a + 0.007BIN4b + 0.075BIN5a + 0.572H_2 + H$$
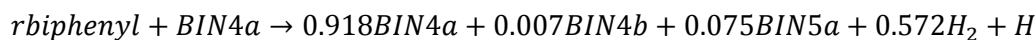
This is visible when analysing Figure 9.1.2d at 2273K – 1bar. BIN1 experiences a peak formation at ~20μs, followed by a steady decrease until ~60μs when it becomes insignificant. This is followed by BIN2, which reaches a peak formation at ~30μs and then dissipates until becoming again insignificant at ~70μs. The shifting of the peak formation can be seen also for BIN3 and BIN4 in Figure 9.1.2d, and can be explained by the competing formation and coalescence/aggregation reactions. As BIN1 and BIN2 are formed by PAHs, at the same time they are aggregating to form BIN3 and so on, causing a time delay and a reduction in number of moles peak each time.

BIN radicals, produced through HACA reactions of the BIN of the same class, played also an important role in BIN growth when reacting with aromatics, such as the example below with BIN5:

$$Indene +\ bin5aj \rightarrow 0.972BIN5a + 0.028BIN6a + 0.525H_2 + H \qquad 9.1.5$$
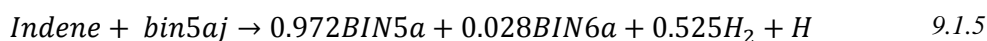
9.1.2   Simulation with air

The same analysis was then extended to oxygen addition to the bubble pyrolitic reaction type described previously. It is known that dissolved oxygen and nitrogen in a diesel fuel can dissolve inside a cavitating bubble, as stated by Henry's and Raoult's law describing the solubility of a gas in a liquid[133], and can therefore participate in the pyrolysis reaction. Table 9.1.3 shows the revised surrogate diesel fuel composition with the addition of 0.5% air (21%O_2 and 79%N_2). It was assumed once again that the components inside the bubble were a homogeneous gas-phase mixture of the species in Table 9.1.3.

Species	Reactants	Molar fraction
N-Paraffins	$nC_{10}H_{22}$ (n-decane)	0.02587
	$nC_{11}H_{24}$ (n-undecane)	0.04776
	$nC_{12}H_{26}$ (n-dodecane)	0.036815
	$nC_{13}H_{28}$ (n-tridecane)	0.040795
	$nC_{14}H_{30}$ (n-tetradecane)	0.028855
	$nC_{15}H_{32}$(n-pentadecane)	0.028855
	$nC_{16}H_{34}$ (n-hexadecane)	0.16915
Naphthenes + Cycloolefins	cyC_6H_{12}(cyclohexane)	0.122385
	cyC_6H_{10}(cyclohexene)	0.122385
	$mcyC_6$ (methylcyclohexane)	0.122385
Mono-Aromatics	C_6H_6 (benzene)	0.082585
	C_7H_8 (toluene)	0.02786
Naphthenic Mono-Aromatics	Indene	0.08955
Di-Aromatics	$C_{10}H_8$ (naphthalene)	0.000995
	$C_{10}H_7CH_3$ (methylnaphthalene)	0.00398
	Biphenyl	0.024875
	$C_{12}H_8$ (acenaphthalene)	0.00995
Tri(+)-Aromatics	$C_{14}H_{10}$ (phenanthrene/anthracene)	0.008955
	bz(a)phnthrn	0.000995
Air	O_2 (oxygen)	0.00105
	N_2 (nitrogen)	0.00395

Table 9.1.3   Detailed composition of the surrogate diesel fuel with addition of 0.5% air utilised in the Chemkin simulation with the new comprehensive soot formation mechanism

Under the same conditions as in Sec.9.1.1, with the addition of 0.5% air as specified in Table 9.1.3, it is possible first of all to observe the variation of number of moles with time, as shown in Figure 9.1.3:

Figure 9.1.3   Variation in number of moles for isotropic profile of major components in the surrogate diesel fuel with 0.5% air addition

b)1273K - 1bar +0.5%air

Paraffins ——
Naphthenes+Cycloolefins ·······
Mono-aromatics ----
Naphthenic Mono-aromatics – –
Di-aromatics –·–
Tri(+) aromatics — —

c)1773K - 1bar +0.5%air

Paraffins ——
Naphthenes+Cycloolefins ·······
Mono-aromatics ----
Naphthenic Mono-aromatics – –
Di-aromatics –·–
Tri(+) aromatics — —

d)2273K - 1bar +0.5%air
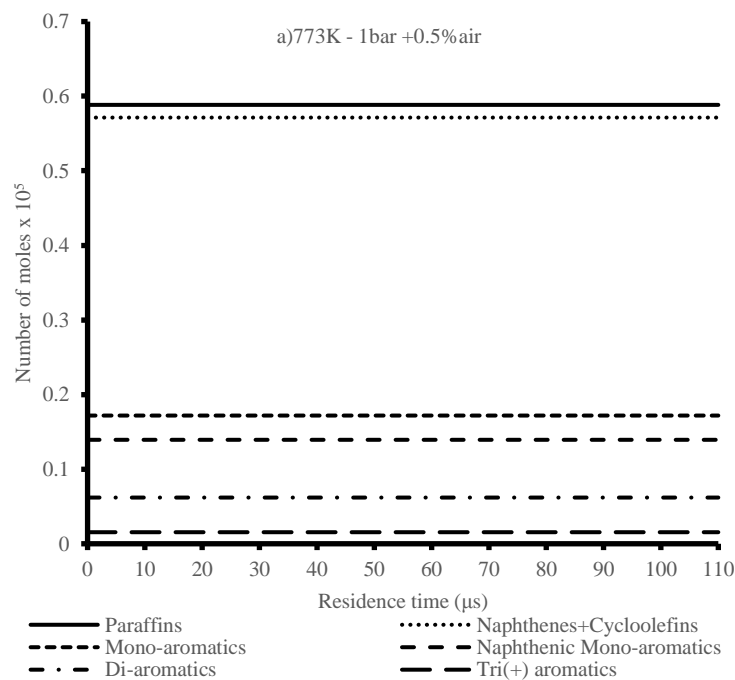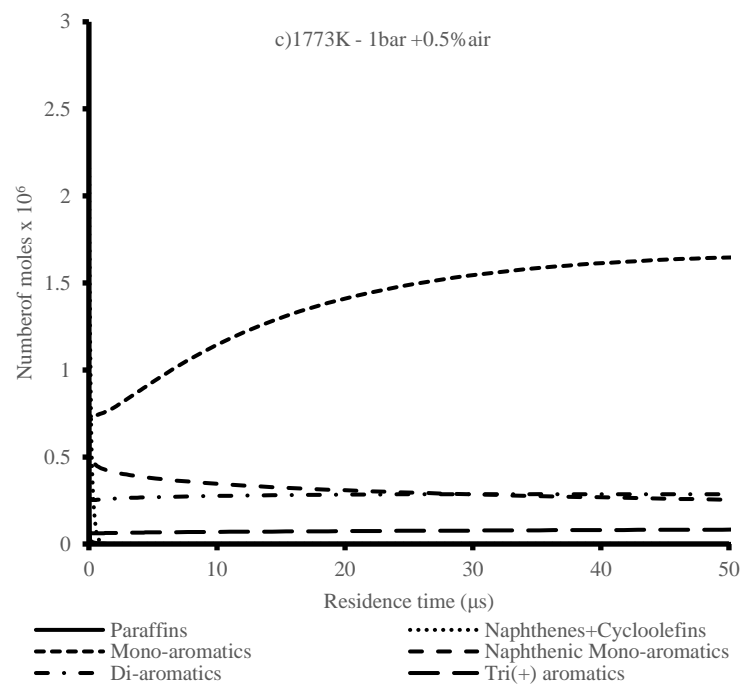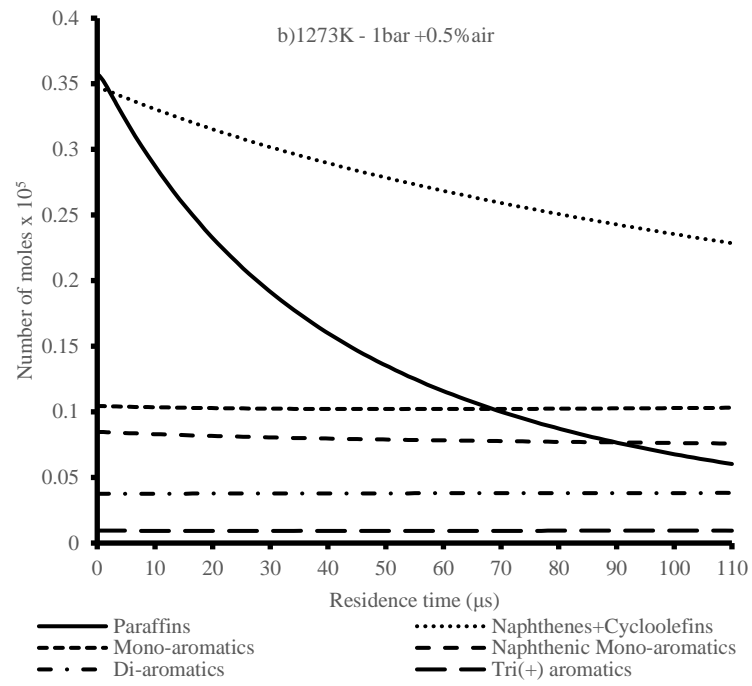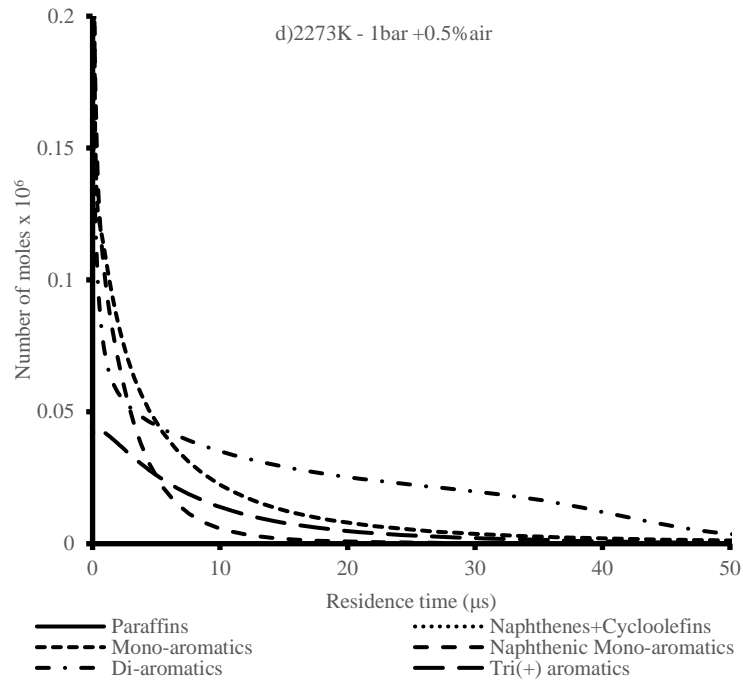
Comparing the plots in Figure 9.1.1 and the plots in Figure 9.1.3, it can be seen that despite the addition of air, the number of moles are almost identical for all species. However, a closer look to Figure 9.1.1c, Figure 9.1.1d, Figure 9.1.3c and Figure 9.1.3d, it can be noticed a variation in the mono-aromatics in the time frame between 0μs and 10μs. In particular, for the simulations with the addition of 0.5% air, the plot lines in this time range are smoother, compared to the simulations without air which present more irregularities.

To better understand the influence of air to the major species comprising the surrogate diesel fuel, plots showing the change in number of moles of oxygen (O_2) and of nitrogen (N_2) are presented in Figure 9.1.4 for all the isotropic temperature and pressure profile cases:

Figure 9.1.4   *Variation in number of moles for isotropic profile of oxygen and nitrogen in the surrogate diesel fuel with 0.5% air addition*

From Figure 9.1.4, it can be noticed that in the 773K – 1bar scenario, both oxygen and nitrogen do not exhibit any variations. From 1273K – 1bar case beyond, whilst nitrogen number of moles remain constant throughout the time range of 110μs, oxygen experie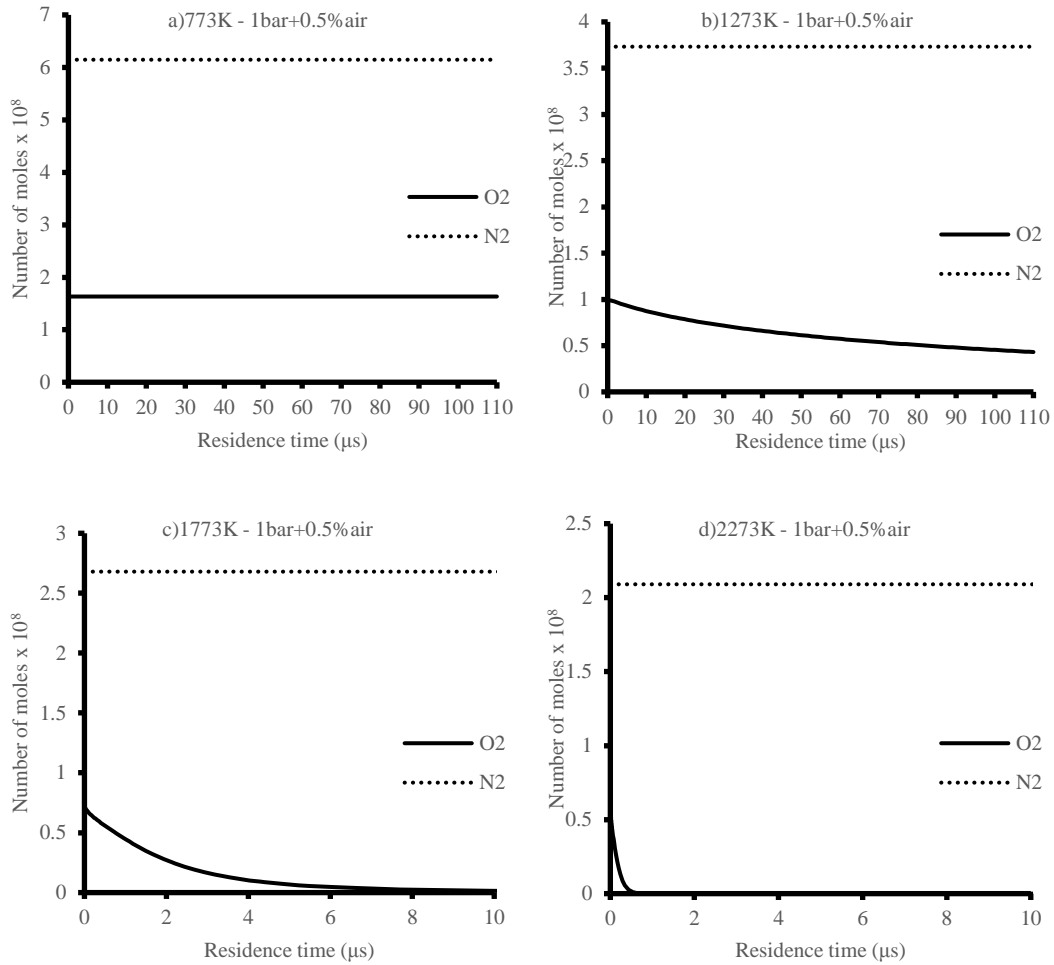nces a decay which starts slower in the 1273K – 1bar case, and it gets faster in the 1773K – 1bar case (it decays within 10μs) and even faster in the 2273K – 1bar case (it decays withing 2μs).

Following a reaction path analysis, it was found that oxygen experienced the following reactions from the start time of 0μs:

$$O_2 + nC_{16}H_{34} \rightarrow HO_2 + nC_{16}H_{33}$$

$$O_2 + mcyC_6 \rightarrow HO_2 + rmcyC_6 \qquad \qquad 9.1.6$$

$$O_2 + indene \rightarrow HO_2 + indenyl$$
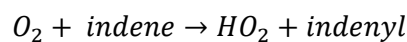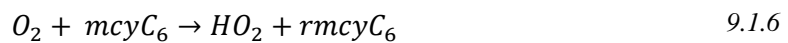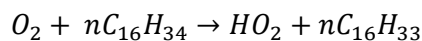
Oxygen is reacting therefore with paraffins, naphthenes and indene to form hydroperoxyl radical (HO_2) and the radical of the major species. The hydroperoxyl radical would then go and react with other radicals, to form in the end hydroxyl radicals (OH), as showin in Eq.9.1.7:

$$HO_2 + H \rightarrow 2OH$$
$$HO_2 + CH_3 \rightarrow CH_3O + OH$$

9.1.7

It was found that OH production was the precursor in the formation of soot particles, by reacting with BINs (See Sec.8.1) and other major species, as shown in Eq.9.1.8:

$$OH + BIN1bj \rightarrow 0.25C_{16}H_9 + 0.75BIN1bj + CO + H$$

9.1.8

The hydroxyl radical, by reacting with BINs obtained previously from naphthenic mono-aromatics (See Sec.9.1.1), cause an oxidation process that even though it reduces the number of moles of the BIN, it produces other radicals that affect the formation of soot particles.

Figure 9.1.5   *Variation in number of moles for isotropic profile of BIN1 to BIN10 in the surrogate diesel fuel with 0.5% air addition*
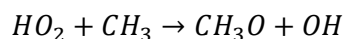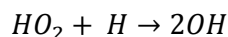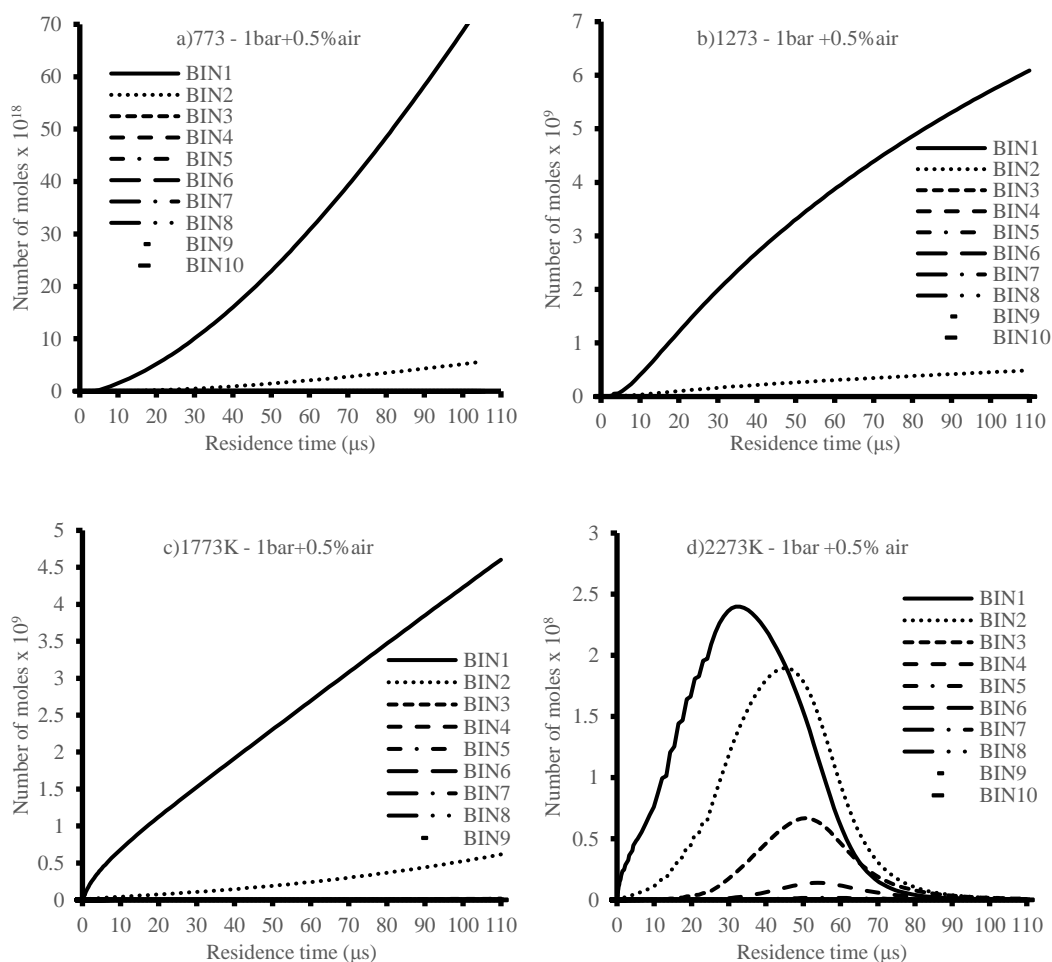
Figure 9.1.5 shows the variation in number of moles of BIN1 to BIN10 with the addition of 0.5% air. Similarly to Figure 9.1.2, the trends and number of moles are almost identical, apart from some irregularities present in Figure 9.1.5c and Figure 9.1.5d in the time region between 10μs and 20μs. Also, comparing Figure 9.1.5d with Figure 9.1.2d (without air addition), it can be noticed how in the former case the peak number of moles are shifted at longer residence time. For instance, BIN1 has a peak at 20μs without air, whilst the peak is at~35μs with air. These irregularities are expected to depend by the oxidation process shown in Eq.9.1.8, having though a minimal effect on the overall soot particle formation, just a delay in BIN formation and decay.

9.2   Polytropic profiles for the kinetics modelling of a collapsing bubble

9.2.1   Simulation without air

The polytropic temperature and pressure profiles provide a more realistic approach in analysing the cavitating bubble collapse of a surrogate diesel fuel. In general, the polytropic relations for pressure and temperature are described as follows:

$$\frac{p_i}{p_o} = \left(\frac{V_o}{V_i}\right)^n$$

$$\frac{T_i}{T_o} = \left(\frac{V_o}{V_i}\right)^{n-1}$$

9.2.9

where n is the polytropic coefficient, while the subscripts o and i represent respectively the initial condition and the condition at a specific time. Both pressure and temperature ratios can therefore be related to the volume ratio by the same polytropic coefficient n.

For the simulation below, it was assumed the volume ratio of the cavitating bubble would double at each time step, meaning that the V_i would halve in size at every time step. At the same time, the polytropic coefficient n was assumed to be 1.1 for this simulation, and the initial volume V_o to be 1×10^{-11} m³. Considering also that in the simulation the components inside the bubble were a homogeneous gas-phase mixture of the species in Table 9.1.1 (i.e. no addition of air), the following polytropic temperature and pressure profiles were generated:

Time 1 (s)	Time 2 (s)	Time 3 (s)	V_i (m³)	V_o/V_i	r_i(m)	P (bar)	T(K)
0	0	0	1×10^{-11}	1	0.000134	0.00015	330.00
0.00005	0.00002	0.00001	5×10^{-12}	2	0.000106	0.00032	353.69
0.0001	0.00004	0.00002	2.5×10^{-12}	4	8.42×10^{-5}	0.00069	379.07
0.00015	0.00006	0.00003	1.25×10^{-12}	8	6.68×10^{-5}	0.00148	406.28
0.0002	0.00008	0.00004	6.25×10^{-12}	16	5.3×10^{-5}	0.00317	435.44
0.00025	0.0001	0.00005	3.13×10^{-13}	32	4.21×10^{-5}	0.00679	466.69
0.0003	0.00012	0.00006	1.56×10^{-13}	64	3.34×10^{-5}	0.015	500.19
0.00035	0.00014	0.00007	7.81×10^{-14}	128	2.65×10^{-5}	0.031	536.09
0.0004	0.00016	0.00008	3.91×10^{-14}	256	2.1×10^{-5}	0.067	574.56
0.00045	0.00018	0.00009	1.95×10^{-14}	512	1.67×10^{-5}	0.14	615.80
0.0005	0.0002	0.0001	9.77×10^{-15}	1024	1.33×10^{-5}	0.31	660.00
0.00055	0.00022	0.00011	4.88×10^{-15}	2048	1.05×10^{-5}	0.66	707.37
0.0006	0.00024	0.00012	2.44×10^{-15}	4096	8.35×10^{-6}	1.41	758.14
0.00065	0.00026	0.00013	1.22×10^{-15}	8192	6.63×10^{-6}	3.03	812.56
0.0007	0.00028	0.00014	6.1×10^{-15}	16384	5.26×10^{-6}	6.49	870.88
0.00075	0.0003	0.00015	3.05×10^{-16}	32768	4.18×10^{-6}	13.90	933.38
0.0008	0.00032	0.00016	1.53×10^{-16}	65536	3.31×10^{-6}	29.80	1000.37
0.00085	0.00034	0.00017	7.63×10^{-17}	131072	2.63×10^{-6}	63.88	1072.17
0.0009	0.00036	0.00018	3.81×10^{-17}	262144	2.09×10^{-6}	136.93	1149.13
0.00095	0.00038	0.00019	1.91×10^{-17}	524288	1.66×10^{-6}	293.51	1231.60
0.001	0.0004	0.0002	9.54×10^{-17}	1048576	1.32×10^{-6}	629.15	1320.00
0.00105	0.00042	0.00021	4.77×10^{-18}	2097152	1.04×10^{-6}	1348.60	1414.74
0.0011	0.00044	0.00022	2.38×10^{-18}	4194304	8.29×10^{-7}	2890.79	1516.28
0.00115	0.00046	0.00023	1.19×10^{-18}	8388608	6.58×10^{-7}	6196.55	1625.11
0.0012	0.00048	0.00024	5.96×10^{-18}	16777216	5.22×10^{-7}	13282.60	1741.75
0.00125	0.0005	0.00025	2.98×10^{-19}	33554432	4.14×10^{-7}	28471.88	1866.76
0.0013	0.00052	0.00026	1.49×10^{-19}	67108864	3.29×10^{-7}	61030.81	2000.75
0.00135	0.00054	0.00027	7.45×10^{-20}	1.34×10^8	2.61×10^{-7}	130822.41	2144.35
0.0014	0.00056	0.00028	3.73×10^{-20}	2.68×10^8	2.07×10^{-7}	280423.96	2298.25
0.00145	0.00058	0.00029	1.86×10^{-20}	5.37×10^8	1.64×10^{-7}	601101.93	2463.21
0.0015	0.0006	0.0003	9.31×10^{-21}	$1.07E \times 10^9$	1.31×10^{-7}	1288490.19	2640.00
0.00155	0.00062	0.00031	4.66×10^{-21}	2.15×10^9	1.04×10^{-7}	2761939.18	2829.48
0.0016	0.00064	0.00032	2.33×10^{-21}	4.29×10^9	8.22×10^{-8}	5920346.24	3032.56
0.00165	0.00066	0.00033	1.16×10^{-21}	8.59×10^9	6.53×10^{-8}	12690539.98	3250.22
0.0017	0.00068	0.00034	5.82×10^{-22}	1.72×10^{10}	5.18×10^{-8}	27202767.95	3483.50

Table 9.2.1   Polytropic temperature and pressure profiles table for the Chemkin simulation with the new comprehensive soot formation mechanism

The initial pressure and temperature conditions for the cavitating bubble was assumed to be 15Pa and 330K. Table 9.2.1 shows the full polytropic pressure and temperature profiles for three time ranges. The first time range is between 0ms and 1.7ms, in steps of 0.05ms; the second time range is between 0ms and 0.68ms, in steps of 0.02ms; the third time range is between 0ms and 0.34ms, in steps of 0.01ms. The profiles are illustrated in the plots below:

Figure 9.2.1   Polytropic temperature and pressure profiles for the three simulations
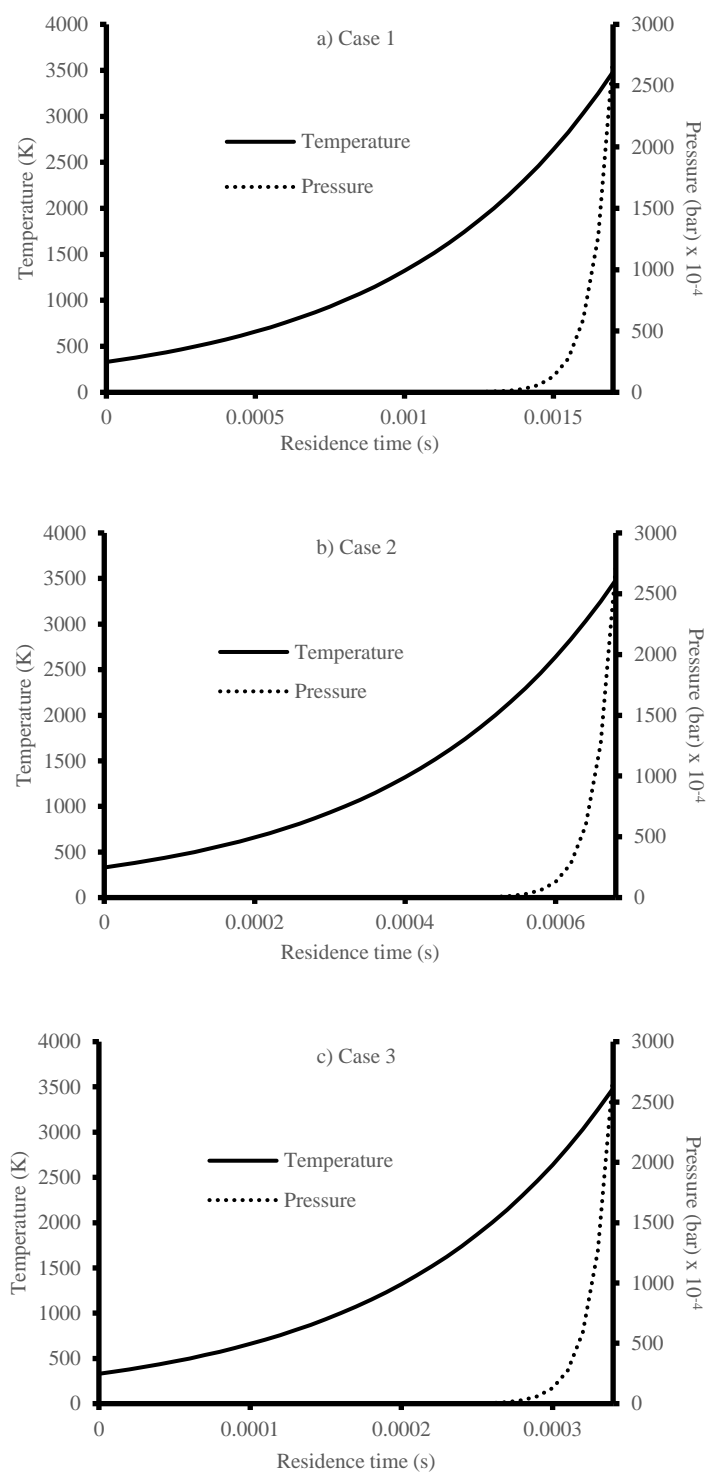
It can be noticed in Figure 9.2.1 how "Case 1" has the lowest pressure and temperature increase, followed by "Case 2" and then "Case 3", which has the fastest pressure and temperature increase.

This simulation ran using Table 9.1.1 surrogate diesel composition and Table 9.2.1 polytropic temperature and pressure profiles. It was possible therefore to observe the variation in number of moles for the major species in Figure 9.2.2.

Figure 9.2.2 *Variation in number of moles for polytropic profile of major components in the surrogate diesel fuel*
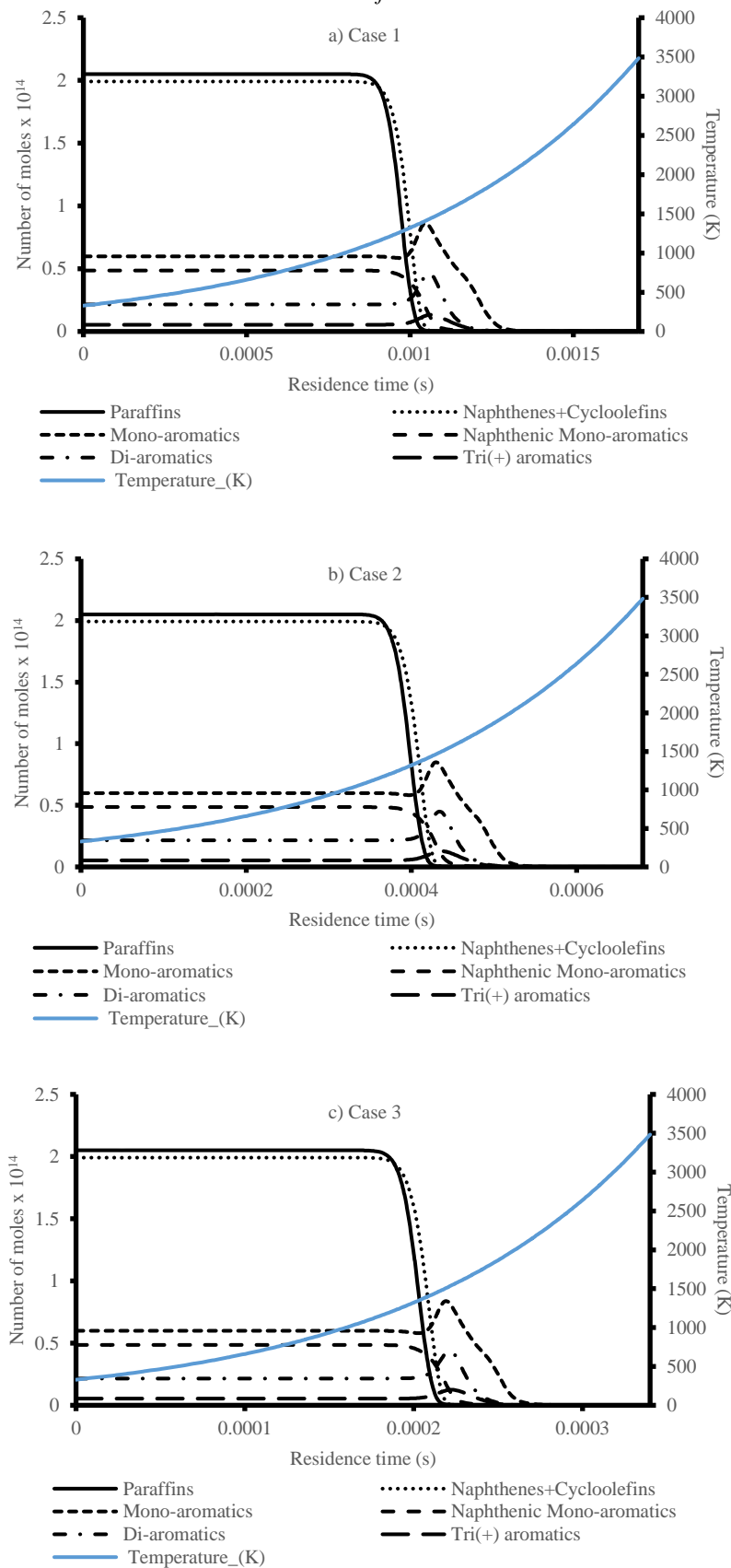
A different situation is presented comparing Figure 9.2.2 with the polytropic profile and Figure 9.1.1 with the isotropic profile. In Figure 9.2.2a, the number of moles remains constant until reaching ~0.9ms

and a temperature of ~1150K, where the paraffins, naphthenes + cycloolefins and naphthenic mono-aromatics start reducing drastically the number of moles. At ~1.1ms (~1500K) these species have completely decayed, while at the same time the other species, i.e. mono-aromatics, di-aromatics and tri(+)-aromatics, all experience an increase in number of moles. The peak is attained at ~1.1ms (~1500K), after which also the aromatics start decaying. In Figure 9.2.2b and Figure 9.2.2c the same trends were observed in the same temperature range of ~1150K to ~1500K, only that in case 2 it corresponds to the time range of ~0.36ms and ~0.44ms, and in case 3 to the time range of ~0.18ms and ~0.22ms.

Furthermore, a closer look to the three different cases allows to notice a slight reduction in the peak number of moles for the aromatics from case 1 to case 3. In case 3, paraffinic decay occurs earlier than in case 1 and in a much faster rate, meaning that there will be less time to form new aromatics.

From the reaction path analysis, it was possible to track down the reactions responsible for the behaviour observed in Figure 9.2.2. It was found that the ethyl radical (C_2H_5) would react with almost all of the paraffins and naphthenes. It is mainly produced by the decomposition of larger paraffins, such as n-hexadecane:

$$nC_{16}H_{34} \rightarrow C_2H_5 + 0.5nC_{12}H_{25} + 0.5nC_{16}H_{33} \qquad \text{9.2.10}$$

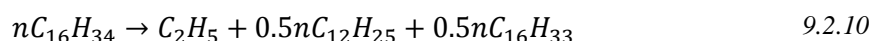N-hexadecane ($nC_{16}H_{34}$) starts decomposing at a faster rate when it reacts with C_2H_5 forming radicals such as $nC_{16}H_{33}$, which in turn decomposes into smaller alkyl radicals. Similarly occurs: to naphthenes such as cyclohexane (cyC_6H_{12}) when reacting with C_2H_5 to form radicals such as cyC_6H_{11}; and to naphthenic mono-aromatics, i.e. indene, when reacting with C_2H_5 to form radicals such as *indenyl*. The phenyl radical (C_6H_5) produced by the decomposition of n-hexadecane, was found to react with most of the paraffins and naphthenes to produce benzene (C_6H_6):

$$C_6H_5 + nC_{16}H_{34} \rightarrow C_6H_6 + nC_{16}H_{33} \qquad \text{9.2.11}$$
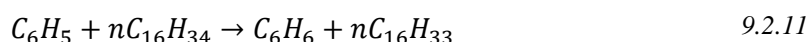
Larger aromatics would then be formed by reactions of the larger radicals with smaller aromatics, such as indenyl with benzene to form phenanthrene, or *cyC_5H_6* with benzene to form naphthalene:
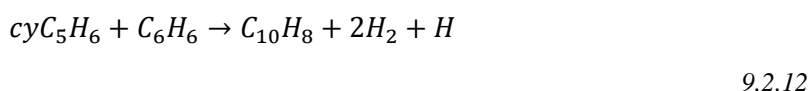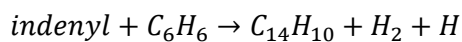
$$cyC_5H_6 + C_6H_6 \rightarrow C_{10}H_8 + 2H_2 + H$$

$$\text{9.2.12}$$

$$indenyl + C_6H_6 \rightarrow C_{14}H_{10} + H_2 + H$$

Moreover, the variation of number of moles with time can be explained through soot formation, as shown in the plots:

Figure 9.2.3   Variation in number of moles for polytropic profile of BIN1 to BIN10 in the surrogate diesel fuel
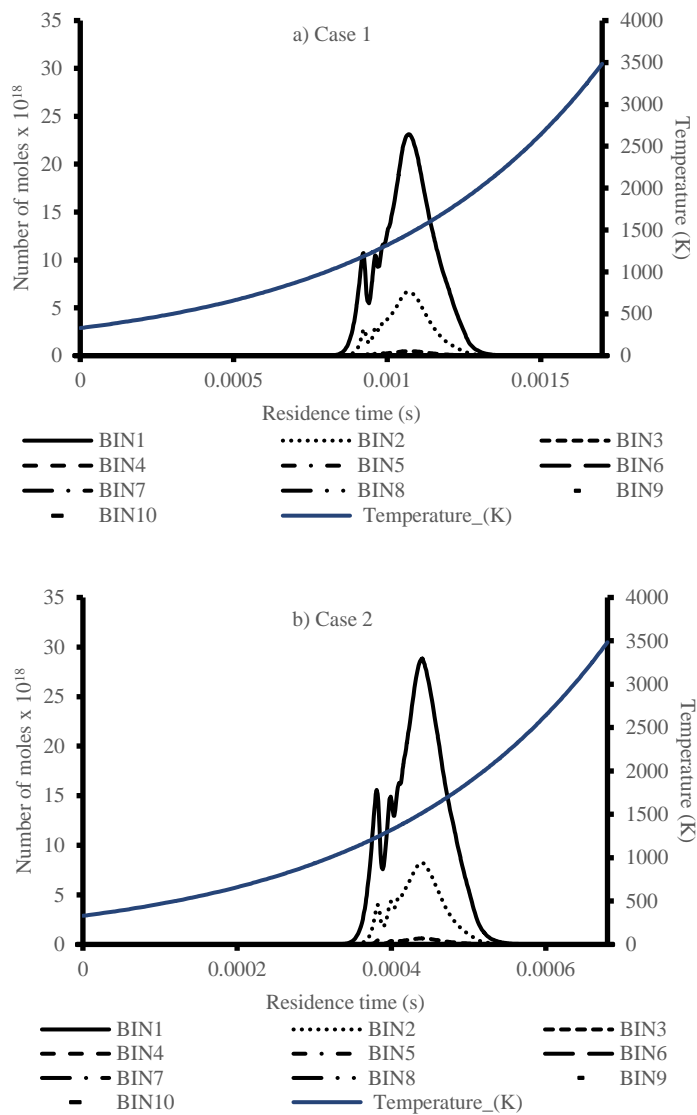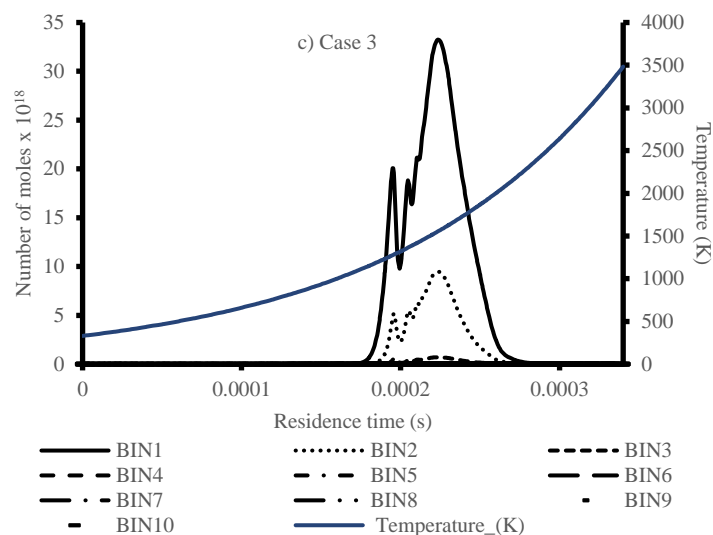
Each BINs shown in Figure 9.2.3 represents the sum of the sub-categories A, B, C (See Sec.8.1). As it can be seen, the higher the BIN size, the lower the number of moles becomes, which is why only the first ten BIN classes are plotted.

It can be observed in Figure 9.2.3 that the BIN mole magnitude decreases as the BIN class increases. For all three cases, it is illustrated how the population of BINs starts increasing at a temperature of ~1150K, coinciding with the decaying of paraffins and naphthenes, until reaching a first peak at a temperature of ~1250K, coinciding with the formation of aromatics, and then a second higher peak at ~1500K, coinciding with the peak of population of the aromatics, after which it decays at the same rate as the aromatics. The affinity with the results in Figure 9.2.2 shows how the reactions of the major species affect soot formation.

From the reaction path analysis, similar results to Sec.9.1.1 are obtained. It can be seen how the small BINs are formed as a result of PAH reactions, in particular for BIN1 and BIN2, while larger BINs are formed from the reactions between BINs. The key precursors in the formation of BIN1 were found to be biphenyl and indenyl radicals when reacting with species such as benzene, indene, phenanthrene and anthracene, which were constantly present in the surrogate diesel as shown in Figure 9.2.2. The first peak was a result of indenyl radical reaction, such as:

$$indenyl + indene \rightarrow 0.143 C_{16}H_{10} + 0.786 BIN1a + H \qquad 9.2.13$$
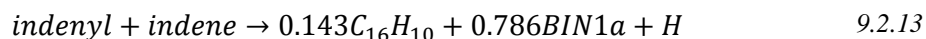
This is even more emphasised when an increase in aromatics population occurs, leading to the second larger peak as result of reactions such as with the biphenyl radical:
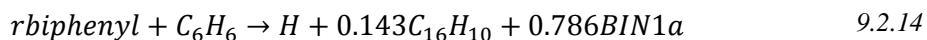
$$rbiphenyl + C_6H_6 \rightarrow H + 0.143C_{16}H_{10} + 0.786BIN1a \qquad \textit{9.2.14}$$

Larger BIN sizes were obtained from the coalescence/aggregation of smaller BIN species, as explained in Sec.8.1. A shift in peak population towards greater residence time as visible between BIN1, BIN2 and BIN3 in Figure 9.2.3 can be therefore explained due to competing formation and coalescence/aggregation reactions. As BIN1 and BIN2 are formed by PAHs, at the same time they are aggregating to form BIN3 and so on, causing a time delay and a reduction in number of moles peak each time.

Furthermore, it can be noticed by comparison of the three different cases in Figure 9.2.3 that the second larger peak of number of moles is at its lowest for case 1 and at its highest for case 3, which counteracts with what was found in Figure 9.2.2 where the peak of aromatics number of moles was at its lowest for case 3 and at its highest for case 1. In case 1, the paraffinic reactions have more time to spend in aromatic formation, whilst in case 3 that amount of time is decreased, accentuating instead the formation of BINs in the region between ~1150K and ~1500K.

9.2.2   Simulation with air

The same analysis was then extended to oxygen addition to the bubble pyrolitic reaction type described previously. Table 9.1.3 shows the revised surrogate diesel fuel composition with the addition of 0.5% air (21%O_2 and 79%N_2). It was assumed once again that the components inside the bubble were a homogeneous gas-phase mixture of the species in Table 9.1.3.

This simulation ran using also Table 9.2.1 polytropic temperature and pressure profiles. It was possible therefore to observe the variation in number of moles for the major species in Figure 9.2.4.

Figure 9.2.4   Variation in number of moles for polytropiv profile of major components in the surrogate diesel fuel with 0.5% air addition
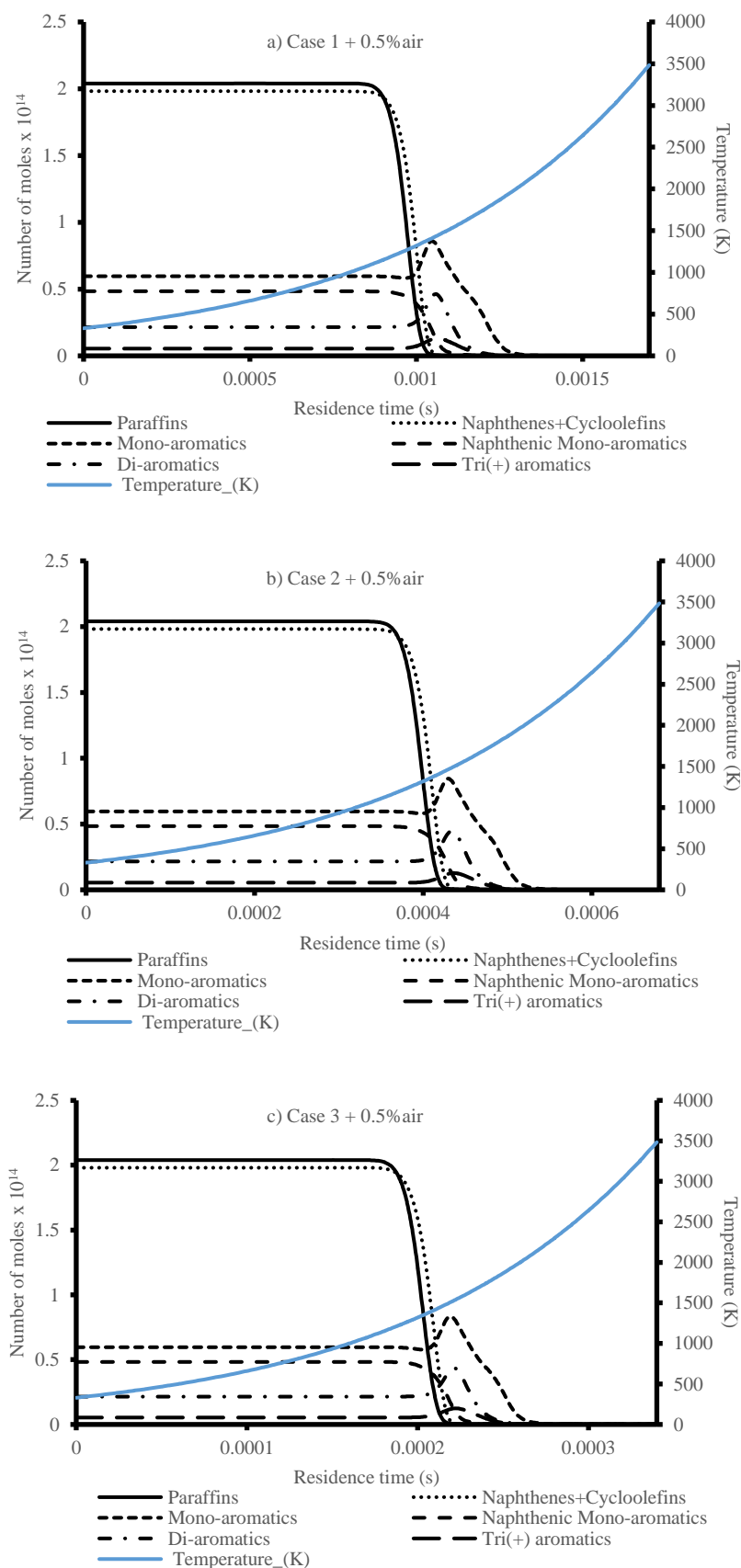
The plots in Figure 9.2.4 show no evident difference compared to the plots in Figure 9.2.2 with no air addition.

To better understand the influence of air to the major species comprising the surrogate diesel fuel, plots showing the change in number of moles of oxygen (O_2) and of nitrogen (N_2) are presented in Figure 9.2.5 for all the polytropic temperature and pressure profile cases:

Figure 9.2.5   *Variation in number of moles for polytropic profile of oxygen and nitrogen in the surrogate diesel fuel with 0.5% air addition*

c) Case 3 + 0.5%air
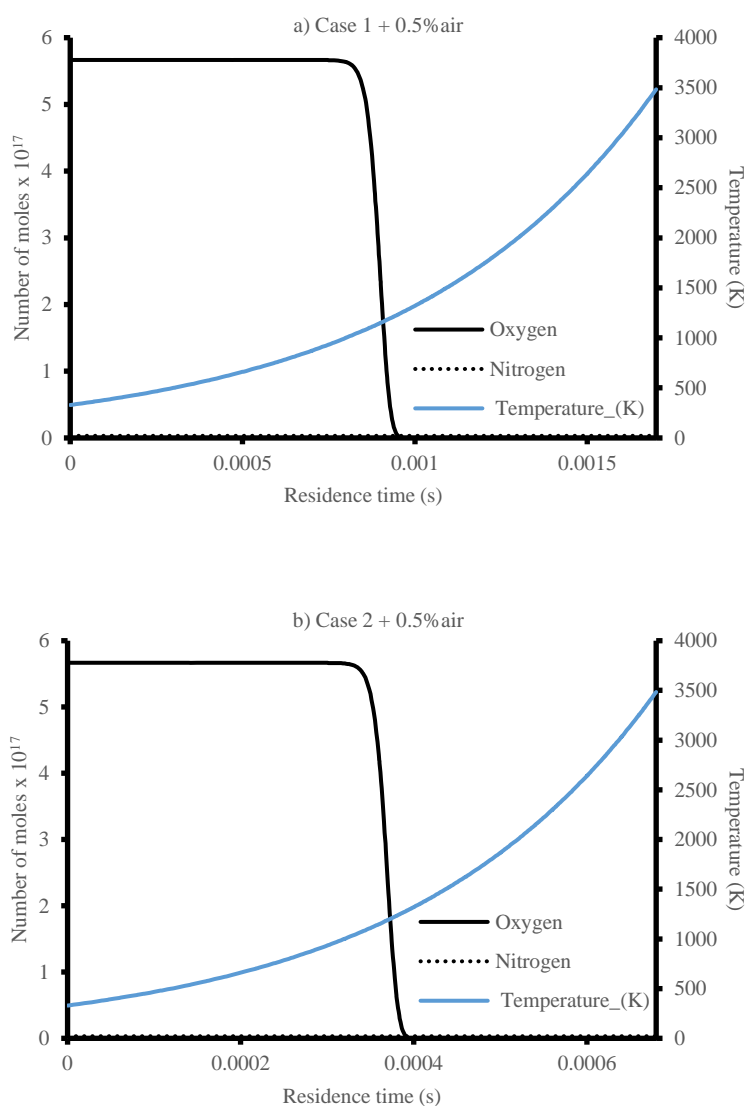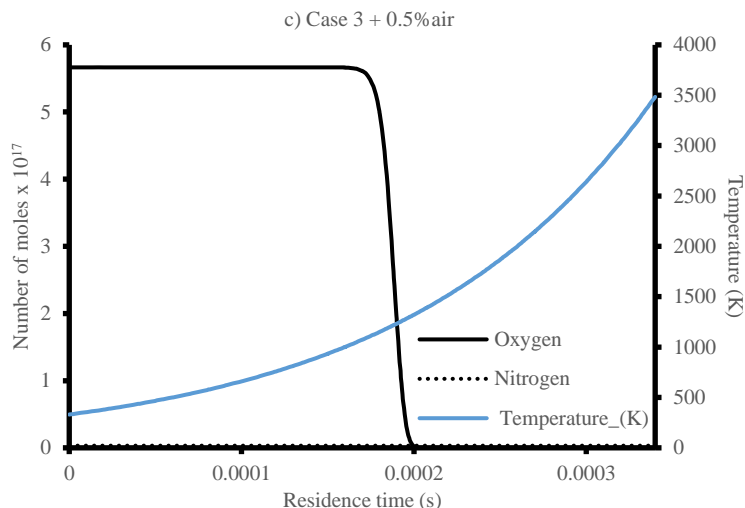
Oxygen population behaves in the same way as the paraffinic, naphthenes and naphthenic mono-aromatics by decaying at ~1150K temperature for all three cases at even a faster rate. From the reaction path analysis the same conclusions were found as in Sec.9.1.2. Oxygen is reacting with paraffins, naphthenes and indene to form hydroperoxyl radical (HO_2) and the radical of the major species. The hydroperoxyl radical would then go and react with other radicals, to form in the end hydroxyl radicals (OH). The hydroxyl radical in turn reacts with BINs obtained previously from naphthenic mono-aromatics and aromatics (See 9.2.1), causing an oxidation process that even though it reduces the number of moles of the BIN, it produces other radicals that affect the formation of soot particles.

Figure 9.2.6   Variation in number of moles for polytropic profile of BIN1 to BIN10 in the surrogate diesel fuel with 0.5% air addition

a) Case 1 + 0.5%air

b) Case 2 + 0.5%air

c) Case 3 + 0.5%air
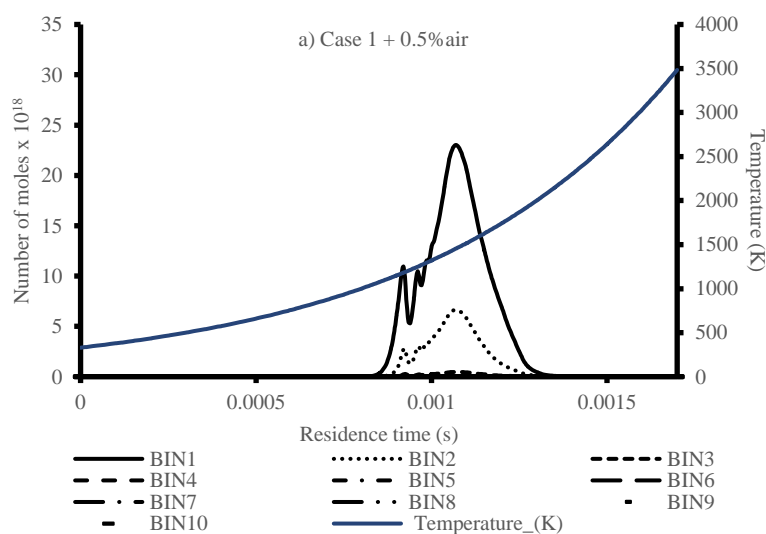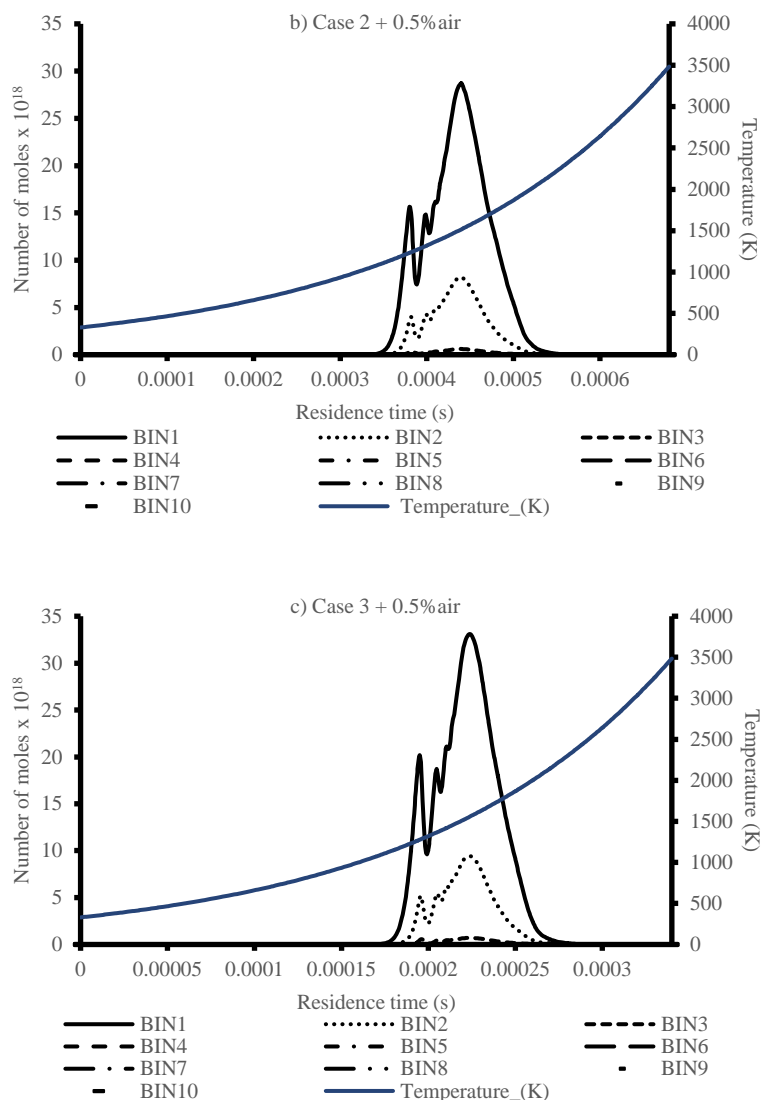
Comparing Figure 9.2.6 with Figure 9.2.3 (without air addition), no significant variation in number of moles are identified. This leads to the conclusion that despite the introduction of 0.5%, the main precursors of soot formation remain the ones mentioned in Sec.9.2.1 for the polytropic temperature and pressure profiles. The variation noticed in the isotropic case occurred at 2273K – 1bar (See Figure 9.1.5d) where the BIN formation was delayed due to the oxidation. In Figure 9.2.6, at 2273K the BINs have already decayed. It can be concluded that the oxidation effect on soot formation is also dependant on the temperature and pressure conditions.

9.3 Discussion arising from simulations

By utilising the new comprehensive soot mechanism explained in Sec.8.1, it was possible to analyse the cavitating bubble collapse reactions occurring in a surrogate diesel fuel. Adding the paraffinic

mechanisms responsible for PAH formation, it was possible to include in the simulation the effect of all the major components in a diesel fuel.

From the isotropic and polytropic simulations explained in Sec.9.2, it was possible to highlight the main precursors of soot formation:

- N-paraffins and naphthenes+cycloolefins would decay with time to form large radicals, such as $nC_{16}H_{33}$ or smaller alkyl radicals, such as CH_3. These would then react with aromatics to form PAHs

- Naphthenic mono-aromatics, such as *indene*, were found in most reactions to decay forming radicals, such as *indenyl*, which also would react with aromatics to form PAHs

- Aromatics, such as *biphenyl*, were reacting with other aromatics to form PAHs

The isotropic profile was useful in order to understand in particular how BINs are formed. It was found at high temperatures that smaller BINs would form, as a consequence of the paraffinic and aromatic reactions, and then decay to allow gradually coalescense/aggregation into larger BINs.

The polytropic profile, resembling the most to the bubble collapse due to cavitation, showed the temperature and pressure dependence in the pyrolytic type reactions. It was found that paraffinic and aromatic reactions would occur in the temperature region of ~1150K to ~1500K, reflected also in the BIN formation, regardless of the speed of temperature increase with residence time.

A primary pyrolysis of the surrogate diesel fuel set of reactions are therefore responsible of formation of precursors which will effect a secondary pyrolysis set of reactions, responsible of soot formation. By analysing different temperature increase rates, it was noticed that the effective time for primary pyrolysis is much shorter when temperature is increasing rapidly. This resulted in an accentuation of BIN formation due to secondary pyrolysis involving all the aromatics not involved in primary pyrolysis.

The effect of air inclusion of 0.5% in the surrogate diesel showed from reaction path analyses that oxygen reacts with n-paraffins and naphthenes+cycloolefins to form OH radicals and other radicals which react with aromatics. Hydroxyl radicals are then responsible in oxidisation processes, in which BIN sizes are reduced.

Chapter 10 Conclusions and Further Work

Three sets of experiments were carried out on models of the two-stage pressure mechanism of the return valve in modern diesel injectors. The first experiment consisted in characterising the flow of different fuel mixtures across two variations of acrylic models of the return system and one variation of fused silica model. A customised mechanical flow low-pressure test rig was utilised in order to vary upstream and downstream pressure conditions across the models and track incipient cavitation conditions. The second experiment consisted in subjecting diesel fuel in the fused silica model to sustained hydrodynamic cavitation by means of a high-pressure recirculating rig. A spectral extinction measurement and ultraviolet-visible spectroscopy analyses were carried out in order to track the variation of composition of diesel fuel with cavitating time. The third experiment consisted in characterising the fluorescence phenomenon experienced in the fused silica model while running in the high-pressure recirculating rig. A spectral analysis was carried out to understand the properties of the diesel fuel under fluorescent conditions. A final part of the project was dedicated on creating a new comprehensive soot mechanism allowing to simulate surrogate diesel fuel in a cavitating bubble collapse situation scenario.

The novelties of this research project can therefore be listed as follows:

- Manufacturing of optically accessible real-sized spill valve models in acrylic and fused silica;

- High-speed imaging of the internal flow occurring in outlet throttle of spill valve;

- Spectral attenuation and UV-Vis spectrum analyses of diesel fuel across the spill valve for pressures up to 300bar;

- Fluorescence phenomenon occurring in outlet throttle at high pressure;

- Development of a comprehensive soot formation chemical model including paraffins mechanisms of PAH formation.

This chapter will focus on highlighting the key findings of this project. In particular Sec.10.1 will list the results from the characterisation of the flow carried out in the first experiment; Sec.10.2 will list the

results from the sustained hydrodynamic cavitation carried out in the second experiment and the results from the fluorescence phenomenon carried out in the third experiment; Sec.10.3 will summarise the innovations of the new kinetic modelling mechanism; finally Sec.10.4 will suggest recommendations of future work in this particular field.

10.1 Characterisation of fuel in two-stage pressure mechanism of the return valve in modern diesel injectors

Variations in the geometrical features of the acrylic and fused silica replicas of the two-state pressure mechanism of the return valve in modern diesel injector allowed to visualise some important features of the flow across this section of the injector. The two acrylic models differed in the outlet throttle diameter, one with Ø225μm and the other with Ø245μm. The three fuel mixtures consisted in a paraffinic model diesel and two fuel mixtures of n-hexadecane and n-octane in 95:5 v/v and 80:20 v/v proportions. A list of the key findings are provided as follows:

- Cavitation onset was observed to begin at the entrance to the outlet throttle, independently of fuel type, geometry variation and cavitation number;

- Cavitation onset was observed to depend on factors such as fuel type, cavitation number, saturated vapour pressure, and needle lift. Cavitation inception in the paraffinic model diesel occurred at the largest cavitation numbers and smallest saturated vapour pressures. This was followed by the 95:5 v/v n-hexadecane and n-octane mixture, and then followed in turn by the 80:20 v/v n-hexadecane and n-octane mixture;

- The needle also played an important role in cavitation inception. It was observed that larger pressure ratios were required to produce cavitation inception for lower needle lift. This occurs because the low needle lift produces a pressure gradient in the annulus around the needle, reducing the pressure gradient developing across the nozzles. Hence a larger pressure difference across the nozzles is required to produce cavitation inception. This effect was confirmed also in the fused silica model assembly, having a more refined needle step increment, where pressure ratios were analysed for low needle lifts exclusively;

- Geometrical variations to the two-pressure stage mechanism showed that by increasing the outlet to inlet throttle diameter ratio also increased the upstream-to-downstream pressure ratio required for incipient cavitation. This occurs because a larger pressure gradient is produced at the needle sealing position when increasing the outlet throttle. Despite varying the inlet throttle from being perpendicular to the outlet throttle to being in-line in the fused silica model, the same occurrence would persist;

- An estimation of the intermediate pressure showed its relation to needle lift and geometrical variations. In particular, the greater the needle lift is, the greater the intermediate pressure will be. On the other hand, the greater the outlet diameter is, the lower the intermediate pressure will be for incipient cavitation to occur;

- The design of modern return valve diesel injector systems allows cavitation only to occur in the outlet throttle, whilst the inlet throttle and valve control chamber never experience cavitation. This occurs to avoid disturbances to the needle injector while injection is underway.

10.2 Effects of hydrodynamic cavitation flow in two-stage pressure mechanism of the return valve in modern diesel injectors

High pressure recirculation tests were carried out in the fused silica model of the two-state pressure mechanism of the return valve in modern diesel injector. The two fuels consisted in a new conventional base diesel fuel and a fuel mixture of the new conventional base diesel fuel and previously cavitated conventional base diesel fuel in 62:38 v/v proportions. Long duration tests allowed the model to be subjected to sustained hydrodynamic cavitation. A list of the key findings are provided as follows:

- The fuel mixture showed chemical changes occurring with time, where consumption and formation of chromophores were detected using the extinction measurement system. The spectral analysis of the fuel samples showed an increase in broadband absorbance at a slow rate, meaning a formation of PAH and particulates was underway. Particulates pre-existing in the cavitated fuel mixture were subjected therefore to more chemical reactions even at 200bar upstream pressures;

- By comparison, the fresh conventional base diesel fuel batch showed no particular variation in spectral attenuation, independently by the 200bar and 300bar pressures. Results from the UV-Vis analyses were not conclusive due to incorrect dilution ratios. Despite chemical reactions occurring due to cavitation, as proved with the fuel mixture, the pressures are thought to be too low to initiate soot formation. This is proved also by the colouring of the diesel samples, which remained unvaried throughout the experiment;

- At high pressures, the cavitating region in the outlet throttle of the model showed a fluorescent phenomenon, where the glowing resembled a flame. It is thought that the occurrence was a consequence of electroluminescence. At high pressures in fact the gases in the cavitated flow are ionised turning the flow into plasma. Since the model was not earthed, this resulted in the glowing effect. A spectral analysis confirmed the presence of CH and H_2 molecules, causing the resemblance to a flame.

10.3   Kinetic modelling of surrogate diesel fuel

A new comprehensive soot mechanism was created by merging three different mechanisms, two of which corresponding to paraffins pyrolysis mechanisms forming PAH while the other corresponding to soot formation mechanisms. After combining and modifying the final mechanism (2438 species and 23413 reactions) to create a unique naming convention for species dataset with no duplicate reactions, it was then validated against previous experimental and computational work. Two applications of the new robust mechanism were also presented in order to simulate cavitating bubble collapse effect on soot formation for a surrogate diesel fuel, one with an isotropic temperature and pressure profile, and one with a polytropic temperature and pressure profile. A list of the key findings are provided as follows:

- The validation of the new comprehensive soot formation mechanism, consisting in auto-ignition delay time simulation and in BSS flame simulation, showed a good agreement with literature result. Despite being a robust mechanism, which requires more computational time, the inclusion of paraffinic pyrolysis reactions are thought to be important in simulations of cavitating bubble collapse;

- From the simulation examples, n-paraffins proved to initiate reactions responsible of increasing the amount of aromatics, which lead to PAH and soot formation;

- The isotropic profile shows that reactions with a constant temperature and pressure lead to soot formation. For temperatures in the 2000K region, PAHs are constantly formed and destroyed to allow greater particles and aggregates to form;

- The polytropic profile shows that by accelerating the temperature increase in shorter intervals of time would result in a greater amount of soot formation. Hence the paraffins play a crucial role, since the more time they have to decompose in forming aromatics, the less soot particle population will be generated;

- Addition of air in the simulation showed that oxygen contributes in soot particle formation by reacting with n-paraffins and naphthenes. On the other hand, oxygen also delays the formation of particulates due to oxidation.

10.4 Recommendations for future work

A few recommendations can be listed as proposal for future work in the two-stage pressure mechanism of return valve in modern diesel injectors:

- Using a silicon mould it could be possible to regenerate the exact geometry of the return valve system in modern DIE. The next challenge would be to find a way of manufacturing transparent materials with this geometry;

- To understand the sustained hydrodynamic cavitation relation with soot formation in this system, it would be necessary to increase pressures to the order of 1600bar and beyond. Therefore, a real modern return valve could be set up in the high pressure recirculation test rig to run this experiment;

- Further investigation of the stepping in the outlet throttle could be studied and its relation with cavitation inception;

- A pressure transducer could be utilised to calculate the pressure in the intermediate valve control chamber. This would allow to investigate the relationship between upstream, intermediate and downstream pressures for incipient cavitation;

- Different fuels could be tested in the high pressure recirculation rig, to observe the soot formation difference occurring when varying fuel chemical composition from the spectral analysis;

- Dilution techniques could be improved for the new conventional diesel fuel in order to investigate better bandwidths at which the spectrometer was not able to provide results;

- Simulations using the new comprehensive soot mechanism could be applied to experimental work. For example, since the fuel recirculates in the high pressure test rig, the simulation could take into account the variation of chemical properties at every cycle and embed it to the bubble collapse replication.

- A gas chromatography analysis of the diesel samples after cavitation could be a useful source to detecting the percentage of the different components. This result could then be compared with the soot formation mechanism for validation.

Appendix A

A.1   Priming of low pressure test rig

TANK A TO TANK B PRIMING

1. Set valve 1 to LP, valve 2 to A and valve 3 to B

2. Check that tank relief A and cap fully closed

3. Priming nitrogen bottle low pressure

4. Open tank A gauge valve (below on tank A side) followed by priming gauge valve (above on tank B side)

5. Open three cylinder valves

6. Watch the transparent exit tubes on bottles 1, 2, 3. When cylinder 1 is filled, fuel will flow out of the tube, hence close the valve. For each of the bottles being filled (notified by fuel going out to receiving bottles) close respectively valve 2 and 3.

7. Close priming gauge valve and tank valve A

8. Set pressure in nitrogen bottle back to ambient

9. Relief the pressure in tank A through the relief valve followed by relief of tank cap

10. Set valve 1 to HP

11. Set nitrogen bottle to desired pressure (this case 5 bar)

12. Check desired pressure is correct on rig pressure gauge

13. Check tank B cap and relief valve are opened

14. Open main high pressure discharge valve (above on tank A side) to discharge high pressure fuel

15. Wait for gas to exit tank B cap before closing discharge valve

16. Turn nitrogen bottle back to ambient

17. Close the valves and depressurise the fuel tanks

TANK B TO TANK A PRIMING

1. Set valve 1 to LP, valve 2 to B and valve 3 to A

2. Check that tank relief B and cap fully closed

3. Priming nitrogen bottle low pressure

4. Open tank B gauge valve (below on tank B side) followed by priming gauge valve (above on tank B side)

5. Open three cylinder valves

6. Watch the transparent exit tubes on bottles 1, 2, 3. When cylinder 1 is filled, fuel will flow out of the tube, hence close the valve. For each of the bottles being filled (notified by fuel going out to receiving bottles) close respectively valve 2 and 3.

7. Close priming gauge valve and tank valve B

8. Set pressure in nitrogen bottle back to ambient

9. Relief the pressure in tank B through the relief valve followed by relief of tank cap

10. Set valve 1 to HP

11. Set nitrogen bottle to desired pressure (this case 5 bar)

12. Check desired pressure is correct on rig pressure gauge

13. Check tank A cap and relief valve are opened

14. Open main high pressure discharge valve (above on tank A side) to discharge high pressure fuel

15. Wait for gas to exit tank A cap before closing discharge valve

16. Turn nitrogen bottle back to ambient
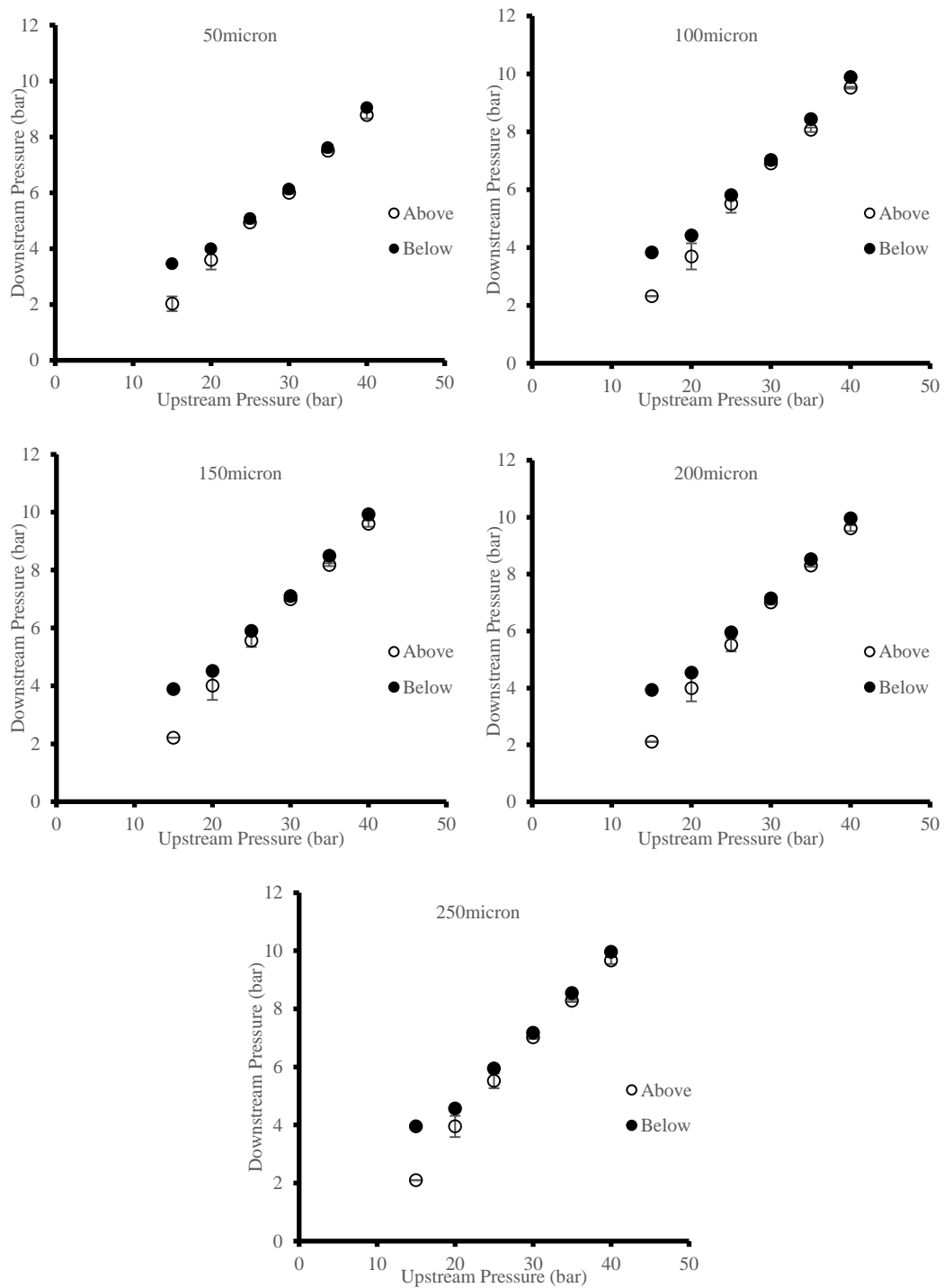
17. Close the valves and depressurise the fuel tank

Appendix B

B.1   Results Low Pressure Test Rig – Paraffin Model Diesel Acrylic

Model Version 1

B.2 Results Low Pressure Test Rig – Mixture 1 (80% C_{16}, 20% C_8)

Acrylic Model Version 1

B.3 Results Low Pressure Test Rig – Mixture 2 (95% C16, 5% C8)

Acrylic Model Version 1

B.4 Results Low Pressure Test Rig – Comparison of all three fuels in Acrylic Model Version 1

B.5 Results Low Pressure Test Rig – Incipient Cavitation Number of all three fuels in Acrylic Model Version 1
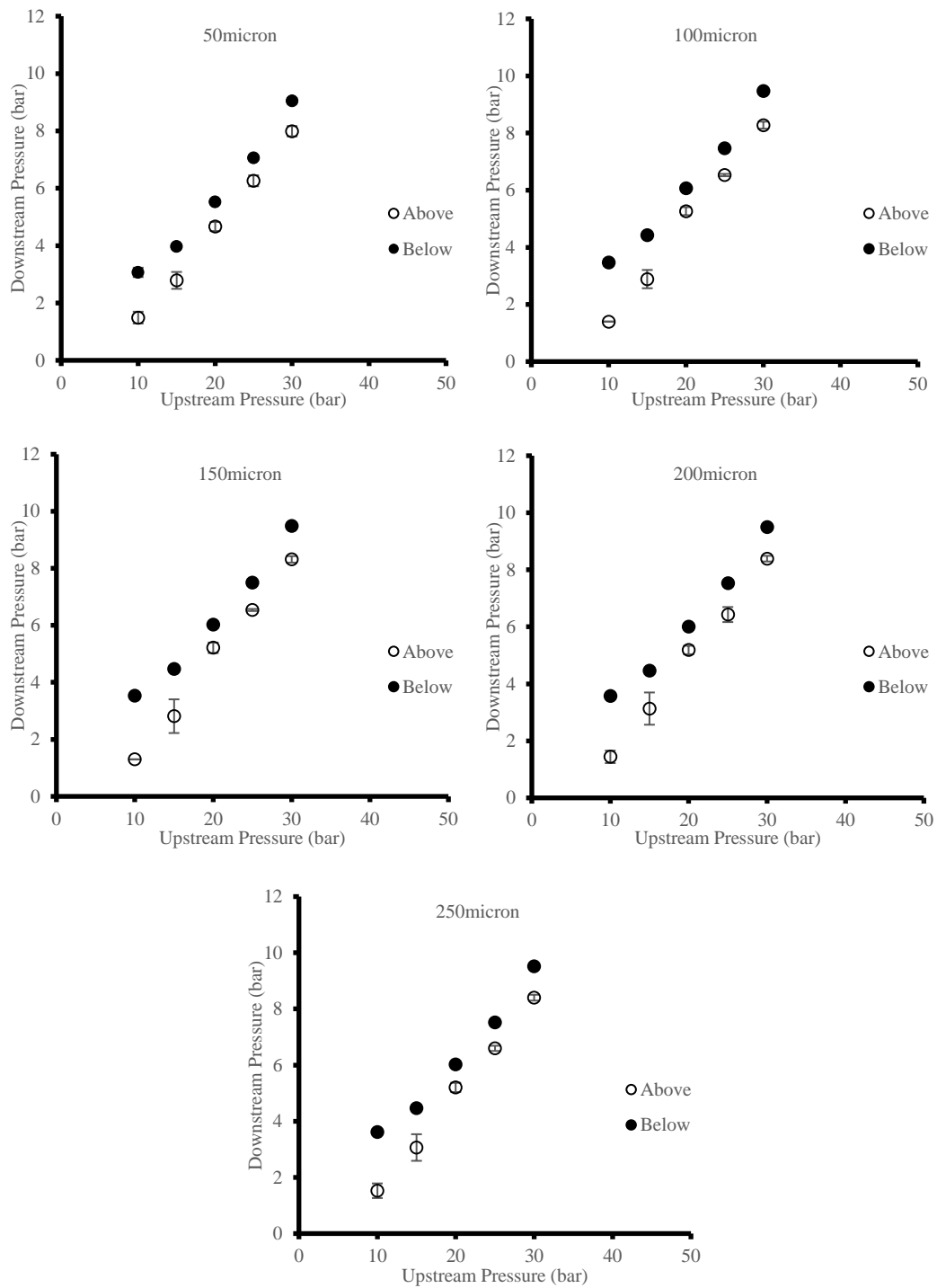
Appendix C

C.1   Results Low Pressure Test Rig – Paraffin Model Diesel Acrylic
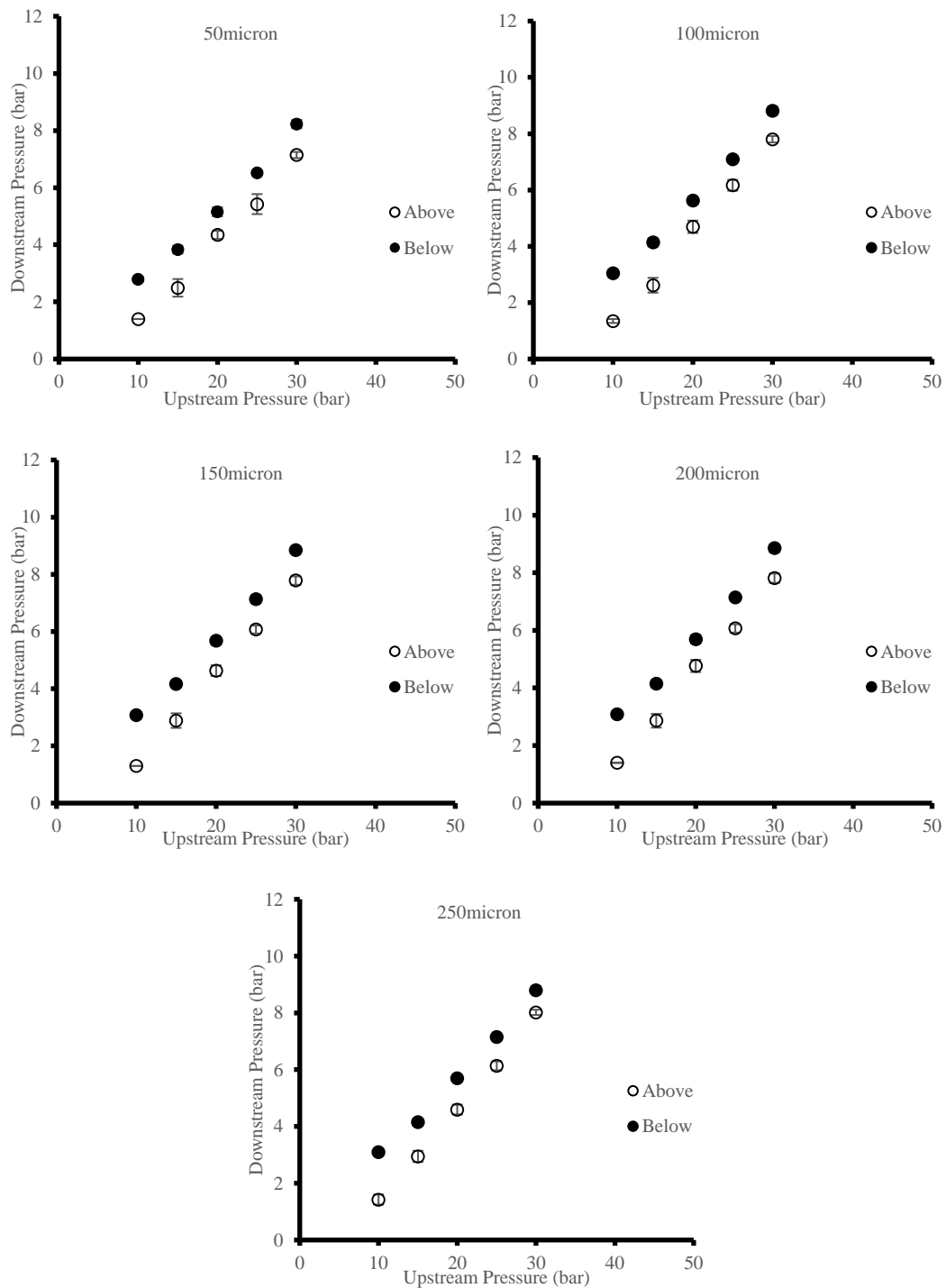
Model Version 2

C.2   Results Low Pressure Test Rig – Mixture 1 (80% C_{16}, 20% C_8)
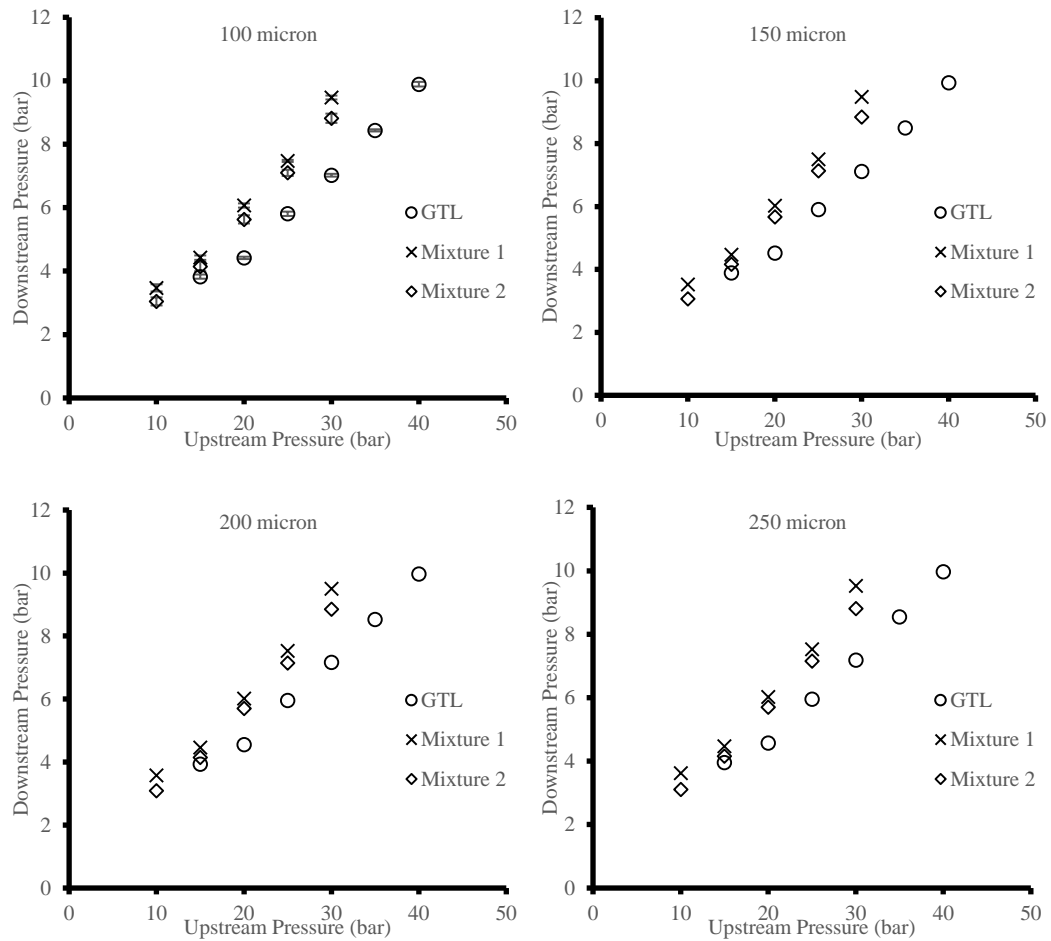
Acrylic Model Version 2

C.3   Results Low Pressure Test Rig – Mixture 2 (95% C16, 5% C8)
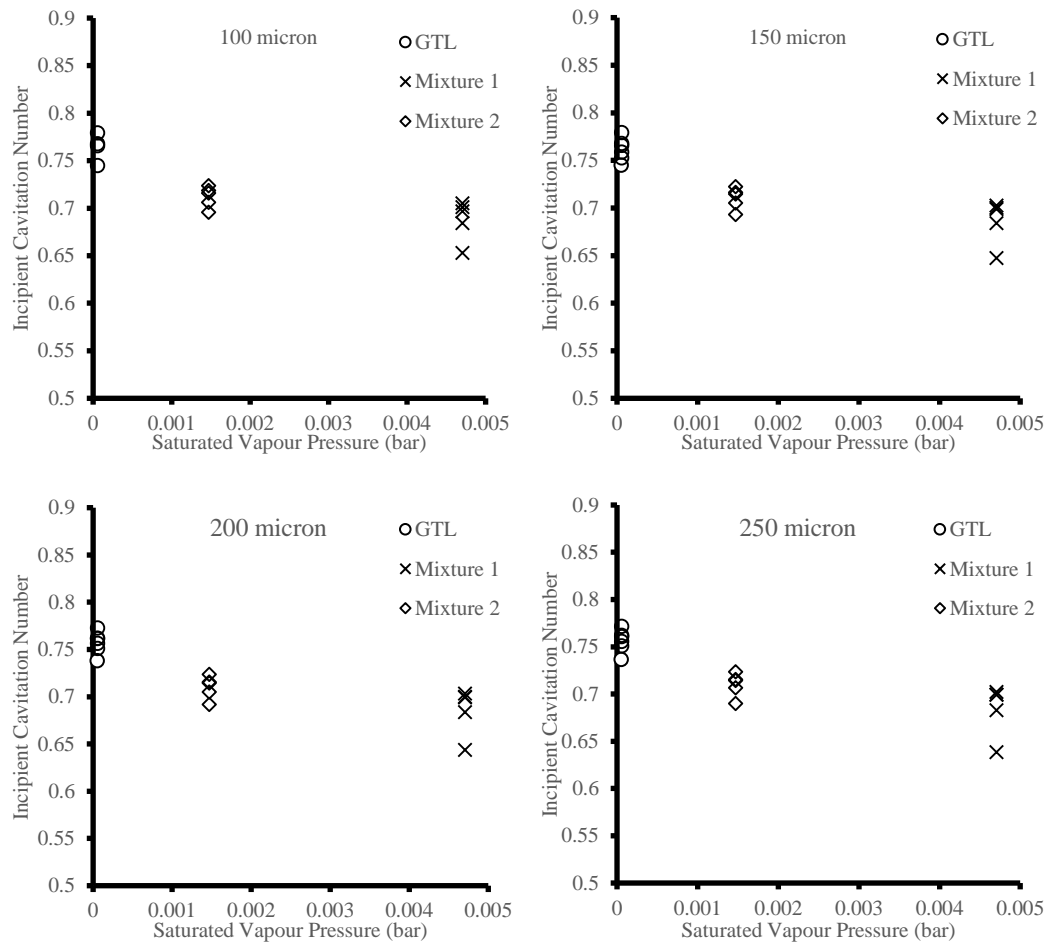
Acrylic Model Version 2
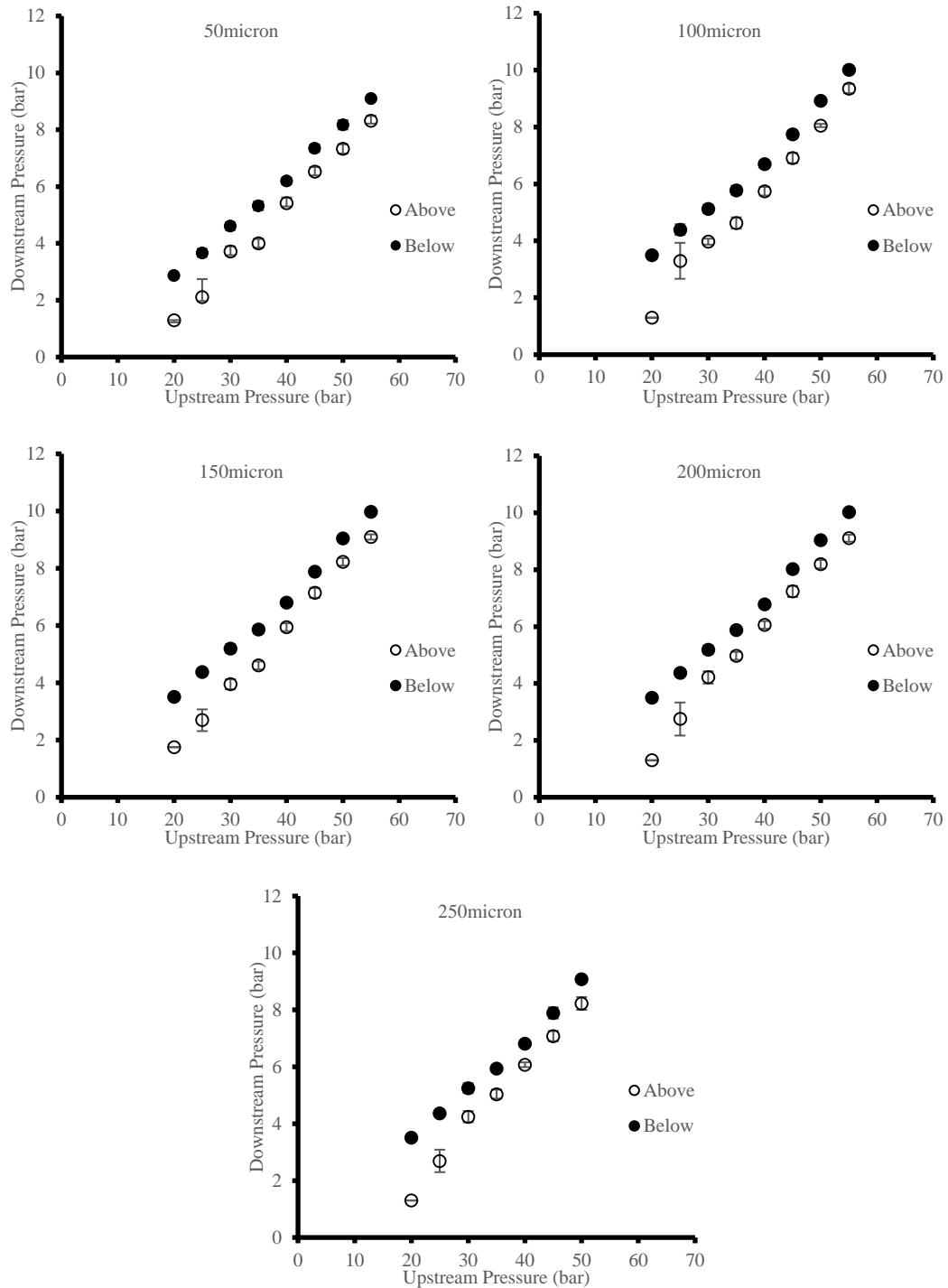
C.4   Results Low Pressure Test Rig – Comparison of all three fuels in

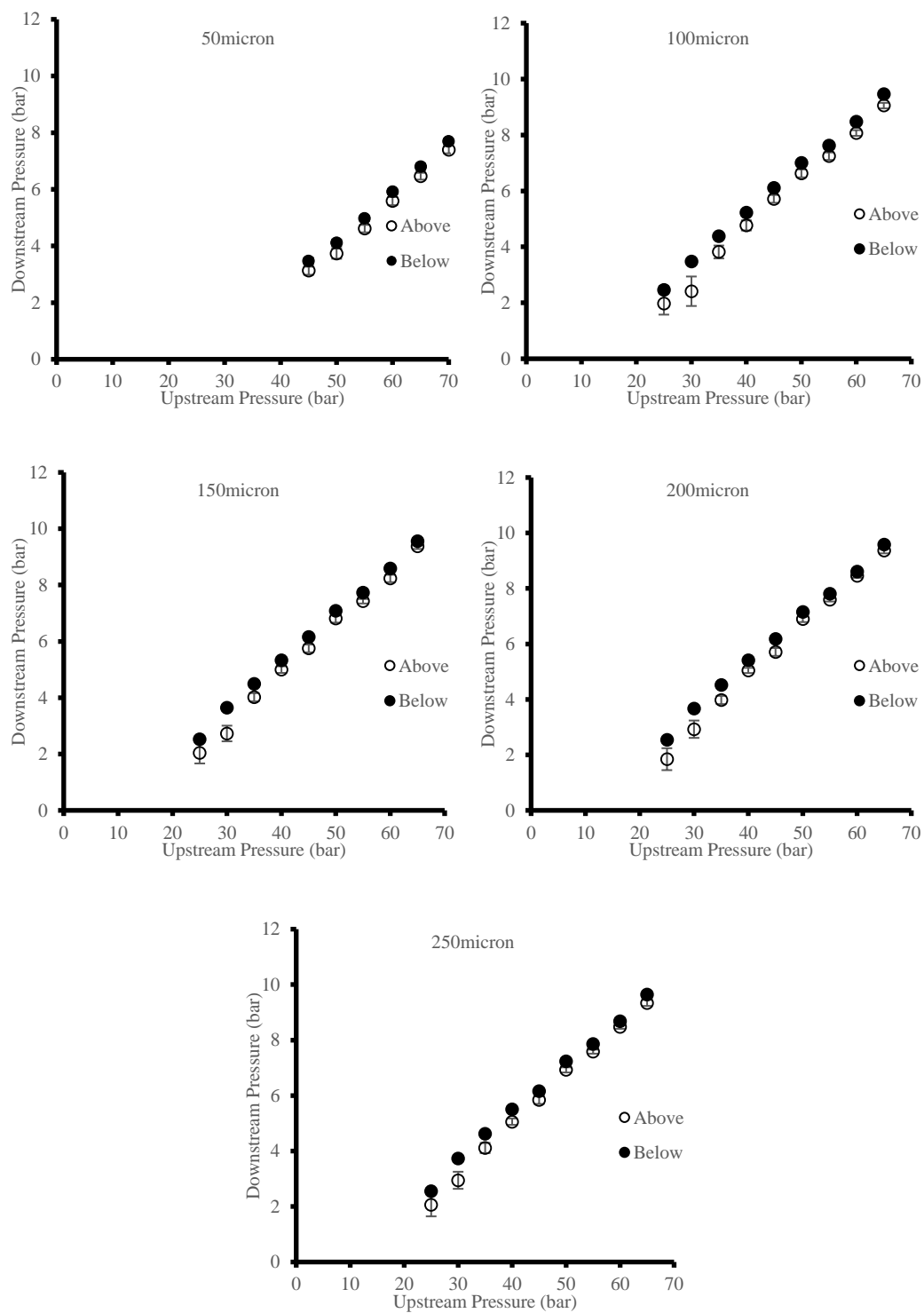## Acrylic Model Version 2

C.5 Results Low Pressure Test Rig – Incipient Cavitation Number of all three fuels in Acrylic Model Version 2
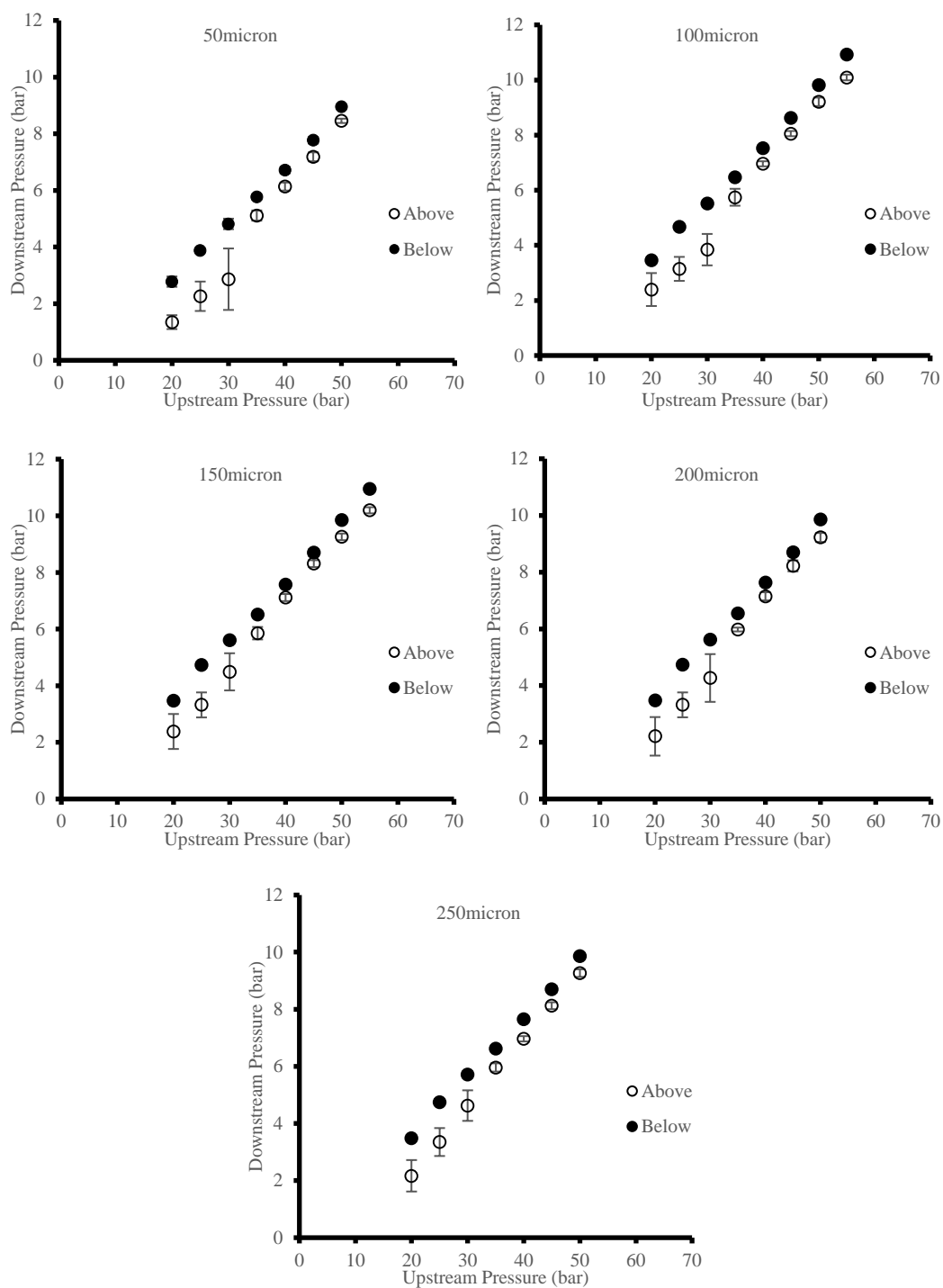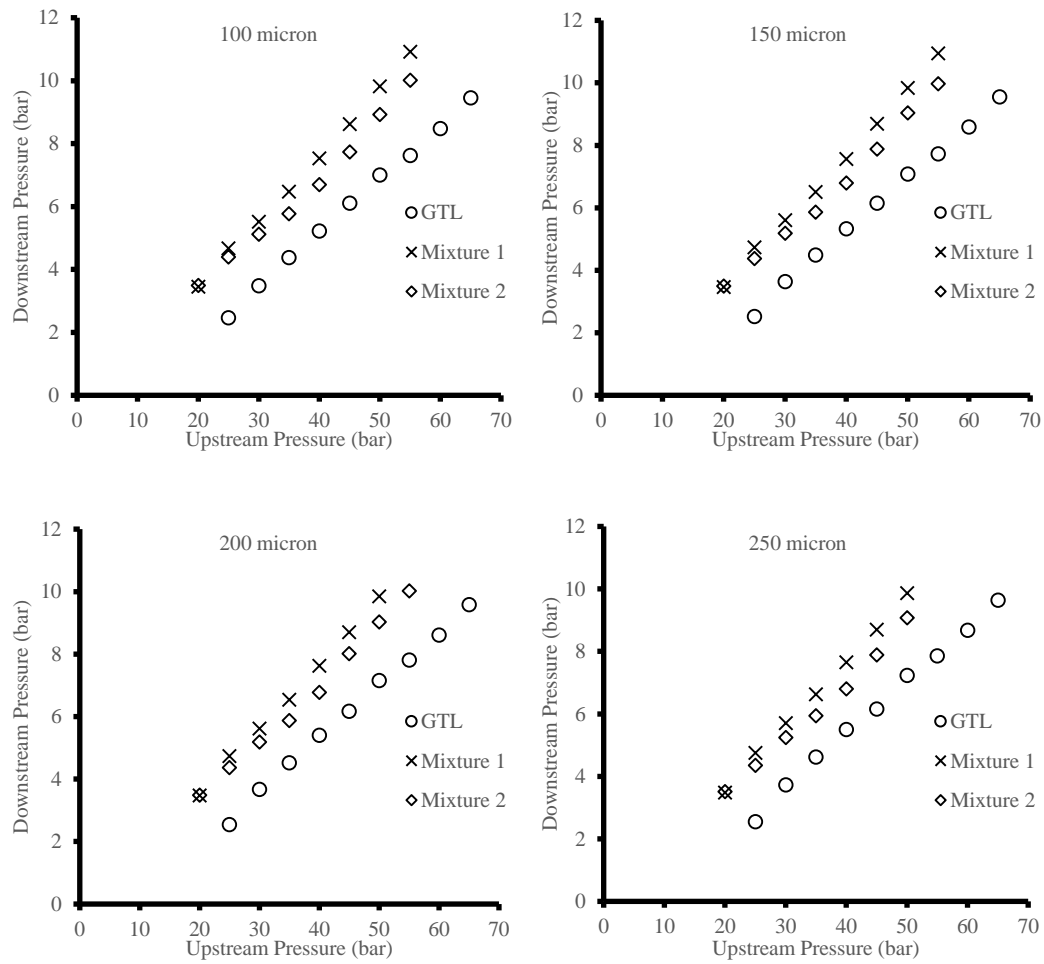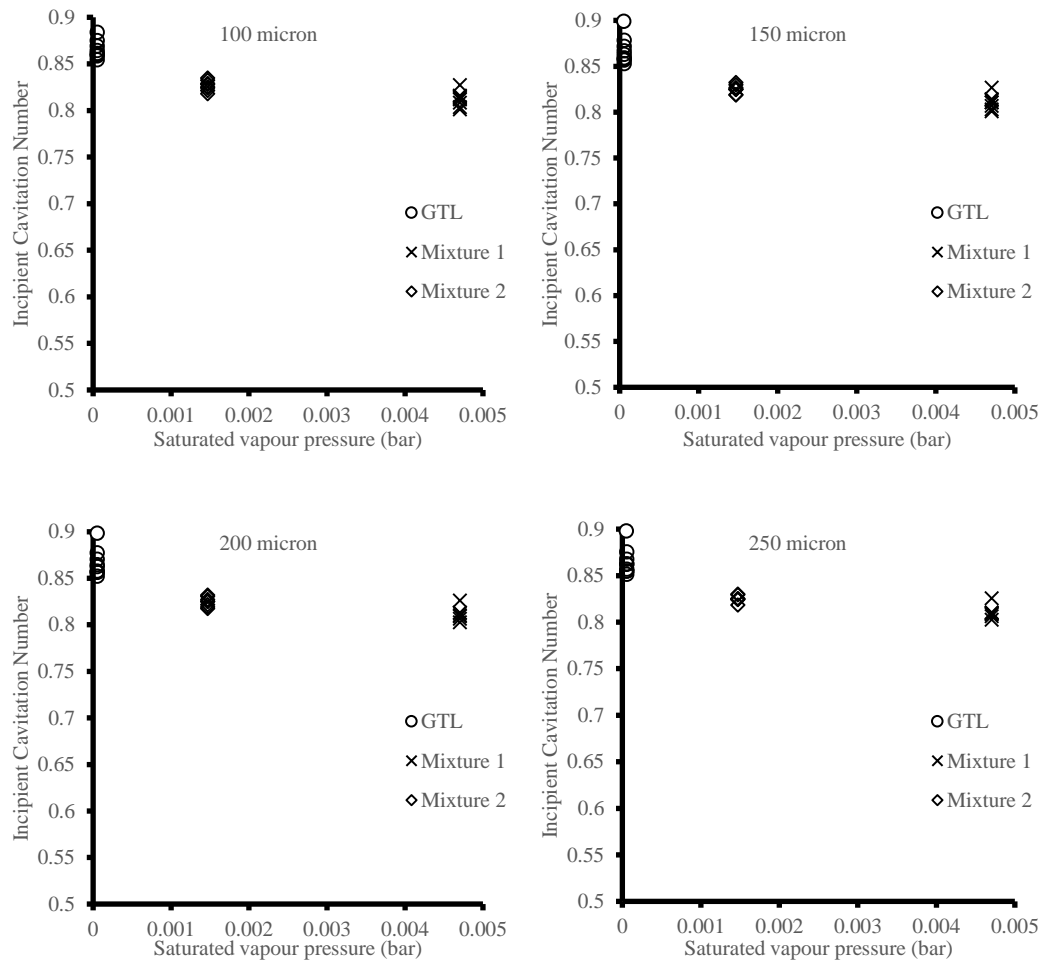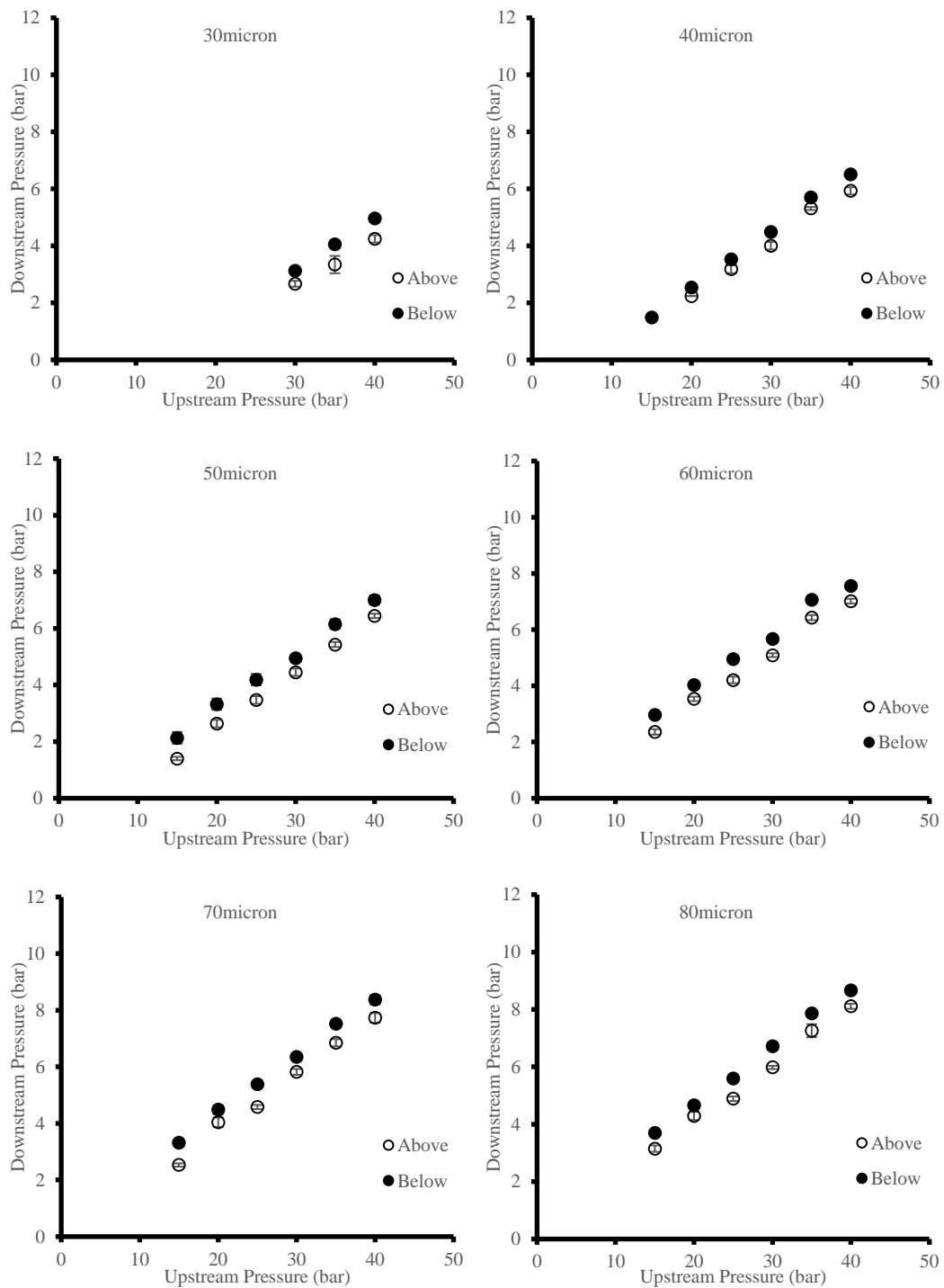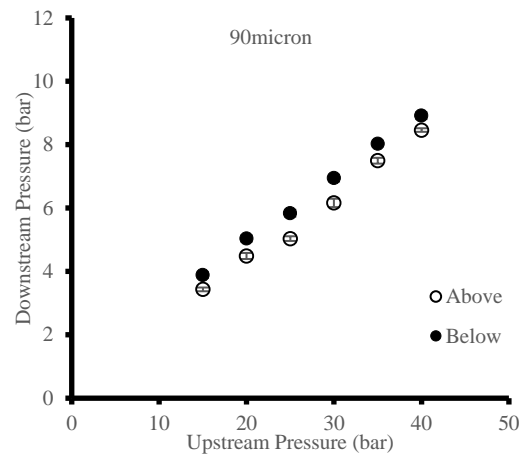
Appendix D

D.1   Results Low Pressure Test Rig – Paraffin Model Diesel Fused Silica Model

90micron

Appendix

Appendix E

E.1   High Pressure Test Rig Draining, Refilling and Flushing Procedure

DRAINING PROCEDURE

1. Make sure all equipment are turned off and mains plug for the test-rig is removed before commencing the draining procedure.

2. Use a suitable beaker/container to catch the drained fuel. It is advisable to use a 500 ml beaker for all drainage points.

3. Valve on the return line to the tank must be opened for draining. It is to be kept closed while the rig is in operation.

4. The test-rig has two drainage valves. 1. Heat Exchanger; 2. Fuel Filter. The test-rig is to be drained in this order as the vertical location of each valve is of importance.

5. Valve 1 is located beneath the heat exchanger (drains approx. 460 mL). Place the beaker on the floor and put the drainage tube in the container before opening the valve. Close the valve once drained.

6. Valve 2 is located under the fuel filter (drains approx. 2050 mL). Place the beaker under the valve and open the valve. The valve will need to be opened/ closed several times during the drain and the beaker will need to be emptied due to the large volume of fuel. Lift the hoses connected to the optical setup to allow fuel-drain from the optical setup.

7. Measure the amount of fuel extracted and compare it to the amount of fuel that was filled.

8. Clean any spills with fuel absorbent paper and absorbent sand (if required) as soon as they occur.

9. Ensure all valves, including the return valve to the tank, are closed properly and the screw in put back in place at the top of the receiver.

REFILLING AND FLUSHING PROCEDURE

1. Before starting the refill procedure, ensure all the drain valves are closed.

2. Measure out the fuel to be refilled into a 1000 mL measuring cylinder.

3. Pour around 2500 mL of the fuel into the fuel tank, check the level marker to ensure the tank is not over-filled.

4. Following the start-up procedure, switch on the feed pump.

5. Valves on the feed and return lines of the optical system can be operated to remove trapped air from the optical setup.

6. Turn on the high-pressure pump and slowly turn the dial to bring the pressure to around 100 bar. Operate the rig at this pressure for 4 - 5 minutes to remove trapped air.

7. In case of flushing the test-rig, ensure there is water supply to the heat exchanger; set the HP pump pressure to around 100 bar and maintain at this level for another 45 – 60 minutes.

8. At the end of the refilling or flushing procedures turn the high HP pump dial to stop the electric motor and the pump.

9. Turn the HP pump off using the stop button.

10. Turn the feed-pump off using the stop button.

11. Press the EM stop button to stop the test-rig.

12. Turn the mains power off from the wall socket.

13. Turn the water tap off.

SAFETY PRECAUTIONS

1. Ensure the screw on the receiver is replaced after the draining procedure.

2. The fan should be switched on for cooling the electric unit; ensure the laser is not connected to the socket.

3. Water supply must be open for cooling the fuel.

4. After the flushing duration is over, allow the fuel to cool before commencing the drainage procedure.

E.2 High Pressure Test Rig Operation and Experimental Setup Procedure

START-UP PROCEDURE

1. Turn the fan ON

2. Turn Mains Power ON from the wall

3. Turn chilled-water valve ON and check the water pressure on the pressure gauge

4. Switch ON the test-rig power on the Atex electric-box, let the display settle down to show the temperature reading

5. Check the Emergency Stop button to display the "EM Stop" green light

6. Turn the key to show the blue light

7. Press the low pressure pump start button

8. Press the high pressure pump start button

9. Turn the coarse dial to start the HP pump and gradually increase pressure to the desired value

SHUT-DOWN PROCEDURE

7. Turn the dial to stop the HP pump

8. Turn OFF the HP pump using the stop button

9. Turn OFF the LP pump using the stop button

10. Press the EM stop button to stop the test-rig and switch OFF the power from the Atex electric-box

11. Turn OFF the Mains power

12. Close chilled-water valve

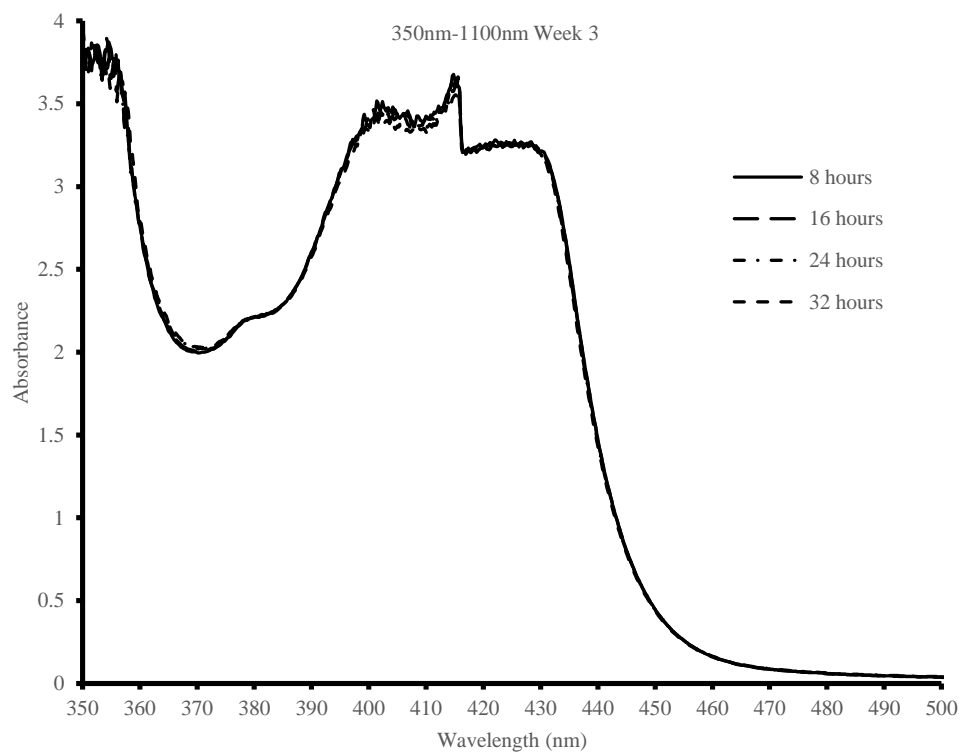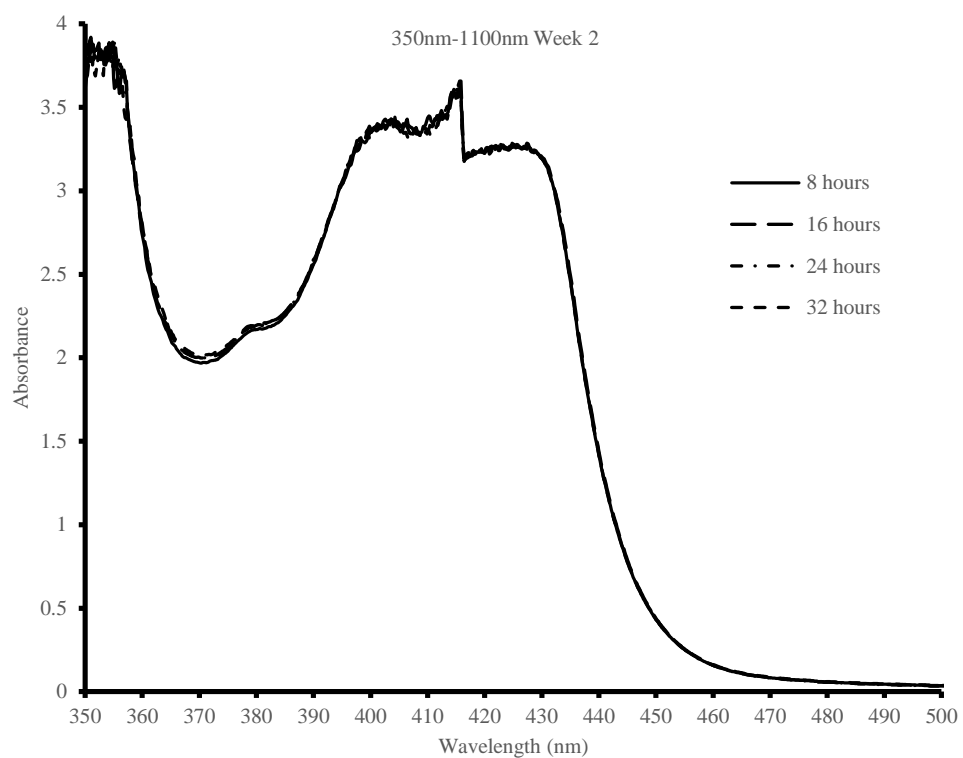## E.3   UV-Visible Absorption Spectrum Sample Preparation and Measurement

1. Use a 4ml cuvette that has been cleaned with n-heptane and dried completely

2. Using a glass syringe (from Socorex Swiss) pour 3ml of the cavitated fuel sample into the cuvette

3. Cap and clean the cuvette with a lint-free paper to remove any dirt or marks

4. Place the cuvette into the Spectrophotometer cell and run the spectra for the wavelength range of 350nm to 500nm at medium scan speed for 3 times (0.2nm steps)

5. To obtain dilution for 240nm-305nm range, use another 4ml cuvette that has been cleaned with n-heptane and dried completely

6. Using a glass syringe (from Socorex Swiss) pour 2.6ml of the diluent n-heptane into the cuvette

7. Using a micro-dispenser (from Drummond) add 5μl of the selected fuel sample to the cuvette (dilution ratio 1:520)

8. Cap the cuvette and agitate to mix the solution well

9. Clean the cuvette with a lint-free paper to remove any dirt or marks

10. Place the cuvette into the Spectrophotometer cell and run the spectra for the wavelength range of 240nm to 305nm at medium scan speed for 3 times (0.1nm steps)

11. Repeat steps 5-10 four times to get the spectra of four diluted samples in the absorption range of 240nm-305nm

12. To obtain dilution for 190nm-405nm range, further dilution of the first diluted sample (dilution ratio 1:520) is required

13. Add 2.6ml of n-heptane in a 4ml clean cuvette

14. Using 100μl and 20μl micro-dispensers add 140μl of the first diluted sample (1:520) into the cuvette (approx.. dilution ratio 1:10000)

15. Cap, clean and place the cuvette in the Spectrophotometer for absorption measurement in the wavelength range of 190nm-405nm. Scan the sample 3 times at fast scan speed (0.5nm steps)

16. Repeat steps 12-15 further three times to get spectra of four diluted samples in the absorption range of 190nm-405nm

17. The maximum absorbance at any wavelength should be below 3. In case of the absorbance being higher further dilute the solution

18. To further dilute, remove a small (measured) volume of the solution and add n-heptane

19. Repeat steps 12-15 until the maximum absorbance falls below 3

Appendix F

F.1   UV-Vis Week 2 and Week 3 350nm-1100nm

F.2 UV-Vis Week 1, Week 2 and Week 3 190nm-405nm

190nm-405nm Week 1

190nm-405nm Week 2

190nm-405nm Week 3

Legend:
- 8 hours
- 16 hours
- 24 hours
- 32 hours
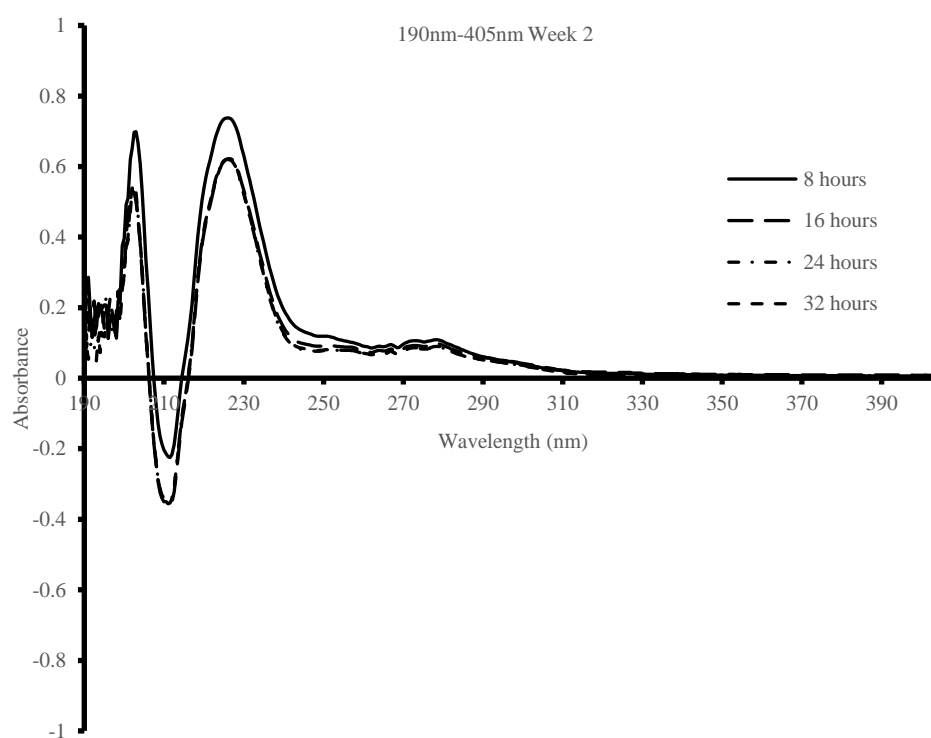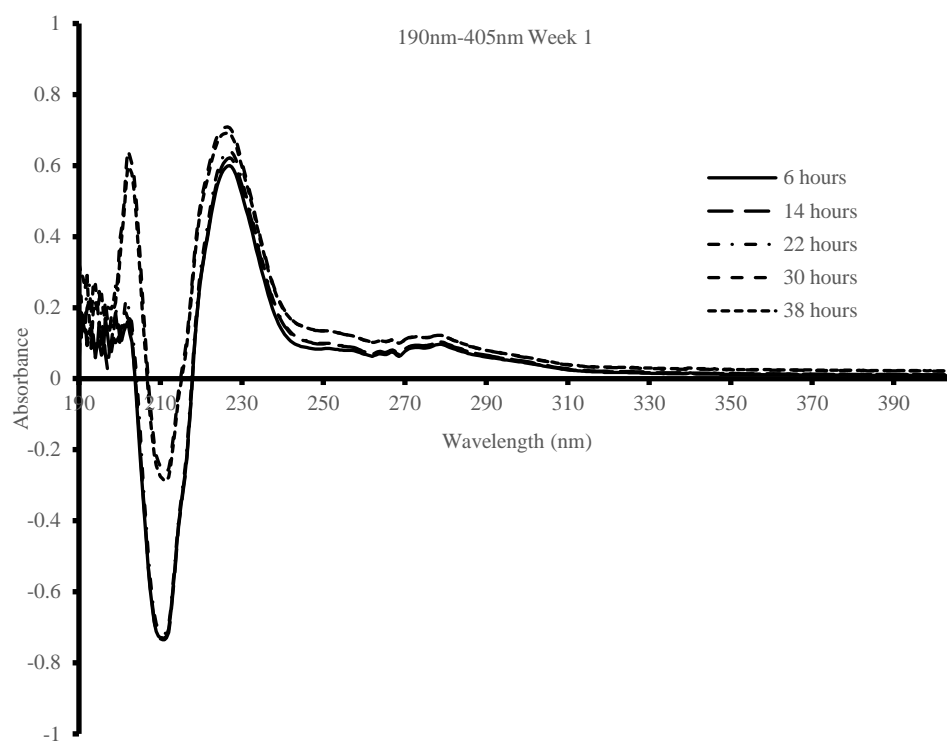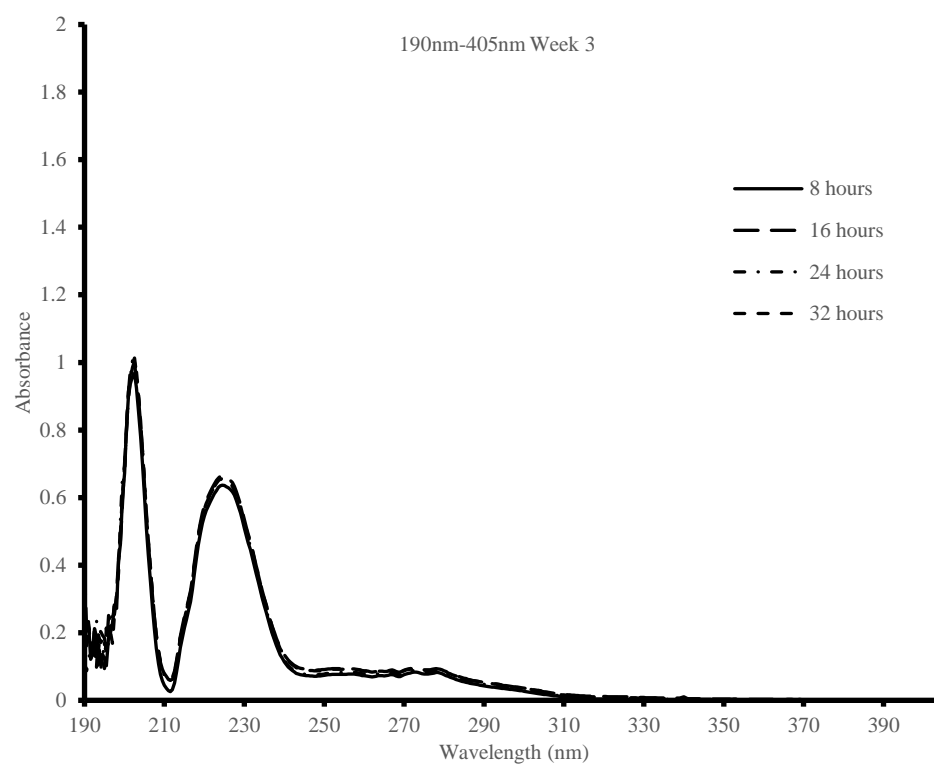
Appendix

Appendix G

G.1　Photographs of fluorescent fuel in high pressure recirculation rig at 200bar upstream pressure
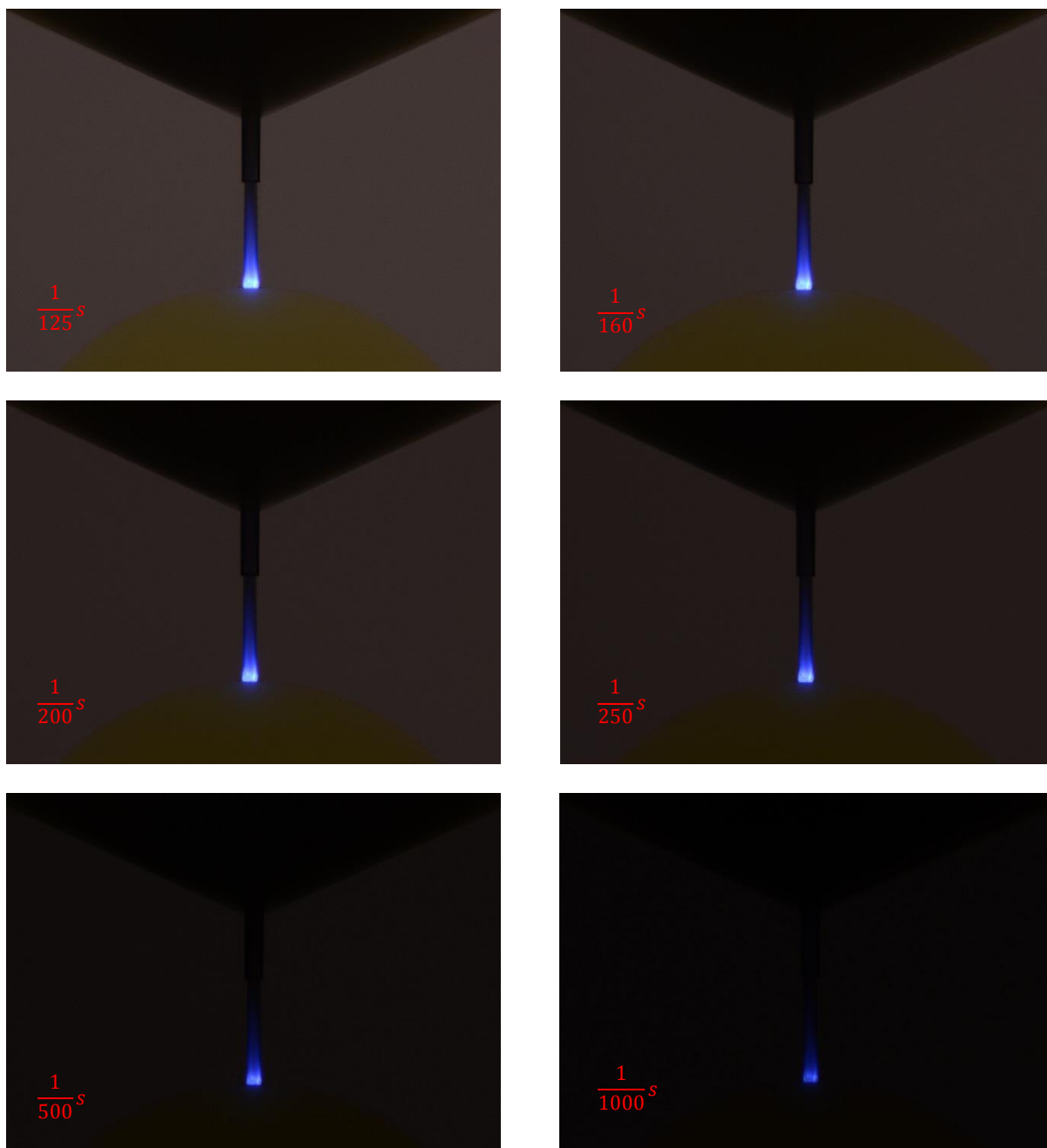
Each number in the images represents the shutter speed

G.2 Photographs of fluorescent fuel in high pressure recirculation rig at 250bar upstream pressure
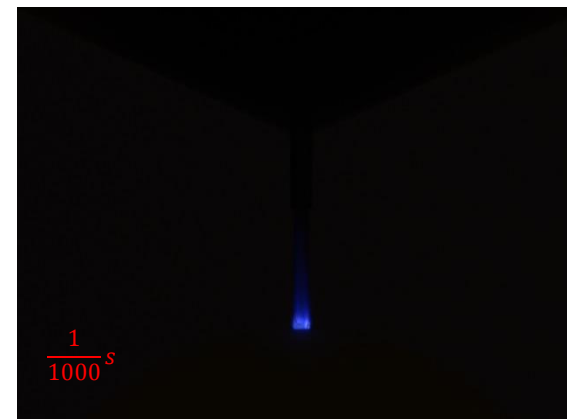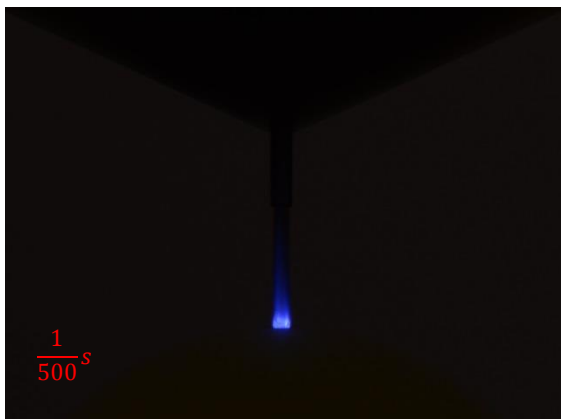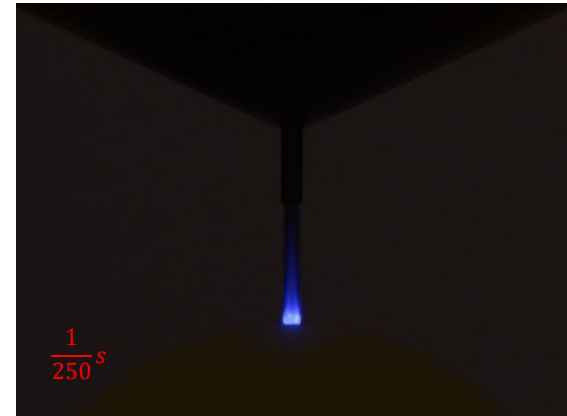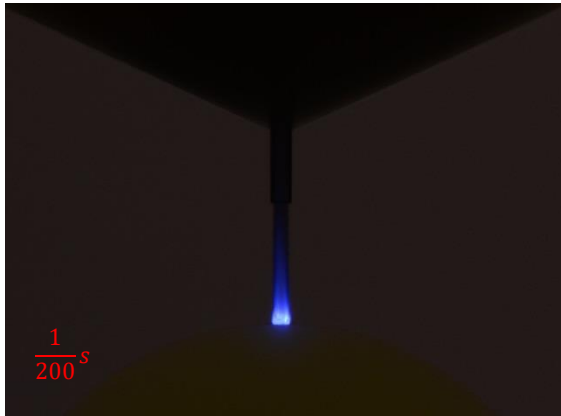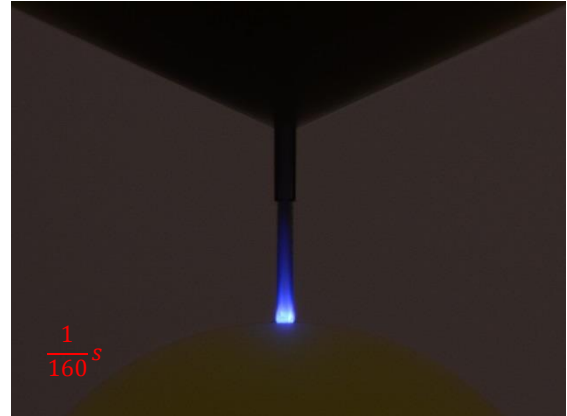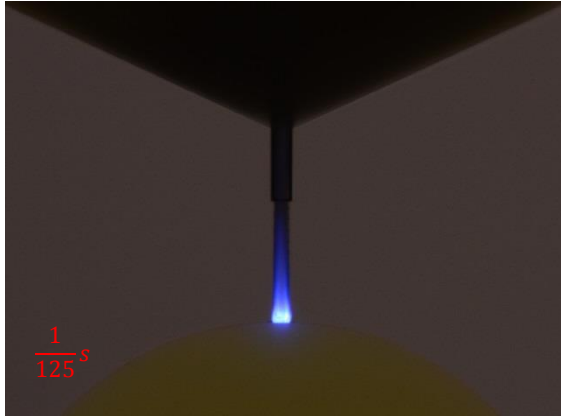
Each number in the images represents the shutter speed

References

[1]   O. Bunes and P. Einang, "Comparing the performance of the common rail fuel injection system with the traditional injection system using computer aided modelling and simulation," *MARINTEK paper at ENSUS*, 2000.

[2]   E. Plamondon and P. Seers, "Development of a simplified dynamic model for a piezoelectric injector using multiple injection strategies with biodiesel/diesel-fuel blends," *Applied Energy*, vol. 131, pp. 411–424, 2014.

[3]   F. Boudy and P. Seers, "Impact of physical properties of biodiesel on the injection process in a common-rail direct injection system," *Energy Conversion and Management*, vol. 50, no. 12, pp. 2905–2912, 2009.

[4]   R. Z. Van Romunde, "Factors affecting the development of sprays produced by multihole injectors for direct-injection engine applications," 2011.

[5]   A. Theodorakakos, N. Mitroglou, and M. Gavaises, "Simulation of heating effects caused by extreme fuel pressurisation in cavitating flows through Diesel fuel injectors," *CAV2012, Singapore*, 2012.

[6]   J. Barker, P. Richards, M. Goodwin, and J. Wooler, "Influence of High Injection Pressure on Diesel Fuel Stability: A Study of Resultant Deposits," *SAE International Journal of Fuels and Lubricants*, vol. 2, no. 1, pp. 877–884, 2009.

[7]   B. F. Wellington, *Diesel engines and fuel systems*, 5th ed. 2012.

[8]   A. Birgel, N. Ladommatos, P. Aleiferis, N. Milovanovic, P. Lacey, and P. Richards, "Investigations on deposit formation in the holes of diesel injector nozzles," *SAE International Journal of Fuels and Lubricants*, vol. 5, no. 1, pp. 123–131, 2012.

[9]   R. J. Price, D. Blazina, G. C. Smith, and T. J. Davies, "Understanding the impact of cavitation on hydrocarbons in the middle distillate range," *Fuel*, vol. 156, pp. 30–39, 2015.

[10]   MISSING:diver2007improving, "MISSING:diver2007improving," 2019.

[11]   K. S. Suslick, J. J. Gawienowski, P. F. Schubert, and H. H. Wang, "Alkane sonochemistry," *The Journal of Physical Chemistry*, vol. 87, no. 13, pp. 2299–2301, 1983.

[12]   G. J. Price and M. McCollom, "The effect of high-intensity ultrasound on diesel fuels," *Ultrasonics sonochemistry*, vol. 2, no. 2, pp. S67–S70, 1995.

[13]   G. J. Price and P. F. Smith, "Ultrasonic degradation of polymer solutions: 2. The effect of temperature, ultrasound intensity and dissolved gases on polystyrene in toluene," *Polymer*, vol. 34, no. 19, pp. 4111–4117, 1993.

[14]   K. S. Suslick, "The chemical effects of ultrasound," *Scientific American*, vol. 260, no. 2, pp. 80–87, 1989.

[15]   R. D. Lockett and M. Jeshani, "An experimental investigation into the effect of hydrodynamic cavitation on diesel," *International Journal of Engine Research*, vol. 14, no. 6, pp. 606–621, 2013.

[16]   R. Lockett, Z. Fatmi, O. Kuti, and R. Price, "An Optical Characterization of the Effect of High-Pressure Hydrodynamic Cavitation on Diesel," *SAE Technical Papers*, pp. 2014–01, 2016.

[17]   R. Payri, B. Tormos, F. Salvador, and A. Plazas, "Using one-dimensional modelling codes to analyse the influence of diesel nozzle geometry on injection rate characteristics," *International Journal of vehicle design*, vol. 38, no. 1, pp. 58–78, 2005.

[18]   R. Payri, H. Climent, F. Salvador, and A. Favennec, "Diesel injection system modelling. Methodology and application for a first-generation common rail system," *Proceedings of the Institution of Mechanical Engineers, Part D: Journal of Automobile Engineering*, vol. 218, no. 1, pp. 81–91, 2004.

[19]   V. Macián, V. Bermúdez, R. Payri, and J. Gimeno, "New technique for determination of internal geometry of a diesel nozzle with the use of silicone methodology," *Experimental techniques*, vol. 27, no. 2, pp. 39–43, 2003.

[20]   P. Aleiferis, Y. Hardalupas, D. Kolokotronis, A. Taylor, and T. Kimura, "Investigation of the internal flow field of a Diesel model injector using particle image velocimetry and CFD," 2007.

[21]   G. Marketing, "Diesel Fuels Technical Review," 2007.

[22]   B. J. Z. Q. L. C. K. Wang, "Optimization of a crude oil distillation unit based on total-process simulation," *ESCAPE 26*, 2016.

[23]   J. Ancheyta, M. S. Rana, and E. Furimsky, "Hydroprocessing of heavy petroleum feeds: Tutorial," *Catalysis Today*, vol. 109, no. 1, pp. 3–15, 2005.

[24]   A. Marcus, "Diesel Fuel Basics: What is Diesel Fuel, and where does it comes from?," *PassageMaker*, 1999.

[25]   A. Standard, "D86, 2007a, Standard Test Method for Distillation of Petroleum Products at Atmospheric Pressure, ASTM International, West Conshohocken, PA."

[26]   C. O'Connor, R. Forrester, and M. Scurrell, "Cetane number determination of synthetic diesel fuels," *Fuel*, vol. 71, no. 11, pp. 1323–1327, 1992.

[27]   J. E. Finnemore and J. B. Franzini, *Fluid mechanics: with engineering applications*. McGraw-Hill, 2002.

[28]   A. H. Lefebvre and V. G. McDonell, *Atomization and sprays*. CRC press, 2017.

[29] N. Hooftman, L. Oliveira, M. Messagie, T. Coosemans, and J. Van Mierlo, "Environmental Analysis of petrol, diesel and electric passenger cars in a Belgian urban setting," *Energies*, vol. 9, no. 2, p. 84, 2016.

[30] M. Williams and R. Minjares, "A technical summary of Euro 6/VI vehicle emissions standards," *ICCT International council on clean transportation*, 2016.

[31] M. Weiss, P. Bonnel, R. Hummel, U. Manfredi, R. Colombo, G. Lanappe, P. Le Lijour, M. Sculati, and others, "Analyzing on-road emissions of light-duty vehicles with Portable Emission Measurement Systems (PEMS)," *JRC Scientific and Technical Reports, EUR*, vol. 24697, 2011.

[32] R. Muncrief, "Comparing Real-World Off-Cycle NO x Emissions Control in Euro IV, V, and VI," *Fonte: http://www. theicct. org/comparing-real-world-nox-euro-iv*, vol. 6, 2015.

[33] M. Bassiony, A. Ibrahim, and M. El-Kassaby, "An experimental study on the effect of using gas-to-liquid (GTL) fuel on diesel engine performance and emissions," *Alexandria Engineering Journal*, vol. 55, no. 3, pp. 2115–2124, 2016.

[34] D. ASTM, "6751-02, Standard Specification for Biodiesel Fuel (B100) Blend Stock for Distillate Fuels," 2002.

[35] V. Ganesan, *Internal combustion engines*. McGraw Hill Education (India) Pvt Ltd, 2012.

[36] A. T. C. of P. A. M. in Europe, "Fuel Additives: Use and Benefits," 2013.

[37] S. P. Srivastava and J. Hancsok, *Fuels and fuel-additives*. John Wiley \& Sons, 2014.

[38] M. S. V. 1 of 2, "DOE FUNDAMENTALS HANDBOOK," 1993.

[39] M. Palanisamy, J. Lorch, R. J. Truemner, and B. Baldwin, "Combustion characteristics of a 3000 bar diesel fuel system on a single cylinder research engine," *SAE International Journal of Commercial Vehicles*, vol. 8, no. 2015–01–2798, pp. 479–490, 2015.

[40] K. Reif, *Diesel engine management*. Springer, 2014.

[41] P. J. Dingle and M.-C. D. Lai, "Diesel common rail and advanced fuel injection systems," 2005.

[42] K. G. Johnson, K. Mollenhauer, and H. Tschöke, *Handbook of diesel engines*. Springer Science \& Business Media, 2010.

[43] H. Heisler, "Advanced engine technology," 1995.

[44] M. K. Khair, "Pump-Line-Nozzle Injection System," *DieselNet.com*, 2010.

[45] R. B. GmbH, *Distributor Type Diesel Fuel Injection Pumps*. 2003.

[46] H. Tschöke, *Diesel Distributor Fuel-injection Pumps VE*. Robert Bosch GmbH, Automotive Equipment Business Sector, Department for Technical Information, 1999.

[47] T. Kitchen, "Common Rail Diesel Fuel Systems," *AK Training*, 2016.

[48] J.-P. Franc and J.-M. Michel, *Fundamentals of cavitation*, vol. 76. Springer Science \& Business Media, 2006.

[49] C. E. Brennen, "An introduction to cavitation fundamentals," 2011.

[50] C. Arcoumanis, H. Flora, M. Gavaises, N. Kampanis, and R. Horrocks, "Investigation of cavitation in a vertical multi-hole injector," 1999.

[51] C. E. Brennen, *Cavitation and bubble dynamics*. Cambridge University Press, 2013.

[52] M. S. Plesset and A. Prosperetti, "Bubble dynamics and cavitation," *Annual review of fluid mechanics*, vol. 9, no. 1, pp. 145–185, 1977.

[53] G. Kuiper, "Cavitation in ship propulsion," *Delft: Delft University of Technology*, 2010.

[54] A. de Bosset, D. Obreschkow, P. Kobel, N. Dorsaz, and M. Farhat, "Direct effects of gravity on cavitation bubble collapse," in *58th International Astronautical Congress IAC*, 2007, no. EPFL-CONF-162238.

[55] M. S. Plesset and R. B. Chapman, "Collapse of an initially spherical vapour cavity in the neighbourhood of a solid boundary," *Journal of Fluid Mechanics*, vol. 47, no. 2, pp. 283–290, 1971.

[56] W. Lauterborn and H. Bolle, "Experimental investigations of cavitation-bubble collapse in the neighbourhood of a solid boundary," *Journal of Fluid Mechanics*, vol. 72, no. 2, pp. 391–399, 1975.

[57] D. R. Stinebring, M. L. Billet, J. W. Lindau, and R. F. Kunz, "Developed cavitation-cavity dynamics," 2001.

[58] P. R. Gogate, R. K. Tayal, and A. B. Pandit, "Cavitation: a technology on the horizon," *Current Science*, vol. 91, no. 1, pp. 35–46, 2006.

[59] V. Moholkar, P. S. Kumar, and A. Pandit, "Hydrodynamic cavitation for sonochemical effects," *Ultrasonics Sonochemistry*, vol. 6, no. 1, pp. 53–65, 1999.

[60] F. Caupin and E. Herbert, "Cavitation in water: a review," *Comptes Rendus Physique*, vol. 7, no. 9–10, pp. 1000–1017, 2006.

[61] P. R. Gogate and A. B. Pandit, "Engineering design methods for cavitation reactors II: hydrodynamic cavitation," *AIChE journal*, vol. 46, no. 8, pp. 1641–1649, 2000.

[62] M. Dular, T. Griessler-Bulc, I. Gutierrez-Aguirre, E. Heath, T. Kosjek, A. K. Klemen\vci\vc, M. Oder, M. Petkov\vsek, N. Ra\vcki, M. Ravnikar, and others, "Use of hydrodynamic cavitation in (waste) water treatment," *Ultrasonics sonochemistry*,

vol. 29, pp. 577–588, 2016.

[63]   H. Soyama and J. Hoshino, "Enhancing the aggressive intensity of hydrodynamic cavitation through a Venturi tube by increasing the pressure in the region where the bubbles collapse," *AIP Advances*, vol. 6, no. 4, p. 045113, 2016.

[64]   T. A. Bashir, A. G. Soni, A. V. Mahulkar, and A. B. Pandit, "The CFD driven optimisation of a modified venturi for cavitational activity," *The Canadian Journal of Chemical Engineering*, vol. 89, no. 6, pp. 1366–1375, 2011.

[65]   M. Sivakumar and A. B. Pandit, "Wastewater treatment: a novel energy efficient hydrodynamic cavitational technique.," *Ultrason Sonochem*, vol. 9, no. 3, pp. 123–31, 2002.

[66]   V. K. Saharan, M. A. Rizwani, A. A. Malani, and A. B. Pandit, "Effect of geometry of hydrodynamically cavitating device on degradation of orange-G.," *Ultrason Sonochem*, vol. 20, no. 1, pp. 345–53, 2013.

[67]   M. Ashokkumar, "The characterization of acoustic cavitation bubbles - an overview.," *Ultrason Sonochem*, vol. 18, no. 4, pp. 864–72, 2011.

[68]   K. S. Suslick, "Sonochemistry," *science*, vol. 247, no. 4949, pp. 1439–1445, 1990.

[69]   S. Cook and P. Richards, "Possible influence of high injection pressure on diesel fuel stability: a review and preliminary study," 2009.

[70]   A. P. Nagalingam and S. Yeo, "Effects of ambient pressure and fluid temperature in ultrasonic cavitation machining," *The International Journal of Advanced Manufacturing Technology*, pp. 1–12, 2018.

[71]   J. P. Lorimer and T. J. Mason, "Sonochemistry. Part 1—the physical aspects," *Chemical Society Reviews*, vol. 16, pp. 239–274, 1987.

[72]   L. A. Crum, "Nucleation and stabilization of microbubbles in liquids," *Applied Scientific Research*, vol. 38, no. 1, pp. 101–115, 1982.

[73]   H. Frenzel and H. Schultes, "Luminescenz im ultraschallbeschickten Wasser," *Zeitschrift für Physikalische Chemie*, vol. 27, no. 1, pp. 421–424, 1934.

[74]   D. F. Gaitan, A. A. Atchley, S. Lewia, J. Carlson, X. Maruyama, M. Moran, and D. Sweider, "Spectra of single-bubble sonoluminescence in water and glycerin-water mixtures," *Physical Review E*, vol. 54, no. 1, p. 525, 1996.

[75]   T. G. Keith Jr and R. W. Honaker, "Investigation of a Method to Reduce Cavitation in Diesel Engine Bearings," 1998.

[76]   S. Mahmood, Y. Yoo, J. Oh, and H.-Y. Kwak, "Hydrodynamic approach to multibubble sonoluminescence.," *Ultrason Sonochem*, vol. 21, no. 4, pp. 1512–8, 2014.

[77] Y. T. Didenko and S. Pugach, "Spectra of water sonoluminescence," *The Journal of Physical Chemistry*, vol. 98, no. 39, pp. 9742–9749, 1994.

[78] E. B. Flint and K. S. Suslick, "Sonoluminescence from nonaqueous liquids: emission from small molecules," *Journal of the American Chemical Society*, vol. 111, no. 18, pp. 6987–6992, 1989.

[79] E. B. Flint and K. S. Suslick, "The temperature of cavitation," *Science*, vol. 253, no. 5026, pp. 1397–1399, 1991.

[80] K. Suslick, W. McNamara, and Y. Didenko, "Hot spot conditions during multi-bubble cavitation," in *Sonochemistry and sonoluminescence*, Springer, 1999, pp. 191–204.

[81] D. Czajczy'nska, L. Anguilano, H. Ghazal, R. Krzy\.zy'nska, A. Reynolds, N. Spencer, and H. Jouhara, "Potential of pyrolysis processes in the waste management sector," *Thermal Science and Engineering Progress*, vol. 3, pp. 171–197, 2017.

[82] G. J. Price and M. McCollom, "Use of high-intensity ultrasound as a potential test method for diesel fuel stability," *Fuel*, vol. 74, no. 9, pp. 1394–1397, 1995.

[83] A. L. Knox-Kelecy and P. V. Farrell, "Spectral characteristics of turbulent flow in a scale model of a diesel fuel injector nozzle," *SAE Transactions*, pp. 1408–1416, 1993.

[84] "Perspex Acrylic & Acrylic Index." [Online]. Available: https://www.theplasticshop.co.uk/perspex-acrylic-index.html. [Accessed: 06-2018].

[85] "Quartz Glass for Optics Data and Properties." [Online]. Available: https://www.heraeus.com/en/hqs/fused_silica/home_hqs.aspx.

[86] "LightFab." [Online]. Available: https://www.lightfab.de/. [Accessed: 11–09-2018].

[87] R. Lockett, N. Ndamuso, and R. Price, "Cavitation Inception in Immersed Jet Shear Flows," in *Journal of Physics: Conference Series*, 2015, vol. 656, no. 1, p. 012090.

[88] N. Ndamuso, "Parametric studies of cavitation dependence on hydrocarbon and biodiesel fuel injection flows," 2017.

[89] "GTL Gas Oil Safety Data Sheet." [Online]. Available: http://www.vidol.eu/m_downloads/upload/GSAP_msds_00323548.PDF.

[90] "Bernoulli's Equation." [Online]. Available: https://www.grc.nasa.gov/www/k-12/airplane/bern.html. [Accessed: 05–02-2019].

[91] "Shell V Power Diesel: Safety Data Sheet." [Online]. Available: https://www.shell.com.au/motorists/shell-fuels/sds-tds/_jcr_content/par/textimage_278c.stream/1527137454667/a88b894b893152440873 845b067bbf9b0775641aeec1274d573c6b9177d4c33c/shell-v-power-diesel-sds.pdf. [Accessed: 02-Apr-2019].

[92] M. Jeshani, "Optical characterisation of cavitating flows in diesel fuel injection equipment," 2013.

[93] *Instruction Manual Operation Guide UV-1800 Shimadzu Spectrophotometer*. 2008.

[94] Z. Fatmi, "Optical and chemical characterisation of the effects of high-pressure hydrodynamic cavitation on diesel fuel ," 2018.

[95] R. W. Burnett, "Accurate measurement of molar absorptivities," *J. Res. Natl. Bur. Stand. A Phys. Chem*, vol. 76, pp. 483–489, 1972.

[96] "Visible and Ultraviolet Spectroscopy." [Online]. Available: https://www2.chemistry.msu.edu/faculty/reusch/virttxtjml/spectrpy/uv-vis/spectrum.htm. [Accessed: 17–09-2018].

[97] R. Shukla, A. Dubey, V. Pandey, D. Golhani, and A. P. Jain, "Chromophore-An Utility in UV Spectrophotometer," *Inventi Rapid: Pharm Ana \& Qual Assur*, 2012.

[98] "Ultraviolet and Visible Absorption Spectroscopy." [Online]. Available: https://www.philadelphia.edu.jo/academics/ajaber/uploads/CHEM%20540-UV-Vis-%20061-lect%201.pdf. [Accessed: 17–09-2018].

[99] A. Csubst, "ARENES. ELECTROPH AROMAT Csubst."

[100] J. Steffens, E. Landulfo, L. C. Courrol, and R. Guardani, "Application of fluorescence to the study of crude petroleum," *Journal of fluorescence*, vol. 21, no. 3, pp. 859–864, 2011.

[101] *125mm SPECTROGRAPH MODEL 77400*. 250 Long Beach Boulevard, Stratford.

[102] A. Bogaerts, E. Neyts, R. Gijbels, and J. van der Mullen, "Gas discharge plasmas and their applications," *Spectrochimica Acta Part B: Atomic Spectroscopy*, vol. 57, no. 4, pp. 609–658, 2002.

[103] R. Baghel and A. Luka, "Phenomena of fluorescence and phosphorescence," *Recent Research in Science and Technology*, vol. 4, no. 8, 2012.

[104] M. Heintze, M. Magureanu, and M. Kettlitz, "Mechanism of C 2 hydrocarbon formation from methane in a pulsed microwave plasma," *Journal of applied physics*, vol. 92, no. 12, pp. 7022–7031, 2002.

[105] M. Quitzau, M. Wolter, V. Zaporojtchenko, H. Kersten, and F. Faupel, "Modification of polyethylene powder with an organic precursor in a spiral conveyor by hollow cathode glow discharge," *The European Physical Journal D*, vol. 58, no. 3, pp. 305–310, 2010.

[106] C. K. Westbrook, W. J. Pitz, O. Herbinet, H. J. Curran, and E. J. Silke, "A comprehensive detailed chemical kinetic reaction mechanism for combustion of n-alkane hydrocarbons from n-octane to n-hexadecane," *Combustion and flame*, vol. 156, no. 1, pp. 181–199, 2009.

[107] C. Chevalier, W. Pitz, J. Warnatz, C. Westbrook, and H. Melenk, "Hydrocarbon ignition: automatic generation of reaction mechanisms and applications to modeling of engine knock," in *Symposium (International) on Combustion*, 1992, vol. 24, no. 1, pp.

93–101.

[108] M. Nehse, J. Warnat, and C. Chevalier, "Kinetic modeling of the oxidation of large aliphatic hydrocarbons," in *Symposium (International) on Combustion*, 1996, vol. 26, no. 1, pp. 773–780.

[109] P. Dagaut, M. Reuillon, J.-C. Boettner, and M. Cathonnet, "Kerosene combustion at pressures up to 40 atm: Experimental study and detailed chemical kinetic modeling," in *Symposium (International) on Combustion*, 1994, vol. 25, no. 1, pp. 919–926.

[110] P. Dagaut, S. Ga\i, M. Sahasrabudhe, and others, "Rapeseed oil methyl ester oxidation over extended ranges of pressure, temperature, and equivalence ratio: Experimental and modeling kinetic study," *Proceedings of the Combustion Institute*, vol. 31, no. 2, pp. 2955–2961, 2007.

[111] E. Olchanski and A. Burcat, "Decane oxidation in a shock tube," *International journal of chemical kinetics*, vol. 38, no. 12, pp. 703–713, 2006.

[112] G. Bikas and N. Peters, "Kinetic modelling of n-decane combustion and autoignition: Modeling combustion of n-decanem," *Combustion and Flame*, vol. 126, no. 1–2, pp. 1456–1475, 2001.

[113] S. P. Zeppieri, S. D. Klotz, and F. L. Dryer, "Modeling concepts for larger carbon number alkanes: a partially reduced skeletal mechanism for n-decane oxidation and pyrolysis," *Proceedings of the Combustion Institute*, vol. 28, no. 2, pp. 1587–1595, 2000.

[114] R. Lindstedt and L. Maurice, "Detailed kinetic modelling of n-heptane combustion," *Combustion Science and Technology*, vol. 107, no. 4–6, pp. 317–353, 1995.

[115] P. Dagaut and M. Cathonnet, "The ignition, oxidation, and combustion of kerosene: A review of experimental and kinetic modeling," *Progress in energy and combustion science*, vol. 32, no. 1, pp. 48–92, 2006.

[116] F. Buda, R. Bounaceur, V. Warth, P.-A. Glaude, R. Fournet, and F. Battin-Leclerc, "Progress toward a unified detailed kinetic model for the autoignition of alkanes from C4 to C10 between 600 and 1200 K," *Combustion and flame*, vol. 142, no. 1–2, pp. 170–186, 2005.

[117] E. Ranzi, A. Frassoldati, S. Granata, and T. Faravelli, "Wide-range kinetic modeling study of the pyrolysis, partial oxidation, and combustion of heavy n-alkanes," *Industrial \& engineering chemistry research*, vol. 44, no. 14, pp. 5170–5183, 2005.

[118] H. Richter, S. Granata, W. H. Green, and J. B. Howard, "Detailed modeling of PAH and soot formation in a laminar premixed benzene/oxygen/argon low-pressure flame," *Proceedings of the Combustion Institute*, vol. 30, no. 1, pp. 1397–1405, 2005.

[119] M. Frenklach, "Reaction mechanism of soot formation in flames," *Physical chemistry chemical Physics*, vol. 4, no. 11, pp. 2028–2037, 2002.

[120] M. Balthasar and M. Kraft, "A stochastic approach to calculate the particle size distribution function of soot particles in laminar premixed flames," *Combustion and*

Flame, vol. 133, no. 3, pp. 289–298, 2003.

[121] C. Saggese, S. Ferrario, J. Camacho, A. Cuoci, A. Frassoldati, E. Ranzi, H. Wang, and T. Faravelli, "Kinetic modeling of particle size distribution of soot in a premixed burner-stabilized stagnation ethylene flame," *Combustion and Flame*, vol. 162, no. 9, pp. 3356–3369, 2015.

[122] S. Granata, F. Cambianica, S. Zinesi, T. Faravelli, and E. Ranzi, "Detailed kinetics of PAH and soot formation in combustion processes: analogies and similarities in reaction classes," in *EUROPEAN COMBUSTION MEETING," ECM2005,"* 2005, p. paper–35.

[123] "C1-C4 mechanism with PAH formation." [Online]. Available: https://combustion.llnl.gov/mechanisms/aromatic-and-pah-formation/c1c4-mechanism-with-pah-formation. [Accessed: 21–09-2018].

[124] "C8-C16 n-Alkanes." [Online]. Available: https://combustion.llnl.gov/archived-mechanisms/alkanes/c8c16-nalkanes. [Accessed: 21–09-2018].

[125] "CRECK Modeling Group: Soot Kinetic Mechanism." [Online]. Available: http://creckmodeling.chem.polimi.it/menu-kinetics/menu-kinetics-special-mechanisms/menu-kinetics-soot-mechanism. [Accessed: 21–09-2018].

[126] N. M. Marinov, W. J. Pitz, C. K. Westbrook, A. M. Vincitore, M. J. Castaldi, S. M. Senkan, and C. F. Melius, "Aromatic and polycyclic aromatic hydrocarbon formation in a laminar premixed n-butane flame," *Combustion and flame*, vol. 114, no. 1–2, pp. 192–213, 1998.

[127] R. Kee, F. Rupley, E. Meeks, and J. Miller, "CHEMKIN: A Software package for the analysis of gas-phase chemical and plasma kinetics," *Sandia National Laboratories Report SAND96-8216, CA*, 2000.

[128] R. Kee, G. Dixon-Lewis, J. Warnatz, M. Coltrin, J. Miller, and H. Moffat, "Transport: a software package for the evaluation of gas-phase, multicomponent transport properties," *Chemkin Collection*, 1999.

[129] D. Davidson and R. Hanson, "Fundamental kinetics database utilizing shock tube measurements," *Mechanical Engineering Department, Stanford University, Stanford CA*, 2005.

[130] S. S. Vasu, D. F. Davidson, and R. K. Hanson, "Shock-tube experiments and kinetic modeling of toluene ignition," *Journal of propulsion and power*, vol. 26, no. 4, pp. 776–783, 2010.

[131] D. Haylett, R. Cook, D. Davidson, and R. Hanson, "OH and C2H4 species time-histories during hexadecane and diesel ignition behind reflected shock waves," *Proceedings of the Combustion Institute*, vol. 33, no. 1, pp. 167–173, 2011.

[132] J. Camacho, C. Liu, C. Gu, H. Lin, Z. Huang, Q. Tang, X. You, C. Saggese, Y. Li, H. Jung, and others, "Mobility size and mass of nascent soot particles in a benchmark premixed ethylene flame," *Combustion and Flame*, vol. 162, no. 10, pp. 3810–3822,

2015.

[133] Y. A. Cengel and M. A. Boles, "Thermodynamics: an engineering approach," *Sea*, vol. 1000, p. 8862, 2002.